

**Wind turbine rotor aerodynamics**  
**The IEA MEXICO rotor explained**

Zhang, Ye

**DOI**

[10.4233/uuid:f8112b0f-d697-4e5c-bbff-ea7eae5ab50c](https://doi.org/10.4233/uuid:f8112b0f-d697-4e5c-bbff-ea7eae5ab50c)

**Publication date**

2017

**Document Version**

Final published version

**Citation (APA)**

Zhang, Y. (2017). *Wind turbine rotor aerodynamics: The IEA MEXICO rotor explained*. [Dissertation (TU Delft), Delft University of Technology]. <https://doi.org/10.4233/uuid:f8112b0f-d697-4e5c-bbff-ea7eae5ab50c>

**Important note**

To cite this publication, please use the final published version (if applicable).  
Please check the document version above.

**Copyright**

Other than for strictly personal use, it is not permitted to download, forward or distribute the text or part of it, without the consent of the author(s) and/or copyright holder(s), unless the work is under an open content license such as Creative Commons.

**Takedown policy**

Please contact us and provide details if you believe this document breaches copyrights.  
We will remove access to the work immediately and investigate your claim.

# **WIND TURBINE ROTOR AERODYNAMICS**

THE IEA MEXICO ROTOR EXPLAINED





# **WIND TURBINE ROTOR AERODYNAMICS**

THE IEA MEXICO ROTOR EXPLAINED

## **Proefschrift**

ter verkrijging van de graad van doctor  
aan de Technische Universiteit Delft,  
op gezag van de Rector Magnificus prof. ir. K. C. A. M. Luyben,  
voorzitter van het College voor Promoties,  
in het openbaar te verdedigen op woensdag 14 juni 2017 om 12:30 uur

door

**YE ZHANG**

Master of Science in Thermal Energy and Power Engineering  
Dalian University of Technology, Dalian, China  
geboren te Heilongjiang, China.

This dissertation has been approved by:

promotor: Prof. dr. ir. G. J. W. van Bussel

copromotor: Dr. ir. A. H. van Zuijlen

Composition of the doctoral committee:

Rector Magnificus,

voorzitter

Prof. dr. ir. G. J. W. van Bussel

Technische Universiteit Delft, promotor

Dr. ir. A. H. van Zuijlen

Technische Universiteit Delft, copromotor

Independent members:

Prof. dr. ir. G. Eitelberg

Technische Universiteit Delft

Prof. dr. N. N. Sørensen

Technical University of Denmark

Prof. dr. A. P. Schaffarczyk

Kie University, Germany

Dr. ir. J. G. Schepers

Energy research Centre of the Netherlands

Other members:

Prof. dr. ir. drs H. Bijl Technische Universiteit Delft & Leiden

Reserved members:

Prof. dr. ir. G. A. M. van Kuik Technische Universiteit Delft



*Keywords:* MEXICO rotor, rotor aerodynamics, CFD, OpenFOAM, ZigZag effects, loads overprediction, transition modeling, turbulence modeling, detached eddy simulation, PIV

*Printed by:* ProefschriftMaken

*Cover:* Photo is taken from <https://www.evwind.es/2015/07/04/offshore-wind-power-630-mw-london-array-wind-farm-with-175-wind-turbines/53165>

Copyright © 2017 by Ye Zhang

ISBN 978-94-6186-815-2

An electronic version of this dissertation is available at  
<http://repository.tudelft.nl/>.

To my family, for their patience, support and love

# CONTENTS

<b>Summary</b>	<b>ix</b>
<b>Samenvatting</b>	<b>xi</b>
<b>1 Introduction</b>	<b>13</b>
1.1 Research background . . . . .	14
1.2 Motivation and objectives. . . . .	19
1.3 Thesis outline. . . . .	21
<b>2 Wind turbine aerodynamics</b>	<b>23</b>
2.1 2D airfoil aerodynamics. . . . .	24
2.2 3D finite wing aerodynamics . . . . .	26
2.3 Wind turbine blade aerodynamics . . . . .	29
2.4 Rotor aerodynamics modeling . . . . .	30
2.4.1 Blade element momentum method . . . . .	30
2.4.2 Vortex wake model. . . . .	35
2.4.3 Navier-Stokes based method. . . . .	37
2.5 Conclusions. . . . .	40
<b>3 Verification and validation of OpenFOAM code</b>	<b>43</b>
3.1 Introduction . . . . .	44
3.2 Validation of turbulence models . . . . .	44
3.2.1 Eddy viscosity turbulence model. . . . .	44
3.2.2 Hybrid RANS/LES model. . . . .	51
3.3 Validation of transition models . . . . .	58
3.3.1 The structure of $k - k_L - \omega$ transition model . . . . .	58
3.3.2 $k - k_L - \omega$ implementation and corrections in OpenFOAM. . . . .	58
3.3.3 Test cases . . . . .	59
3.4 Conclusions. . . . .	68
<b>4 Experimental and numerical study of the non-rotating MEXICO blade</b>	<b>69</b>
4.1 Introduction . . . . .	70
4.2 Experimental and numerical setup . . . . .	70
4.2.1 Experimental approach . . . . .	70
4.2.2 Numerical approach . . . . .	76
4.3 Results and analysis. . . . .	78
4.3.1 Flow at low angles of attack . . . . .	78
4.3.2 The effects of ZigZag tape . . . . .	90
4.3.3 Flow at high angles of attack . . . . .	98
4.4 Conclusions. . . . .	101

<b>5</b>	<b>Numerical investigation of 3D rotating MEXICO rotor</b>	<b>103</b>
5.1	Introduction . . . . .	104
5.2	Wind tunnel measurement database . . . . .	104
5.2.1	Rotating measurements of the MEXICO rotor at DNW . . . . .	104
5.2.2	Non-rotating measurement of the MEXICO blades at TUDelft . . . . .	106
5.2.3	2D static airfoil wind tunnel measurement. . . . .	106
5.3	Rotation modeling in OpenFOAM. . . . .	106
5.4	Results and discussion . . . . .	108
5.4.1	Aerodynamic loads comparison between experiment and BEM re- sults . . . . .	108
5.4.2	Velocity field comparison with PIV. . . . .	110
5.4.3	Crosssectional rotational effects . . . . .	114
5.4.4	Radial flow and Coriolis force . . . . .	122
5.4.5	Transitional effects. . . . .	127
5.4.6	Stall condition at $\lambda = 4.17$ . . . . .	133
5.5	Conclusions. . . . .	137
<b>6</b>	<b>Aerodynamics study of the TUDelft Blade 2 rotor</b>	<b>139</b>
6.1	Introduction . . . . .	140
6.2	Experimental and numerical description of TUDelft Blade 2 rotor . . . . .	140
6.3	Results and analysis. . . . .	143
6.3.1	Velocity decomposition . . . . .	143
6.3.2	Force estimation and decomposition . . . . .	148
6.4	Conclusions. . . . .	151
<b>7</b>	<b>Conclusions and recommendations</b>	<b>155</b>
7.1	Conclusions. . . . .	156
7.1.1	OpenFOAM performance . . . . .	156
7.1.2	Causes of deviation . . . . .	157
7.1.3	Advanced numerical modeling. . . . .	158
7.2	Recommendations . . . . .	159
7.2.1	3D fluid structure interaction . . . . .	159
7.2.2	Flow control modeling on wind turbine blade . . . . .	159
	<b>ACKNOWLEDGEMENTS</b>	<b>169</b>
	<b>List of Publications</b>	<b>171</b>
	<b>Curriculum Vitæ</b>	<b>173</b>

# SUMMARY

Wind turbines are operating under very complex and uncontrolled environmental conditions, including atmospheric turbulence, atmospheric boundary layer effects, directional and spatial variations in wind shear, etc. Over the past decades, the size of a commercial wind turbine has increased considerably. All the complex and uncontrolled conditions mentioned above result in uncertainties of aerodynamic loads calculation on very large wind turbine blades and thus better numerical codes are needed for predicting the loads in the design phase. With the aim to eliminate these uncontrolled effects and improve the aerodynamic models, in last decades, several important experimental campaigns of different wind turbine models have been performed in large wind tunnels. The objective of such experiments (e.g. using the NREL wind turbine and the MEXICO rotor) is to provide high quality measurement data which can be used to validate numerical models and improve different fidelity numerical codes, particularly for predicting wind turbine aerodynamic loads.

Problems arose as a result of blind comparisons between (initially not disclosed) measured data and numerical predictions, in which large deviations were observed in both comparison campaigns, even at the easy-to-predict conditions. For instance, all numerical models, including high fidelity CFD codes, show a poor prediction of sectional normal force for the MEXICO rotor at design tip speed ratio, especially a significant overprediction at the tip region ( $r/R = 0.82, 0.92$ ). These discrepancies are observed and presented in many research reports and publications without a clear understanding of the causes.

Therefore, in this thesis, a detailed and thorough investigation of wind turbine rotor aerodynamics is performed with both experimental and numerical approaches. Firstly, the open source CFD code (OpenFOAM-2.1.1) is improved and validated to obtain better wind turbine aerodynamics loads prediction. Before applying the open source code for investigating complex 3D flow, an OpenFOAM code has been extensively validated and evaluated for several two-dimensional flow cases, which is presented in Chapter 3. The numerical results of the OpenFOAM code compare well with another already validate code, theoretical solution or experimental data. The most popular linear eddy viscosity turbulence models (Spalart-Allmaras and  $k - \omega$  SST), implemented in OpenFOAM, have been validated. Moreover, an implementation error of recently developed transition model  $k - k_L - \omega$  in OpenFOAM has been corrected and the code has been further improved to predict laminar-turbulent boundary layer transition on a wind turbine airfoil. Based on the numerical results of these two-dimensional cases, confidence is obtained for simulating more complex 3D flow using this code.

Secondly, the causes of large discrepancies between the MEXICO measurement and the numerical results are identified in the thesis. This has been accomplished by re-assessing the loads prediction in the first MEXICO campaign and analyzing the possible causes of discrepancies such as: 1) the very complicated geometry of the MEXICO rotor



giving yield to 3D effects at places not expected, 2) the role of applying ZigZag tape on the rotor blades and its effect on the experimental results and 3) the malfunctioning of several Kulites pressure sensors. A unique new campaign has been set up to assess both experimentally and numerically these discrepancies and to find ways to mitigate them. In the experiments, the non-rotating MEXICO blades have been measured under a well-controlled conditions with the same Reynolds numbers in the low-speed low turbulence wind tunnel at the Delft University of Technology. The aerodynamic characteristics of three different blade sections with different airfoils (DU, RISØ, NACA) have been determined experimentally and compared with OpenFOAM simulation results. This study revealed two important insights into MEXICO experiments: The first insight is that the ZigZag tape, which had been used on the MEXICO blade, significantly affects the aerodynamic characteristics, especially for the tip region ( $r/R = 0.92$ ). The ZigZag tape effects on the non-rotating MEXICO blade have been quantitatively analyzed from experimental data. The second insight is the different post-stall aerodynamic characteristics of the DU and RISØ airfoils. A pair of counter-rotating vortices is generated behind the spanwise position  $r/R = 0.55$  as has been observed in the numerical study. At this span wise position the transition from RISØ airfoil to DU airfoil takes place. The induced velocity caused by these vortices alters the local velocity at each section, and consequently the upwash/downwash change the sectional loads of RISØ airfoil family considerably.

Thirdly, numerical predictions for the first and second series of MEXICO experiments are made using advanced numerical codes to check the improvements. For the MEXICO rotor at the design tip speed ratio  $\lambda = 6.67$ , to mitigate the possible causes of discrepancies, an OpenFOAM calculation with the improved boundary layer transition model is used. It is concluded that the knowledge and models obtained from the previous campaign result are much better predicted by comparison to the second set of the MEXICO rotor experiments in the DNW wind tunnel with improved calibration and clean blade measurements. It also demonstrated that the ZigZag tape used to trip the boundary layer on the blade was an important reason for the large discrepancy between CFD prediction and experimental results in the previous MEXICO blind comparison. A fully turbulent simulation, as initially also implemented in OpenFOAM, will significantly overpredict the aerodynamic loads near the tip for the MEXICO rotor with ZigZag tape blade configuration. The case with tip speed ratio  $\lambda = 4.17$  is challenging to simulate due to deep stall occurring over a large part of the blade. However, the hybrid LES/RANS approach (DDES) provides very good results of aerodynamic loads prediction, showing a reduction of the error in the sectional aerodynamic loads to  $\sim 5\%$  compared to RANS ( $\sim 20\%$ ). This OpenFOAM CFD implementation does an excellent job in predicting loads on a model rotor set-up ( the "TUDelft Blade 2 rotor experiment"). The comparisons show the superior performance of the current CFD code to predict aerodynamic loads compared to BEM and panel methods. The numerical studies of two different wind turbine rotors also reveal that the current tip loss correction models in BEM codes can be still improved.

# SAMENVATTING

Windturbines werken in zeer complexe en ongecontroleerde externe omstandigheden (o.a. turbulentie, atmosferische grenslaageffecten en ruimtelijke variaties in windscheuring). En in de afgelopen twintig jaar zijn de commerciële windturbines ook steeds groter geworden. De hierboven genoemde complexe en ongecontroleerde omstandigheden leiden tot onzekerheden in het berekenen van aerodynamische belastingen op zeer grote windturbinebladen, en dus zijn er in de ontwerpfase betere numerieke berekeningsmethoden nodig. Om het effect van de ongecontroleerde externe omstandigheden te elimineren zijn belangrijke, uitgebreide meetcampagnes uitgevoerd in grote windtunnels, gebruikmakend van verscheidene windturbine modellen. Het doel van dergelijke experimenten (b.v. uitgevoerd met de NREL windturbine en de MEXICO rotor) is om nauwkeurige data te verzamelen, die gebruikt kunnen worden voor het valideren van numerieke modellen en verbeteren van numerieke codes. Numerieke codes zijn met name geschikt voor het voorspellen van aerodynamische belastingen op windturbine rotoren maar verschillen onderling in de mate van detail en in het niveau van betrouwbaarheid.

In een aantal gevallen, waarbij de resultaten van experimenten niet werden geopenbaard voordat er berekeningen werden gemaakt (een "blinde" validatie) werden onverklaarbaar grote afwijkingen gevonden, zelfs voor de zeer normale operationele condities. Zo wordt de normaalkracht op de MEXICO rotor bij de ontwerp snellopendheid door alle CFD codes slecht voorspeld, zelfs door de meest geavanceerde codes. Met name voor de blad secties in de tip regio ( $r/R = 0.82$  en  $0.92$ ) wordt deze normaalkracht sterk overschat. Deze afwijkingen worden beschreven in veel onderzoeksrapporten en publicaties, zonder dat er een duidelijke verklaring voor gegeven wordt.

Vandaar dat in dit proefschrift een gedetailleerd en uitvoerig experimenteel en numeriek onderzoek is gedaan naar de rotor aerodynamica van wind turbine rotoren. Als eerste wordt de open-source CFD code (OpenFOAM-2.1.1) verbeterd en gevalideerd met betrekking tot het voorspellen van aerodynamische belastingen op windturbine rotoren. Maar voor dat deze open-source code wordt gebruikt voor het onderzoeken van complexe 3D stromingen, is OpenFOAM code uitgebreid gevalideerd aan de hand van 2D casussen, die beschreven zijn in hoofdstuk 3. De numerieke voorspellingen met de OpenFOAM code komen goed overeen met zowel de numerieke voorspellingen van andere CFD code, met analytische oplossingen en met de experimentele data. De meest gebruikte turbulentie modellen, die uitgaan van een lineaire wervelviscositeit, zoals Spalart-Allmaras en  $k - \omega$  SST, zijn hierbij gevalideerd. Bovendien is een programmeerfout in het  $k - k_L - \omega$  transitie model van OpenFOAM gecorrigeerd en vervolgens is de code verbeterd met betrekking tot het voorspellen van grenslaagtransitie op bladprofielen van windturbines. Op basis van numerieke voorspellingen voor de 2D casussen is voldoende vertrouwen opgebouwd, om te mogen verwachten dat ook de complexere 3D casussen goede voorspellingen worden verkregen.

Ten tweede zijn in dit proefschrift de oorzaken van grote discrepanties geïdentifi-

ceerd tussen de experimentele MEXICO metingen en de numerieke voorspellingen uit de wetenschappelijke literatuur. Dit is gedaan door opnieuw te kijken naar de manier waarop belasting experimenteel werden bepaald in het eerste MEXICO meetcampagne en mogelijke oorzaken van de discrepanties te analyseren, zoals: 1) 3D effecten veroorzaakt door de zeer gecompliceerde geometrie van de MEXICO rotor bladen, 2) het rol van het gebruik van ZigZag tape op de rotorbladen en het effect op de experimentele resultaten en 3) het slecht of niet functioneren van een aantal Kulite druksensoren. Een unieke nieuwe experimentele en numerieke campagne is vervolgens uitgevoerd om deze discrepanties te bepalen en om de oorzaken ervan te vinden. In deze campagne hebben metingen plaatsgevonden aan stationaire (niet roterende) MEXICO bladen in de lage snelheid, lage turbulentie windtunnel van de Technische Universiteit Delft bij goed gedefinieerde operationele condities bij de dezelfde Reynoldsgetallen. De aerodynamische karakteristieken van drie verschillende profielen (DU, RISØ en NACA) zijn daarbij gemeten op drie locaties langs de spanwijdte van het rotorblad. Deze meetresultaten zijn vergeleken met voorspellingen gemaakt met de OpenFOAM software. Deze studie leverde twee belangrijke ontdekkingen op. De eerste vondst heeft betrekking op de zigzagstrip (die toegepast werd op het MEXICO blad), en die een significant effect heeft op de aerodynamische karakteristieken, met name in de tipregio ( $r/R = 0.92$ ). Het effect van het gebruik van de zigzagstrip op de statische MEXICO rotorblad is in de campagne experimenteel gekwantificeerd. De tweede vondst betreft het verschil in de aerodynamische karakteristieken van de DU en de RISØ profielen in het post-overtrek regime. Te zien is dat een contra roterend wervelpaar wordt gevormd net achter de achter rand op spanwijdte positie  $r/R = 0.55$  net als in de numerieke simulaties. Dit is ook de locatie waar zich de overgang bevindt van het RISØ profiel naar het DU profiel. De geïnduceerde snelheid als gevolg van deze wervels verandert de lokale snelheid en daardoor ook de sectionele belastingen van met name de RISØ bladprofiel familie.

Ten derde zijn er simulaties gedaan met de geavanceerde numerieke codes en zijn deze vergeleken met de eerste en tweede MEXICO experimentele campagnes om de verbeteringen te valideren. Voor de ontwerp snellopendheid  $\lambda = 6.67$  is een OpenFOAM berekening uitgevoerd met het nieuwe grenslaag transitie model, om zoveel mogelijk de oorzaken van de discrepantie te elimineren. Deze vergelijking toont aan dat de kennis en de daaruit voortvloeiende aangepaste modelering opgedaan in de voorgaande campagne, een veel betere overeenkomst laten zien met de resultaten van de tweede serie MEXICO metingen, die zijn uitgevoerd voor "schone" rotor bladen in een heter gekalibreerde DNW tunnel. Daarbij is aangetoond dat de zigzagstrip een belangrijke oorzaak is voor de grote discrepanties tussen de CFD berekeningen en de eerste MEXICO experimenten. In de simulaties met een volledig turbulent stromingsveld, zoals aanvaankelijk ook in OpenFOAM, worden de aerodynamische belastingen in het tipgebied van de MEXICO rotor met zigzagstrip sterk overschat. De experimenten met een snellopendheid  $\lambda = 4.17$  zijn lastig te simuleren vanwege diepe overtrek over een groot gedeelte van de rotorbladen. Echter, ook hier worden de aerodynamische belastingen goed voorspeld bij gebruik van hybride LES/RANS simulatiemethodes zoals DDES, waarmee verschillen gereduceerd zijn tot 5%, in tegenstelling tot RANS die afwijkingen van 20% laat zien. Voor verdere validatie van het nieuwe transitie model in OpenFOAM is er nog een vergelijking gemaakt met experimentele resultaten. Deze vergelijking laat zien dat

de voorspelde belastingen bij een TU Delft wind tunnel rotor model (het "TUDelft Blade 2 rotor experiment") in excellente overeenstemming zijn met de gemeten belastingen. Ook zijn de OpenFOAM resultaten vergeleken de voorspellingen van een BEM code en een panelen code. Deze vergelijking toont aan dat de CFD methodes veel geschikter zijn dan de BEM en panelen methode voor het voorspellen van aerodynamische belastingen. Tenslotte is, door het vergelijken van numerieke resultaten voor de twee verschillende windturbinerotoren aangetoond dat de tipverliescorrecties zoals gebruikt in BEM codes nog verbeterd kunnen worden.



# LIST OF FIGURES

1.1	Smoke visualization of tip vortices generated from the blade tip in the second phase of MEXICO experiment (Boorsma and Schepers, 2014)	13
1.2	Global wind power cumulative capacity from the year 1996 to 2014 (Council, 2015)	14
1.3	The historical size of leading commercial wind turbines in the present and concepts for the near future (EWEA, 2012)	15
1.4	Schematic diagram to show dynamic stall (Leishman, 2002)	16
1.5	Visualization of complicated 3D root flow from SPIV measurements (Akay et al., 2014)	16
1.6	View of the NASA-Ames wind tunnel and measured two-bladed wind turbine with smoke visualization of tip vortices behind the rotor (Hand et al., 2001)	17
1.7	The MEXICO Wind turbine test set-up in the DNW wind tunnel (Schepers and Snel, 2007)	18
1.8	The experimental set-ups for the TUDelft rotor (Micallef, 2012)	18
1.9	Comparison of normal force distribution along the blade between CFD predictions and measurement, $U_\infty = 15\text{m/s}$ , $\lambda = 6.67$ (Schepers et al., 2011).	19
1.10	Comparison of tangential force distribution along the blade between CFD predictions and measurement, $U_\infty = 15\text{m/s}$ , $\lambda = 6.67$ (Schepers et al., 2011).	20
2.1	The sketch of streamlines past an airfoil and generating forces.	24
2.2	$c_l$ and $c_d$ behavior of DU91-W2-250 airfoil at $Re = 1.0 \times 10^6$ .	25
2.3	Reynolds number effects on $c_l$ and $c_d$ of DU91-W2-250 airfoil.	25
2.4	Schematic of flow transition and laminar separation bubble (LSB) on the airfoil suction side (Horton, 1968).	26
2.5	Lifting line theory of the finite wing and downwash effect.	27
2.6	Blade sections with blade angle.	28
2.7	Twist of blade.	28
2.8	$C_P - \lambda$ curve.	29
2.9	Wind turbine in axial (left) and yawed (right) flow conditions.	30
2.10	Normal force coefficients verse azimuth angles at $30\%R$ and $47\%R$ for NREL rotor under wind speed $15\text{m/s}$ , yaw angle $30^\circ$ (Simms et al., 2001).	31
2.11	Sketch of flow past the ideal wind turbine rotor. The free-stream velocity $U_0$ is decreased to $U$ at the rotor location $x_{rotor}$ and finally to $U_1$ in the far wake.	33
2.12	Sketch of a blade section in axial flow at radius $r$ .	34
2.13	Trailing and shed vorticity filaments of lifting line and lifting surface models. Adapted from (Micallef, 2012).	36

2.14 Representation of panel method. . . . .	37
2.15 Actuator line model (left) and actuator disk model (right) simulations (Tossas and Leonardi, 2013). . . . .	39
3.1 Schematic of 2D flat plate . . . . .	45
3.2 Law of the wall (Nezu and Tominaga, 2000) . . . . .	45
3.3 The comparisons of mean velocity profile in the turbulent boundary layer at $x = 0.97m$ for S-A turbulence model . . . . .	46
3.4 The comparisons of eddy viscosity distribution at $x = 0.97m$ for S-A turbulence model . . . . .	47
3.5 The comparisons of mean velocity profile in the turbulent boundary layer at $x = 0.97m$ for SST turbulence model . . . . .	47
3.6 The comparisons of eddy viscosity distribution at $x = 0.97m$ for SST turbulence model . . . . .	48
3.7 The view of the coarse computational grid ( $133 \times 33$ ) for NACA0012 airfoil (Rumsey, 2014) . . . . .	49
3.8 The comparison of pressure coefficient on the upper surface at $\alpha = 0^\circ$ , $Re = 6 \times 10^6$ for different grids. . . . .	49
3.9 The comparison of skin friction on the upper surface at $\alpha = 0^\circ$ , $Re = 6 \times 10^6$ for different grids. . . . .	50
3.10 The numerical convergence of aerodynamic drag $c_d$ and corresponding observed order of accuracy $p = 5.9042$ . . . . .	52
3.11 The turbulent velocity boundary layer profile at $x = 0.97m$ for flat plate . . . . .	55
3.12 Computational grid around NACA0021 airfoil. . . . .	56
3.13 Span-averaged lift and drag coefficient of DDES and URANS calculations. . . . .	57
3.14 Instantaneous vorticity snapshot ( $tU_0/c = 200$ ) from DDES calculation. . . . .	57
3.15 The comparison of mean velocity profiles in fully developed turbulent channel at $Re_\tau = 395$ (Moser et al., 1999) . . . . .	60
3.16 The comparison of total fluctuation kinetic energy ( $k_{TOT} = k_T + k_L$ ), normalized by the friction velocity . . . . .	60
3.17 Comparisons of freestream turbulence intensity distribution for T3A case. . . . .	62
3.18 Comparisons of skin friction coefficient distribution over the flat plate for T3A case. . . . .	62
3.19 Comparisons of freestream turbulence intensity distribution for T3B case. . . . .	63
3.20 Comparisons of skin friction coefficient distribution over the flat plate for T3B case. . . . .	63
3.21 Comparisons of freestream turbulence intensity distribution for T3A- case. . . . .	64
3.22 Comparisons of skin friction coefficient distribution over the flat plate for T3A- case. . . . .	64
3.23 Grid around the DU91-W2-250 airfoil. . . . .	65
3.24 $C_L - \alpha$ , $C_D - \alpha$ and $C_L - C_D$ curves at $Re_c = 1.0 \times 10^6$ . . . . .	66
3.25 Transition onset location comparison at $Re_c = 1.0 \times 10^6$ . $\square$ represents the laminar separation points and $\times$ represents the turbulent reattachment points. . . . .	67
4.1 The layout of LTT wind tunnel (source: (Dimchev, 2012) ) . . . . .	71

4.5	Kulite pressure sensors . . . . .	71
4.2	Airfoil distributions over the span of the MEXICO blade. In grey: transition zones. . . . .	72
4.3	Chord and twist distribution of the MEXICO blade. . . . .	72
4.4	Schematic view of the balance system . . . . .	73
4.6	Experimental set-up of the model: the MEXICO blade 1 . . . . .	75
4.7	Experimental set-up of the models: the MEXICO blade 2 and blade 3 . . .	75
4.8	Numerical set-up of the model: Blade 1 configuration (Zhang et al., 2014)	76
4.9	Numerical set-up of the models: Blade 2 and Blade 3 configuration (Zhang et al., 2014) . . . . .	76
4.10	Schematic of the computational domain and blade surface mesh . . . . .	77
4.11	Grid convergence study, $C_p$ comparison between coarse, medium and fine grids . . . . .	79
4.12	Grid convergence study, $C_f$ comparison between coarse, medium and fine grids on the suction side . . . . .	79
4.13	Pressure coefficient comparison of the DU91-W2-250 airfoil at 35% spanwise section of the blade 1: $\alpha_{0.35} = 1^\circ, 5^\circ$ and $8^\circ$ with inflow velocity $U_\infty = 35m/s, Re_c = 4.6 \times 10^5$ . . . . .	80
4.14	Pressure coefficient comparison of the RISØ-A1-21 airfoil at 60% spanwise section of the blade 2: $\alpha_{0.60} = 0^\circ, 5^\circ$ and $8^\circ$ with inflow velocity $U_\infty = 35m/s, Re_c = 3.4 \times 10^5$ . . . . .	81
4.15	Pressure coefficient comparison of the NACA 64-418 airfoil at 92% spanwise section of the blade 3: $\alpha_{0.92} = 2^\circ, 5^\circ$ and $8^\circ$ with inflow velocity $U_\infty = 60m/s, Re_c = 4.0 \times 10^5$ . . . . .	81
4.16	Blade 3 configuration: flow topology comparison between CFD limiting streamline and experimental oil flow visualization, flow is from right to left, angle of attack $\alpha_{0.82} = 8^\circ$ , CFD result is colored by the pressure. . . . .	82
4.17	Distribution of geometric angle of attack and lift coefficient from CFD results of the blade 1 . . . . .	84
4.18	Distribution of geometric angle of attack and lift coefficient from CFD results of the blade 2 . . . . .	84
4.19	Blade 1 configuration: 3D visualization of vortex structure, isosurface $Q = 2 \times 10^5$ colored by vorticity magnitude, $\alpha_{0.35} = 5^\circ$ . . . . .	85
4.20	Blade 1 configuration: 3D visualization of vortex structure, isosurface $Q = 2 \times 10^5$ colored by vorticity magnitude, $\alpha_{0.35} = 8^\circ$ . . . . .	85
4.21	$C_L - \alpha$ comparison between 3D CFD calculation and 2D experimental data. $\alpha_{0.35} = 5^\circ$ (left) $\alpha_{0.35} = 8^\circ$ (right) . . . . .	87
4.22	Measured $C_L - \alpha$ polar data for the DU91-W2-250 ( $Re = 5 \times 10^5$ ) and the RISØ-A1-21 ( $Re = 1.6 \times 10^6$ ) airfoils . . . . .	87
4.23	Blade 1 configuration: the vertical velocity $u$ and spanwise velocity $v$ contour in the plane $z = -0.20m$ behind the blade 1, $\alpha_{0.35} = 5^\circ$ . . . . .	89
4.24	Blade 1 configuration: the vertical velocity $u$ and spanwise velocity $v$ contour in the plane $z = -0.20m$ behind the blade 1, $\alpha_{0.35} = 8^\circ$ . . . . .	89
4.25	Blade 2 configuration: the vertical velocity $u$ and spanwise velocity $v$ contour in the plane $z = -0.20m$ behind the blade 2, $\alpha_{0.60} = 5^\circ$ . . . . .	89



4.26	The shape and critical parameters of ZigZag tape and flow visualization over ZigZag tape, from the paper (Selig, 1995). . . . .	90
4.27	The ZigZag tape applied on the suction side of the MEXICO blade, located at 10% chord. The tape is removed at the locations of pressure sensors. . .	90
4.28	The influence of ZigZag tape on local pressure distribution in the experiment. $C_p$ comparison with and without ZigZag tape at $r/R = 0.35$ radial location, $\alpha = 8^\circ, 11^\circ$ and $20^\circ$ . . . . .	92
4.29	The influence of ZigZag tape on local pressure distribution in the experiment. $C_p$ comparison with and without ZigZag tape at $r/R = 0.92$ radial location, $\alpha = 8^\circ, 10^\circ$ and $16^\circ$ . . . . .	93
4.30	The influence of ZigZag tape on the lift $C_L$ and drag $C_D$ polar of the DU91-W2-250 airfoil at section $r/R = 0.35$ . . . . .	94
4.31	The influence of ZigZag tape on the lift $C_L$ and drag $C_D$ polar of the NACA 64-418 airfoil at section $r/R = 0.92$ . . . . .	94
4.32	The influence of ZigZag tape on local pressure distribution. $C_p$ comparison with and without ZigZag stripe and CFD prediction at $r/R = 0.92$ , $\alpha = 8^\circ$ . .	95
4.33	The results of sectional normal force at $r/R = 0.92$ with angle of attack $\alpha = 8^\circ$ . Three cases are clean blade, rough blade and fully turbulent CFD simulation. . . . .	96
4.34	The comparison of pressure distribution between <i>Rfoil</i> and experiment for the clean NACA64-418 airfoil. The Reynolds number is $Re = 0.7 \times 10^6$ and the geometric angle of attack is $\alpha = 8^\circ$ . It demonstrates that <i>Rfoil</i> presents good capability for predicting $C_p$ distribution. . . . .	97
4.35	The comparison of pressure distribution between <i>Rfoil</i> and experiment for the rough NACA64-418 airfoil tripped by ZigZag tape. The Reynolds number is $Re = 0.7 \times 10^6$ and the geometric angle of attack is $\alpha = 8^\circ$ . The configurations of ZigZag tapes are: at suction side $x/c = 5\%$ with ZigZag tape height of $0.2mm$ and at pressure side $x/c = 10\%$ with ZigZag tape height of $0.32mm$ . . . . .	98
4.36	The distribution of chordwise pressure and wall shear stress $\tau_w$ at high geometric angle of attack, $\alpha = 19^\circ$ . DU airfoil at 35% $R$ section. . . . .	99
4.37	Blade 1 configuration: 3D visualization of vortical structure by RANS and DDES calculations, iso-surface $Q = 3 \times 10^4$ , colored by the velocity. Geometric angle of attack $\alpha = 19^\circ$ at $r/R = 0.35$ . . . . .	100
4.38	Blade 1 configuration: Surface streamtraces pattern of the averaged streamwise flow field over DU91-W2-250 airfoil at 35% $R$ for RANS and DDES simulations. These streamlines overlap with streamwise velocity field contour, the inflow direction is negative $Z$ . . . . .	100
5.1	The MEXICO experiment in DNW wind tunnel (Snel et al., 2007). Three bladed wind turbine with 4.5m diameter rotor. . . . .	105
5.2	Smoke visualization of tip vortices generated from the blade tip in the second phase of MEXICO experiment (Boorsma and Schepers, 2014) . . . . .	105
5.3	The overview of CFD computational domain and the generated mesh . . .	107

5.4	Comparison of aerodynamic normal force $F_N$ and tangential force $F_T$ between numerical results from CFD, BEM and experimental measurement at different wind speeds $U_\infty = 10\text{m/s}$ , $15\text{m/s}$ and $24\text{m/s}$ , corresponding tip speed ratios $\lambda = 10.0$ , $6.67$ and $4.17$ . . . . .	109
5.5	Limiting streamline visualization on the suction side of the MEXICO blades with $\lambda = 10.0$ , $6.67$ and $4.17$ , which corresponds to incoming wind speed $U_\infty = 10\text{m/s}$ , $15\text{m/s}$ and $24\text{m/s}$ , respectively. . . . .	111
5.6	Schematic of the measured locations by PIV in the horizontal plane at 9 o'clock, azimuth angle $\theta = 270^\circ$ . The azimuth angle is $0^\circ$ when the blade 1 is vertically oriented upwards. The axial velocity traverse is measured at two radial locations $r/R = 0.61$ and $r/R = 0.82$ . The radius of this rotor is $2.25\text{m}$ . . . . .	111
5.7	Axial velocity component $u$ along the axial traverse at the mid-span ( $r/R = 0.61$ ) and the outboard positions ( $r/R = 0.82$ ). The grey box at $x/R = 0$ indicates the location of rotor plane, dashed line represents the numerical results with coarse near wake mesh, the dot dash line represents the results with medium near wake mesh, and solid line represents the numerical results with finest near wake mesh. . . . .	112
5.8	Comparison of axial velocity field surrounding the blade between CFD and phase locked PIV measurement at various azimuth angles $\theta = 240^\circ$ , $260^\circ$ , $280^\circ$ , $300^\circ$ of blade 3 for the optimal tip speed ratio $\lambda = 6.67$ . The velocity contours are normalized with free-stream velocity $U_\infty$ . . . . .	113
5.9	Local forces on a blade section and inflow angle $\alpha$ , twist angle $\beta$ , pitch angle $\phi$ . . . . .	115
5.10	The comparisons of sectional lift polar $C_L - \alpha$ between experimental measurements of 3D rotating blade, non-rotating blade, 2D airfoil and CFD numerical prediction of 3D rotating blade. The sections are located at $0.25R$ , $0.35R$ , $0.60R$ , $0.82R$ and $0.92R$ radial positions. . . . .	117
5.11	The comparisons of sectional lift polar $C_D - \alpha$ between experimental measurements of 3D rotating blade, non-rotating blade, 2D airfoil and CFD numerical prediction of 3D rotating blade. The sections are located at $0.25R$ , $0.35R$ , $0.60R$ , $0.82R$ and $0.92R$ radial positions. . . . .	119
5.12	Comparison of pressure coefficient $C_p$ distribution between 3D CFD simulation, experiment on the rotating blade and static 2D airfoil wind tunnel measurement at $r/R = 0.25$ section with $\lambda = 6.67$ and $4.17$ . Estimated local angle of attack $\alpha \approx 11^\circ$ (left) and $\alpha \approx 26^\circ$ (right). The 2D airfoil data with upper/lower bar represents the measured results with $\pm 1^\circ$ $\alpha$ difference. . . . .	120
5.13	Comparison of pressure coefficient $C_p$ between 3D CFD, experiment on the rotating blade and static 2D airfoil wind tunnel measurement at $r/R = 0.35$ with $\lambda = 6.67$ and $4.17$ . Estimated local angle of attack $\alpha \approx 9^\circ$ (left) and $\alpha \approx 22^\circ$ (right). The 2D airfoil data with upper/lower bar represents the measured results with $\pm 1^\circ$ $\alpha$ difference. . . . .	120

5.14 Comparison of pressure coefficient $C_p$ between 3D CFD simulation, experiment on the rotating blade and static 2D airfoil wind tunnel measurement at $r/R = 0.82$ with $\lambda = 6.67$ and $4.17$ . Estimated local angle of attack $\alpha \approx 7^\circ$ (left) and $\alpha \approx 14^\circ$ (right). The 2D airfoil data with upper/lower bar represents the measured results with $\pm 1^\circ$ $\alpha$ difference. . . . .	121
5.15 Comparison of pressure coefficient $C_p$ between 3D CFD simulation, experiment on the rotating blade and static 2D airfoil wind tunnel measurement at $r/R = 0.92$ with $\lambda = 6.67$ and $4.17$ . Estimated local angle of attack $\alpha \approx 8^\circ$ (left) and b) $\alpha \approx 14^\circ$ (right). The 2D airfoil data with upper/lower bar represents the measured results with $\pm 1^\circ$ $\alpha$ difference. . . . .	122
5.16 Normalized radial flow field distribution at $r/R = 0.25$ section and corresponding Coriolis force components in x and y directions, $\lambda = 4.17$ . . . . .	123
5.17 Normalized radial flow field distribution at $r/R = 0.35$ section and corresponding Coriolis force components in x and y directions, $\lambda = 4.17$ . . . . .	123
5.18 Radial pressure gradient field distribution at $r/R = 0.25$ and $r/R = 0.35$ . Oil flow visualization on the blade surface is also indicated by the wall shear stress with the line integral convolution technique (Cabral and Leedom, 1993) . . . . .	124
5.19 Vorticity field comparison between 25%R sectional airfoil of 3D rotating blade and 2D static airfoil at same $\alpha$ and Reynolds number, $\lambda = 4.17$ , $\alpha = 26^\circ$ and $Re = 5.0 \times 10^5$ . . . . .	125
5.20 The positions of separation point on the suction side of rotating blade at different radial locations. . . . .	126
5.21 Comparison of separation point positions at 35%R radial location on the suction side between rotating and non-rotating blades. . . . .	126
5.22 Transitional effects on normal force along the blade at optimal tip speed ratio $\lambda = 6.67$ . The blue bar indicates the relative difference between two predictions. . . . .	128
5.23 Transitional effects on tangential force along the blade at optimal tip speed ratio $\lambda = 6.67$ . The blue bar indicates the relative difference between two predictions. . . . .	128
5.24 $C_p$ comparison between fully turbulent and transitional flow at $r/R = 0.35$ radial section . . . . .	129
5.25 $C_p$ comparison between fully turbulent and transitional flow at $r/R = 0.92$ radial section . . . . .	129
5.26 Comparison of normal force distribution along the blade between numerical predictions and experimental measurements. Three different experimental conditions are MEXICO rough ( $U_\infty = 14.93m/s$ , $n = 424.5rpm$ , $\rho = 1.246kg/m^3$ ), new MEXICO clean ( $U_\infty = 15.03m/s$ , $n = 425.1rpm$ , $\rho = 1.191kg/m^3$ ) and new MEXICO rough ( $U_\infty = 14.86m/s$ , $n = 425.1rpm$ , $\rho = 1.20kg/m^3$ ). . . . .	130

5.27	Comparison of tangential force distribution along the blade between numerical predictions and experimental measurements. Three different experimental conditions are MEXICO rough ( $U_\infty = 14.93\text{ m/s}$ , $n = 424.5\text{ rpm}$ , $\rho = 1.246\text{ kg/m}^3$ ), new MEXICO clean ( $U_\infty = 15.03\text{ m/s}$ , $n = 425.1\text{ rpm}$ , $\rho = 1.191\text{ kg/m}^3$ ) and new MEXICO rough ( $U_\infty = 14.86\text{ m/s}$ , $n = 425.1\text{ rpm}$ , $\rho = 1.20\text{ kg/m}^3$ ). . . . .	131
5.28	Transition onset on the suction side (upper figure) and pressure side (lower figure) of the blade, overlap with LIC texture for wall shear stress in ParaView.	132
5.29	Transition onset locations along the blade span at suction and pressure sides with two different tip speed ratios: $\lambda = 10.0$ and $6.67$ . . . . .	132
5.30	Unsteady thrust force on the rotor and power density spectrum of thrust force. . . . .	134
5.31	Normal force prediction along the blade with tip speed ratio $\lambda = 4.17$ . The numerical results are obtained from RANS and DDES computations, comparing against with MEXICO experiment and new MEXICO experiment. .	135
5.32	Relative error along the blade with tip speed ratio $\lambda = 4.17$ for RANS and DDES. . . . .	135
5.33	Instantaneous flow field at azimuth angles $\theta = 0^\circ, 40^\circ, 80^\circ, 120^\circ$ over the blade section $r/R = 0.25$ , $\lambda = 4.17$ . . . . .	136
6.1	Schematic of Open Jet Facility. . . . .	141
6.2	Geometry of the Blade 2 TUDelft rotor. . . . .	141
6.3	DU-96-W180 airfoil, chord and twist distribution along the blade. . . . .	141
6.4	Experimental setup of the TUDelft Blade 2 rotor at Open Jet Facility. . . . .	142
6.5	The computational domain of the TUDelft Blade 2 rotor in the simulation. . . . .	143
6.6	Surface mesh on the pressure and suction sides of blade, and hybrid mesh near blade section $r/R = 0.50$ . . . . .	144
6.7	Axial velocity distribution at three different radial locations from $r/R = 0.40$ to $r/R = 0.91$ , normalized with the free-stream wind speed $U_\infty$ . Inflow direction is $+z/R$ . The PIV data at $x/R = 0.025$ and $z/R = 0.05$ of section $r/R = 0.40$ is marked due to laser reflection. . . . .	145
6.8	Tangential velocity distribution at three different radial locations from $r/R = 0.40$ to $r/R = 0.91$ , normalized with the free-stream wind speed $U_\infty$ . Inflow direction is $+z/R$ . The PIV data at $x/R = 0.025$ and $z/R = 0.05$ of section $r/R = 0.40$ is marked due to laser reflection. . . . .	146
6.9	Radial velocity distribution at three different radial locations from $r/R = 0.40$ to $r/R = 0.91$ , normalized with the free-stream wind speed $U_\infty$ . Inflow direction is $+z/R$ . The PIV data at $x/R = 0.025$ and $z/R = 0.05$ of section $r/R = 0.40$ is marked due to laser reflection. . . . .	147
6.10	Contour approach to calculate aerodynamic forces on 2D airfoil. Figure is adapted from (Anderson Jr, 2010). . . . .	148
6.11	Airfoil flow representation in the absolute (left) and relative (right) reference frame. Figure is adapted from (Ragni, 2012). . . . .	148

6.12 Aerodynamic loads comparisons along the blade between PIV results and numerical methods, including CFD, BEM, panel codes.(left: normal force and right: tangential force). . . . .	152
6.13 The contribution of different force terms to the normal and tangential forces at different radial locations ( $r/R = 0.40, 0.61, 0.76, 0.91$ ). . . . .	153

# LIST OF TABLES

1.1	The relative errors at radial location $r/R = 0.82$ and $0.92$ between measured results and predicted normal force by different CFD codes, data from (Schepers et al., 2011). . . . .	20
1.2	The relative errors at radial location $r/R = 0.82$ and $0.92$ between measured results and predicted tangential force by different CFD codes, data from (Schepers et al., 2011). . . . .	20
3.1	The value of $c_d$ with three different grid levels . . . . .	51
3.2	Model constants in Spalart-Allmaras turbulence model . . . . .	54
3.3	Integral forces comparison between RANS, URANS and DDES. . . . .	56
3.4	The implementations of $k - k_L - \omega$ transition models in different versions of OpenFOAM . . . . .	59
3.5	Inflow condition of T3 series flat plate . . . . .	61
4.1	Specifications of Kulite XCQ-95-062-5A . . . . .	71
4.2	Conditions in the experiment . . . . .	75
4.3	The characteristics of three different grids . . . . .	77
4.4	ZigZag tape parameters used in the experiment . . . . .	91
5.1	Rotor geometry and part of test conditions . . . . .	105
5.2	Incoming wind speeds and corresponding tip speed ratios of the computations . . . . .	114
5.3	Shedding frequencies and Strouhal numbers for $\lambda = 4.17$ case. . . . .	137
6.1	Blade geometry and operating conditions of TUDelft Blade 2 rotor . . . . .	142



# NOMENCLATURE

$\alpha$	Local angle of attack	$^{\circ}$
$\delta$	Half channel height	$m$
$\mu$	Dynamic viscosity	$\frac{kg}{m \cdot s}$
$\mu_t$	Turbulent viscosity	$\frac{kg}{m \cdot s}$
$\mu_{eff}$	Effective dynamic viscosity	$\frac{kg}{m \cdot s}$
$\Omega$	Rotor rotational speed	$rad/s$
$\omega$	Angular velocity vector	$rad/s$
$\omega$	Specific turbulence dissipation rate	$s^{-1}$
$\Psi$	Yaw angle	$^{\circ}$
$\rho$	Fluid density	$kg/m^3$
$\tau_w$	Wall shear stress	$\frac{kg}{m \cdot s^2}$
$\mathbf{n}$	Normal vector	—
$\mathbf{r}$	Position vector	$m$
$\mathbf{u}_I$	Velocity vector in inertial reference frame	$m/s$
$\mathbf{u}_R$	Velocity vector in rotating reference frame	$m/s$
$\theta$	Pitch angle	$^{\circ}$
$a$	Axial induction factor	—
$a'$	Tangential induction factor	—
$C_D$	Drag coefficient	—
$C_f$	Skin friction coefficient	—
$C_L$	Lift coefficient	—
$C_p$	Pressure coefficient	—
$C_T$	Thrust coefficient	—



$D$	Rotor diameter	$m$
$d$	Drag force per unit length	$N/m$
$k_L$	Laminar kinetic energy	$m^2/s^2$
$k_T$	Turbulent kinetic energy	$m^2/s^2$
$l$	Lift force per unit length	$N/m$
$N$	Normal force	$N$
$n$	Rotational speed	$rpm$
$P$	Observed order of accuracy	–
$p$	Static Pressure	$Pa$
$p_\infty$	Static freestream pressure	$Pa$
$R$	Rotor radius	$m$
$r$	Constant grid refinement ratio	–
$Re$	Reynolds number	–
$Re_\tau$	Friction Reynolds number	–
$Re_c$	Chord based Reynolds number	–
$S$	Surface of control volume	$m^2$
$u', v', w'$	Velocity fluctuation	$m/s$
$U_\infty$	Inflow wind speed	$m/s$
$u_\tau$	Friction velocity	$m/s$
$V$	Control volume	$m^3$
$V_{rel}$	Relative velocity	$m/s$
$Z$	Blade number	–

# 1

## INTRODUCTION

*Problems are not stop signs,  
they are guidelines.*

Robert H. Schuller



Figure 1.1: Smoke visualization of tip vortices generated from the blade tip in the second phase of MEXICO experiment (Boorsma and Schepers, 2014)

## 1.1. RESEARCH BACKGROUND

### WIND ENERGY

As a renewable resource, wind energy has been developing fast in the last two decades to satisfy the energy needs. The cumulative capacity of wind power is increasing significantly all over the world. Figure 1.2 presents the global wind power capacity over the past twenty years, showing clearly the increasing trend of installed power capacity. To compete with conventional generation sources on a cost basis, reducing the cost of wind power is an ongoing challenge. For near future perspective, with the effort of cutting down the cost of energy (COE) by advanced technology, the high scenario expects 392 GW installed in 2030, which meets 31% of EU electricity demand (EWEA, 2015).

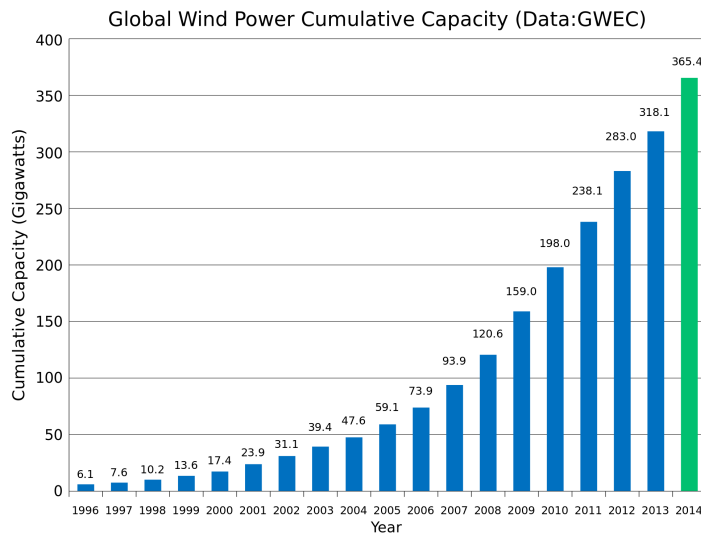


Figure 1.2: Global wind power cumulative capacity from the year 1996 to 2014 (Council, 2015)

To decrease the COE, the rotor size of commercial wind turbine became larger and larger in order to capture more energy from the wind. Figure 1.3 illustrates the history of leading commercial wind turbine size in the past and concepts for the near future. The world's largest commercial wind turbine with 8MW rated capacity at the present time has 80m long blades and a 164m rotor diameter, which is twice than the commercial Airbus 380 aircraft wing span. In the future, the next generation of wind turbines is most probably going to be 10 – 20MW with much longer and more flexible blades. Such huge machines definitely need excellent design and analysis to avoid structural failure and ensure turbine performance. Multiple disciplines such as material science, control, aeroelasticity and aerodynamics need to be critically considered during the design phase.

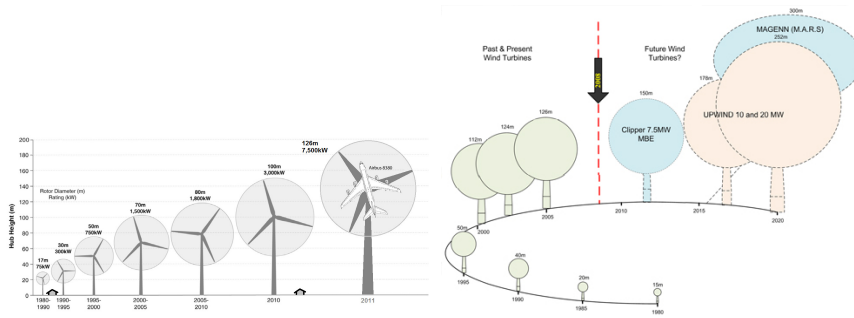


Figure 1.3: The historical size of leading commercial wind turbines in the present and concepts for the near future (EWEA, 2012)

### WIND TURBINE AERODYNAMICS

One of such challenging disciplines is aerodynamics. "Aerodynamics is the mother of all sciences for wind turbines." said by Prof G. van Kuik<sup>1</sup> from Delft University of Technology (TUDelft). Indeed, as the performance of the turbine is strongly related to its aerodynamic design, the ability to model and predict the flow around a wind turbine blade is of the most importance. It is generally accepted that the Navier-Stokes equations are an accurate model for any flow problem. However, a closed-form solution does not exist, apart from some simplified academic problems. Some challenges exist to predict the flow, especially in wind turbine aerodynamics because normally wind turbines are subjected to complicated and uncontrolled environmental conditions. These uncontrolled conditions include atmosphere turbulence, ground boundary layer effects, directional and spatial variations in wind shear, yaw misalignment, tower shadow effects, 3-D geometric and rotational effects, stall, etc (Leishman, 2002). All these effects result in the fact that numerically modeling wind turbine aerodynamics is tough and complicated. As an illustration, Figure 1.4 shows the unsteady aerodynamic loads and flow physics for a two-dimensional airfoil undergoing dynamic stall phenomena, which is well known difficult to be predicted numerically. Regarding rotor aerodynamics of wind turbine, the situation is more challenging and the flow over the wind turbine rotor is more difficult. Figure 1.5 presents the complicated 3D root flow of horizontal axis wind turbine by visualizing the radial velocity from Stereo Particle Image Velocimetry (PIV) measurements.

### UNCERTAINTIES OF AERODYNAMIC MODELS

Such complexity due to uncontrolled external conditions have been observed in the past from large uncertainties in aerodynamic modeling, for instance, the predictions of power and aerodynamic loads on blades. To reduce the uncertainties for more reliable design purpose, several representative high-quality wind tunnel experiments were carried out under controlled conditions (without considering atmospheric turbulence, wind shear, etc.) in order to improve the aerodynamic models.

One of such experiments is NREL unsteady aerodynamics experiment in the NASA-Ames wind tunnel, which was conducted in 2000. An extensively instrumented two

<sup>1</sup>A famous wind turbine scientist from TUDelft, working on wind turbine aerodynamics. He was the scientific director of DUWIND and former president of the European Academy for Wind Energy

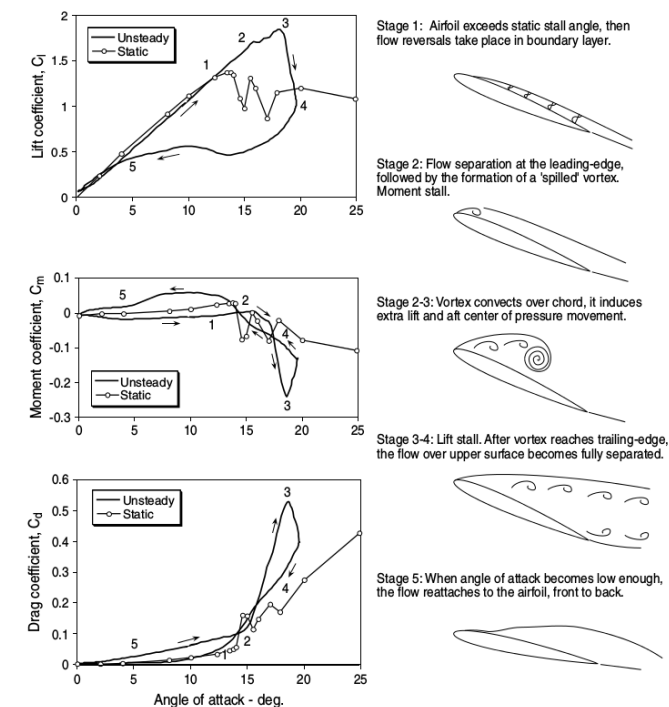


Figure 17. Schematic diagram showing unsteady airloads and flow physics for a two-dimensional aerofoil undergoing dynamic stall

Figure 1.4: Schematic diagram to show dynamic stall (Leishman, 2002)

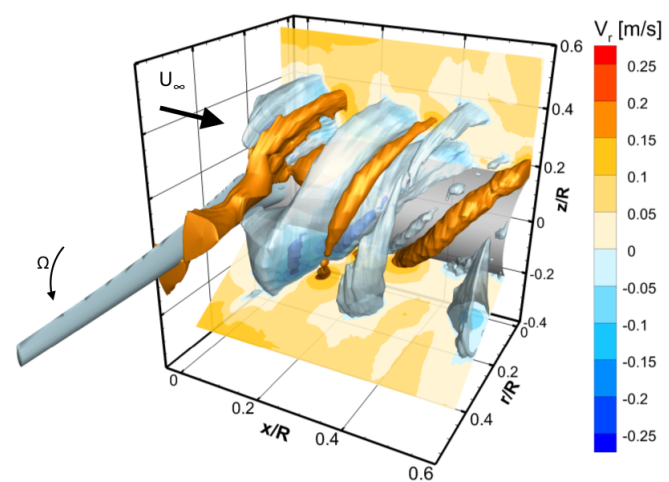


Figure 1.5: Visualization of complicated 3D root flow from SPIV measurements (Akay et al., 2014)

bladed stall-regulated wind turbine with 10-meter diameter was measured in the world's largest wind tunnel. In the  $24.4 \times 36.6 \text{ m}^2$  test section, the detailed local sectional aerodynamic force, instantaneous pressure distribution and wind turbine performance were acquired in the presence of strictly controlled inflow conditions (Simms et al., 2001). Figure 1.6 presents the overlook of the NASA-Ames wind tunnel and measured two-bladed wind turbine with tip vortex smoke visualization. As a benchmark of validation database, the experiment was really successful that more than 1700 different turbine test conditions were provided for blind comparisons with different aerodynamic models.

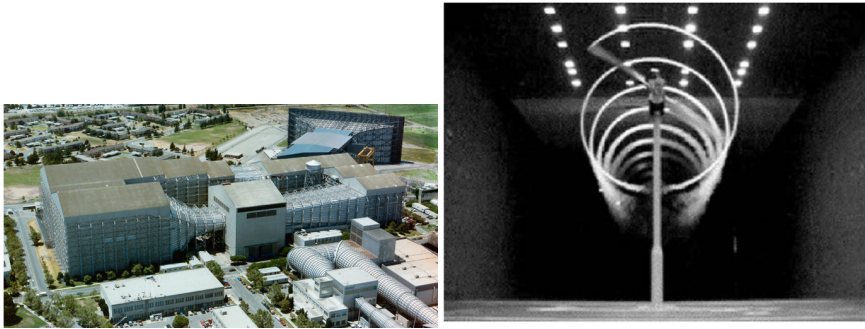


Figure 1.6: View of the NASA-Ames wind tunnel and measured two-bladed wind turbine with smoke visualization of tip vortices behind the rotor (Hand et al., 2001)

Six years later, another representative experimental campaign was performed in December 2006. The MEXICO (Model EXperiment In Controlled cOndition) project measured a wind turbine model in the Large Low speed Facility (LLF) of German-Dutch Wind Tunnel (DNW) with a test section of  $9.5 \times 9.5 \text{ m}^2$ . Opposed to the previous NASA experiment, a three-bladed pitch-regulated wind turbine was measured. Not only the pressure and loads on the blades were acquired but also detailed near wake velocity field data was obtained by Particle Image Velocimetry (PIV) technique. Figure 1.7 shows the tested wind turbine set-up in the DNW wind tunnel. Blind comparisons were also done with aerodynamic models with different fidelity in the following project MexNext (Schepers and Boorsma, 2015).

Many experimental studies (Vermeer et al., 2003) (Haans et al., 2007) (Haans et al., 2008) (Micallef et al., 2013) (Akay et al., 2014) have been carried out in the Wind Energy Group of Delft University of Technology in order to investigate wind turbine rotor/wake aerodynamics. Under controlled wind tunnel conditions, the wind turbine performance operating in axial and yawed conditions, near wake aerodynamics, 3D flow fields and root flow has been extensively investigated by using different measurement techniques. Figure 1.8 presents the experimental set-ups for the TUDelft rotor, using Stereoscopic particle-image velocimetry (SPIV) technique to acquire the 3D velocity field around the wind turbine blades in the spanwise and chordwise directions.

#### PROBLEM STATEMENT

One of the issues observed in these two blind comparisons mentioned above is that a large discrepancy exists between experimental measurement and numerical predictions



Figure 1.7: The MEXICO Wind turbine test set-up in the DNW wind tunnel (Scheepers and Snel, 2007)

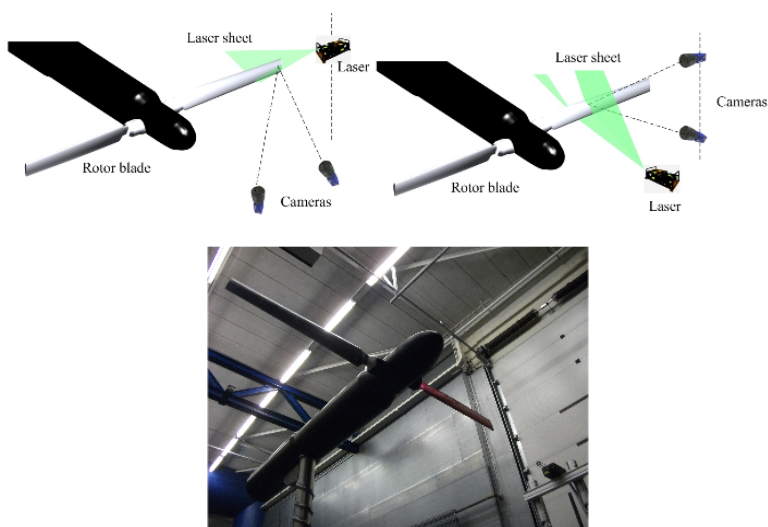


Figure 1.8: The experimental set-ups for the TUDelft rotor (Micallef, 2012)



of aerodynamic models, even at typical wind turbine design operating conditions. For instance, under steady-state, no-yaw, no-stall conditions, the power prediction deviates from 25% to 175% from the measurement. Blade bending-force prediction ranges from 85% to 150% of measured (Simms et al., 2001). A similar level of disagreement is also observed in the blind comparison with experimental data from MEXICO, where all loads along the blade are consistently overpredicted by computational results, whereas they are randomly distributed in a wide spread around the measured results in NREL experiment (Schepers et al., 2012). Such overprediction is not only observed in engineering models, i.e., lifting line code but also appears in the more sophisticated high fidelity CFD codes. Figure 1.9 shows the comparison of normal force (the force normal to the local chord) distribution along the blade between predicted results from different CFD codes and experimental data. The tip speed ratio of the simulated condition is  $\lambda = 6.67$ , which is the optimal design case. The flow over the blade should be mostly attached. From the comparison, clearly it can be seen that almost all CFD RANS simulations significantly overpredict the normal force at radial locations  $r/R = 0.82$  and  $0.92$ . For the tangential force (the force parallel to the local chord), the comparison becomes even worse than the normal force at these locations, which is shown in Figure 1.10. The relative errors from different CFD codes are listed in Table 1.1 and 1.2. Although it has been known that wind tunnel effects could be a possible cause of the discrepancies between CFD and the experimental results, the origin of these large differences is not yet (fully) understood.

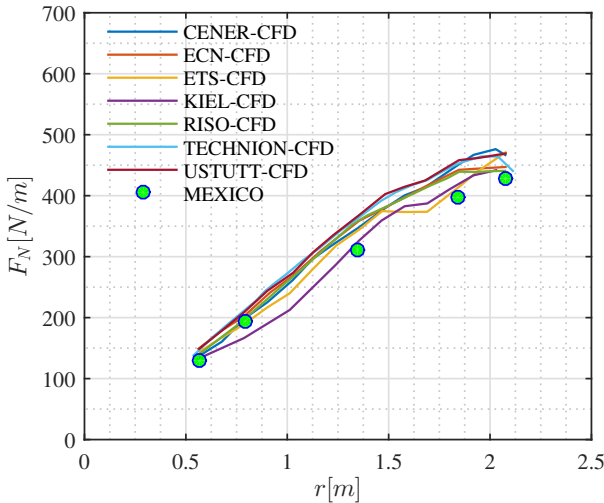


Figure 1.9: Comparison of normal force distribution along the blade between CFD predictions and measurement,  $U_\infty = 15 \text{ m/s}$ ,  $\lambda = 6.67$  (Schepers et al., 2011).

## 1.2. MOTIVATION AND OBJECTIVES

Therefore, the aim of this thesis is to investigate the possible causes of large discrepancies between measurement and numerical results, and additionally to improve the



Table 1.1: The relative errors at radial location  $r/R = 0.82$  and  $0.92$  between measured results and predicted normal force by different CFD codes, data from (Scheepers et al., 2011).

$r/R$	CENER	ECN	ETS	KIEL	RISØ	TECHNION	USTUTT
0.82	+13.3%	+11.1%	+4.2%	+5.5%	+10.3%	+13.8%	+15.0%
0.92	+8.6%	+4.1%	+9.7%	+2.8%	+2.5%	+5.3%	+9.3%

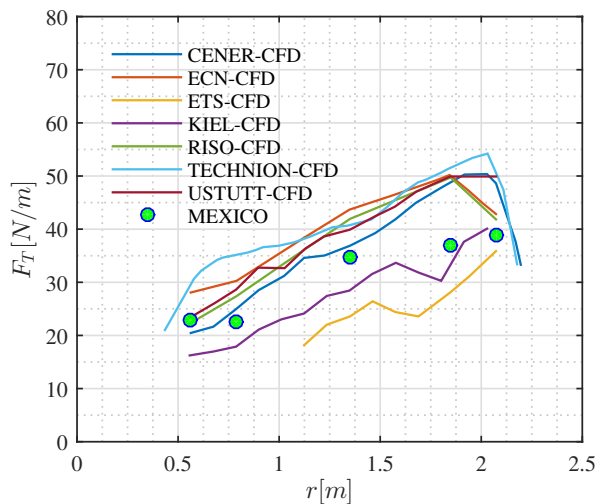


Figure 1.10: Comparison of tangential force distribution along the blade between CFD predictions and measurement,  $U_\infty = 15 \text{ m/s}$ ,  $\lambda = 6.67$  (Scheepers et al., 2011).

Table 1.2: The relative errors at radial location  $r/R = 0.82$  and  $0.92$  between measured results and predicted tangential force by different CFD codes, data from (Scheepers et al., 2011).

$r/R$	CENER	ECN	ETS	KIEL	RISØ	TECHNION	USTUTT
0.82	+32.8%	+36.1%	-23.8%	-10.5%	+34.8%	+39.3%	+35.5%
0.92	+25.0%	+10.1%	-7.7%	+2.8%	+7.5%	+28.5%	+28.5%

current CFD approach for better aerodynamic loads prediction. The main objectives of the present work, therefore, can be summarized as follows:

- Evaluation and validation of an open source code OpenFOAM (Open source Field Operation And Manipulation) with particular attention to wind energy application. The content of this work can be found in Chapter 3 and Chapter 6 of this thesis.
- Investigating the possible reasons which cause the large discrepancies between experiment and CFD simulations found in the blind comparisons for the MEXICO rotor. It can be achieved by experimental and numerical investigation of detailed flow physics over the non-rotating MEXICO blade with less complexities and the validation of the MEXICO experimental set-up. The causes of large deviation are not fully understood at that time. This study is mainly discussed in Chapter 4.
- To bridge the research gap, wind turbine aerodynamics with more advanced turbulence models are investigated by considering laminar to turbulent transition simulation and detached eddy simulation, which can be found in Chapter 5.

### 1.3. THESIS OUTLINE

The structure of this thesis is described in this section. The overview of each chapter attends to guide the readers briefly.

- Chapter 2 - *State of the art of horizontal axis wind turbine rotor aerodynamics.*

In this chapter, the numerical modeling techniques of HAWT rotor aerodynamics is comprehensively reviewed, from widely used engineering approach to high fidelity CFD approach. Meanwhile, the finite volume method (FVM) and numerical algorithm which OpenFOAM uses are introduced. In particular, the state of the art in turbulence and transition modeling for wind turbine aerodynamics are described.

- Chapter 3 - *Evaluation and validation of OpenFOAM code.*

In this chapter, evaluation and validation of OpenFOAM is performed on 2D test cases before applying it to more complex 3D flow investigations. Several benchmark cases which represent different flow features are simulated and compared with either other validated numerical codes or experimental measurement. The implementation errors in transition model of OpenFOAM are corrected for and the improved code is further validated for wind turbine airfoil flow.

- Chapter 4 - *Experimental and numerical study of non-rotating MEXICO blade.*

Following the previous chapter, 3D flow over non-rotating MEXICO wind turbine blade is experimentally and numerically investigated in this chapter. By simplifying the experimental setup and reducing the uncertainties in the rotating MEXICO experiment, sectional aerodynamic characteristics of the parked MEXICO blades are measured in the low-speed wind tunnel, and CFD computations are carried out to compare with experimental measurement and to give more insight into the

MEXICO blade. The probable reasons resulting in the large discrepancy between MEXICO experiment and CFD simulations are discussed.

- Chapter 5 - *Numerical investigation of 3D rotating MEXICO rotor in axial flow condition.*

In this chapter, the axial flow over 3D rotating MEXICO rotor is investigated at different tip speed ratios  $\lambda = 10, 6.67$  and  $4.17$ , representing fully attached, design and stalled flow conditions. The numerical predictions of aerodynamic loads and velocity field are compared against experimental measurements. The rotational effects are discussed regarding lift enhancement at inboard part of the blade, radial flow and Coriolis force, separation points, etc. Secondly, transitional flow considering laminar-turbulent boundary layer transition is investigated numerically to improve the aerodynamic loads prediction, and the transitional line along 3D blade is identified. Lastly, the challenging stalled case with  $\lambda = 4.17$  is studied using more advanced detached eddy simulation approach, aiming to acquire a better agreement with experiments compared to RANS and URANS results.

- Chapter 6 - *Aerodynamics study of TUDelft rotor*

To further quantify the flow characteristics, the 3D flow field surrounding the blade itself of TUDelft rotor, operating at tip speed ratio  $\lambda = 7.0$ , is numerically investigated by CFD. The numerical prediction of velocity components in three directions at different radial sections are compared against detailed PIV measurements. The aerodynamic forces along the blade are compared between numerical results, including CFD, BEM and panel methods and forces derived from PIV data. The contribution of each force term to normal and tangential forces is investigated.

- Chapter 7 - *Conclusions.*

This chapter concludes the outcome of previous chapters and presents the recommendations for the future work.

# 2

## WIND TURBINE AERODYNAMICS

*All truths are easy to understand once they are discovered;  
the point is to discover them.*

Galileo Galilei

*This chapter presents the basic concepts of wind turbine rotor aerodynamics and rotor aerodynamics modeling techniques. First, the aerodynamics of steady 2D airfoil is introduced and successively extended to 3D rotating wind turbine blade. Secondly, an overview of state of the art in rotor aerodynamics modeling is given, ranging from industry's workhorse BEM model to more sophisticated CFD methods. The literature survey mainly focuses on work relevant to the study of wind turbine aerodynamics in axial flow conditions and identify physics modeled on wind turbine which introduce most uncertainty.*

## 2.1. 2D AIRFOIL AERODYNAMICS

When an airfoil is submerged into a uniform flow with velocity  $U_\infty$ , the streamlines become curved around the airfoil geometry due to the shape of the airfoil. A pressure difference between upper side and lower side of the airfoil is present due to the curvature of the streamline and thus giving a lifting force on the airfoil. Combined with friction force acting on the airfoil surface, an integral resultant force  $r$  is determined. This force  $r$  can be further decomposed into a lift force  $l$ , perpendicular to the free stream velocity  $U_\infty$ , and a drag force  $d$ , which is parallel to  $U_\infty$ . These forces are per unit length and can be seen in Figure 2.1.

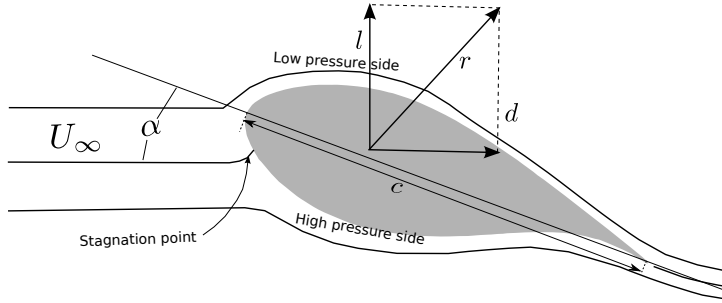


Figure 2.1: The sketch of streamlines past an airfoil and generating forces.

The lift and drag force coefficients are defined as:

$$c_l = \frac{l}{0.5\rho U_\infty^2 c}, \quad c_d = \frac{d}{0.5\rho U_\infty^2 c}, \quad (2.1)$$

where  $\rho$  is the fluid density and  $c$  is the (local) chord length.

For incompressible flow, the force coefficients  $c_l$  and  $c_d$  are functions of geometric angle of attack  $\alpha$  and  $Re$ . The geometric angle of attack is defined as the angle between the chordline and free-stream velocity  $U_\infty$ .  $Re$  is the Reynolds number based on the chord length and  $U_\infty$ , representing the ratio of inertial forces to viscous forces.  $Re = U_\infty c / \nu$ , where  $\nu$  is the kinematic viscosity of fluid.

Figure 2.2 presents the  $c_l$  and  $c_d$  of a given airfoil DU91-W2-250 versus the angle of attack  $\alpha$ . At a relatively low angle of attack, the flow remains attached over airfoil surface and  $c_l$  is increasing linearly as  $\alpha$  increases. The slope of the lift coefficient versus  $\alpha$  is  $2\pi$  based on thin airfoil theory see e.g. (Abbott and Doenhoff, 1959). The flow starts to separate from the airfoil and eventually stalls when  $\alpha$  is larger than a certain value  $\alpha_{c_{l_{max}}}$ , which is known as the critical angle of attack (stall angle).  $c_l$  significantly decreases after stall angle and  $c_d$  sharply increases.

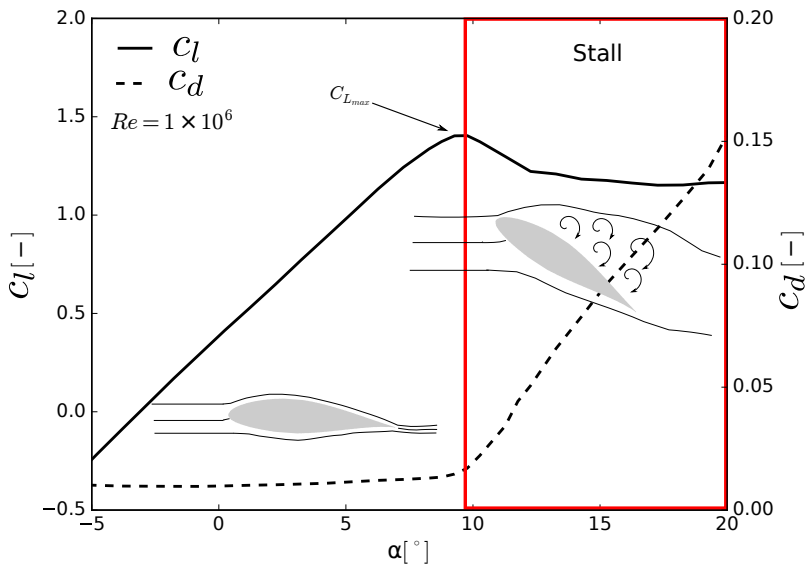


Figure 2.2:  $c_l$  and  $c_d$  behavior of DU91-W2-250 airfoil at  $Re = 1.0 \times 10^6$ .

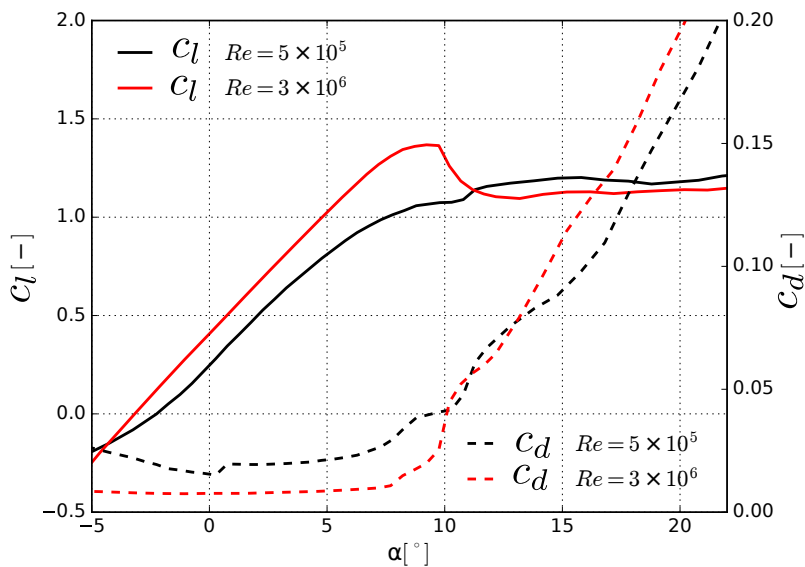


Figure 2.3: Reynolds number effects on  $c_l$  and  $c_d$  of DU91-W2-250 airfoil.

The effect of Reynolds number on  $c_l$  and  $c_d$  can be clearly seen in Figure 2.3. At lower Reynolds number, the viscous forces play more significant role in the flow than the inertial force. A boundary-layer transition from laminar to turbulent flow normally occurs in fluids. Since the laminar flow is characterized by being more unstable in regions of adverse pressure gradients, the laminar boundary layer easily separates and reversed flow occurs downstream. A bubble, named as Laminar Separation Bubble (LSB), is normally formed on the airfoil surface at a low angle of attack. The process of transition from laminar to turbulent flow and formation of LSB is illustrated in Figure 2.4. One consequence of LSB is the reduction of the lift force and the increase of the drag for the airfoil in the linear region, which can be observed in Figure 2.3.

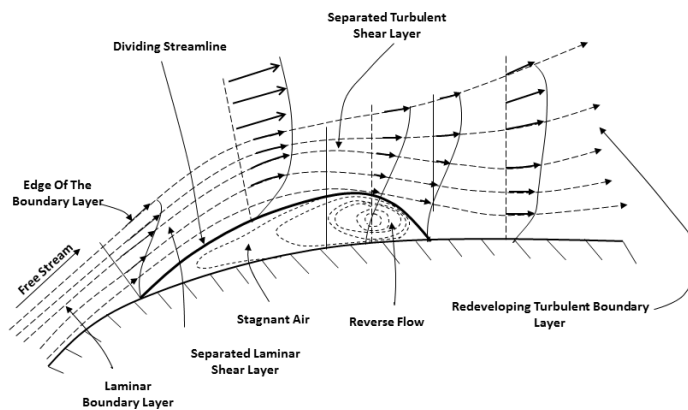


Figure 2.4: Schematic of flow transition and laminar separation bubble (LSB) on the airfoil suction side (Horton, 1968).

## 2.2. 3D FINITE WING AERODYNAMICS

In fact, the real wind turbine has a blade of finite span, which is different from the "infinite span 2D airfoil" aerodynamics. Therefore, in this chapter, the aerodynamics of a finite wing is present before moving on to rotating wind turbine blade with finite span.

Because the wing is finite, at the tips, the pressure difference between the lower side and upper side (see Figure 2.1) pushes the air flow around the tips from lower side to the upper side (Hansen, 2000). An area of concentrated vorticity is shed from the tip, which is known as the tip vortex. This tip vortex causes induction velocities which result in a downwash component on the free-stream velocity  $U_\infty$  at the location of the wing. As a result, the effective angle of attack becomes smaller. The effective angle of attack is

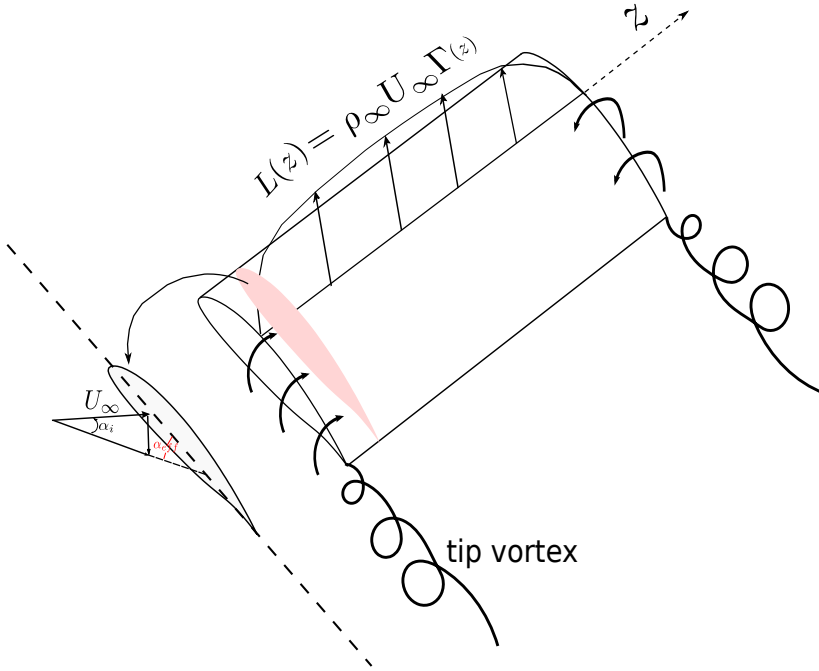


Figure 2.5: Lifting line theory of the finite wing and downwash effect.

determined from

$$\alpha_{eff} = \alpha - \alpha_i, \quad (2.2)$$

where  $\alpha_i$  is the induced angle caused by the downwash velocity at the wing.

To calculate finite wing characteristics, Prandtl (Anderson Jr, 2010) developed a theory (the Prandtl lifting line theory) which models the sectional airfoil as a vortex filament of strength  $\Gamma$ . Then the lift of the finite wing can be obtained from the distribution of circulation over the span  $\Gamma(z)$

$$L = \int_{-\frac{b}{2}}^{\frac{b}{2}} \rho U_\infty \times \Gamma(z) dz, \quad (2.3)$$

where  $\Gamma(z)$  is the circulation at spanwise location  $z$ .

The lifting line theory was developed and is limited to incompressible and inviscid flow. It is also assumed that the three-dimensionality is only limited to downwash, which means the spanwise velocity is small and can be neglected compared to streamwise velocity.



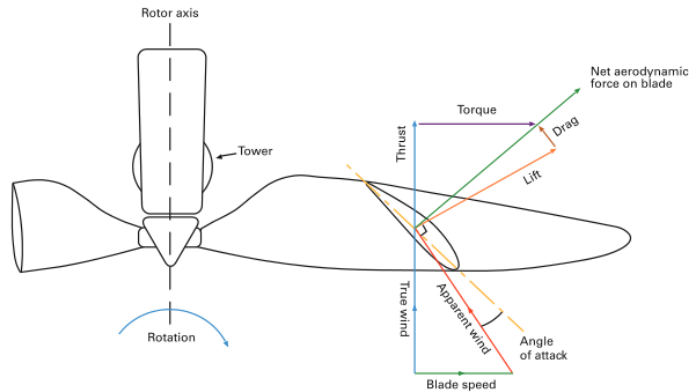


Figure 2.6: Blade sections with blade angle.

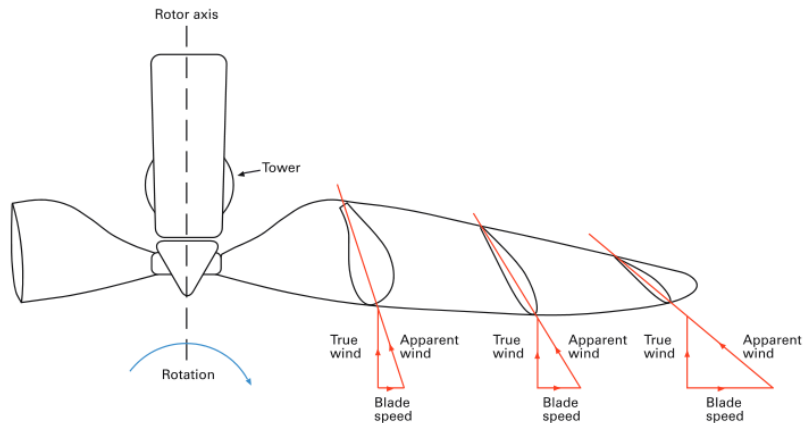


Figure 2.7: Twist of blade.

## 2.3. WIND TURBINE BLADE AERODYNAMICS

A wind turbine rotor extracts energy from the wind and produces power by the rotational motion of its blades through the air. This is similar as the finite wing producing lift by relative movement to the flow. Each airfoil section on the rotating wind turbine blade generates aerodynamic forces. The angle between airfoil chord line and resultant velocity, which is the combination of axial and tangential velocity, defines the incidence angle of the flow, see Figure 2.6.

When the blade radial location moves closer to the tip, the tangential velocity increases, such that the resulting local angle of attack at the tip is smaller than at the root. Therefore, in order to get best aerodynamic characteristics at each blade section, the wind turbine blade is designed with a twist distribution along the span, see Figure 2.7.

The overall performance of wind turbine rotor is characterized by the thrust and power coefficients  $C_T$  and  $C_P$ , which are functions of an important dimensionless property  $\lambda = \frac{\omega R}{U_\infty}$ . This  $\lambda$  is the ratio between the tangential speed of the tip and the actual speed of the wind, a factor to identify the designed blade efficiency and is called the tip speed ratio. A schematic relation between power coefficient  $C_P$  and tip speed ratio  $\lambda$  is shown in Figure 2.8.

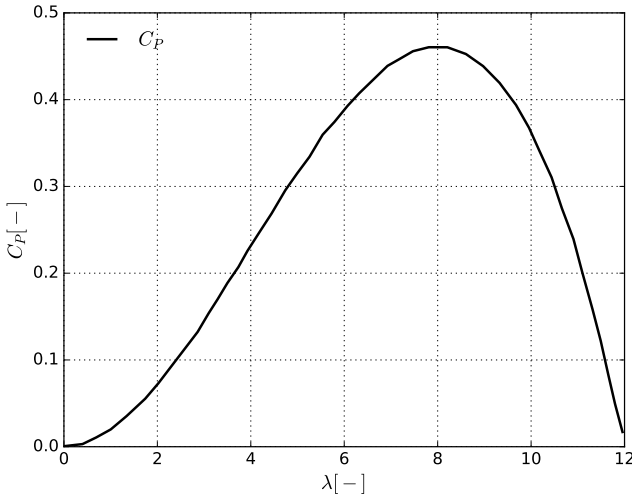


Figure 2.8:  $C_P - \lambda$  curve.

Regarding the aerodynamic loads on a wind turbine blade, the load on the blade is in principle constant during rotation if the incoming wind is perpendicular to the rotor plane (axial flow condition), see the left image in Figure 2.9. The blade section at particular radial location encounters the same local angle of attack at different azimuth angle. When the wind is turbulent, the local inflow and hence the local angle of attack may change over one rotation. However, when there is a misalignment between wind and turbine pointing position (yaw angle), the local angle of attack at particular blade section is periodically varying at every azimuth position of the blade. Therefore, the forces

on blade per phase angle vary and present unsteady features. Figure 2.10 shows an example of the unsteady sectional normal force in one revolution at 30% $R$  and 47% $R$  under 30° yaw angle.

2

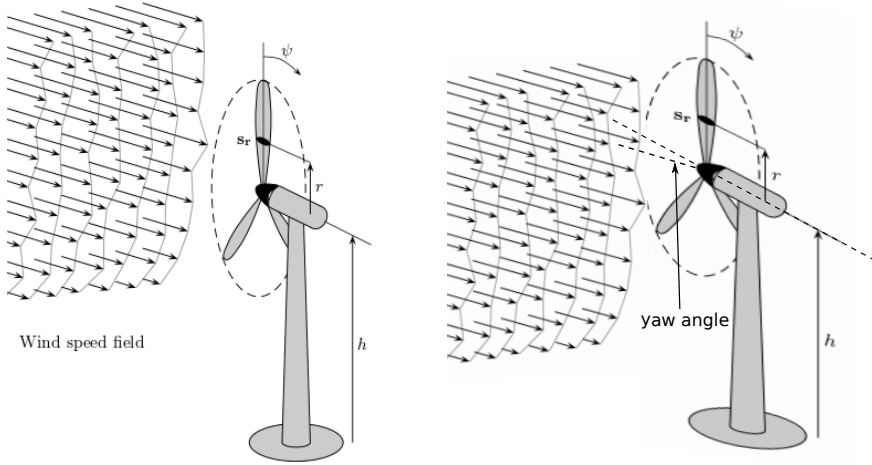


Figure 2.9: Wind turbine in axial (left) and yawed (right) flow conditions.

## 2.4. ROTOR AERODYNAMICS MODELING

To numerically calculate the aerodynamic performance of a wind turbine rotor, several numerical modeling approaches, from low fidelity to high fidelity, have been developed in particular for wind energy application. This section will briefly introduce these modeling techniques.

### 2.4.1. BLADE ELEMENT MOMENTUM METHOD

The most classical model is the Blade Element Momentum (BEM) method from Glauert (Glauert, 1935), still widely being used in wind turbine design as the industry's workhorse. This method combines the 1-D momentum theory and local blade element theory. The momentum theory assumes that the wind turbine rotor is an ideal and a permeable disc, see Figure 2.11, which means the flow is inviscid and no losses at tip occur (Brøndsted and Nijssen, 2013). Because the disc extracts energy from the wind, the wind speed slows down from  $U_0$  far upstream of the rotor to  $U$  at the rotor plane, finally to  $U_1$  in the far wake. Close to the rotor plane, there is a pressure rise from free stream pressure  $p_0$  to  $p$  and a  $\Delta p$  pressure decrease is present over the disc. The development of velocity and pressure from far upstream to far downstream can also be seen in Figure 2.11.

Applying Bernoulli equation before the rotor plane and after the rotor plane, we get

$$p_0 + \frac{1}{2}\rho U_0^2 = p + \frac{1}{2}\rho U^2 \quad (2.4)$$

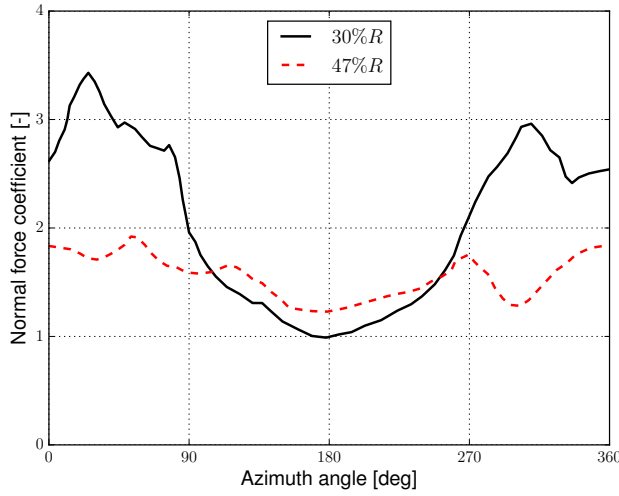


Figure 2.10: Normal force coefficients verse azimuth angles at 30%R and 47%R for NREL rotor under wind speed 15 m/s, yaw angle 30° (Simms et al., 2001).

and

$$p - \Delta p + \frac{1}{2}\rho U^2 = p_0 + \frac{1}{2}\rho U_1^2. \quad (2.5)$$

Combining Equation 2.4 and Equation 2.5 provides the pressure drop over rotor:

$$\Delta p = \frac{1}{2}\rho(U_0^2 - U_1^2). \quad (2.6)$$

Based on the conservation of mass, Equation 2.7:

$$\dot{m} = \rho U_0 A_0 = \rho U A = \rho U_1 A_1 \quad (2.7)$$

Therefore, the thrust  $T$  on the rotor can be expressed by  $\Delta p$  as well as momentum difference:

$$\Delta p A = T = \dot{m}(U_0 - U_1) \quad (2.8)$$

Coupling Equations 2.6, 2.7 and 2.8 shows

$$U = \frac{1}{2}(U_0 + U_1) \quad (2.9)$$

The axial induction factor  $a$  is again introduced here:

$$U = (1 - a)U_0 \quad (2.10)$$

The far wake velocity  $U_1$ , the extracted power  $P$  and the corresponding thrust  $T$  in terms of  $a$  can then be rewritten as,

$$U_1 = (1 - 2a)U_0 \quad (2.11)$$

$$P = \frac{1}{2} \rho U (U_0^2 - U_1^2) A = 2 \rho a (1 - a)^2 U_0^3 A \quad (2.12)$$

$$T = \Delta p A = 2 \rho a (1 - a) U_0^2 A \quad (2.13)$$

Figure 2.12 shows a section at radial  $r$  on the rotor blade to illustrate the velocity diagram. The resultant velocity is given by:

$$V_{rel} = \sqrt{U_0(1 - a)^2 + (\omega r(1 + a'))^2} \quad (2.14)$$

$$\alpha = \varphi - \theta \quad (2.15)$$

$$\tan \varphi = \frac{(1 - a)U_0}{(1 + a')\omega r} \quad (2.16)$$

The normal and tangential force can be calculated from the lift and drag coefficients, which can be determined from airfoil data. The relations are

$$C_N = C_L \cos \varphi + C_D \sin \varphi \quad (2.17)$$

and

$$C_T = C_L \sin \varphi - C_D \cos \varphi. \quad (2.18)$$

The thrust and torque for each annular element can then be written as

$$dT = \frac{1}{2} \rho V_{rel}^2 c B C_N dr \quad (2.19)$$

$$dQ = \frac{1}{2} \rho V_{rel}^2 c B C_T r dr \quad (2.20)$$

Assuming the thrust and torque derived from momentum theory are equal to the expression from the blade element, we have

$$4a(1 - a)U_0^2 = \sigma V_{rel}^2 C_N \quad (2.21)$$

$$4a'(1 - a)\omega r U_0 r = \sigma V_{rel}^2 C_T r \quad (2.22)$$

where  $\sigma = \frac{cB}{2\pi r}$  is the rotor solidity,  $c$  is the chord and  $B$  is the number of blades.

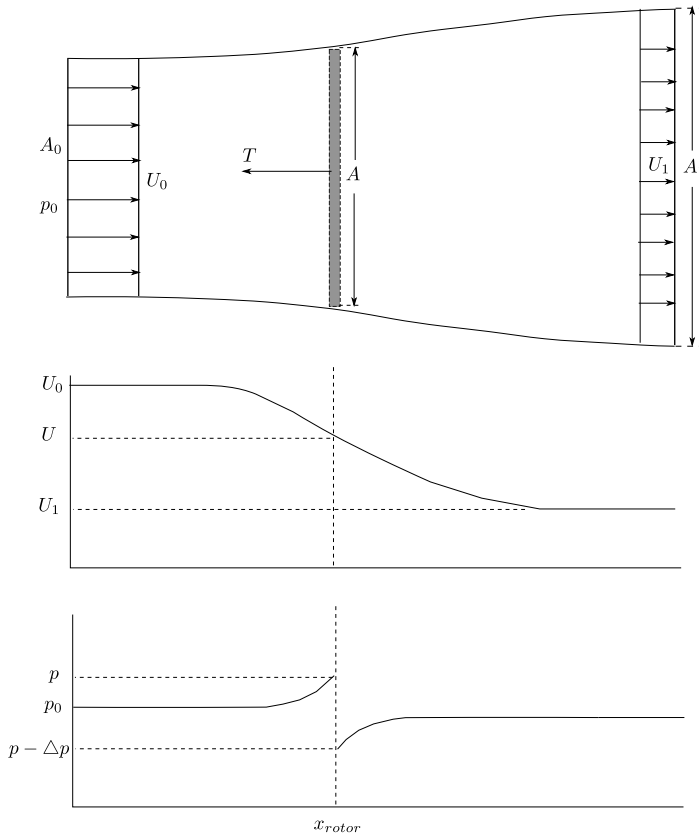


Figure 2.11: Sketch of flow past the ideal wind turbine rotor. The free-stream velocity  $U_0$  is decreased to  $U$  at the rotor location  $x_{rotor}$  and finally to  $U_1$  in the far wake.

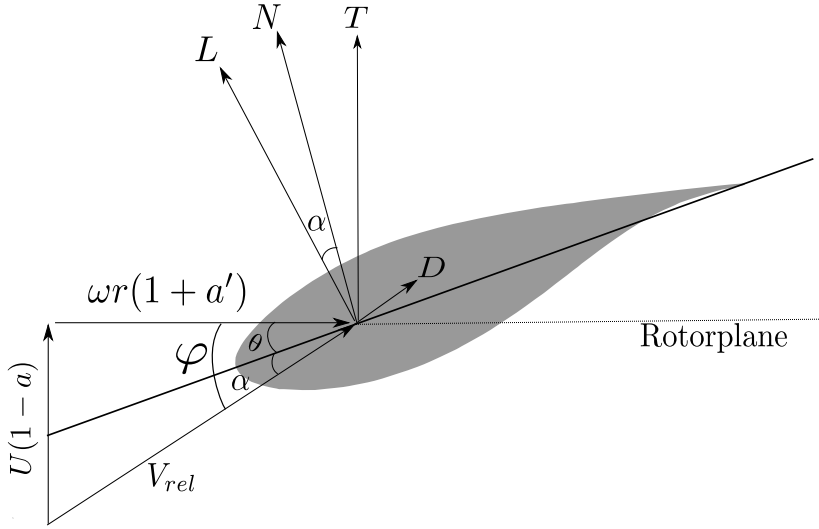


Figure 2.12: Sketch of a blade section in axial flow at radius  $r$ .

#### TIP-LOSS CORRECTION

Due to the assumption of infinite number of blades in momentum theory, a correction model of Prandtl (Glauert, 1935) is used to take into account the effect of finite number of blades, which is known as tip loss correction. The tip loss correction factor is expressed as:

$$F = \frac{2}{\pi} \cos^{-1} e^{-\frac{B}{2} \frac{R-r}{r \sin \varphi}} \quad (2.23)$$

Therefore, by applying this correction factor on momentum part of blade element momentum equations, Equations 2.21 and 2.22 become

$$4a(1-a)FU_0^2 = \sigma V_{rel}^2 C_N \quad (2.24)$$

$$4a'(1-a)\omega r F U_0 r = \sigma V_{rel}^2 C_T r \quad (2.25)$$

The iterative procedures of applying BEM method are as follows:

1. Guess values of  $a$  and  $a'$ .
2. Calculate the angle of relative wind from Equation 2.16.
3. Calculate the angle of attack  $\alpha$  from Equation 2.15, and determine  $C_L$  and  $C_D$  from 2D airfoil aerodynamic coefficients.
4. Update  $a$  and  $a'$  from Equation 2.24 and 2.25.

The above procedure is repeated until convergence criteria are satisfied.

Because of its simplicity and the reasonable accuracy of BEM theory, it is being commonly used and further improved for calculating wind turbine rotor aerodynamics. (Shen et al., 2005) developed a new tip loss correction model for aerodynamic computations of wind turbine. The new model is mathematically consistent and is validated for the NREL experiment and the Swedish WG 500 rotor for a wide range of tip speed ratios. A better prediction of force distribution in the vicinity of the tip is obtained compared to the original Prandtl tip loss correction. (Glauert, 1926a) proposed a correction in BEM theory to compute the aerodynamic loads for highly loaded rotors, which is known as the turbulent wake state ( $a > 0.5$ ) and is applicable when the basic BEM theory become invalid. Many researchers attempt to use BEM method for wind turbine rotor computation in yawed condition by introduction of skewed wake correction models. Relevant work can be found in the references (Glauert, 1926b) (RP Coleman and Stempin, 1945) (Pitt and Peters, 1981) (Snel and Schepers, 1995). One limitation of using skewed wake model is that a cylindrical wake is assumed, which is not always true for wind turbine rotors. Meanwhile, there is no firm theoretical basis for applying this correction to BEM theory (Moriarty and Hansen, 2005).

### 2.4.2. VORTEX WAKE MODEL

#### LIFTING LINE AND LIFTING SURFACE MODELS

A specific class of vortex wake models uses lifting line or lifting surface to represent the rotor blades. The blade trailing vorticity and shed vorticity is convected into the wake with the local total velocity, calculated as the vectorial sum of the free stream velocity  $U_0$  and the relevant velocities induced by the existing vorticity elements (Snel, 1998). For the lifting line model, the blade lift is lumped into a single line with bound vorticity  $\Gamma$ , representing vortex strength. The variation of the vorticity along the lifting line gives rise to trailing vortex filaments with a strength determined by the gradient of vorticity along the span. In yawed flow, the shed vorticity is generated due to the change of bound circulation on the lifting line in time. For the lifting surface model, the blade geometry is simplified to a lifting surface with zero-thickness, coinciding with the camber line (Haans, 2011). All these methods need to calculate the induced velocities due to the trailing vorticity and shed vorticity using the law of Biot-Savart:

$$\vec{V} = \frac{1}{4\pi} \int_Q \frac{\vec{\omega} \times (\vec{r}_0 - \vec{r}_1)}{(\vec{r}_0 - \vec{r}_1)^3} dQ \quad (2.26)$$

where  $\vec{V}$  is the velocity vector at a particular point,  $\vec{\omega}$  is the vorticity,  $\vec{r}_0$  is the position vector of a point on vortex filament,  $\vec{r}_1$  is the position vector of a point which is calculated, and  $Q$  is the volume of fluid encompassing the vortex region. Figure 2.13 illustrates the trailing and shed vorticity in lifting line and lifting surface models.

(Robison et al., 1995b) apply a lifting line model with a prescribed wake model to predict the steady axial flow for horizontal axis wind turbine rotors. Afterward, the authors extended this model to yawed flow condition (Robison et al., 1995a). The numerical results are compared with both experimental data and results from a free wake model, and modest agreement is found with measurements. (Coton and Wang, 1999) use a lifting line model with prescribed wake model to predict wind turbine performance in yawed



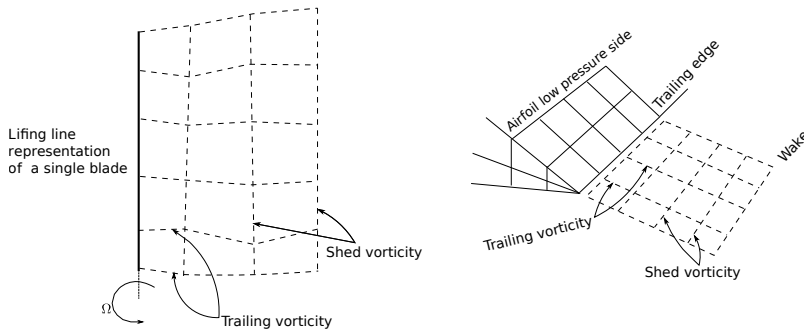


Figure 2.13: Trailing and shed vorticity filaments of lifting line and lifting surface models. Adapted from (Micallef, 2012).

condition. Generally, good agreement with measurements is obtained. The challenge of modeling three-dimensional effects and dynamic stall result in the differences with measured field data. (van Garrel, 2003) developed a free wake lifting line code AWSM at ECN. The model is verified for some test cases with analytical solutions. (Snel et al., 2008) further validated AWSM code with MEXICO experiments in both axial and yawed flow conditions.

Compared to the lifting line model, a lifting surface method is applied less to wind turbine rotors. (Tangler, 2002) predicts the NASA Ames rotor performance with lifting-surface, prescribed-wake model and blade-element momentum method. The results indicate that lifting surface model shows significant improvement over BEM method. As a recommendation from (Tangler, 2002), lifting surface model is recommended for future analytical improvements. (Tangler, 2004) later continues to use this model to investigate wind turbine stall and post-stall aerodynamics. (Pesmajoglou and Graham, 2000) use a free wake lifting surface method to simulate the inviscid flow field of a rotor in yaw. The simulated results are compared with experimental and wind tunnel measurements. The numerical results compare reasonably well with measured cycle averaged hub yaw moments over a large range of yaw angles.

#### PANEL METHOD

For the panel methods, the rotor blade geometry is distributed with sources  $\sigma$  and doublets  $\mu$  on the blade surface, and the wake is modeled as a sheet of distributed doublets, see Figure 2.14. The potential flow field can be obtained as:

$$V(x; t) = V_0 + \nabla\Phi(x; t) \quad (2.27)$$

$$\Phi(x; t) = -\frac{1}{4\pi} \int_{S_B} \sigma\left(\frac{1}{x}\right) dS + \frac{1}{4\pi} \int_{S_B + S_W} \mu\left[\frac{\partial}{\partial n}\left(\frac{1}{x}\right)\right] dS + \nabla\Phi_\infty \quad (2.28)$$

where  $x$  is the distance from panel to a point P in the flow field,  $S_B$  is the blade body surface,  $S_W$  represents the wake surface,  $n$  represents the normal direction to a surface,  $\Phi$  is the potential function,  $\Phi_\infty$  is the freestream potential field,  $\mu$  is the doublet strength

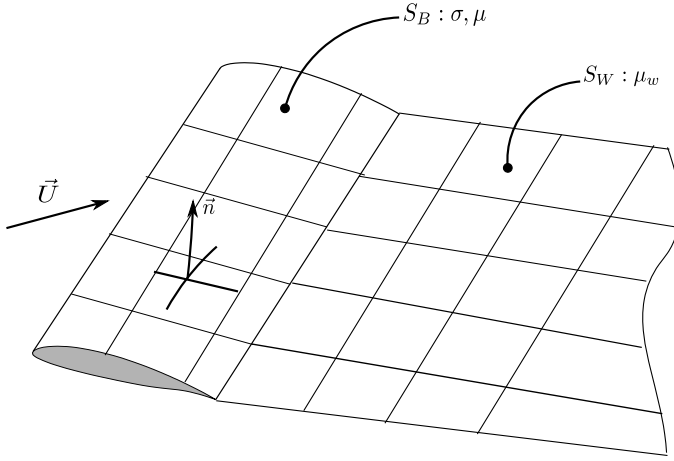


Figure 2.14: Representation of panel method.

and  $\sigma$  is the source strength. More detailed and extensive description of panel method can be found in literature (Katz and Plotkin, 1991).

Since panel methods include the exact geometry of blade, more accurate blade modeling can be achieved compared to lifting line and lifting surface methods. Meanwhile, the aerodynamic characteristics of airfoil data are not required in panel model. However, the main limitation of a panel method is that this model can not model flow separation. Although the method is developed for inviscid flow, the viscous effect can be taken into account by using vortex core models or vortex viscous dissipation models.

The application of panel methods on wind turbine has been carried out both on horizontal axis wind turbine and vertical axis wind turbine. (Whale et al., 2000) show that the panel method has a good qualitative agreement with PIV data regarding the wake structures behind a two-blade rotor operating in the range  $\lambda = 3 - 8$ . (Micallef, 2012) uses a 3D, unsteady panel method to simulate 3D flows near several different horizontal axis wind turbine rotors. Overall speaking, good agreement of velocity field is found between numerical results and experimental measurement in the mid-span and root region, but distinct differences are observed behind the trailing edge at the tip region. (Dixon, 2008) developed an unsteady, free-wake panel method and successfully applied it on vertical axis wind turbine rotors.

### 2.4.3. NAVIER-STOKES BASED METHOD

An alternative to advanced panel methods for wind turbine rotor aerodynamics is computational fluid dynamic (CFD) technique, in which the Navier-Stokes equations are solved numerically. The non-linear governing equations of any fluid motion in incom-

pressible form are:

$$\nabla \cdot \mathbf{u} = 0 \quad (2.29)$$

$$\frac{\partial \mathbf{u}}{\partial t} + (\mathbf{u} \cdot \nabla) \mathbf{u} = -\frac{1}{\rho} \nabla p + \nu \nabla^2 \mathbf{u} + \mathbf{f}_b \quad (2.30)$$

where  $\mathbf{u}$  is the velocity,  $p$  is the pressure,  $\nu$  is the kinematic viscosity,  $\mathbf{f}_b$  is the body force.

According to different methodologies of modeling wind turbine rotor, several techniques including actuator disk, actuator line and fully resolved rotor methods have been developed by implementation of different forms of body force.

The actuator disk method models the wind turbine rotor as a disk and imposing corresponding forces on the fluid. The thrust force applied as body force in Equation 2.30 is determined from

$$f_b = T = \frac{1}{2} \rho u_0^2 A C_T \quad (2.31)$$

where  $T$  is the thrust force,  $\rho$  is the density,  $u_0$  is the unperturbed resolved velocity of the axial incident flow in the center of the rotor disk.  $A$  is the rotor swept area,  $C_T$  is the thrust coefficient.

The actuator disk model uses a one directional thrust force and therefore does not model rotation of wind turbine rotor. However, the rotational effect can be taken into account in this model by introducing a tangential force, which can be determined from 2D airfoil characteristics, similar as blade element method in Section 2.4.1. Even though the actuator disk model may simulate the rotor and its wake, it does not create the tip vortices that are carried onto the wake (Troldborg, 2009).

The actuator line method models the wind turbine blade as a lifting line along the blade axis. The lift and drag forces for each element of the lifting line are calculated from the tabulated airfoil data. These forces then are imposed on the fluid as the body force.

$$f_{2D} = \frac{1}{2} \rho V_{rel}^2 c(c_l e_l + c_d e_d) \quad (2.32)$$

where  $c_l$  and  $c_d$  are lift and drag coefficients,  $V_{rel}$  is the resultant velocity and  $e_l$  and  $e_d$  are the unit vector in the direction of lift and drag.

Compared to an actuator disk model, the actuator line method provides more accurate results and especially the flow structures near the blade such as root and tip vortices can be investigated in this model. More extensive description of actuator disk and actuator line methods are referred to the references (Mikkelsen, 2003) (Troldborg, 2009) (Tossas and Leonardi, 2013).

As the computational power increased, recently fully resolved rotor simulation with CFD has attracted researchers' interest. Since there are no simplifications for modeling the geometry of wind turbine rotor, more accurate results and more flow physics can be modeled by this approach.

The first complete CFD simulations for wind turbine rotors were carried out by (Sørensen and Hansen, 1998). Sørensen solved incompressible RANS equations using  $k - \omega$  SST

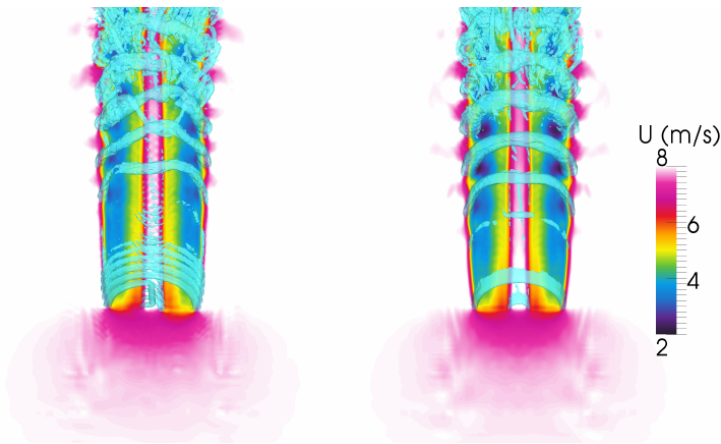


Figure 2.15: Actuator line model (left) and actuator disk model (right) simulations (Tossas and Leonardi, 2013).

turbulence model proposed by (Menter, 1994) in a rotating frame of reference. The predicted loads match very well with the experimental result for wind speed up to  $10 \text{ m/s}$ , but start to deviate from experimental results as the velocity increases. Mesh resolution and turbulence modeling in highly separated flows are two possible reasons which may cause these deviations. (EP Duque and Yee, 2000) evaluated the ability of a RANS method and two other methods, BEM and vortex lattice method for predicting the aerodynamic performance. Compared with experimental data, good power and sectional force predictions are obtained at pre-stall wind conditions for all three methods, but the RANS method fails to predict the performance when the flow stalls. (Sørensen et al., 2002) used an incompressible Reynolds-averaged Navier-Stokes solver to predict the wind turbine performance for NREL/NASA Ames wind tunnel tests. The DTU in-house code named EllipSys3D with  $k-\omega$  SST turbulence model is applied in the simulation. Aerodynamic coefficients and pressure distribution were investigated at several wind speeds. Except for the case at wind speed  $10 \text{ m/s}$ , the numerical results show good qualitative and quantitative agreement with the measurements. Massive flow separation and unstable flow behavior is observed in the  $10 \text{ m/s}$  case, which is the main reason for the large deviation. In the work of (Duque et al., 2003), RANS code and lifting line code are compared for NREL phase VI experiment. The aerodynamic performance of a two-bladed wind turbine were predicted at axial conditions. For all wind speeds, RANS method does a better job of predicting not only the correct trend in normal force, but also the correct absolute magnitude within the standard deviation of the measured data. The results show significant spanwise flow upon onset of stall. (Tachos et al., 2009) used commercial software Fluent to predict span-wise loading of wind turbine rotor at the wind speed  $7.2 \text{ m/s}$  with Spalart-Allmaras turbulent model. Three dimensional steady flow around the wind turbine rotor are solved by using the single reference frame (SRF) technique. Calculated pressure distribution and the experiment data is in satisfactory agreement. Important discrepancies are observed in the  $r/R = 0.30$  station near the blade root. The limiting streamlines showed that strong 3D effects and flow separations occur near the root. The

results showed that CFD code can accurately predict the loads. To overcome the difficulties in predicting highly separated flow which fails conventional RANS simulation, (Johansen et al., 2002) used DES method to simulate the flow around the non-rotating NREL Phase VI wind turbine blade under parked conditions and undergoing sinusoidal pitching motion along the blade axis. Good agreement of the force and pressure distribution prediction was obtained at low angles of attack, while when the flow is totally separated at high angle of attack, the agreement is only fair. Compared to the conventional two-equation RANS  $k-\omega$  SST turbulence model, DES computations do not seem to improve the predicted blade characteristics. For the complete rotor simulation, (Li et al., 2012) applied overset CFD simulations for NREL Phase VI rotor and concluded that little difference in the averaged forces and moments are observed between RANS and DES simulations, but significant improvements in the transient response are seen when using DES. Regarding numerical modeling of a boundary layer transitional flow from laminar to turbulent on the rotating wind turbine blade, there are few works related to this research by means of affordable RANS modeling approach. (Sørensen, 2009) used a correlation based transition model  $\gamma - Re_\theta$  to predict transitional flow over S809 airfoil and NREL Phase VI wind turbine rotor. The computations show good agreement and distinct improvement in the drag predictions, compared with using fully turbulent computations for the 2D airfoil case. The work shows that transition model improves the prediction by enhancing stall in the inboard part of the blade. However, in the work of (Sørensen, 2009) the two missing correlation functions in the transition model have been tuned based on a series of zero-pressure gradient flat-plate boundary layers, which could be further improved. There are many aspects that need to be improved and investigated regarding full rotor CFD simulation. The first aspect is to evaluate the performance of advanced turbulence models (DES, DDES and hybrid LES/RANS) in predicting highly separated flow for different wind turbine rotors, to investigate whether these approaches show superior performance compared to RANS simulations in dealing with such challenging flow. Another aspect is reliable laminar-turbulent boundary layer transition modeling for wind turbine airfoils and rotors with relatively cheap simulations, such as RANS calculations. Finally, all these numerical results of full rotor simulations have to be validated with experimental data. High quality wind tunnel measurements of different wind turbine rotors are still far limited.

## 2.5. CONCLUSIONS

This chapter presents the basic concepts of the fundamental aerodynamics of airfoils and wind turbine flows. 2D aerodynamics of steady state airfoil, 3D finite wing aerodynamics and rotating wind turbine blade aerodynamics are successively introduced and discussed in this chapter. More specifically, the state of the art of numerical modeling techniques for wind turbine aerodynamics is reviewed, from simple BEM theory to sophisticated CFD approach. The advantage and limitation of each model are also discussed.

As the computational power increases, the numerical simulations of wind turbine flow based on solving Navier-Stokes equations system becomes popular both in academia and industry since more flow physics can be resolved in such approaches. Although many work has been done and validated in predicting aerodynamic loads for the NREL

wind turbine rotor under different operating conditions, some research should be done and further investigated by using full CFD rotor simulation in uniform flow. There are many deficits in both the validation study and the numerical modeling. Besides the NREL rotor experiment, more wind tunnel measurements with high quality experimental data definitely are needed to validate CFD results. Regarding the numerical modeling, more advanced turbulence modeling approach (DES, DDES, hybrid LES/RANS) is preferred to apply and validate for wind turbine rotor operating at highly separated flow condition. Boundary layer transition modeling from laminar to turbulent has received little attention for 3D full rotor simulation and it is recommended to include it in the simulations. Therefore, in order to reduce the research gap, in this study different CFD modeling approaches including physics-based transition model  $k-k_L-\omega$  in RANS and delayed detached eddy simulation (DDES) will be applied for predicting the aerodynamic loads for the MEXICO rotor, measured under different operating conditions in wind tunnel.



# 3

## VERIFICATION AND VALIDATION OF OPENFOAM CODE

*Risk comes from not knowing what you're doing.*

Warren Buffett

*This chapter presents the verification and validation of the turbulence and transition models of OpenFOAM code which need to be addressed before utilizing them in a 3D complex flow. The chapter is separated into two main branches. The first part focuses on turbulence modeling. Both RANS simulations with linear-eddy viscosity models and delayed detached eddy simulations (DDES) are evaluated and validated for relatively simple 2D and 2.5D cases. The second part of work in this chapter is laminar-turbulence boundary layer transition modeling. The implementation errors of transition model  $k - k_L - \omega$  are observed in OpenFOAM-2.1.1, and the correct formulation has been implemented afterward. The transition onset predictions of this correct implementation, the wrong implementation in OpenFOAM-2.1.1, and the same model which has been already corrected in OpenFOAM-3.0.1 are compared together to evaluate the transition model performance.*

*The results indicate that the linear eddy viscosity models, including Spalart-Allmaras and  $k - \omega$  SST turbulence models, have a good agreement with well validated code CFL3D from NASA and experimental data. For predicting stalled flow over the airfoil, DDES shows significant improvement compared to RANS and URANS approaches. Finally, the correct implementation of transition model is developed in OpenFOAM-2.1.1 and shows very promising results regarding  $c_l$ ,  $c_d$  and transition onset prediction.*

---

Part of this chapter is adapted from (Zhang et al., 2015)



### 3.1. INTRODUCTION

In this chapter different methods of turbulence and transition modeling in OpenFOAM code are evaluated which affect the accuracy of numerical prediction for wind turbine aerodynamics. The purpose is to answer the questions below:

- Standard turbulence models (Spalart-Allmaras,  $k - \omega$  SST) are widely used in external flow for the industry in the open source code OpenFOAM. Are these models showing the same results with the well validated code?
- When massively separated flow occurs, how does the delayed detached eddy simulation perform in predicting lift  $C_L$  and drag  $C_D$ ?
- Is the transition model  $k - k_L - \omega$  correctly implemented in OpenFOAM? How does it perform in terms of prediction of transition onset,  $c_l$  and  $c_d$ ?

For each question, several classical and simple 2D (2.5D) simulation cases are performed and compared with either numerical results from validated codes or experimental results. The evaluation and validation of turbulence modeling, including RANS with linear eddy viscosity models and DDES with Smagorinsky model, are discussed in Section 3.2. The laminar-turbulent transition model is evaluated in Section 3.3. Conclusions are described in Section 3.4.

### 3.2. VALIDATION OF TURBULENCE MODELS

In this section, the widely used eddy viscosity turbulence models (S-A,  $k - \omega$  SST) in OpenFOAM are validated with a 2D flat plate case and the classic NACA0012 airfoil. The numerical prediction will be compared with either theoretical solution or results from other validated CFD code. Afterward, hybrid LES/RANS will be validated and evaluated with a flat plate case and a 2.5D NACA0021 airfoil in deep stall case.

#### 3.2.1. EDDY VISCOSITY TURBULENCE MODEL

##### 2D FLAT PLATE WITH ZERO PRESSURE GRADIENT

The first test case is a 2D turbulent flat plate with a zero pressure gradient. The Reynolds number is  $Re_x = 5 \times 10^6$  at  $x = 1m$ . The grid has  $545 \times 385 \times 2$  points with  $y^+ = 0.1$ , see Figure 3.1. The inlet turbulent boundary condition parameter is chosen as  $\tilde{\nu}/\nu = 3$  in order to have the same setting and make comparison possible with publicly available CFL3D code of NASA (Krist et al., 1998).

There are self-similar solutions for the mean velocity parallel to the wall for high  $Re$  number flows, which is proposed by (von Kármán, 1931) in 1931. The solutions depend on the distance from a certain point to the "wall". A dimensionless wall distance is defined as:

$$y^+ = \frac{yu_\tau}{\nu} \quad (3.1)$$

where  $u_\tau$  is the friction velocity,  $\nu$  is the kinematic viscosity, and  $y$  is the distance to the wall.

Based on the distance to the wall, the turbulent boundary layer can be separated into the inner layer and the outer layer, as seen from Figure 3.2. In the outer layer, the flow is

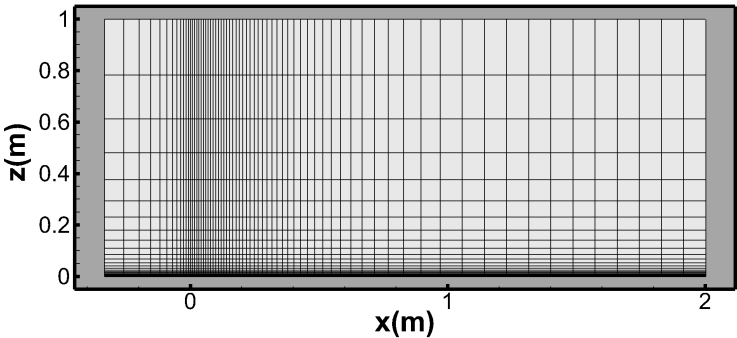


Figure 3.1: Schematic of 2D flat plate

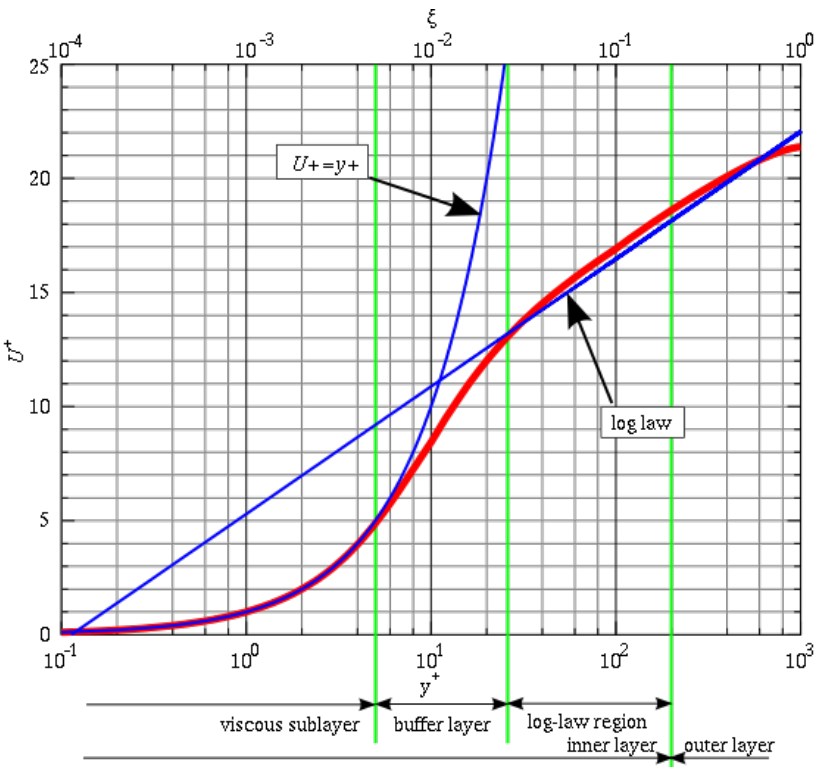


Figure 3.2: Law of the wall (Nezu and Tominaga, 2000)

not affected by the shear at the wall. The inner layer is subdivided into three layers: the viscous sublayer, the buffer layer and the turbulent region governed by the logarithmic law.

**Viscous sublayer:** In the viscous sublayer ( $y^+ < 5$ ), the mean velocity has a relation with wall distance:

$$u^+ = \frac{u}{u_\tau} = y^+, \quad (3.2)$$

where  $u_\tau = \sqrt{\frac{\tau_w}{\rho}}$  is the friction velocity.

**Log law layer:** In the log-law layer  $y^+ > 30$ , the mean velocity can be calculated from

$$u^+ = \frac{1}{\kappa} \ln y^+ + C^+, \quad (3.3)$$

where the Von Kármán constant  $\kappa \approx 0.41$  and  $C^+ \approx 5.0$  for a smooth wall.

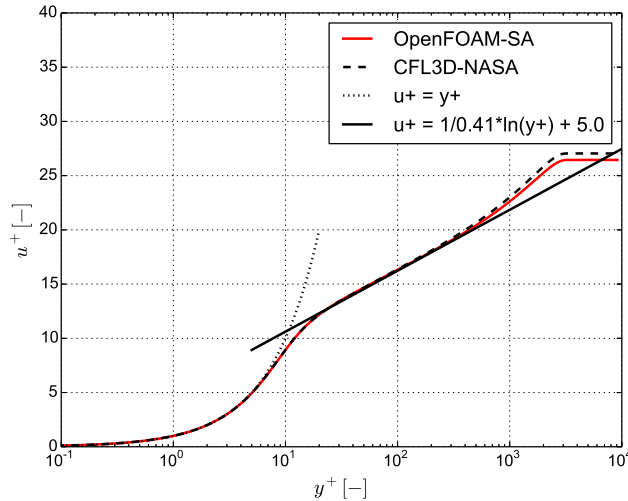


Figure 3.3: The comparisons of mean velocity profile in the turbulent boundary layer at  $x = 0.97m$  for S-A turbulence model

Figure 3.3 and 3.5 show the numerical results of the averaged velocity in the turbulent boundary layer from the S-A and SST turbulence models at the location  $x = 0.97m$ . The calculated velocity profiles are compared both with the results of the CFL3D code and the theory of the law of the wall. Excellent agreement can be found between OpenFOAM and CFL3D in the inner layer region (the viscous sublayer, the buffer layer and the log-law layer), both numerical results from two different codes fit the theoretical line well. OpenFOAM with SST turbulence model presents an identical velocity profile as CFL3D code, while some difference is observed for S-A model in the outer layer region. Slightly lower velocity is predicted by OpenFOAM compared to CFL3D code. The comparisons of turbulent viscosity at  $x = 0.97m$  are shown in Figure 3.4 and 3.6. Similarly, the difference in  $\mu_t$  can be observed only for S-A model, mainly appearing at outer layer

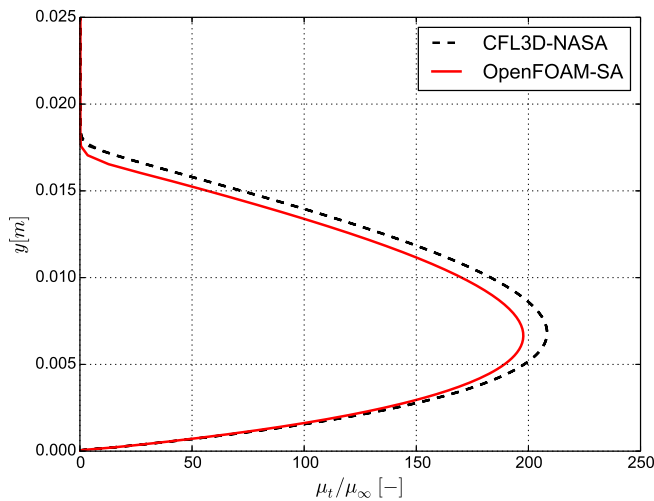


Figure 3.4: The comparisons of eddy viscosity distribution at  $x = 0.97m$  for S-A turbulence model

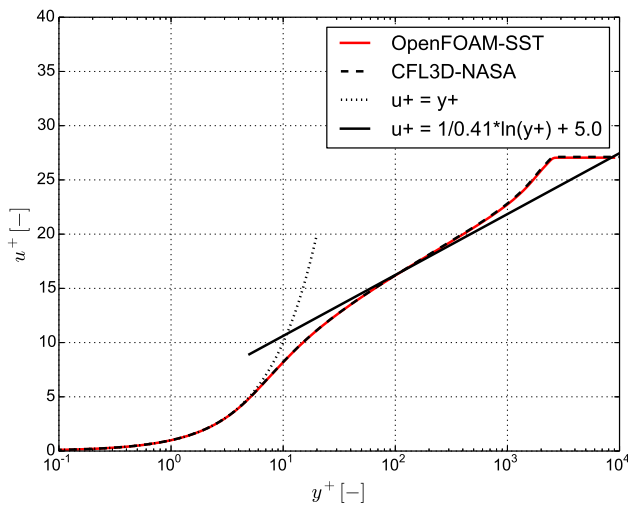


Figure 3.5: The comparisons of mean velocity profile in the turbulent boundary layer at  $x = 0.97m$  for SST turbulence model

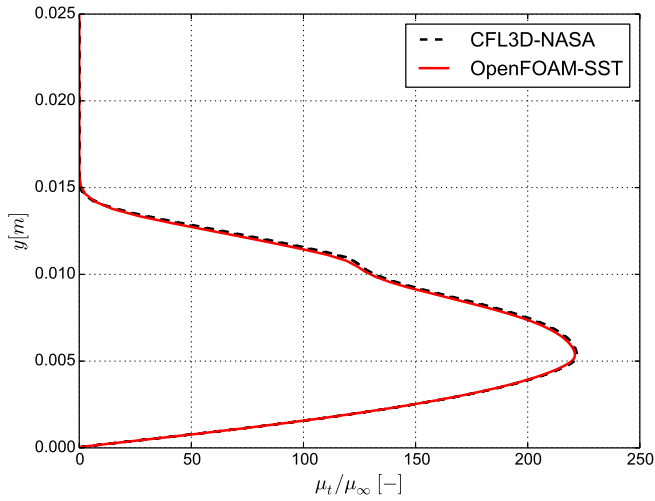


Figure 3.6: The comparisons of eddy viscosity distribution at  $x = 0.97 m$  for SST turbulence model

region. The possible reason why the numerical results show some discrepancies in S-A model between the two codes is that S-A model as implemented in OpenFOAM is the model with the  $f_{v3}$  term, first presented in the paper (Ashford and Powell, 1996). While the S-A model in CFL3D code is the standard version without the  $f_{v3}$  term. The model of  $SA - f_{v3}$  version is devised to prevent negative values of the source term and present unusual transition behavior at low Reynolds numbers (Rumsey et al., 2001).

#### TURBULENT FLOW OVER NACA0012 AIRFOIL AT $Re = 6.0 \times 10^6$

Another test case is the turbulent flow over a NACA0012 airfoil at  $\alpha = 0^\circ$ ,  $Re = 6 \times 10^6$  calculated with  $k - \omega$  SST turbulence model. An adverse pressure gradient exists when the flow passes the airfoil surface, and experimental measurements  $C_L$ ,  $C_D$  and pressure distribution  $C_P$  are available from Turbulence Modeling Resource database of NASA (Rumsey, 2014). Therefore, this is a good validation case.

Three grids with different spacial resolutions are available in the database and used to investigate mesh refinement. The coarser grid is exactly every-other-point of the next finer grid. Figure 3.7 presents the coarse computational grid near the NACA0012 airfoil. Regarding the discretization schemes, second-order upwind is used for the convective terms and second-order linear interpolation scheme is used for the diffusive terms. The convergence criteria is specified as  $10^{-6}$ .

Figure 3.8 and 3.9 compare the pressure distribution  $C_P$  and skin friction  $c_f$  over the upper surface.  $C_P$  and  $c_f$  are defined as

$$C_P = \frac{p - p_\infty}{\frac{1}{2} \rho U_\infty^2}, \quad (3.4)$$

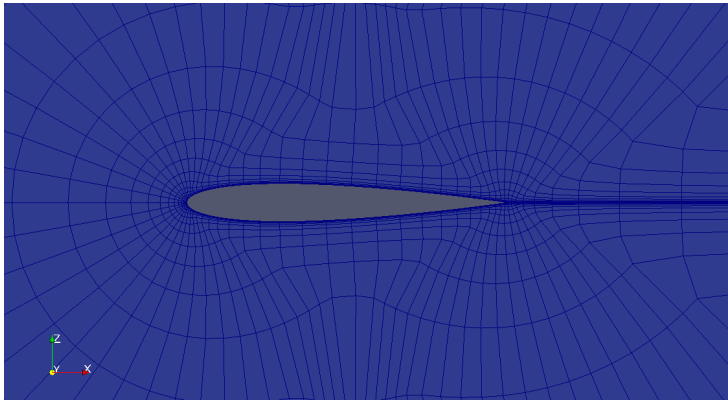


Figure 3.7: The view of the coarse computational grid ( $133 \times 33$ ) for NACA0012 airfoil (Rumsey, 2014)

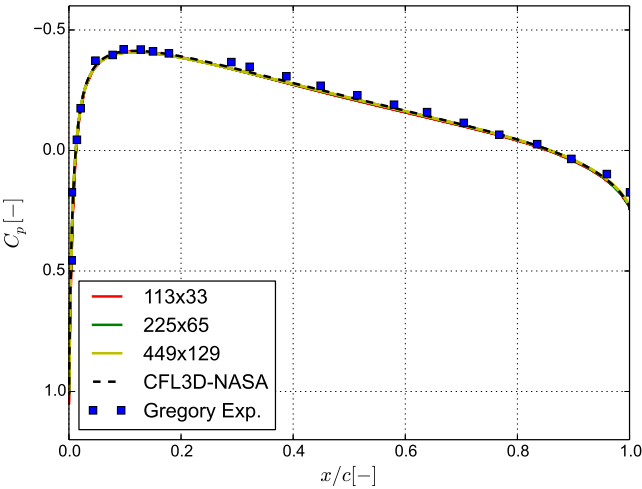


Figure 3.8: The comparison of pressure coefficient on the upper surface at  $\alpha = 0^\circ$ ,  $Re = 6 \times 10^6$  for different grids.

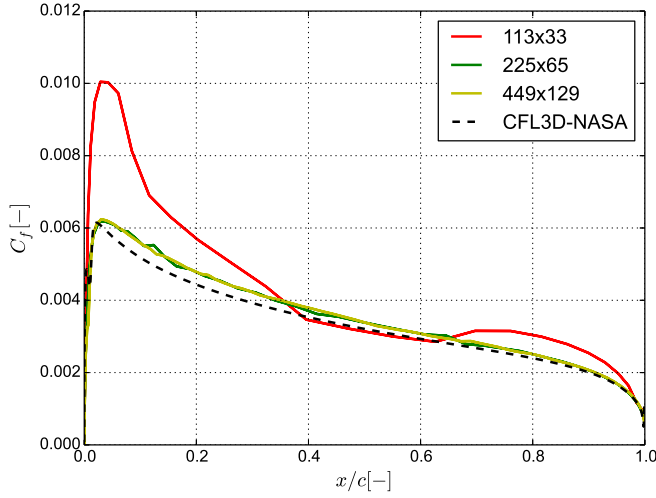


Figure 3.9: The comparison of skin friction on the upper surface at  $\alpha = 0^\circ$ ,  $Re = 6 \times 10^6$  for different grids.

and

$$c_f = \frac{\tau_w}{\frac{1}{2}\rho U_\infty^2}, \quad (3.5)$$

where  $p$  is the static pressure,  $p_\infty$  is the static freestream pressure,  $\rho$  is the fluid density and  $U_\infty$  is the freestream velocity,  $\tau_w$  is the wall shear stress on the surface. It can be determined from the velocity gradient at the wall  $\tau_w = \mu \frac{\partial u}{\partial n}|_{wall}$ .

The comparison shows that the OpenFOAM code gives the same prediction of  $C_P$  as CFL3D code. Moreover, both numerical predictions of the chordwise pressure from two different codes agree very well with the experimental results. A grid independent solution is obtained for  $C_P$  already on the coarse grid. However, the skin friction is more sensitive to the grid density. It can be seen that  $c_f$  becomes grid independent for the medium mesh resolution when comparing to the grid independent solution obtained with CFL3D. The numerical prediction of  $c_f$  from OpenFOAM code has a slightly higher friction.

Table 3.1 lists the values of aerodynamic drag for the three grid levels. The observed order of accuracy  $p$  can be calculated from

$$p = \ln \left( \frac{\phi_{coarse} - \phi_{medium}}{\phi_{medium} - \phi_{fine}} \right) / \ln(r) = \ln \left( \frac{0.0108018 - 0.00874222}{0.00874222 - 0.00870783} \right) / \ln(2) = 5.9042, \quad (3.6)$$

where  $r$  is the constant grid refinement ratio. Once the observed order of accuracy  $p$  is determined, the extrapolated values of  $c_d$  with zero grid spacing can be estimated by

using Richardson's extrapolation method (Ferziger and Peric, 2012):

$$\phi_{extrap} = \phi_{fine} + \frac{\phi_{fine} - \phi_{medium}}{r^p - 1} = 0.008707246. \quad (3.7)$$

Figure 3.10 plots the convergence of  $c_d$  with three different grid levels and estimated extrapolated value by using Richardson's method.

Table 3.1: The value of  $c_d$  with three different grid levels

No.	Grid point[N]	$c_d[-]$
coarse	$113 \times 33$	0.01080180
medium	$225 \times 65$	0.00874222
fine	$449 \times 129$	0.00870783

Regarding the observed order of accuracy  $p$  calculated above, the obtained value is really high and therefore unreliable (theoretical order of accuracy is 2). The possible cause is that the coarse mesh is too coarse and a grid independent solution is almost achieved for the medium and fine meshes. If a theoretical order of accuracy  $p = 2$  to is used to calculate the extrapolated value, the value of 0.008696367 is obtained, which is very close to the value calculated with observed order of accuracy. The difference between these two values is around  $1.0 \times 10^{-5}$ .

### 3.2.2. HYBRID RANS/LES MODEL

As mentioned before, when massively separated flow occurs, a promising solution is the Detached Eddy Simulation (DES), which was first proposed by (Spalart et al., 1997). This approach is a hybrid LES/RANS method which resolves the large-scale detached turbulent eddies by using an LES approach and models the small-scale turbulent eddies in the boundary layer with a RANS approach. Compared to a RANS approach, DES improves the accuracy when massive separation exists, but with less computational cost compared to LES.

#### FILTERED NAVIER-STOKES EQUATION

By applying the LES-filter (Pope, 2000) which removes a range of small scales from the solution to the incompressible Navier-Stokes equations, the LES governing equation of the resolved large eddy can be described as:

$$\frac{\partial \bar{u}_i}{\partial x_i} = 0, \quad (3.8)$$

$$\frac{\partial \bar{u}_i}{\partial t} + \frac{\partial}{\partial x_j} (\bar{u}_i \bar{u}_j) = -\frac{1}{\rho} \frac{\partial \bar{p}}{\partial x_i} + \nu \frac{\partial^2 \bar{u}_i}{\partial x_j \partial x_j} - \frac{\partial \tau_{ij}}{\partial x_j}, \quad (3.9)$$

where the sub-grid scale stress  $\tau_{ij}$  can be modeled using Smagorinsky's model. This approach uses an eddy viscosity hypothesis to the small eddies only. The equation yields:

$$\tau_{ij} = -2\nu_{sgs} \bar{S}_{ij} = -\nu_{sgs} \left( \frac{\partial \bar{u}_i}{\partial x_j} + \frac{\partial \bar{u}_j}{\partial x_i} \right). \quad (3.10)$$



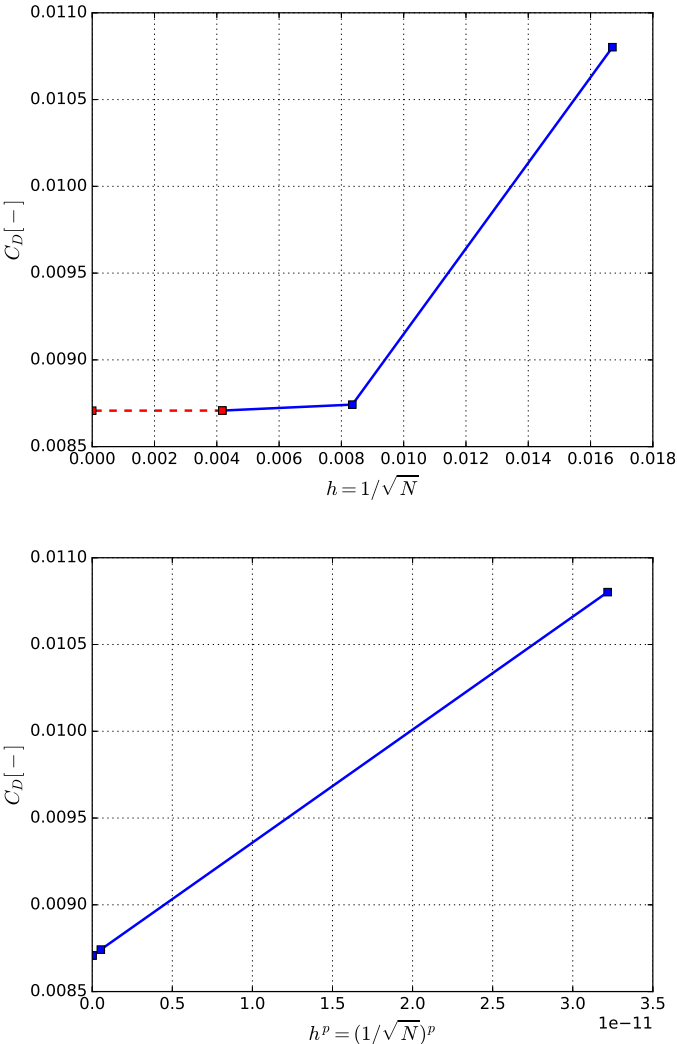


Figure 3.10: The numerical convergence of aerodynamic drag  $c_d$  and corresponding observed order of accuracy  $p = 5.9042$

The subgrid-scale eddy viscosity can be expressed as a function of filter width  $\Delta$ :

$$\nu_{sgs} = l_{sgs}^2 |\tilde{S}| = (C_s \Delta)^2 |\tilde{S}|, \quad (3.11)$$

where  $\tilde{S} = (2\tilde{S}_{ij}\tilde{S}_{ij})^{1/2}$ ,  $l_{sgs}$  is the length scale of the subgrid motions and  $C_s$  is the Smagorinsky constant. The filter width  $\Delta$  is determined by the local grid spacing.

#### SPALART-ALLMARAS TURBULENCE MODEL

As mentioned before, the DES approach switches to the well-known URANS model in the flow close to the wall, where a turbulent boundary layer often exists. The one equation eddy viscosity Spalart-Allmaras turbulence model is then used to model the turbulence in this regime

$$\frac{D\tilde{v}}{Dt} = c_{b1}\tilde{S}\tilde{v} + \frac{1}{c_\sigma} [\nabla \cdot ((\nu + \tilde{v})\nabla\tilde{v}) + c_{b2}(\nabla\tilde{v})^2] - c_{w1}f_w[\frac{\tilde{v}}{\tilde{d}}]^2, \quad (3.12)$$

where  $\tilde{v}$  is the transport variable in S-A model and  $c_{b1}$ ,  $c_\sigma$ ,  $c_{w1}$  are the model constants, which can be found in Table 3.2. Other relations are:

$$\nu_t = \tilde{v}f_{v1}, \quad f_{v1} = \frac{\chi^3}{\chi^3 + c_{v1}^3}, \quad \chi = \frac{\tilde{v}}{\nu}, \quad (3.13)$$

$$\tilde{S} = \omega + \frac{\tilde{v}}{\kappa^2 \tilde{d}} f_{v2}, \quad f_{v2} = 1 - \frac{\chi}{1 + \chi f_{v1}}, \quad (3.14)$$

$$f_w = g[\frac{1 + c_{w3}^6}{g^6 + c_{w3}^6}]^{1/6}, \quad g = r + c_{w2}(r^6 - r), \quad r = \frac{\tilde{v}}{\tilde{S}\kappa^2 \tilde{d}^2}. \quad (3.15)$$

In the S-A model, the turbulence production term  $c_{b1}\tilde{S}\tilde{v}$  is balanced with the turbulence destruction term  $c_{w1}f_w[\frac{\tilde{v}}{\tilde{d}}]^2$  if the flow is in local equilibrium (Rodi et al., 2013). This results in the relation  $\tilde{v} \sim \tilde{S}\tilde{d}^2$ , which has similar relation as  $\nu_{sgs}$  in Equation 3.11. To combine LES and RANS approaches together in DES calculation, a new length scale  $l_{DES}$  is defined to determine whether the LES or RANS equations need be solved in the flow. The expression for this length scale yields:

$$l_{DES} = \min(d_w, C_{DES}\Delta), \quad \Delta = \max(\Delta x, \Delta y, \Delta z), \quad (3.16)$$

where  $d_w$  is the distance to the wall and  $C_{DES} = 0.65$ , which is calibrated by (Shur et al., 1999) using simulations of homogeneous and isotropic turbulence. The new length scale  $l_{DES}$  ensures that near the wall ( $d_w \ll C_{DES}\Delta$ ), the RANS equations are solved. On the other hand, when the flow is far from the wall surface ( $d_w \gg C_{DES}\Delta$ ), the LES calculations are carried out.

#### DELAYED DETACHED EDDY SIMULATION

To overcome the Grid Induced Separation (GIS) problem reported by (Spalart et al., 2006), an improved approach called Delayed-Detached Eddy Simulation (DDES) is used. In this approach, a blending function is used to define the length scale:

$$l_{DES} = d_w - f_d \max(0, d_w - C_{DES}\Delta), \quad (3.17)$$

Table 3.2: Model constants in Spalart-Allmaras turbulence model

$c_{b1} = 0.135$	$c_{b2} = 0.622$
$c_\sigma = 2/3$	$\kappa = 0.41$
$c_{w2} = 0.3$	$c_{w3} = 2$
$c_{v1} = 7.1$	$c_{w1} = c_{b1}/\kappa^2 + (1 - c_{b2})/c_\sigma$

where the shielding function  $f_d = 1 - \tanh(8r_d^3)$  and  $r_d$  is calculated by:

$$r_d = \frac{\nu_t + \nu}{\max[\sqrt{U_{ij}U_{ij}}, 10^{-10}]\kappa^2 d_w^2}, \quad (3.18)$$

where  $\kappa = 0.41$  is the von Karman constant. The shielding function is 0 in the boundary layer and equals 1 at the edge of the boundary layer. Therefore, the shielding function  $f_d$  can be used to indicate whether the calculated cell is located inside the boundary layer or not.

#### TURBULENT FLAT PLATE

The first test case is a turbulent flat plate with zero pressure gradient. The Reynolds number  $Re_x = 5 \times 10^6$  at  $x = 1m$ . The grid is  $545 \times 385 \times 2$  points with  $y^+ = 0.1$ , see Figure 3.1. The inlet turbulent boundary condition parameter is chosen as  $\tilde{\nu}/\nu = 3$  in order to have the same setting and to make comparison with the public CFL3D code (Krist et al., 1998).

Figure 3.11 shows the averaged turbulent velocity boundary layer profile at  $x = 0.97m$ . The dimensionless distance normal to the flat plate varies from  $1 < y^+ < 10^4$ . The blue and green dashed lines give the theoretical relation for the viscous sublayer and the log-law layer, respectively. The steady-state RANS results with Spalart-Allmaras turbulence model from CFL3D code can capture this velocity profile very well. To validate the DDES code in OpenFOAM, the DDES calculation is simulated for the total computational time  $t = 0.7s$  and the time-averaged solutions are used for the comparison. The DDES results shown by the black solid line does give the same velocity profile as CFL3D code. Meanwhile, as expected, grid induced separation problem does not occur in the simulation. Therefore, the Spalart-Allmaras turbulence model in DDES approach is assumed to be properly implemented.

#### NACA 0021 IN DEEP STALL ( $\alpha = 60^\circ$ , $Re = 2.7 \times 10^5$ )

Another typical test case is the flow over an airfoil in a deep stall. The conventional URANS modeling approach fails for this kind of massively separated flow. Originally, DES approach was designed for handling this difficulty (Spalart et al., 1997). The flow over NACA0021 airfoil at  $60^\circ$  angle of attack is considered to further validate the DDES simulation. The numerical results will be compared with the experimental study carried out by (Swalwell et al., 2003).

The flow is studied at the chord-based Reynolds number  $Re_c = 2.7 \times 10^5$ . O-grid topology is used and the first grid spacing on the airfoil surface satisfies the dimensionless wall distance  $y^+ < 1$ . Therefore, no wall function is applied in this study. Figure 3.12 gives the overview of the computational grid. The farfield boundary is located 15 chord

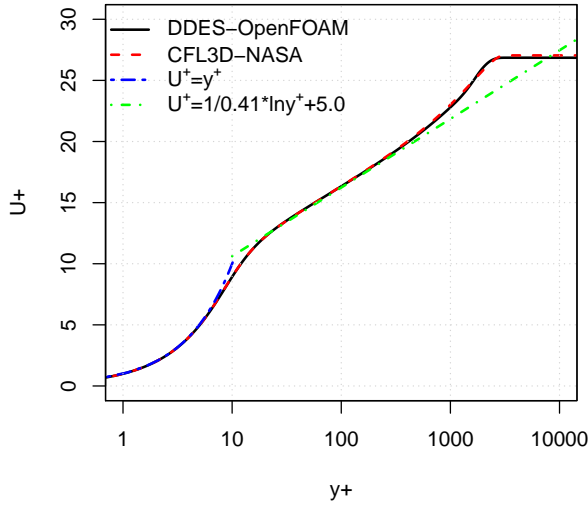


Figure 3.11: The turbulent velocity boundary layer profile at  $x = 0.97m$  for flat plate

units away from the airfoil, and the spanwise length is 1 chord unit. The whole grid has  $70 \times 160 \times 33$  nodes with equal spanwise grid spacing  $0.03c$ . The second-order linear-upwind stabilized transport (LUST) scheme (Weller, 2012), blending linear-upwind scheme with linear interpolation to stabilize solution while maintaining second-order behavior, is employed for the convective term of the velocity. The total variation diminishing (TVD) limited linear interpolation scheme is used for the divergence and gradient terms of  $\tilde{v}$ . A second-order backward scheme is used for the time derivatives. The physical time step is  $\Delta t = 1 \times 10^{-3}s$  ( $\Delta t U_0/c = 0.004$ ). In order to get statistically steady numerical results, the simulation is run for  $tU_0/c = 320$  convective time units.

Table 3.3 shows the time-averaged numerical results of lift and drag coefficients by means of RANS, URANS and DDES calculations as well as the experimental results. The Spalart-Allmaras turbulence model is used for both the RANS and URANS calculations. Compared to the experimental data, DDES calculation gives the best prediction with around 10% higher prediction than the experiment. In addition, URANS simulation shows even worse results than RANS: the integral force is overpredicted by around 50%, whereas RANS has an average of about 25%. The span-averaged lift and drag coefficients are compared in Figure 3.13 both for DDES and unsteady RANS simulations. Unsteady RANS gives familiar periodic force oscillation after initial transient effect, while DDES presents chaotic and disordered force oscillation. Figure 3.14 shows the instantaneous vorticity field at the mid-span at the dimensionless time  $tU_0/c = 200$ , as expected, large-scale turbulent vortical structures in the massively separated wake region can be resolved by DDES.

Table 3.3: Integral forces comparison between RANS, URANS and DDES.

NACA0021	RANS	URANS	DDES	Exp
$\overline{C_L}$	1.184(+27.2%)	1.391(+49.4%)	1.038(+11.5%)	<b>0.931</b>
$\overline{C_D}$	1.911(+25.9%)	2.428(+59.7%)	1.678 (+10.6%)	<b>1.517</b>

3

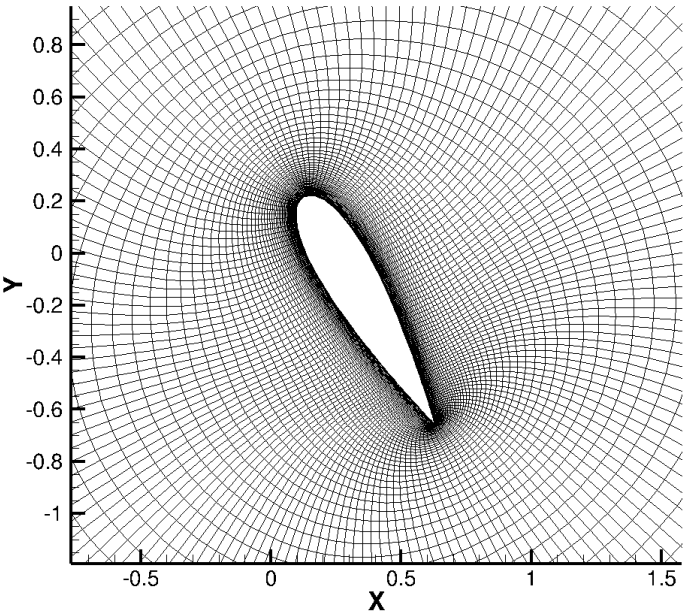


Figure 3.12: Computational grid around NACA0021 airfoil.

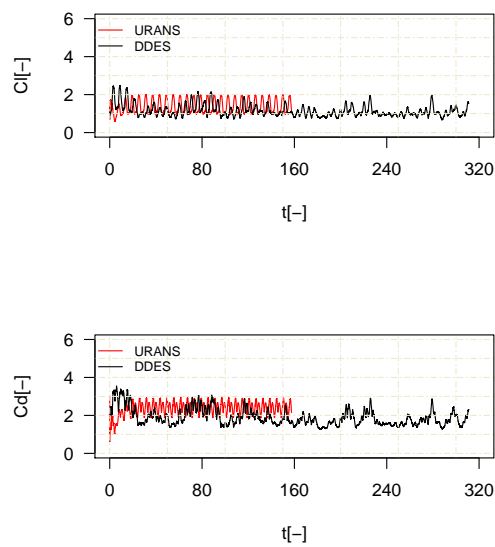


Figure 3.13: Span-averaged lift and drag coefficient of DDES and URANS calculations.

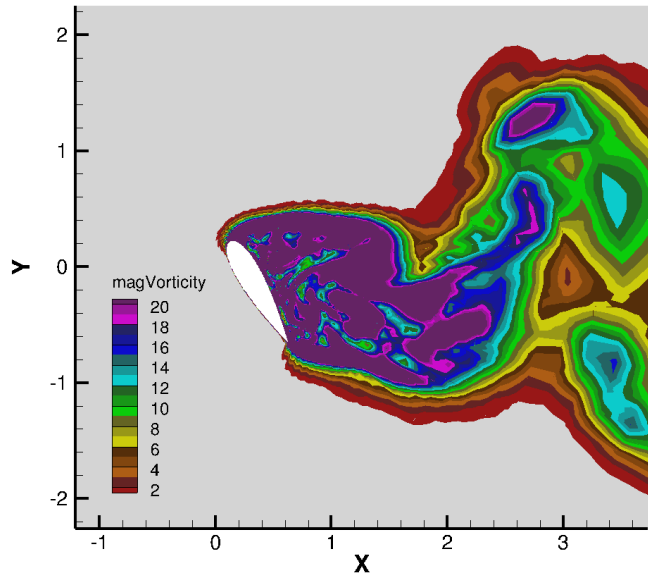


Figure 3.14: Instantaneous vorticity snapshot ( $tU_0/c = 200$ ) from DDES calculation.

### 3.3. VALIDATION OF TRANSITION MODELS

#### 3.3.1. THE STRUCTURE OF $k - k_L - \omega$ TRANSITION MODEL

The concept of laminar kinetic energy in boundary layer transition was originally proposed by (Mayle and Schulz, 1997) to predict bypass transition in gas turbine engines. However, the original model containing  $k_L$  is not a single point model and still requires pre-knowledge of the flow field. The true single-point transition model using laminar kinetic energy was actually proposed later by (Walters and Leylek, 2002) through the implementation of three transport equations for  $k_L$ ,  $k_T$  and turbulent dissipation, respectively, and is named the  $k - k_L - \epsilon$  transition model. The turbulent dissipation equation is shortly replaced by that of specific dissipation rate by (Walters and Leylek, 2005) and forms the  $k - k_L - \omega$  model. Some of the terms in the Walters-Leylek  $k - k_L - \omega$  model were later introduced by (Walters and Cokljat, 2008) to take into account shear-sheltering effect. The implementation of Walters-Cokljat  $k - k_L - \omega$  model in OpenFOAM soon receives attention and has been discussed and further improved by (Fürst et al., 2013).

The bases of  $k - k_L - \omega$  transition model published in 2005 and 2008 are the same. The transport equations for the turbulent kinetic energy  $k_T$ , the laminar kinetic energy  $k_L$  and the specific dissipation rate  $\omega$  in incompressible form are written below:

$$\begin{aligned} \frac{Dk_T}{Dt} = & \underbrace{P_{k_T}}_{\text{production}} + \underbrace{R_{BP} + R_{NAT}}_{\text{bypass and natural transition}} - \underbrace{\omega k_T}_{\text{destruction}} - \underbrace{D_T}_{\text{anisotropic dissipation}} \\ & + \underbrace{\frac{\partial}{\partial x_j} \left[ \left( \nu + \frac{\alpha_T}{\sigma_k} \right) \frac{\partial k_T}{\partial x_j} \right]}_{\text{diffusion}} \end{aligned} \quad (3.19)$$

$$\begin{aligned} \frac{Dk_L}{Dt} = & \underbrace{P_{k_L}}_{\text{production}} - \underbrace{R_{BP} + R_{NAT}}_{\text{bypass and natural transition}} - \underbrace{D_L}_{\text{anisotropic dissipation}} + \underbrace{\frac{\partial}{\partial x_j} \left[ \nu \frac{\partial k_L}{\partial x_j} \right]}_{\text{diffusion}} \end{aligned} \quad (3.20)$$

$$\begin{aligned} \frac{D\omega}{Dt} = & \underbrace{C_{\omega 1} \frac{\omega}{k_T} P_{k_T}}_{\text{production}} + \underbrace{\left( \frac{C_{\omega R}}{f_W} - 1 \right) \frac{\omega}{k_T} (R_{BP} + R_{NAT})}_{\text{bypass and natural transition}} - \underbrace{C_{\omega 2} f_W^2 \omega^2}_{\text{destruction}} \\ & + \underbrace{C_{\omega 3} f_\omega \alpha_T f_W^2 \frac{\sqrt{k_T}}{d^3}}_{\text{boundary layer wake correction}} + \underbrace{\frac{\partial}{\partial x_j} \left[ \left( \nu + \frac{\alpha_T}{\sigma_\omega} \right) \frac{\partial \omega}{\partial x_j} \right]}_{\text{diffusion}} \end{aligned} \quad (3.21)$$

#### 3.3.2. $k - k_L - \omega$ IMPLEMENTATION AND CORRECTIONS IN OPENFOAM

However, there are some bugs in this model of OpenFOAM-2.1.1/2.3.0 and these bugs seem to be fixed in the later released versions of OpenFOAM-2.4.0/3.0 based on the paper (Fürst et al., 2013). The small difference between OpenFOAM-2.4.0/3.0 and the revised model of Fürst can only be found in the dissipation terms  $D_T$  and  $D_L$ . Fürst

proposed that these terms should be multiplied by a factor 2 by considering the balance between the dissipation and diffusion in the laminar sublayer (the same as  $k - \epsilon$  model or the older versions of  $k - k_L - \epsilon$  (Launder and Sharma, 1974) and  $k - k_L - \omega$ ), but the implementation of OpenFOAM-2.4.0/3.0 keeps the formula as the one in the paper (Walters and Cokljat, 2008). In this thesis, the revised model of Fürst is implemented in OpenFOAM-2.1.1 to check the influence of these dissipation terms and is named as *corrected kkLOmega* in this thesis. The difference, as mentioned before, is the dissipation term in the  $k_T$  and  $k_L$  equations, which is two times larger than the one in OpenFOAM-2.4.0/3.0.

The different implementations of  $k - k_L - \omega$  transition model in original OpenFOAM-2.1.1/2.3.0 and OpenFOAM-2.4.0/3.0 are described in Table 3.4. In addition, the original equations from the corresponding papers are also included.

Table 3.4: The implementations of  $k - k_L - \omega$  transition models in different versions of OpenFOAM

Terms	OpenFOAM-2.1.1/2.3.0	OpenFOAM-2.4.0/3.0	paper(2008 (Walters and Cokljat, 2008)	paper(2005 (Walters and Leylek, 2005)
Destruction	$C_{\omega} 2 \omega^2$	$C_{\omega} 2 f_W^2 \omega^2$	$C_{\omega} 2 \omega^2$	$C_{\omega} 2 f_W^2 \omega^2$
$f_{INT}$	$\min(\frac{k_L}{C_{INT} k_{TOT}}, 1)$	$\min(\frac{k_L}{C_{INT} k_{TOT}}, 1)$	$\min(\frac{k_L}{C_{INT} k_{TOT}}, 1)$	$\min(\frac{k_L}{C_{INT} k_{TOT}}, 1)$
$f_{\tau, l}$	$1 - \exp(-C_{\tau, l} \frac{k_{T, l}}{\lambda_{eff}^2} \omega^2)^{\dagger}$	$1 - \exp(-C_{\tau, l} \frac{k_{T, l}}{\lambda_{eff}^2} \Omega^2)$	$1 - \exp(-C_{\tau, l} \frac{k_{T, l}}{\lambda_{eff}^2} \Omega^2)$	$1 - \exp(-C_{\tau, l} \frac{k_{T, l}}{\lambda_{eff}^2} \Omega^2)$
$\lambda_T$	$\lambda_T = \frac{\sqrt{k_{TOT}}}{\omega} *$	$\lambda_T = \frac{\sqrt{k_T}}{\omega}$	$\lambda_T = \frac{\sqrt{k_T}}{\omega}$	$\lambda_T = \frac{k^{\frac{3}{2}}}{\epsilon}$
$f_W$	$f_W = \frac{\lambda_{eff}}{\lambda_T}$	$f_W = (\frac{\lambda_{eff}}{\lambda_T})^{\frac{2}{3}}$	$f_W = \frac{\lambda_{eff}}{\lambda_T}$	$f_W = (\frac{\lambda_{eff}}{\lambda_T})^{\frac{2}{3}}$
$D_T$	$\nu \frac{\partial k_T}{\partial x_j} \frac{\partial k_T}{\partial x_j}$	$\nu \frac{\partial k_T}{\partial x_j} \frac{\partial k_T}{\partial x_j}$	$\nu \frac{\partial k_T}{\partial x_j} \frac{\partial k_T}{\partial x_j}$	$2\nu \frac{\partial k_T}{\partial x_j} \frac{\partial k_T}{\partial x_j}$
$D_L$	$\nu \frac{\partial k_L}{\partial x_j} \frac{\partial k_L}{\partial x_j}$	$\nu \frac{\partial k_L}{\partial x_j} \frac{\partial k_L}{\partial x_j}$	$\nu \frac{\partial k_L}{\partial x_j} \frac{\partial k_L}{\partial x_j}$	$2\nu \frac{\partial k_L}{\partial x_j} \frac{\partial k_L}{\partial x_j}$

<sup>†</sup>the magnitude of vorticity  $\Omega$  is wrongly implemented in OpenFOAM 2.1.1/2.3.0 by using specific turbulence dissipation rate  $\omega$ .

\*The total fluctuation kinetic energy  $k_{TOT}$  is implemented in older versions of OpenFOAM, instead of turbulent kinetic energy  $k_T$ .

### 3.3.3. TEST CASES

In order to investigate which published model/implementation is most accurate, three different types of test cases are considered: channel flow, zero pressure gradient flat plate and wind turbine airfoil. For each test case, the numerical results are compared to each other and reference DNS or experimental results.

#### CHANNEL FLOW

First of all, the test case of 2D channel flow is tested for the  $k - k_L - \omega$  transition model to verify the code. The friction Reynolds number is  $Re_{\tau} = 395$  based on the half channel height  $\delta$ ,  $Re_{\tau} = \frac{u_{\tau} \delta}{\nu}$ . The DNS data of (Moser et al., 1999) is used to compare the predicted mean velocity profile and total fluctuation kinetic energy of  $k - k_L - \omega$  transition model.

Figure 3.15 shows the mean velocity profile in the fully developed turbulent channel flow. The comparison indicates that the implementation of the  $k - k_L - \omega$  model in OpenFOAM-2.1.1/2.3.0 is wrong. Although the velocity in the viscous sublayer near the wall is captured quite well, the velocity is significantly over predicted in the log-law layer compared to the DNS results. On the other hand, the corrected implementation  $k - k_L - \omega$  transition model in OpenFOAM-2.1.1 presents correct velocity profile, similar as the one in OpenFOAM-2.4.0/3.0. Slight overprediction of the velocity is found in the log-law region both in *corrected kkLOmega* and OpenFOAM-2.4.0/3.0 models.



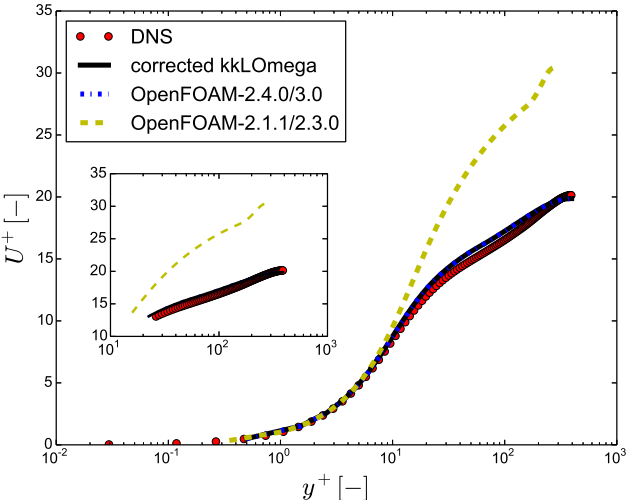


Figure 3.15: The comparison of mean velocity profiles in fully developed turbulent channel at  $Re_\tau = 395$  (Moser et al., 1999)

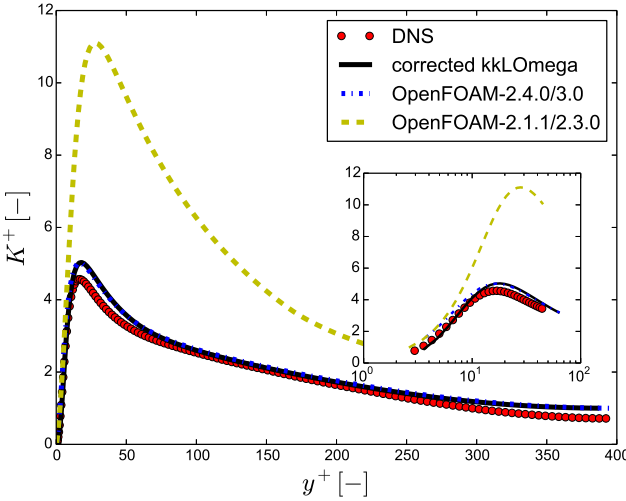


Figure 3.16: The comparison of total fluctuation kinetic energy ( $k_{TOT} = k_T + k_L$ ), normalized by the friction velocity

In terms of the total fluctuation kinetic energy  $k = \frac{1}{2}(u' u' + v' v' + w' w')$ , which corresponds to the  $k_{TOT} = k_T + k_L$  within the transition model, the comparison shows that not only the mean velocity is significantly overpredicted by the wrong implementation, but also the fluctuation in the outer layer. The corrected implemented model and the  $k - k_L - \omega$  model in OpenFOAM-2.4.0/3.0 give reasonable results, but with slight overprediction of total fluctuation kinetic energy in the regions  $10 < y^+ < 50$  and  $y^+ > 300$ .

#### TRANSITIONAL FLAT PLATE WITHOUT PRESSURE GRADIENT

Table 3.5: Inflow condition of T3 series flat plate

	U[m/s]	$k_t [m^2/s^2]$	$\omega[1/s]$	$\nu_t/\nu[-]$	Tu[%]
T3A	5.4	0.04763	23.8	12	3.3
T3B	9.2	0.5364	33.066	120	6.5
T3A-	19.8	0.0564	43.8934	12	0.91

To evaluate the capability of transition onset prediction, the T3 series experimental flat plate test cases are used to validate the model. The inflow condition of each test case is described in Table 3.5.

By comparing the results from different implementations, it is found that there are no differences in freestream turbulence decay for the three cases, which are measured at different inflow turbulence intensities. Regarding the transition onset prediction and skin friction coefficient, for the T3A case with turbulence intensity  $Tu = 3.3\%$ , see Figure 3.18, OpenFOAM-2.1.1/2.3.0 obviously gives an incorrect distribution. The transition onset is predicted earlier by this implementation than the experimental measurement. Meanwhile, the  $C_f$  has a good agreement with experiments only in the laminar region ( $Re_x < 1.0 \times 10^5$ ), but is seriously underpredicted in the turbulent region. The models of *corrected kkLomega* and OpenFOAM-2.4.0/3.0 show much better agreement both in transition onset and  $C_f$  distribution. Almost the same  $C_f$  distribution is given by these two implementations, but only slightly higher friction is observed in OpenFOAM-2.4.0/3.0 for the turbulent flow. For the T3B and T3A- cases in Figures 3.20 and 3.22, OpenFOAM-2.1.1/2.3.0 also fails to predict transition onset and friction coefficient correctly. However, the *corrected kkLomega* model and OpenFOAM-2.4.0/3.0 implementation present reasonable results, and the latter implementation gives better agreement with experimental data with respect to the transition onset position and the value of friction coefficient.

#### 2D WIND TURBINE AIRFOIL

The simulations of flow over the 2D wind turbine airfoil DU91-W2-250 are carried out to evaluate the performance of transition model  $k - k_L - \omega$  in terms of aerodynamic characteristics and transition onset. The chord-based Reynolds number is  $Re_c = 1.0 \times 10^6$ . A fully structured O-type grid is used for the CFD simulations, see Figure 3.23. The computational domain is about 100 chords in order to minimize the influence of the boundary. The first wall-normal grid distance from the airfoil surface is small enough to ensure the dimensionless wall distance  $y^+ < 1$ , such that the viscous sublayer of the turbulent boundary layer can be resolved.

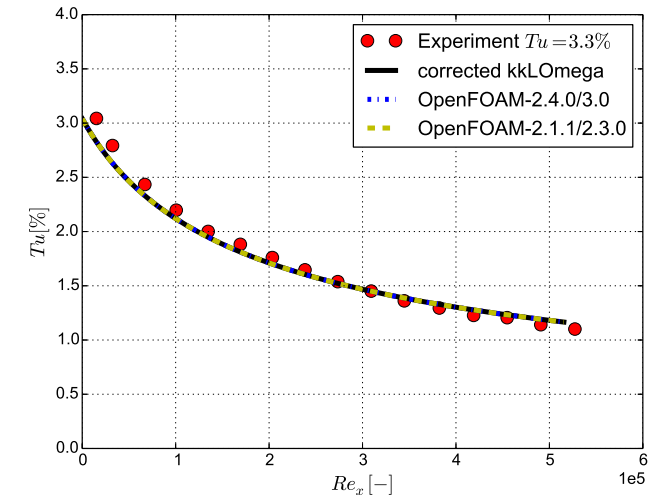


Figure 3.17: Comparisons of freestream turbulence intensity distribution for T3A case.

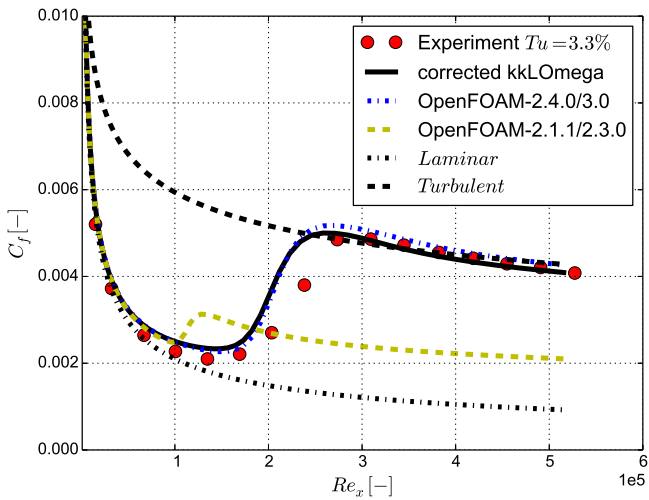


Figure 3.18: Comparisons of skin friction coefficient distribution over the flat plate for T3A case.

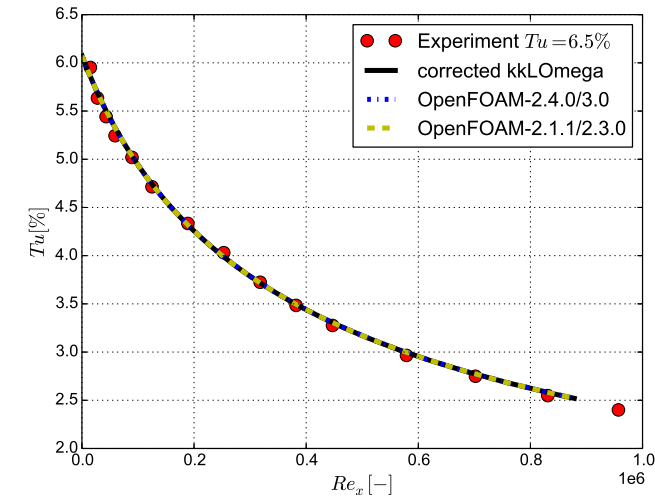


Figure 3.19: Comparisons of freestream turbulence intensity distribution for T3B case.

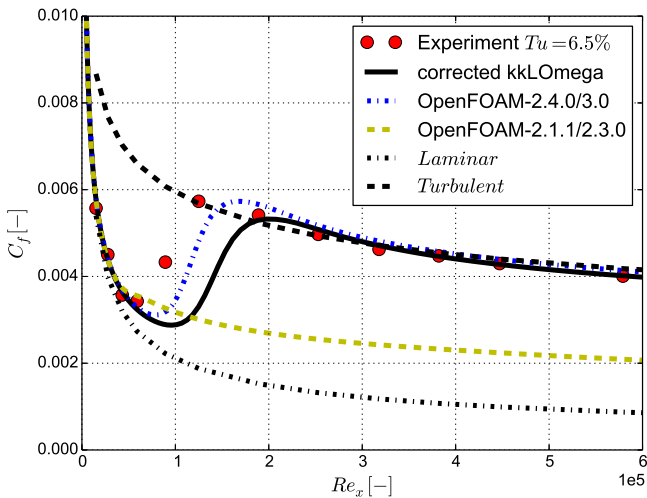


Figure 3.20: Comparisons of skin friction coefficient distribution over the flat plate for T3B case.

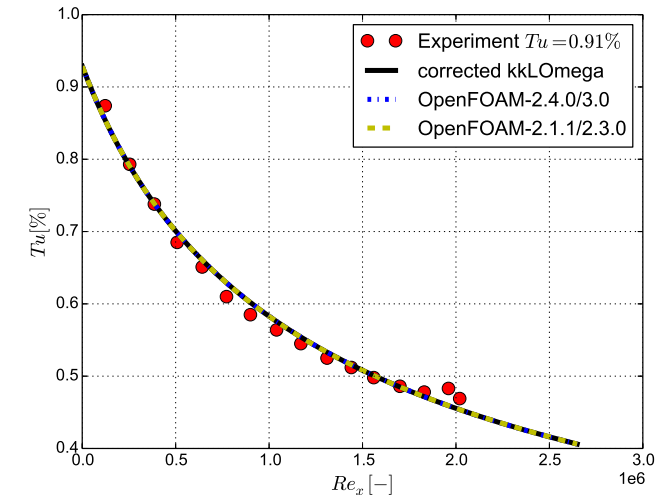


Figure 3.21: Comparisons of freestream turbulence intensity distribution for T3A- case.

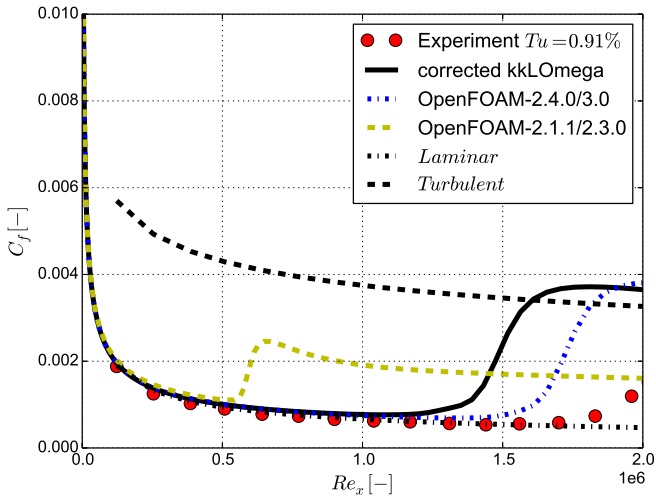


Figure 3.22: Comparisons of skin friction coefficient distribution over the flat plate for T3A- case.

The SIMPLE algorithm (Patankar and Spalding, 1972) is used to decouple the pressure and velocity of the steady-state incompressible Navier-Stokes equations. Second-order discretization scheme is chosen for both the convection and diffusion terms. The total variation diminishing limited linear differencing schemes with Sweby limiter are applied for velocity and turbulence quantities. All the residuals converge to a magnitude less than  $10^{-4}$  after  $10^4$  iterations. The boundary condition at the inlet is specified as Dirichlet-type condition with fixed value for the velocity and turbulent intensity, while Neumann boundary condition with zero gradient is set at the outlet boundary. A non-slip wall condition is applied at the airfoil surface. The turbulence intensity is 0.08% in all these simulations.

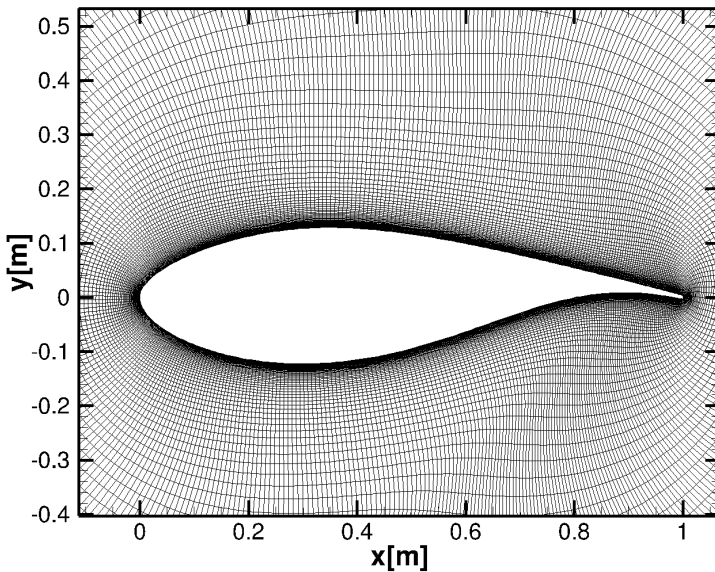


Figure 3.23: Grid around the DU91-W2-250 airfoil.

Figure 3.24 compares the numerical results of airfoil aerodynamic characteristics with experimental measurements at  $Re_c = 1.0 \times 10^6$ . The numerical prediction not only includes the results from different implementations of the  $k - k_L - \omega$  transition model, but also two equations shear stress transport (SST) turbulence model of Menter. The  $C_L - \alpha$  polar shows that, in the linear region transition models slightly overpredict the lift. However, the  $k - \omega$  SST turbulence model gives a perfect match with the experiment. Above  $C_{Lmax}$ , all numerical models show a large overshoot in the lift. This can be understood because a RANS approach with linear-eddy viscosity models delays the flow separation and therefore leads to higher  $C_L$ . In terms of drag force, the transition model presents much closer agreement to the experiment in the linear region since laminar-turbulent transition is taken into account. The value of  $C_D$  is largely overpredicted by the

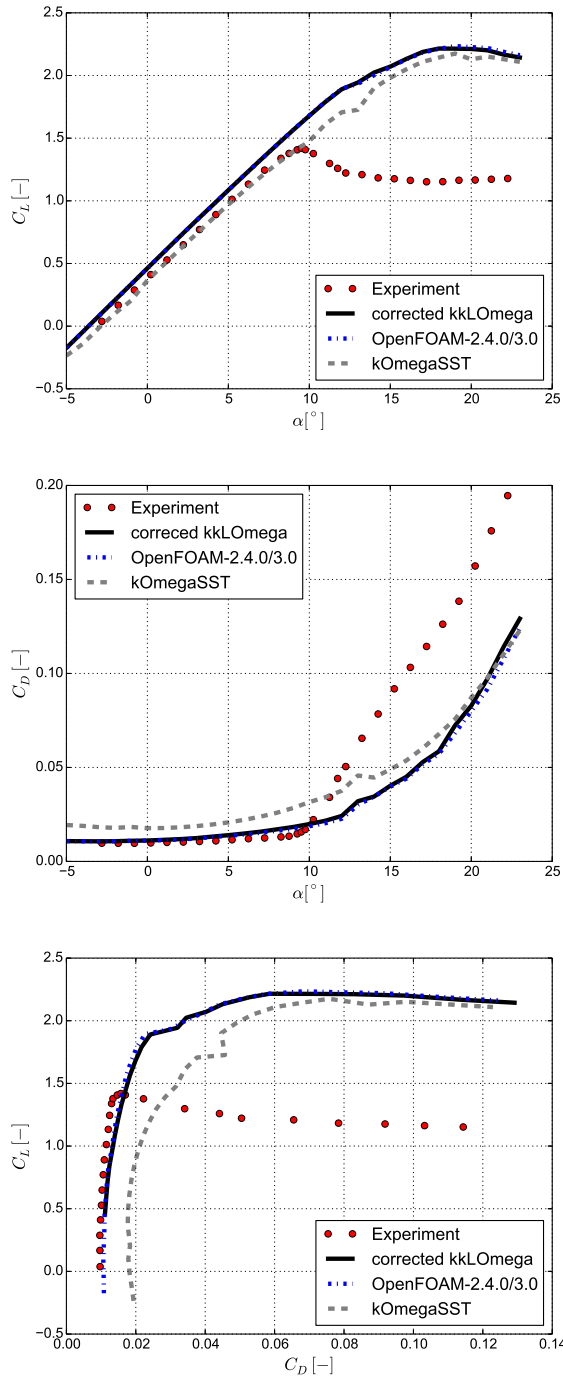


Figure 3.24:  $C_L - \alpha$ ,  $C_D - \alpha$  and  $C_L - C_D$  curves at  $Re_c = 1.0 \times 10^6$

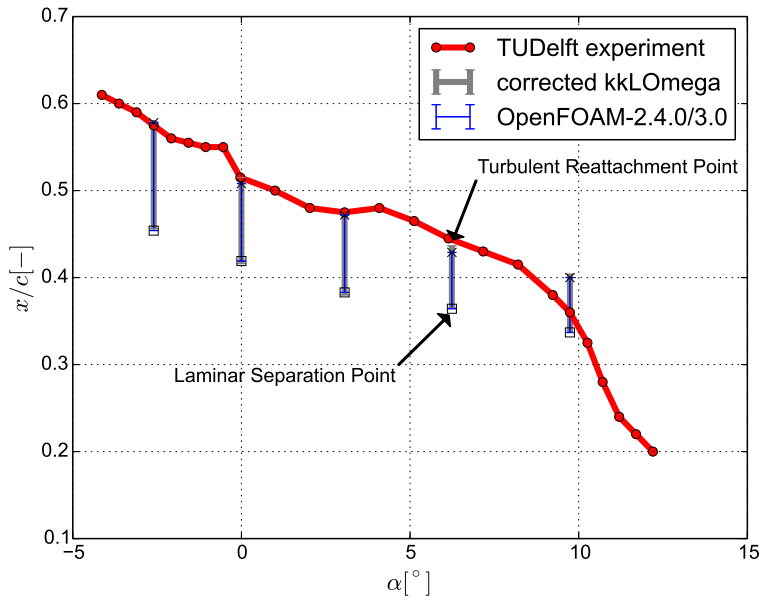


Figure 3.25: Transition onset location comparison at  $Re_c = 1.0 \times 10^6$ .  $\square$  represents the laminar separation points and  $\times$  represents the turbulent reattachment points.



turbulence model  $k - \omega$  SST which assumes the flow to be fully turbulent. Furthermore, the two implementations of the *corrected  $kkLOmega$*  model and OpenFOAM-2.4.0/3.0 show almost identical results.

Another important aspect of the concerns about the  $k - k_L - \omega$  model is the transition onset prediction: the position where laminar flow become turbulent. Figure 3.25 shows the comparison of transition onset locations on the suction surface of DU91-W2-250 airfoil at  $Re_c = 1.0 \times 10^6$  as measured experimentally by microphone detection and predicted numerically, where in the numerical results the laminar separation and turbulent reattachment points are indicated. The numerical prediction of the turbulent reattachment point agrees well with the measured data for a large range of angles of attack. Only at  $\alpha = 9.24^\circ$  the turbulent reattachment prediction is delayed compared to the experiment. What is more, the distance between laminar separation point and turbulent reattachment point could be considered as the laminar separation bubble length. As the angle of attack increases, the predicted laminar separation bubble length decreases.

### 3.4. CONCLUSIONS

In this chapter, a verification and validation process has been performed on OpenFOAM with several test cases before using it for complex 3D flow. Specifically, turbulence models with different fidelity modeling approaches are evaluated. Additionally, a RANS-based transition model  $k - k_L - \omega$  has been corrected in OpenFOAM-2.1.1. Transitional flow over wind turbine airfoil DU91-W2-250 is simulated at  $Re = 1.0 \times 10^6$ . The conclusions of this chapter are summarized as:

- The linear eddy viscosity models (Spalart-Allmaras and  $k - \omega$  SST) in OpenFOAM are verified and validated with several test cases (flat plate and NACA0012 airfoil). Good agreement is observed with theoretical results and a well validated code (CFL3D) in attached flow.
- The Hybrid LES/RANS approach (DDES) shows promising prediction capability when largely separated flow occurs. DDES calculations give the best results with around 10% higher predictions than the experiment. In addition, URANS simulation shows worse results than RANS, the integral force is overpredicted by around 50%.
- The *corrected  $kkLOmega$*  model has been implemented in OpenFOAM-2.1.1 and validated for DU91-W2-250 airfoil for considering laminar-turbulent transition. This implementation predicts much closer results to the measurement in terms of  $C_L/C_D$ ,  $C_D$  and transition location in the linear region.

# 4

## EXPERIMENTAL AND NUMERICAL STUDY OF THE NON-ROTATING MEXICO BLADE

*The ability to simplify means to eliminate the unnecessary  
so that the necessary may speak.*

Hans Hofmann

*This chapter presents an experimental and numerical study on the MEXICO wind turbine blades. Previous work by many other researchers shows that large differences exist in the loads comparison between numerical predictions and experimental data for the rotating MEXICO wind turbine. In order to reduce uncertainties and increase fidelity of the measured data, a non-rotating experimental campaign has been carried out on the MEXICO blades in the low speed low turbulence (LTT) wind tunnel at Delft University of Technology. In this new measurement set up, quasi-2D aerodynamic characteristics of the MEXICO blades on three radial sections are measured at different inflow velocities and a range of angles of attack. Oil flow visualization is also obtained for investigating the flow topology over the blades. In addition, Reynolds-averaged Navier-Stokes (RANS) simulations are performed for the flow at low angles of attack to compare the numerical results against the measured data. Afterwards, the influence of ZigZag tape on aerodynamic loads is discussed by analyzing experimental data and numerical results. Detached eddy simulations are performed to study the highly separated flow over this 3D twisted blade, aiming to improve the numerical predictions.*

---

Main part of this chapter is adapted from (Zhang et al., 2015) and (Zhang et al., 2017)

## 4.1. INTRODUCTION

In this chapter, an in-depth experimental and numerical comparison of the MEXICO blades is performed in order to explore the possible reasons for the discrepancies in the comparison between measurements and numerical results for the MEXICO experiment. By reducing the complexity of the flow and the uncertainties in the experiment, each MEXICO blade is measured separately under parked (non-rotating) conditions in the wind tunnel of TUDelft. The aim is to find answers to the following questions:

- By simplifying the experiment from 3D rotating condition to quasi-2D, without considering rotation, to what extent can CFD predict the aerodynamic loads and flow field around 3D blades, both for attached and separated flow conditions?
- Can we find the probable reasons that result in large discrepancy for the previous rotating MEXICO rotor loads comparisons between measurement and numerical predictions in the current non-rotating blade study?
- Does the ZigZag tape used in the experiment have a significant effect on the loads predicted by CFD codes which do not take ZigZag tape geometry into account?

This chapter is organized as follows: first, the experimental and numerical set-up of non-rotating MEXICO blades are briefly described in Section 4.2. CFD simulations are carried out to compare with measurement at low angles of attack and give more insight into the aerodynamic loads and 3D flow behavior on the non-rotating MEXICO blades, which will be shown in Section 4.3.1. Secondly, the influence of ZigZag tape is discussed in Section 4.3.2 with measured data and numerical results. Lastly, for highly separated flow condition at high angles of attack, the more advanced turbulence modeling approach DDES is applied for this 3D twisted MEXICO blade. The superiority compared to RANS approach is shown in Section 4.3.3.

## 4.2. EXPERIMENTAL AND NUMERICAL SETUP

### 4.2.1. EXPERIMENTAL APPROACH

#### WIND TUNNEL, THE MODEL AND THE APPARATUS

The wind tunnel measurements on the non-rotating MEXICO blades are performed in the low speed low turbulence (LTT) wind tunnel at Delft University of Technology. The LTT is a closed return wind tunnel with an exchangeable, octagonal test section 2.60 m long, 1.80 m wide, and 1.25 m high. The free-stream turbulence intensity in the test section varies from 0.015 % at 20 m/s to 0.10 % at 120 m/s. The inflow velocity is kept constant at 35 m/s and 60 m/s in this experiments. The layout of the LTT wind tunnel is shown in Figure 4.1.

The models measured in the experiment are the blades of the three-bladed, horizontal axis MEXICO wind turbine rotor. The blades are tapered and have a length of 2.04 m. Three different airfoils are used along the span of the blades. From the root to the tip, these are the DU91-W2-250 airfoil from 20 % to 45.6 % span, the RISØ-A1-21 airfoil from 54.4 % to 65.6 % span and the NACA 64-418 airfoil from 74.4 % span to the tip. The intermediate regions connecting two adjacent airfoil sections are shaped with a smooth

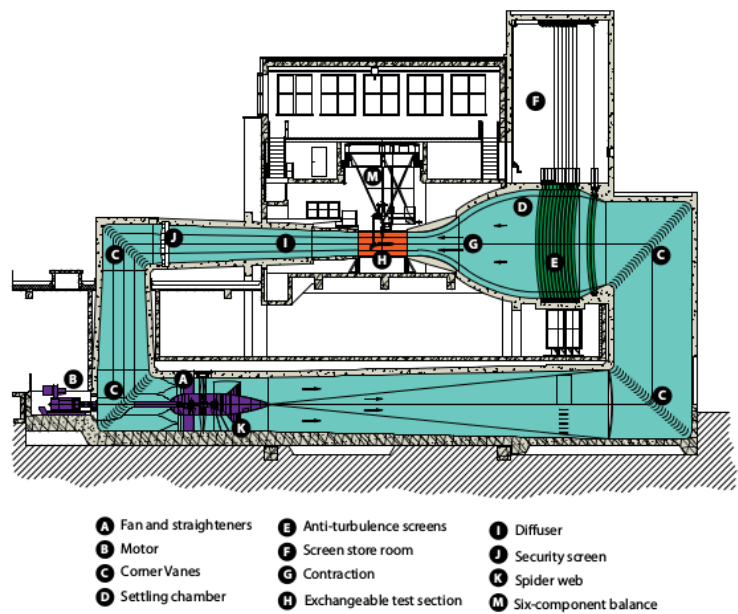


Figure 4.1: The layout of LTT wind tunnel (source: (Dimchev, 2012) )

transition. Figure 4.2 shows the airfoil distributions over the blade span. The chord and twist distributions of the MEXICO blades are given in Figure 4.3.

The instrumentation used in the experiment are balance systems, Kulite pressure transducers, a wake rake, and fluorescent oil.

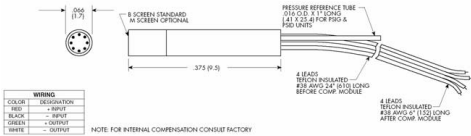

Balance system

The blade models are connected to the external six-component balance system equipped with the tunnel. The mechanical balances measure 6 forces to determine the lift force, the drag force, the side force, the pitching moment, the yawing moment and the rolling moment. In this experiment, forces in 2 directions and a moment in 1 direction are applied. The schematic view of the balance system is shown in Figure 4.4.

Kulites

**XCQ-062 SERIES**

- Available All Standard Pressure Ranges
- Ideal For Wind Tunnel Applications
- Excellent Static And Dynamic Performance
- Rugged



COLOR	DESIGNATION
RED	— INPUT
BLACK	— INPUT
GREEN	— OUTPUT
WHITE	— OUTPUT

NOTE: FOR INTERNAL COMPENSATION CONSULT FACTORY

Pressure range	0-35kPa
Measuring range	40-106 kPa absolute
Excitation	10V DC/AC
Temperature	-55° C - +120° C
Operational mode	Absolute
Residual unbalance	± 3% FSO
Natural frequency	> 150 KHz

Figure 4.5: Kulite pressure sensors

The Kulite pressure sensor is Kulite XCQ-95-062-5A. Detailed information and speci-

Table 4.1: Specifications of Kulite XCQ-95-062-5A

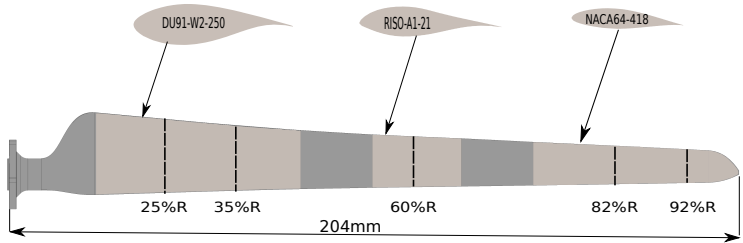


Figure 4.2: Airfoil distributions over the span of the MEXICO blade. In grey: transition zones.

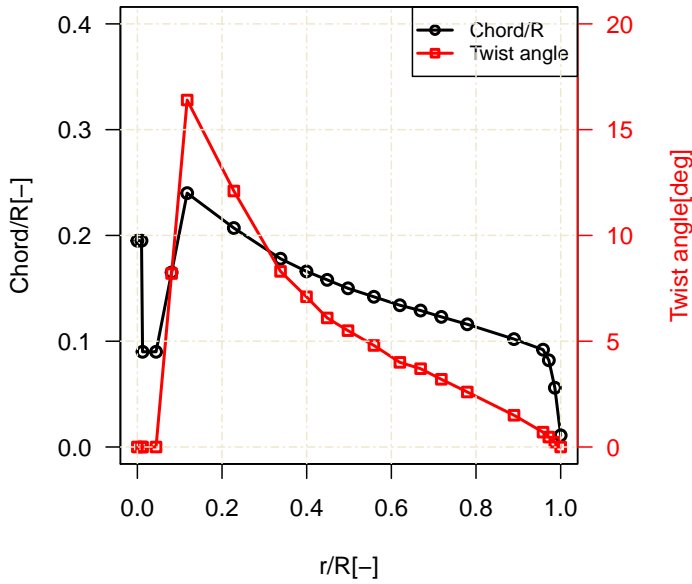


Figure 4.3: Chord and twist distribution of the MEXICO blade.

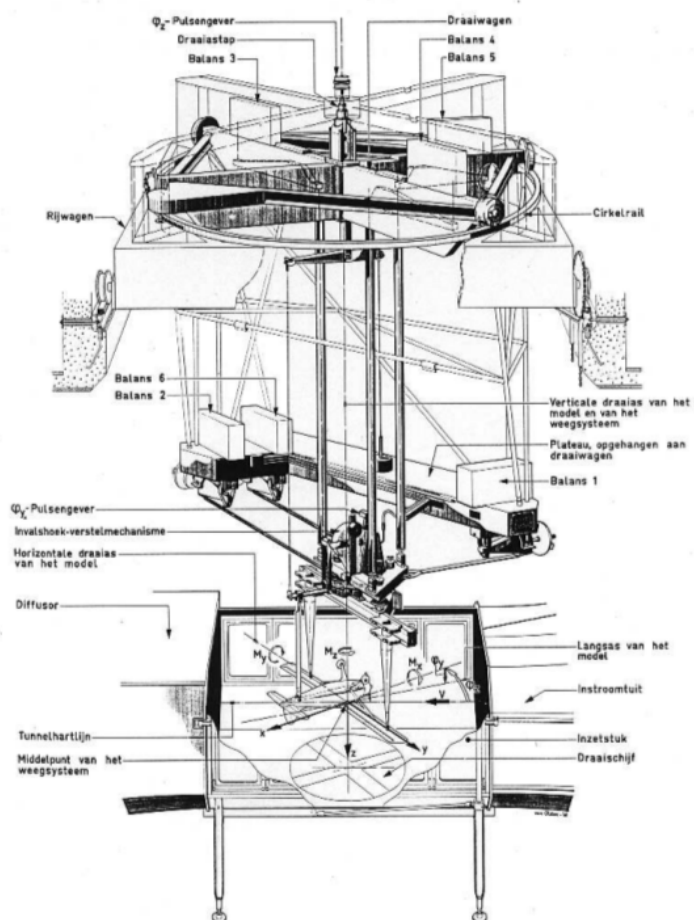


Figure 4.4: Schematic view of the balance system

fications of the Kulite can be found in Figure 4.5 and Table 4.1. There are 148 Kulite pressure transducers in total on the three blades, distributed over five instrumented cross sections. These transducers measure the pressure distribution over the airfoil sections, which are at 25 %R and 35 %R spanwise locations on blade 1, 60 %R spanwise location on blade 2, and 82 %R and 92 %R spanwise locations on blade 3. A calibration of the pressure sensors and an estimation of the uncertainty of the sensors are made before the non-rotating measurements, covering the pressure range observed throughout the measurement campaign. The analysis of the uncertainty results indicates that for the inboard sections the accuracy of sensors is rather poor. Moreover, a relative increase of loads due to the new calibration is also present for the different sections, which can be found in (Boorsma and Schepers, 2014).

#### Wake rake

The pressure drag can be obtained by integrating the pressure distribution around the sectional airfoil in the streamwise direction. To measure the total drag, a wake rake is used to measure the velocity deficit behind the blades with 16 static, and 67 total pressure tubes mounted on a spar, see Figure 4.7. The total pressure tubes have the same height as the mounting strut, while the static pressure tubes are 200 mm higher.

#### Fluorescent oil

Using fluorescent oil flow visualization techniques, the flow topology over the blade surface such as laminar/turbulence transition, flow separation and 3D effects can be clearly seen. Transition can be identified by a sudden color change, that the laminar region is brighter than the turbulent region because the skin friction coefficient  $C_f$  is lower.

#### EXPERIMENTAL SET-UP AND PROCEDURE

Each blade is mounted vertically in the test section and since the blades' span is longer than the test section height, two experimental setups are used. As shown in Figure 4.6, the pressure at 35 % span location is measured on blade 1 with the tip of the blade outside of the test section. The pressure at 60 % and 92 % span is measured on blade 2 and blade 3 respectively, which are mounted with a free blade tip inside the test section, see Figure 4.7. The ZigZag tape is applied on both pressure and suction sides at 10 % chord to trigger boundary layer transition and avoid free laminar to turbulent transition.

In order to keep the chord-based Reynolds number  $Re_c$  identical to the rotating experiments, the inflow velocities are chosen as  $35\text{ m/s}$  and  $60\text{ m/s}$ . The quasi-2D aerodynamic characteristics on these three test sections are obtained at angles of attack ranging from  $-20^\circ$  to  $20^\circ$ . The rotating table at the top of the test section can adjust the tip pitch angle of the blades, in such a way that the desired geometric angle of attack  $\alpha$  (defined as the angle between inflow direction and chord line) is obtained. Calibrated Kulite pressure transducers are used to measure the sectional pressure distribution. By integrating the pressure, the lift force and the pressure drag can be calculated. Wake rake measurements are used to determine the sectional total drag. From the differences between wake rake drag and pressure drag, the viscous drag can be estimated. Apart from the pressure measurements, an oil flow measurements are carried out to visualize the flow phenomena over the blade 3 surface. Table 4.2 summaries the experimental configurations that will be used for validation of the CFD simulations.





Figure 4.6: Experimental set-up of the model: the MEXICO blade 1

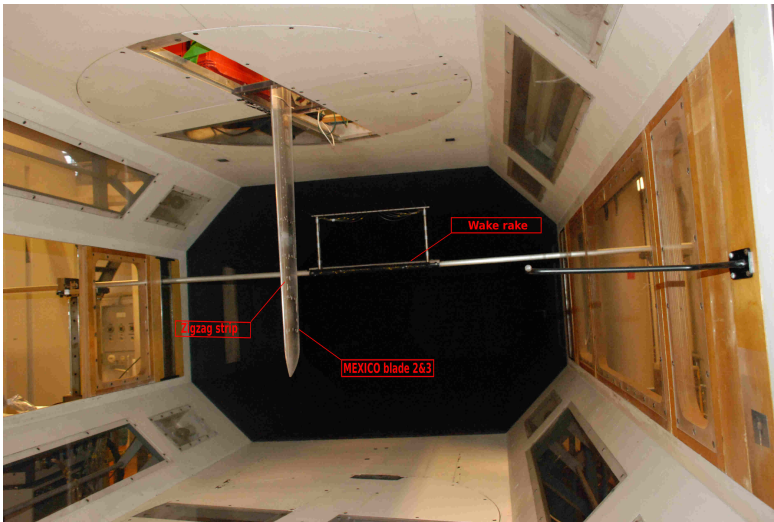


Figure 4.7: Experimental set-up of the models: the MEXICO blade 2 and blade 3

Table 4.2: Conditions in the experiment

Blade number	No.1	No.2	No.3
Measured section[-]	35%R	60%R	92%R
Geometric angle of attack $\alpha$ [°]	1, 5, 8, 15, 19	0, 5, 8, 15, 19	2, 5, 8, 15, 19
Inflow velocity[m/s]	35	35	60
Reynolds number $Re_c$ [-]	$4.6 \times 10^5$	$3.4 \times 10^5$	$4.0 \times 10^5$



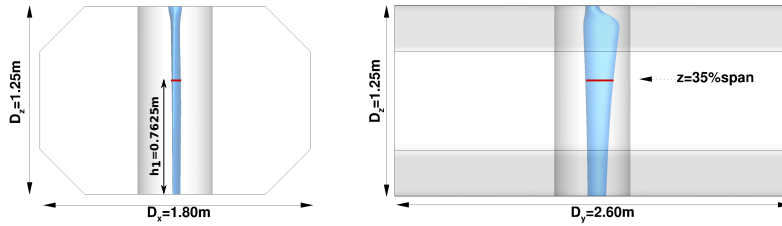


Figure 4.8: Numerical set-up of the model: Blade 1 configuration (Zhang et al., 2014)

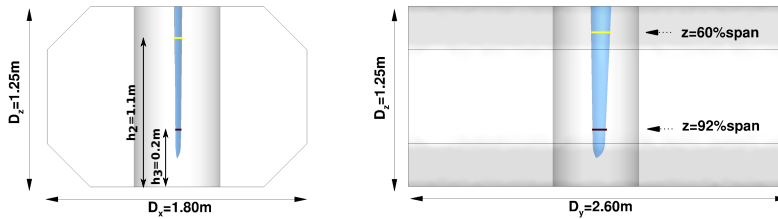


Figure 4.9: Numerical set-up of the models: Blade 2 and Blade 3 configuration (Zhang et al., 2014)

#### 4.2.2. NUMERICAL APPROACH

##### GEOMETRY MODELING AND GRID GENERATION

The CFD simulations are performed on a computational domain that is identical to the experimental setup. The whole wind tunnel test section, including wind tunnel walls are modeled, not only the blades. Therefore, the blockage effects present are also considered by CFD. Similar to the experimental setups, there are two different computational domains, one with the blade extending from top to bottom of the test section (Figure 4.8) and one with a free blade tip (Figure 4.9). A cylindrical domain which includes the blade is created, and it can be rotated to the desired pitch angle to match the geometric angle of attack  $\alpha$  corresponding to the measurement. The measured sections are located at a distance from the bottom of the test section wall:  $h_1 = 0.7625m$ ,  $h_2 = 1.1m$  and  $h_3 = 0.2m$ , respectively.

A hybrid mesh strategy is used for generating the CFD mesh. A structured hexahedral grid is applied near the blade where the viscous flow in the boundary layer is solved with high grid resolution. The outer region is filled with a coarse, unstructured mesh. The non-dimensional value  $y^+$  is below 2 and approximately 20 cell layers are used in the viscous region. An illustration of the mesh and blade surface mesh is given in Figure 4.10. Three different grid levels are generated for examining the spatial convergence in total (see Table 4.3 for details).

##### ASSUMPTIONS, BOUNDARY CONDITIONS AND NUMERICAL SCHEMES

To model and investigate the flow physics over the blades, some simplifications of numerical modeling are used:

Table 4.3: The characteristics of three different grids

Grid Characteristic	Coarse	Medium	Fine
Chordwise nodes	90	120	150
Spanwise nodes	80	100	125
First grid spacing(mm)	0.015	0.009	0.005
$y^+$	1.5	1.0	0.5
Maximum skewness	1.1	0.97	1.05
Maximum orthogonality	65.8	65.6	66.1
Maximum aspect ratio	1675	3543	4191
Total cells	$5.26 \times 10^5$	$8.74 \times 10^5$	$1.45 \times 10^6$

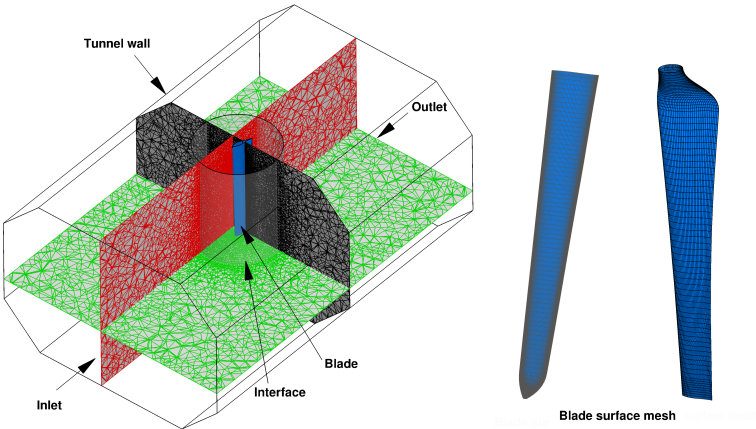


Figure 4.10: Schematic of the computational domain and blade surface mesh

- To save the computational time, steady-state Navier-Stokes solver with RANS turbulence modeling approach is chosen for predicting the cases where the flow is attached in the experiment.
- Considering simplification of flow physics, fully turbulent flow over the blades is assumed. Hence laminar-to-turbulent transition is not considered in the simulation.
- It is assumed that ZigZag stripe has little influence on the integrated pressure when the flow is still attached. Therefore, the geometry of ZigZag is not modeled and considered for the CFD model.
- In the direction of the flow, rectangular surface is used to model the wind tunnel test section. In reality, the side walls of the tunnel in the experiment are designed with a slightly diverging shape to compensate for the displacement effect of the tunnel wall boundary layers. In addition, under the assumption that viscous effects on the wall are not expected to have a major influence on the pressure distributions, especially for the sections (35 %R and 92 %R) far from the wall, the boundary layer developed at the wind tunnel wall is not resolved in order to decrease the grid size.

Since the viscous effects from the wind tunnel wall are neglected, the slip boundary condition is chosen at the wind tunnel wall. The boundary condition for the velocity field is applied as the Dirichlet boundary condition with a constant inflow velocity at the inlet boundary and the von Neumann boundary condition at the outlet. The pressure is set as a von Neumann boundary condition at all boundaries. The solid blade surface is enforced as no-slip boundary condition. An arbitrary mesh interface (Farrell and Madison, 2011) boundary condition is used between the two adjacent mesh domains. The free-stream turbulence intensity  $I$  is estimated as 0.06 % at the inflow velocity  $U_\infty$ :

$$I = \frac{u'}{U_\infty} = 0.06\%. \quad (4.1)$$

where  $u' = \sqrt{\frac{2}{3}k}$  is the root-mean-square of the turbulent velocity fluctuations. Based on the turbulence intensity, the turbulent variables  $k$  and  $\omega$  can be calculated as the reference (Menter and Esch, 2001) and the boundary conditions are specified in the simulation. The order of accuracy of selected numerical schemes for N-S equations discretization is second-order upwind. The SIMPLE algorithm (Patankar and Spalding, 1972) is used to correct the pressure in the iterations.

### 4.3. RESULTS AND ANALYSIS

#### 4.3.1. FLOW AT LOW ANGLES OF ATTACK

##### GRID REFINEMENT STUDY

Figure 4.11 and Figure 4.12 show the results of the grid refinement study based on three different grid levels. In the figures, the pressure and skin friction coefficient distribution

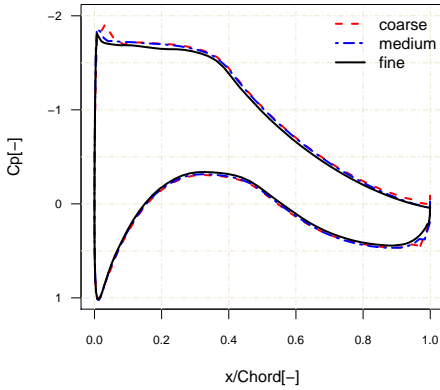


Figure 4.11: Grid convergence study,  $C_p$  comparison between coarse, medium and fine grids

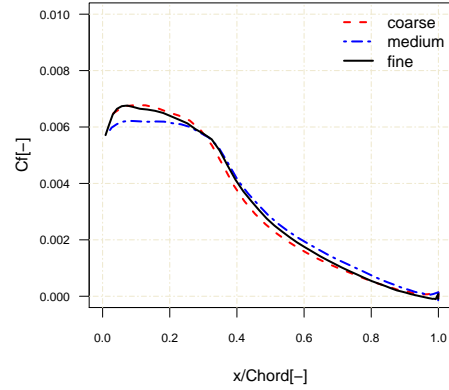


Figure 4.12: Grid convergence study,  $C_f$  comparison between coarse, medium and fine grids on the suction side

on the DU airfoil section at 35% span with a geometric angle of attack  $\alpha = 8^\circ$ , which is depicted as  $\alpha_{0.35} = 8^\circ$ .

As the grid density increases, the pressure tends to a converged solution and only small differences can be seen close to the suction peak and trailing edge between the coarse and fine mesh solution, with a difference 6.7% integral lift force (see Figure 4.11). The skin friction coefficient, however, is more sensitive to the mesh resolution and does not seem to present a monotonic convergence behavior.  $C_f$  on the medium mesh is underestimated between  $x/c = 0.0$  and  $x/c = 0.30$  compared with  $C_f$  on the coarse and fine mesh. The difference between the medium mesh and fine mesh is about 6% integral drag force, which is considered acceptable in the simulations. Therefore, the solutions on the fine mesh are taken to achieve spatial convergence and the numerical results presented below are based on the fine mesh.

#### DU SECTION AT 35m/s, 35% SPAN

Figure 4.13 presents the comparison of the calculated and measured pressure distribution at 35% spanwise section of the blade 1. At this section, the airfoil is the DU91-W2-250 airfoil with 25% thickness. The geometric angles of attack are  $\alpha_{0.35} = 1^\circ, 5^\circ, 8^\circ$ . Overall a fairly good agreement within less than 10%  $\Delta C_p$  ( $\Delta C_p$  is defined as  $C_{p_{max}} - C_{p_{min}}$  with pressure sensor value) difference is obtained between CFD results and experiment except for a few locations. These locations are indicated by red squares. The pressure transducers on the suction side which are located at  $x/c = 0.053$  and  $x/c = 0.3$  show unexpected pressures for the  $\alpha_{0.35} = 5^\circ$  and  $\alpha_{0.35} = 8^\circ$  cases, while at  $\alpha_{0.35} = 1^\circ$ , the pressure sensor at  $x/c = 0.053$  shows expected value. This phenomenon has been pointed out both in the rotating MEXICO wind turbine experiment and CFD simulations by other researchers, see (Scheepers and Snel, 2007) and (Bechmann et al., 2011). Although the pressure sensors were calibrated before the non-rotating experiment, they

obviously show unexpected pressure during the wind tunnel measurements. Another difference can be seen near the trailing edge on the suction side, when the geometric angle of attack increases from  $\alpha_{0.35} = 5^\circ$  to  $\alpha_{0.35} = 8^\circ$ . The measured pressure indicates that the flow separates at the trailing edge in the experiment, which is not captured by the current simulation.

Regarding the pressure comparison on the pressure side, CFD results show similar pressure distribution trends as the experimental measurements. However, consistent pressure overprediction is found over the pressure side between  $x/c = 0.3$  and  $x/c = 0.5$  for all cases.

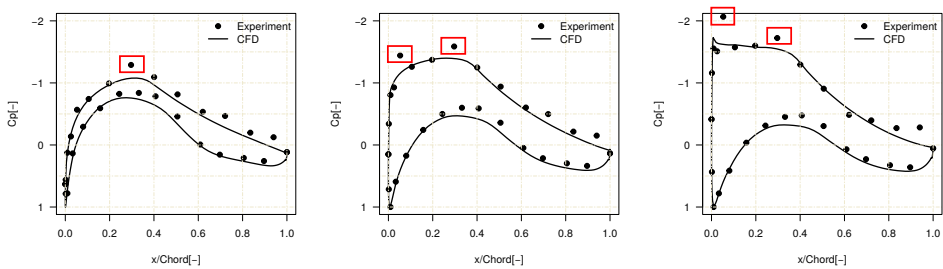


Figure 4.13: Pressure coefficient comparison of the DU91-W2-250 airfoil at 35% spanwise section of the blade 1:  $\alpha_{0.35} = 1^\circ, 5^\circ$  and  $8^\circ$  with inflow velocity  $U_\infty = 35 \text{ m/s}$ ,  $Re_c = 4.6 \times 10^5$

#### RISØ SECTION AT $35 \text{ m/s}$ , 60% SPAN

At 60% spanwise section of the blade 2 with RISØ-A1-21 airfoil, the CFD results and experimental measurements of pressure distribution are compared in Figure 4.14. The maximum difference between CFD and experiment is less than  $10\% \Delta C_p$  for all the measured points. On the pressure side, good agreement is obtained for all pressure sensors except for the ones between  $x/c = 0.146$  and  $x/c = 0.344$ . Similar behavior that over predicts the pressure is observed as the case for the DU91-W2-250 airfoil section. For all the cases  $\alpha_{0.60} = 0^\circ, 5^\circ$ , and  $8^\circ$ , the numerical results on the suction side all underpredict the pressure compared to the experiments. Therefore, the integrated sectional lift force is over predicted for the RISØ-A1-21 airfoil section.

#### NACA SECTION AT $60 \text{ m/s}$ , 92% SPAN

Figure 4.15 shows the pressure comparison at 92% spanwise section of the blade 3. The NACA 64-418 airfoil profile is present at this location, which is close to the tip of the blade. Even though the flow is complex and challenging due to the existence of the tip vortex effects, at the three angles of attack  $\alpha_{0.92} = 2^\circ, 5^\circ$  and  $8^\circ$ , all the computations show a very good agreement with experimental results. For each case, the pressure distribution over the NACA airfoil is well captured by the simulation.

In the experiment, the flow over the blade is visualized by oil flow techniques for the blade 3 at the inflow velocity  $U_\infty = 60 \text{ m/s}$ . In Figure 4.16, the right image shows the oil flow visualization over the blade surface for the geometric angle of attack  $\alpha_{0.82} = 8^\circ$  at

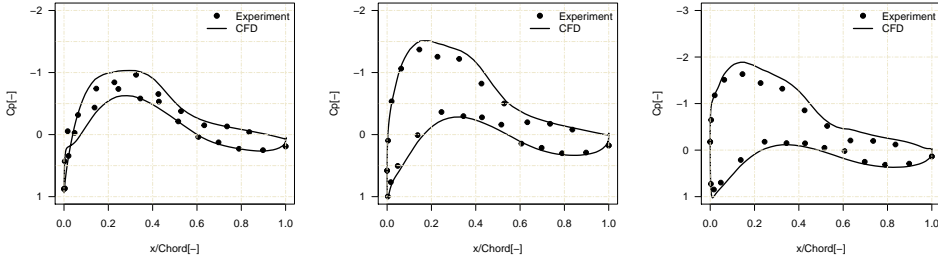


Figure 4.14: Pressure coefficient comparison of the RISØ-A1-21 airfoil at 60% spanwise section of the blade 2:  $\alpha_{0,60} = 0^\circ, 5^\circ$  and  $8^\circ$  with inflow velocity  $U_\infty = 35 \text{ m/s}$ ,  $Re_c = 3.4 \times 10^5$

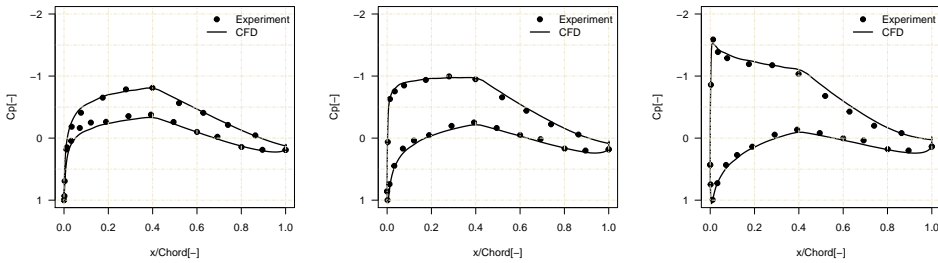


Figure 4.15: Pressure coefficient comparison of the NACA 64-418 airfoil at 92% spanwise section of the blade 3:  $\alpha_{0,92} = 2^\circ, 5^\circ$  and  $8^\circ$  with inflow velocity  $U_\infty = 60 \text{ m/s}$ ,  $Re_c = 4.0 \times 10^5$

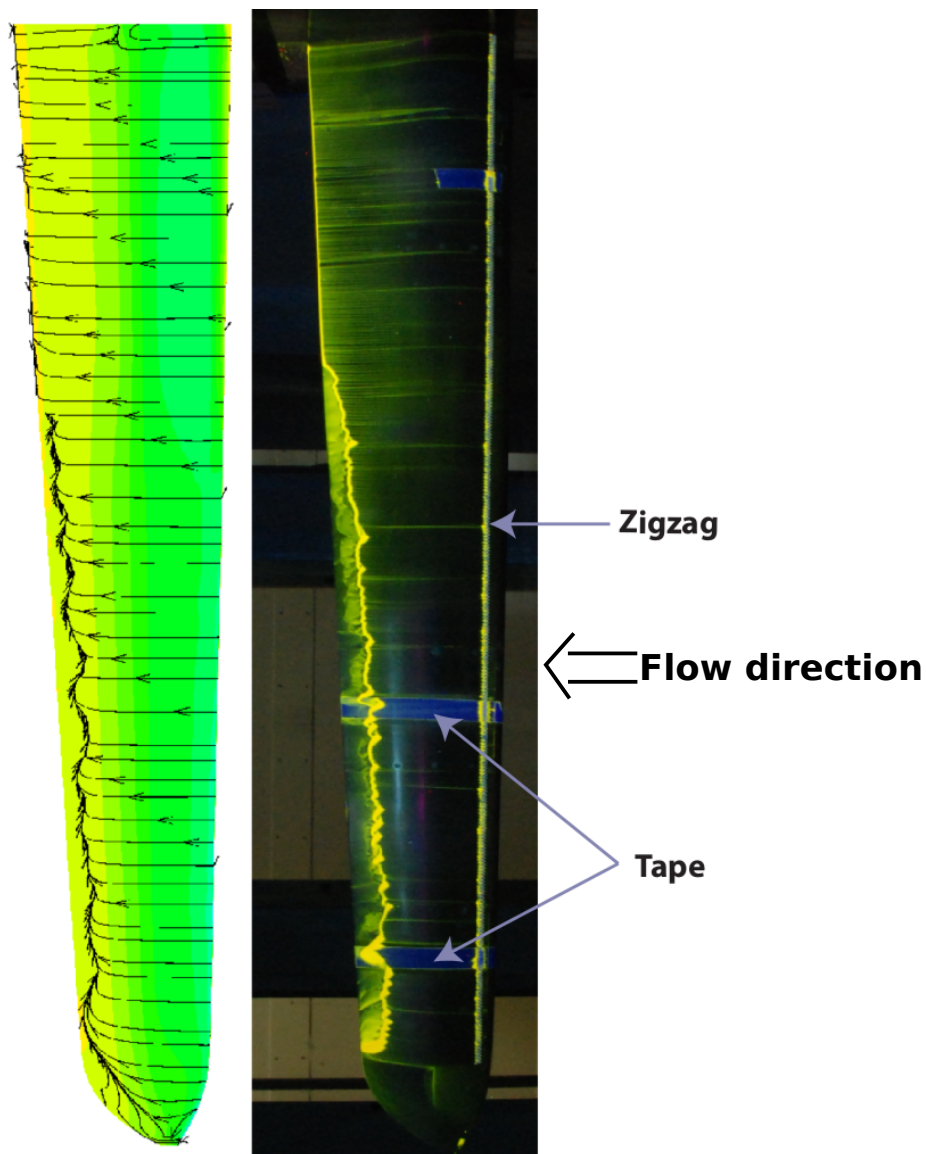


Figure 4.16: Blade 3 configuration: flow topology comparison between CFD limiting streamline and experimental oil flow visualization, flow is from right to left, angle of attack  $\alpha_{0.82} = 8^\circ$ , CFD result is colored by the pressure.

82% spanwise section. The flow direction is from right to left. The ZigZag tape is used to trigger a transition to turbulent flow at 10% chord and can be clearly seen in the oil flow image, except for the blade tip, where no tape is applied. Tape in the horizontal direction is applied on the pressure sensors at the sections 60%, 82%, 92% of the blade to prevent them from being damaged by the oil. The bright line indicates the location where the flow starts to separate. It can be seen that the flow remains fully attached at the root of the measured model. With the increased angle of attack towards to the tip, the flow starts to separate near the trailing edge from  $r/R \approx 0.70$  to the tip. Compared with the simulated limiting streamline visualization in the left image, good flow topology agreement with respect to flow separation is obtained between CFD and experimental oil flow measurement.

#### AERODYNAMIC LOADS

Figure 4.17 shows the geometric angle of attack and corresponding numerical lift force coefficient distribution from the sections  $r/R = 0.20$  to  $r/R = 0.65$  of the blade 1, where the geometric angle of attack at 35% spanwise section are  $\alpha_{0.35} = 5^\circ$  and  $8^\circ$ , respectively. At  $\alpha_{0.35} = 5^\circ$ , with the increase of the radial position, a higher lift force is obtained as a result of the blade twist leading to an increased geometric angle of attack. A sudden lift drop at  $r/R = 0.55$  is observed. When  $\alpha_{0.35}$  is increased to  $8^\circ$ , the lift force increases on all different sections as expected, except for  $r/R = 0.55$ , which gives the same  $C_L$  value as the case  $\alpha_{0.35} = 5^\circ$ . Moreover, the amount of the increased lift gradually decreases as the radial position transits from the DU91-W2-250 airfoil to the intermediate region, which is from  $r/R = 0.45$  to  $r/R = 0.55$ . The observation shows that the transition of lift distribution from the RiSØ airfoil family to the DU airfoil family is not smooth enough. This phenomenon will be discussed in the following section.

Similarly, Figure 4.18 presents the geometric angle of attack and the results of lift coefficient distribution of the blade 2 from  $r/R = 0.60$  to  $r/R = 0.95$ . From the lift distribution curve, it can be observed that the lift distribution is much smoother compared to blade 1 and no sudden kink is visible. An almost uniform lift increase over all the sections is obtained when the geometric angle of attack at 60% span is increased from  $5^\circ$  to  $8^\circ$ . Near the tip region ( $r/R = 0.90 \sim 0.95$ ), significant lift reduction can be clearly seen for both  $\alpha_{0.60} = 5^\circ$  and  $\alpha_{0.60} = 8^\circ$  cases due to the tip vortex effect.

#### 3D FLOW FIELD

To better understand how the non-smooth transition between the DU91-W2-250 and the RiSØ-A1-21 airfoil observed in the previous section influences the flow in the particular region near  $r/R = 0.55$ , the  $Q$  criterion (Hunt et al., 1988) is chosen to identify the vortical structures in the flow field.  $Q$  is the second invariant of the velocity gradient tensor  $\nabla u$ , which can be written as:

$$Q = \frac{1}{2} (\|\Omega\|^2 - \|S\|^2), \quad (4.2)$$

where  $S$  and  $\Omega$  are the symmetric and antisymmetric parts of the tensor  $\nabla u$ , and  $\|S\| = \text{tr}(SS^T)^{\frac{1}{2}}$ ,  $\|\Omega\| = \text{tr}(\Omega\Omega^T)^{\frac{1}{2}}$ .

Three-dimensional large-scale vortical structures over blade 1 can be seen in Figure 4.19 and Figure 4.20, colored by vorticity magnitude. In Figure 4.19, large-scale vortical



4

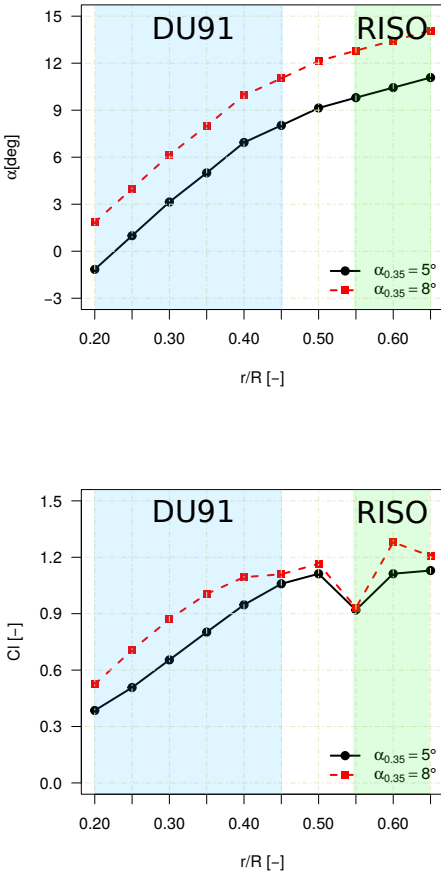


Figure 4.17: Distribution of geometric angle of attack and lift coefficient from CFD results of the blade 1

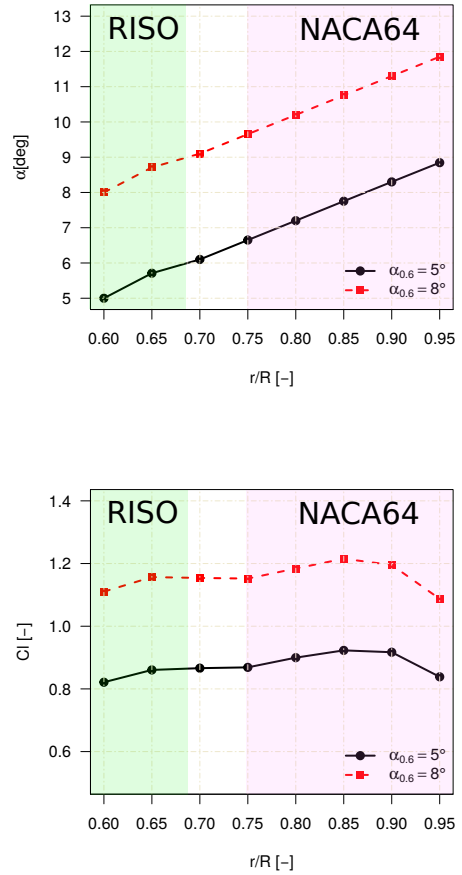


Figure 4.18: Distribution of geometric angle of attack and lift coefficient from CFD results of the blade 2

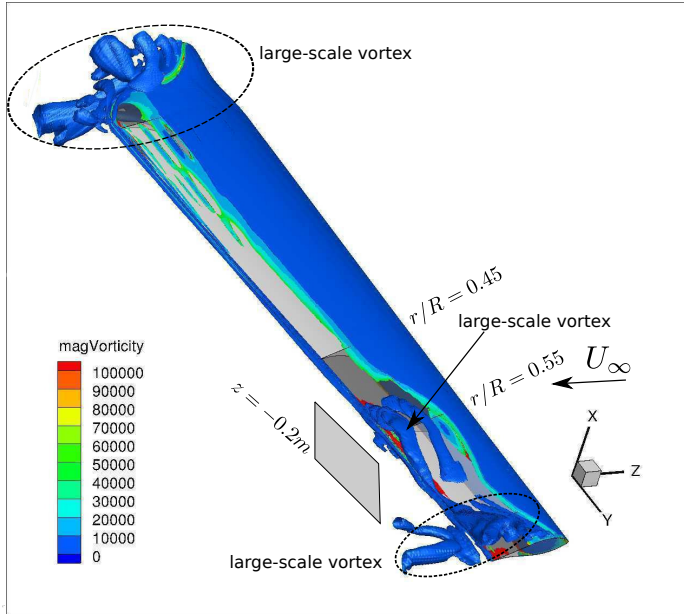


Figure 4.19: Blade 1 configuration: 3D visualization of vortex structure, isosurface  $Q = 2 \times 10^5$  colored by vorticity magnitude,  $\alpha_{0.35} = 5^\circ$

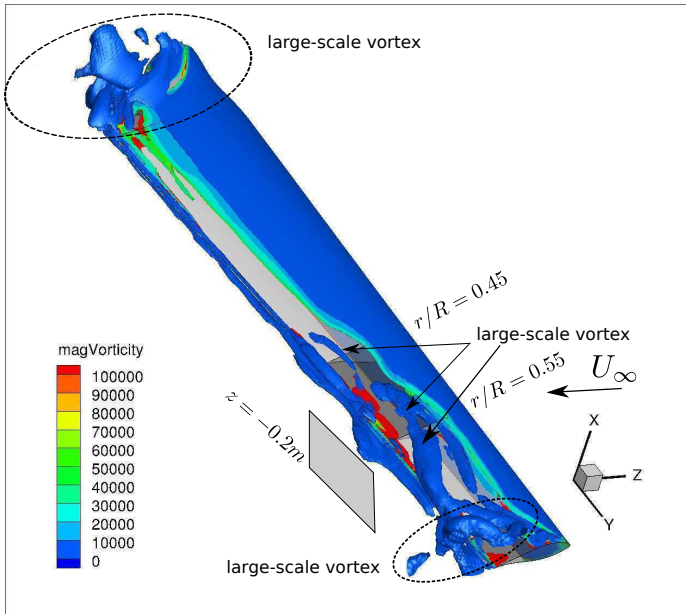


Figure 4.20: Blade 1 configuration: 3D visualization of vortex structure, isosurface  $Q = 2 \times 10^5$  colored by vorticity magnitude,  $\alpha_{0.35} = 8^\circ$

structures mainly appear at three locations, which are the two extremities close to the tunnel wall and the location  $r/R = 0.55$ .

The clear large-scale vortical structure is seen at the root region of the blade (top left), which can be attributed to the transition from the DU91-W2-250 airfoil family to the cylinder. The other extremity with large-scale vortical structure caused by separated flow can be clearly seen at RISØ-A1-21 section (bottom right). This section encounters high angle of attack ( $\alpha = 11^\circ$  and  $14^\circ$ ) due to blade twist. Apart from that, the influence of tunnel wall on the two regions could be considered as one additional cause for these large-scale vortical structures. The last position  $r/R = 0.55$ , the transition region starting from the RISØ-A1-21 airfoil family to the DU91-W2-250 airfoil family. As a consequence of the sudden dip in the lift distribution (see Figure 4.17), large scale vortices emerge at the transition area. When the angle of attack increases from  $\alpha_{0.35} = 5^\circ$  to  $\alpha_{0.35} = 8^\circ$ , more vortical structures can be found towards to the root direction, which is close to the transition part as well, see Figure 4.20. The main region influenced by vortical structures can be estimated from the loads calculation in Figure 4.17 and runs from  $r/R = 0.40$  to  $r/R = 0.60$ .

Based on Prandtl lifting line theory (Anderson Jr, 2010), the lift force over an airfoil can be calculated from

$$L = \rho V_\infty \Gamma, \quad (4.3)$$

where  $\Gamma$  is the circulation over the airfoil section, representing the bound vortex strength. As a result of the sudden lift drop at  $r/R = 0.55$  (see Figure 4.17), the rapid change in the circulation leads to a lower strength of the bound vortex at  $r/R = 0.55$  than at adjacent sections. Consequently trailing vortices are expected to be generated behind this position, which will be discussed below in more detail.

In order to quantify the influence of the 3D flow on the airfoil aerodynamic characteristics, the lift curve derived from 3D CFD calculations and 2D experimental measurements are plotted together versus the geometric angles of attack in Figure 4.21. The geometric angle of attack corresponds to the angle between inflow direction and chord line of airfoil section both for the 2D and 3D cases. The chord based  $Re_c$  distribution along the blade span from 3D CFD calculations is also added on these graphs. The experimental 2D airfoil characteristics available in the database of the MEXICO project are measured at  $Re = 5 \times 10^5$  for the DU91-W2-250 airfoil, and at  $Re = 1.6 \times 10^6$  for the RISØ-A1-21 airfoil, as indicated in Figure 4.22.

For the case with a geometric angle of attack  $\alpha_{0.35} = 5^\circ$ , the comparison shows that  $C_L$  values in the region  $r/R = 0.30 \sim 0.45$  between 3D CFD results and 2D experimental measurements match very well. However, there are large differences at the root  $r/R = 0.20 \sim 0.30$  and the mid-span  $r/R = 0.55 \sim 0.65$ . The 3D results give much higher  $C_L$  at the root, but lower  $C_L$  at the mid-span. The differences can be explained by the influence of induced velocity which alters the local angle of attack. Figure 4.23 presents the contour of vertical and spanwise velocity distribution at the plane  $z = -0.20m$  behind blade 1 to illustrate the induced effects. The velocity components correspond to x and y directions respectively in Figures 4.19 and 4.23. At the root region,  $r/R = 0.20$  there are upwash effects induced by the velocity. These effects increase the local angle of attack and therefore results in higher  $C_L$  at this section in 3D calculations compared to 2D experimental data.

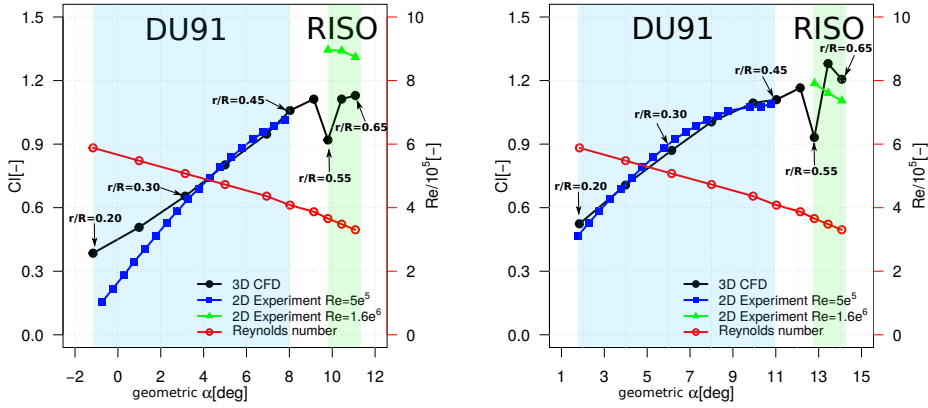


Figure 4.21:  $C_L - \alpha$  comparison between 3D CFD calculation and 2D experimental data.  $\alpha_{0.35} = 5^\circ$  (left)  $\alpha_{0.35} = 8^\circ$  (right)

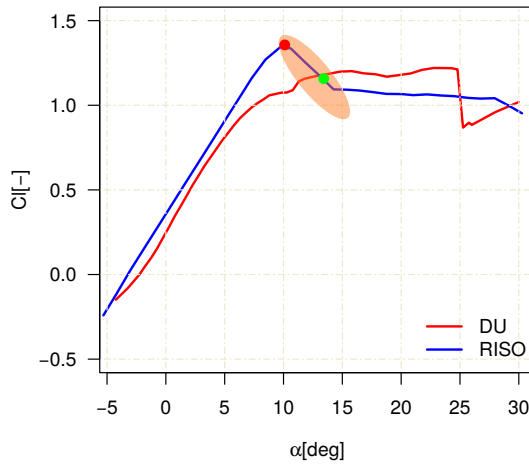


Figure 4.22: Measured  $C_L - \alpha$  polar data for the DU91-W2-250 ( $Re = 5 \times 10^5$ ) and the RISO-A1-21 ( $Re = 1.6 \times 10^6$ ) airfoils

At  $r/R = 0.55$ , due to the circulation difference as discussed above, a pair of counter-rotating vortices are observed near the same radial position in the plane  $z = -0.2m$  (see Figure 4.19), which causes large upwash effects at  $r/R = 0.55$ , but downwash effects about  $0.05r/R$  away from the location  $r/R = 0.55$ . The velocity contour indicates these effects in Figure 4.23. However, the increased local angle of attack caused by this upwash effects decreases the lift at  $r/R = 0.55$ , as seen from the results in Figure 4.21. The cause of this consequence can be explained by looking at the stall characteristics of the RISØ-A1-21 airfoil. The critical stall angle is about  $10^\circ$  for the RISØ-A1-21 airfoil, which can be determined in 2D experimental airfoil characteristics, see the red point in Figure 4.22. Meanwhile, the current geometric angle of attack for the RISØ-A1-21 airfoil at  $r/R = 0.55$  location is about  $10^\circ$ , as shown in Figure 4.17. The upwash effects induced by the counter-rotating vortices at  $r/R = 0.55$  increase the geometric angle of attack (close to the critical angle of attack  $10^\circ$ ) and the airfoil enters the stall regime. Due to the property of sharp stall characteristics of the RISØ airfoil, see the blue lift curve in Figure 4.22, lift decreases sharply in the stall regime. Therefore, the  $r/R = 0.55$  section produces much smaller lift even with a higher local angle of attack than the 2D case. On the contrary, the RISØ-A1-21 airfoil section between  $r/R = 0.60$  and  $r/R = 0.65$  is, because of the downwash effects, experiences a reduced local angle of attack, which is within the linear regime. Thus, the lift from 3D CFD at sections  $r/R = 0.60 \sim 0.65$  is significantly lower than 2D experimental data.

When the geometric angle of attack increases to  $8^\circ$  at the  $35\%R$  section, the comparison shows the maximum difference between 3D and 2D results has decreased at  $r/R = 0.55$  on the RISØ-A1-21 airfoil section. In addition, 3D effects show little influence on the DU91-W2-250 airfoil aerodynamic characteristics. From Figure 4.24, near the root region  $r/R = 0.20$ , less upwash effects can be observed compared to the case  $\alpha_{0.35} = 5^\circ$ . Therefore, as a result, the  $C_L$  curve obtained from 3D results fits well with 2D experimental measurement.

At  $r/R = 0.55$ , the difference between 3D CFD results and 2D experimental values becomes smaller compared to the case  $\alpha_{0.35} = 5^\circ$  even though this position has much stronger upwash effects, indicated by the velocity contour in Figure 4.24. The reason is that the geometric angle of attack of the RISØ-A1-21 airfoil at  $r/R = 0.55$  is above  $13^\circ$ , as can be seen in Figure 4.17, which is indicated by the green point in Figure 4.22. The  $C_L - \alpha$  curve in this regime is flat without too much lift decrease if the angle of attack increases further. This leads to smaller difference found between 2D  $C_L$  values and 3D results observed for the case  $\alpha_{0.35} = 8^\circ$  compared to the case  $\alpha_{0.35} = 5^\circ$ . In the region  $r/R = 0.60 \sim 0.65$ , the downwash effect decreases the local angle of attack of the airfoil in the stall regime and increases the lift consequently.

For blade 2, the vertical and spanwise velocity field at the plane  $z = -0.20m$  is shown in Figure 4.25. Very small gradients in velocity are observed except from the blade tip region. The strong tip vortex is clearly seen and these tip effects are dominating the flow. A well-known effect of a tip vortex is the decrease of lift, which is in accordance with the results presented in Figure 4.18. No particularly unexpected loads distribution and velocity field are observed and therefore the influence of 3D effects on the airfoil characteristics of the blade 2 will not be discussed here.

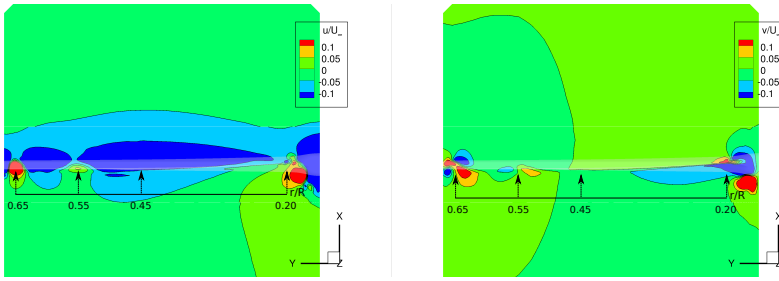


Figure 4.23: Blade 1 configuration: the vertical velocity  $u$  and spanwise velocity  $v$  contour in the plane  $z = -0.20m$  behind the blade 1,  $\alpha_{0.35} = 5^\circ$ .

4

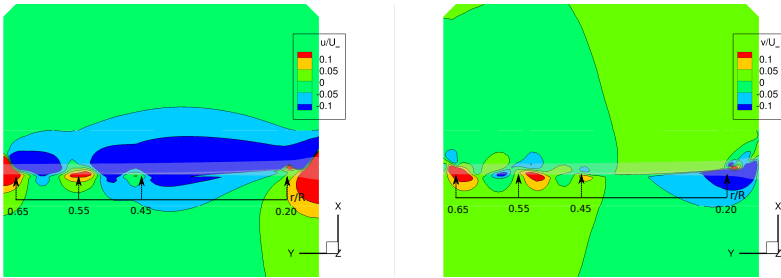


Figure 4.24: Blade 1 configuration: the vertical velocity  $u$  and spanwise velocity  $v$  contour in the plane  $z = -0.20m$  behind the blade 1,  $\alpha_{0.35} = 8^\circ$ .

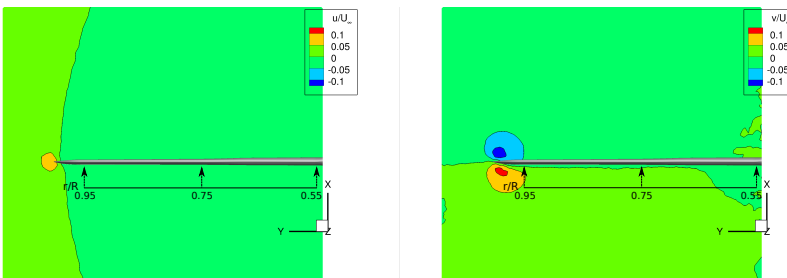


Figure 4.25: Blade 2 configuration: the vertical velocity  $u$  and spanwise velocity  $v$  contour in the plane  $z = -0.20m$  behind the blade 2,  $\alpha_{0.60} = 5^\circ$ .

### 4.3.2. THE EFFECTS OF ZIGZAG TAPE

In the study shown above, the ZigZag tape is assumed to have little influence on the integrated forces when the flow over the blade is still attached in CFD simulations. This assumption has been proposed because the physical dimension of the ZigZag tape is very small (the height is 0.2mm) and consequently it is challenging to mesh such 3D ZigZag tape along the whole blade. However, the influence of ZigZag tape on 2D airfoil aerodynamics characteristics can be studied and quantified by using the measured data in the experiment. The following section will investigate this effect.

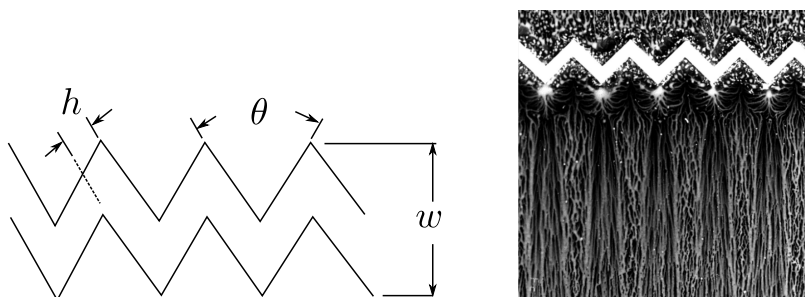


Figure 4.26: The shape and critical parameters of ZigZag tape and flow visualization over ZigZag tape, from the paper (Selig, 1995).

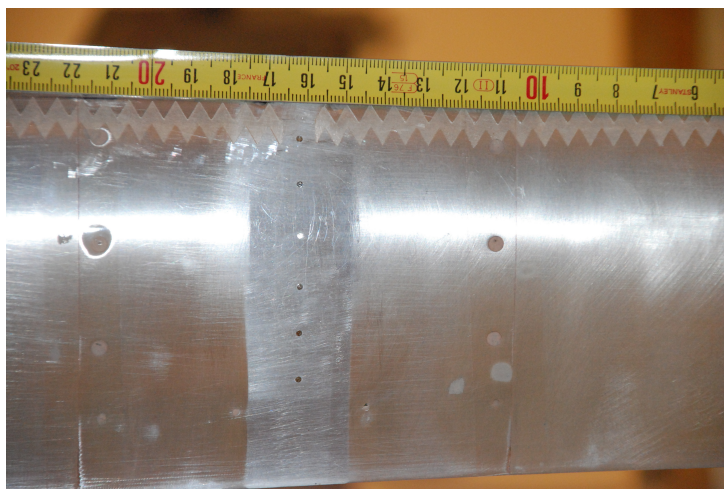


Figure 4.27: The ZigZag tape applied on the suction side of the MEXICO blade, located at 10% chord. The tape is removed at the locations of pressure sensors.

Regarding the ZigZag tape effect on 2D airfoil aerodynamic characteristics, (Selig, 1995) discussed the effects of ZigZag width, height and trip location on airfoil performance for two specific sailplane airfoils: *E374* and *SD7037*. For wind turbine airfoils, (Van Rooij and Timmer, 2003) discussed the ZigZag tape effect on the momentum thickness of the turbulent boundary layer. The comparisons of airfoil performance between

clean and rough configurations are also shown for several 2D thick airfoil classes. They conclude that an effective ZigZag tape will lead to a significant increase in momentum thickness of the turbulent boundary layer and sometimes will reduce (the maximum) lift. The critical distributed roughness height  $h$  is determined according to the method in the paper (Braslow and Knox, 1958). Moreover, critical roughness Reynolds number plays a role as well. The required roughness height which is sufficient to trigger transition is reduced when the undisturbed air velocity increases (Van Rooij and Timmer, 2003). Figure 4.26 presents the shape and critical parameters of ZigZag tape as well as flow visualization over ZigZag tape. Figure 4.27 shows the ZigZag tape attached on the MEXICO blade suction side in the non-rotating experiment. Table 4.4 lists the parameters of ZigZag tape used in this experiment.

Table 4.4: ZigZag tape parameters used in the experiment

$r/R$	[-]	$0 \sim 0.95$
$h$	[mm]	0.20
$w$	[mm]	10
$\theta$	[°]	60

#### ZIGZAG TAPE EFFECT ON LOCAL PRESSURE OF STATIC BLADE

Figure 4.28 compares the chordwise pressure distribution for the DU91-W2-250 airfoil at  $0.35R$  radial location with and without ZigZag tape for several angles of attack in order to understand the roughness effect on the measured local pressure. The gray arrow indicates the ZigZag tape location, which is located at the 10% local chord position. On the pressure side of the blade with ZigZag tape roughness, it can be seen that the pressure is lower compared to the clean blade. The main deviation is found at  $x/c = 0.30 \sim 0.50$  on the pressure side. While on the suction side, the rough blade has less suction, especially near the leading edge region as  $x/c = 0 \sim 0.30$ . This effect decreases when the angle of attack increases from  $8^\circ$  to  $20^\circ$ . When  $\alpha = 20^\circ$ , a slight pressure difference is observed only on the suction side. These comparisons also imply that the ZigZag tape changes the airfoil boundary layer displacement thickness and further decambers the airfoil. In addition, more influence on  $C_p$  is observed for the attached flow, but less influence for the separated flow for this specific 35% $R$  airfoil section.

Figure 4.29 presents the results of pressure distribution for the NACA 64-418 airfoil at radial location  $r/R = 0.92$  for three different angles of attack,  $\alpha = 8^\circ, 10^\circ$  and  $16^\circ$ . Similarly, rough blade with ZigZag tape acquires lower pressure on the pressure side than clean blade. On the other hand, on the suction side, without ZigZag tape stronger suction peak is observed near the leading edge. This lower pressure occurs in the regions  $x/c = 0 \sim 0.30$  and  $x/c = 0.40 \sim 0.70$ , respectively. After  $x/c = 0.70$ , conversely, a bit higher pressure is observed on the clean blade near the trailing edge. When the angle of attack increases, the ZigZag tape effect seems to play a less important role in local pressure distribution.



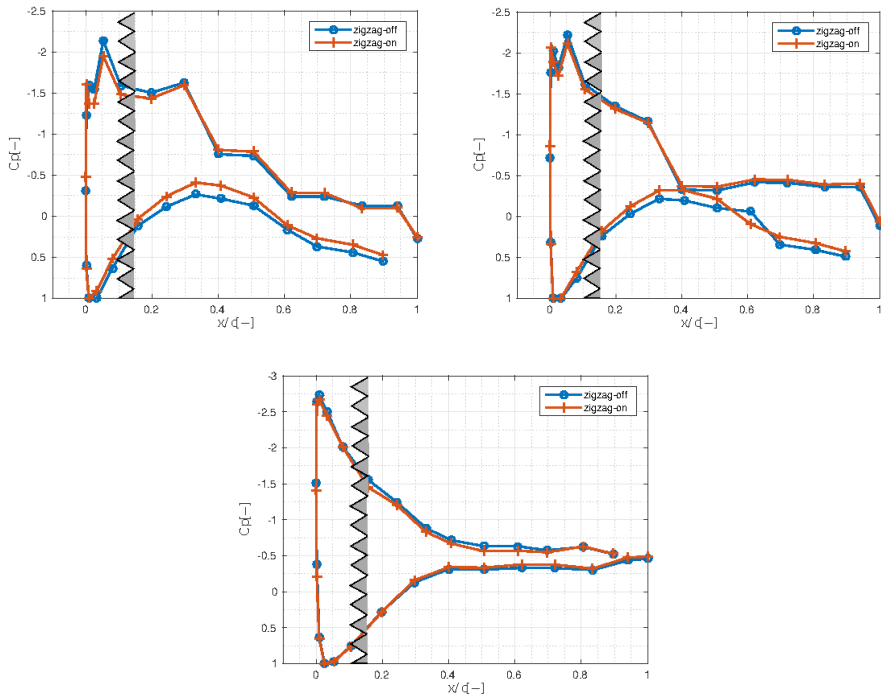


Figure 4.28: The influence of ZigZag tape on local pressure distribution in the experiment.  $C_p$  comparison with and without ZigZag tape at  $r/R = 0.35$  radial location,  $\alpha = 8^\circ, 11^\circ$  and  $20^\circ$ .

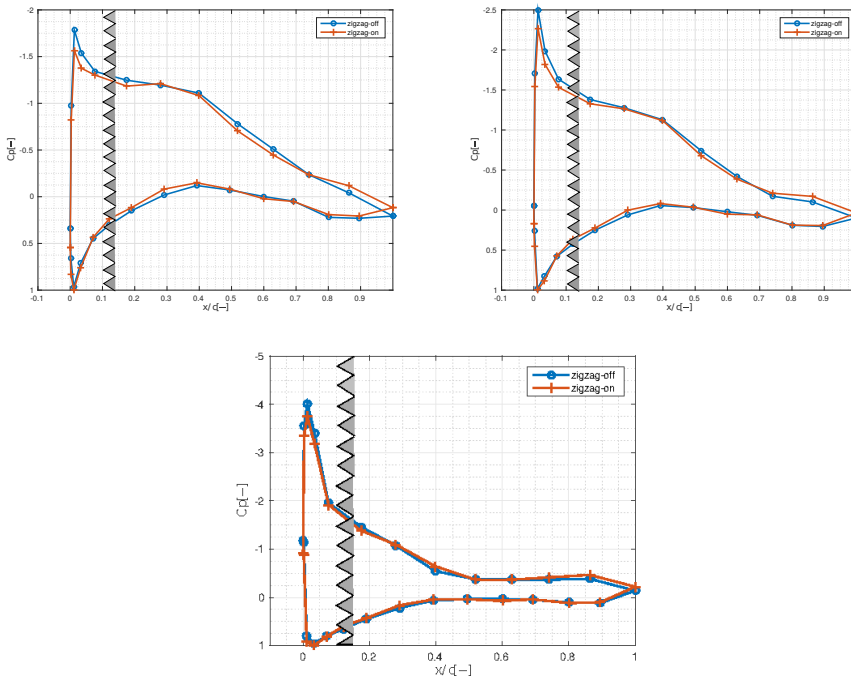


Figure 4.29: The influence of ZigZag tape on local pressure distribution in the experiment.  $C_p$  comparison with and without ZigZag tape at  $r/R = 0.92$  radial location,  $\alpha = 8^\circ, 10^\circ$  and  $16^\circ$ .

## ZIGZAG EFFECT ON LIFT AND DRAG

After investigating the effect of ZigZag tape on the local pressure, it is also relevant to see how the ZigZag tape influences the integral lift and drag forces.

Figure 4.30 shows the comparison of integral lift and drag force between clean and rough blade versus angles of attack. At  $0.35R$  radial location, it can be clearly seen that the lift force is reduced by the existence of ZigZag tape. As discussed before, the ZigZag tape has more influence on local pressure at attached flow condition than separated flow condition. The observation is further supported with  $C_L$  polar comparison. In terms of the effect of ZigZag tape on drag force  $C_D$ , the drag force is increased over the whole range of angles of attack.

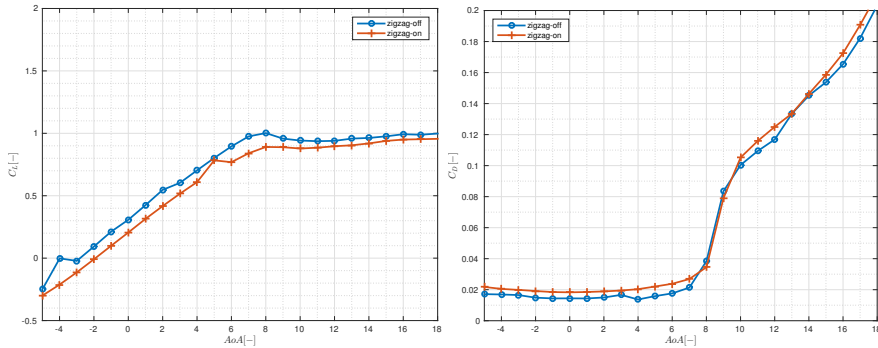


Figure 4.30: The influence of ZigZag tape on the lift  $C_L$  and drag  $C_D$  polar of the DU91-W2-250 airfoil at section  $r/R = 0.35$ .

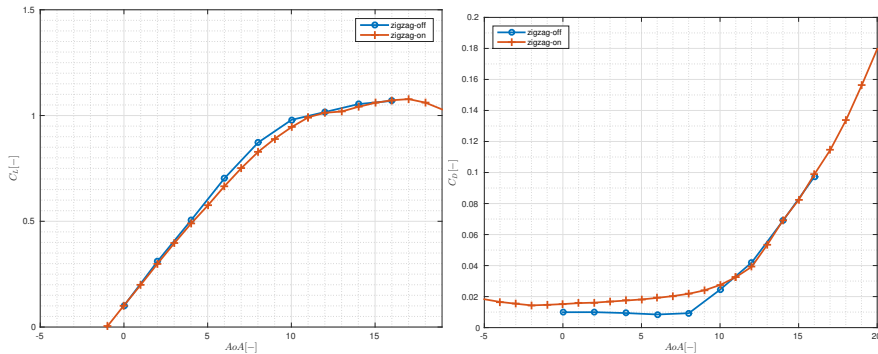


Figure 4.31: The influence of ZigZag tape on the lift  $C_L$  and drag  $C_D$  polar of the NACA 64-418 airfoil at section  $r/R = 0.92$ .

Figure 4.31 presents the  $C_L$  and  $C_D$  polar for clean and rough blade at  $0.92R$  radial location. The airfoil profile at this section is NACA 64-618. Different from the ZigZag tape effect on the lift of  $0.35R$  sectional airfoil, the ZigZag tape only plays a significant role in reducing lift force in particular flow regimes, which is when  $\alpha = 4^\circ \sim 11^\circ$ . However, at attached flow condition where  $\alpha < 4^\circ$ , the ZigZag tape has little influence on lift reduction.

The same effect is observed at a higher angle of attack  $\alpha > 11^\circ$  as well. Meanwhile, the drag force is not influenced by the ZigZag tape significantly when the angle of attack is larger than  $10^\circ$ . But considerably higher drag force is obtained with the rough blade, and the largest difference in drag force between clean and rough blade appears at  $\alpha = 8^\circ$ .

#### ESTIMATED ZIGZAG TAPE EFFECTS ON CFD RESULTS

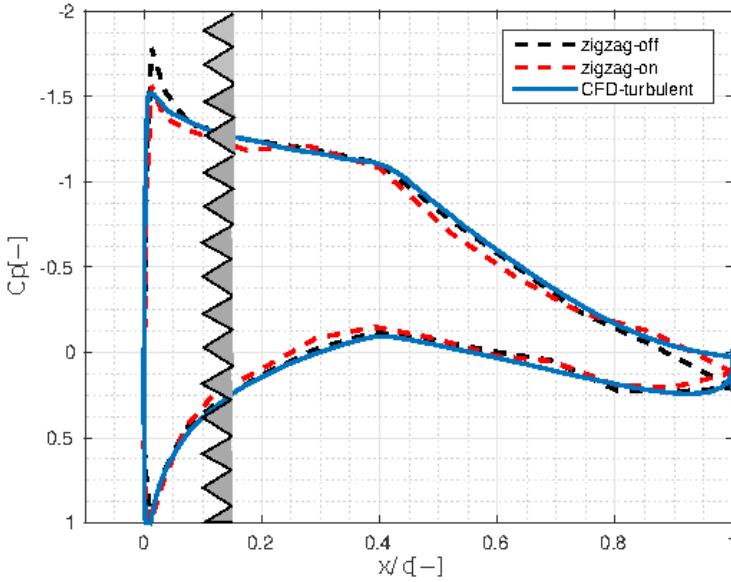


Figure 4.32: The influence of ZigZag tape on local pressure distribution.  $C_p$  comparison with and without ZigZag stripe and CFD prediction at  $r/R = 0.92$ ,  $\alpha = 8^\circ$ .

Figure 4.32 shows the comparison of local chordwise pressure distribution at  $r/R = 0.92$  between experimental measurement and CFD result at  $\alpha = 8^\circ$ . From the  $C_p$  comparison, on the pressure side it can be observed that 3D CFD result with fully turbulent simulation has closer  $C_p$  agreement with the clean blade measurement than with the blade with ZigZag tape measured. On the suction side, a similar observation is found at  $0.05 < x/c < 0.80$ , that fully turbulent CFD results agree well with clean blade measurement. Except from the locations  $x/c < 0.05$  and  $x/c > 0.80$ , the prediction of CFD is closer to the results obtained on rough blade.

Although the aim of installing ZigZag tape on the blade is to trigger the flow turbulent immediately in the rotating MEXICO experiment, the fully turbulent flow over rough blade was believed much easier to simulate with CFD codes. However, the  $C_p$  comparison shows a clear proof that the ZigZag tape has significant influence on the  $C_p$  prediction. The existence of ZigZag tape clearly alters the airfoil boundary layer displacement thickness and the airfoil camber, as mentioned before.

Figure 4.33 plots the comparison of the sectional normal force at  $r/R = 0.92$  by integrating the experimental and numerical pressure values at the same locations. Similar to the pressure distribution comparison, it is expected that the normal force for the clean blade is larger than for the rough blade. The difference is about  $7\%F_{N_{rough}}$ . Due to the ZigZag tape effects, significant overprediction is obtained by the fully turbulent CFD simulation compared to the rough blade measurements. However, almost the same normal force is predicted by CFD as measurement for the clean blade. In other words, the fully turbulent CFD simulation overpredicts the normal force on the blade with ZigZag tape. Most probably because ZigZag tape alters the boundary layer displacement thickness and airfoil camber.

4

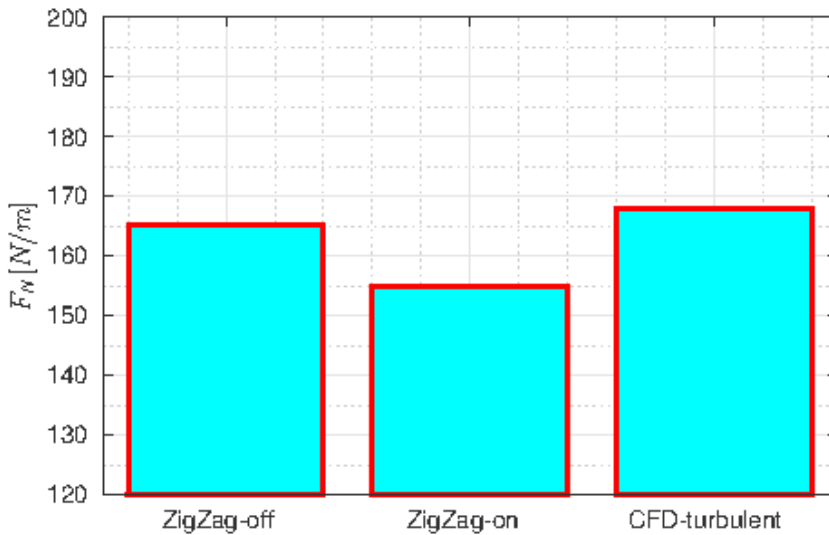


Figure 4.33: The results of sectional normal force at  $r/R = 0.92$  with angle of attack  $\alpha = 8^\circ$ . Three cases are clean blade, rough blade and fully turbulent CFD simulation.

The question that needs to be answered here is whether the difference in  $C_p$  distribution discussed above between the clean blade and the rough blade is an expected result when boundary layer is tripped or more than expected. Figure 4.34 and 4.35 further demonstrate the hypothesis that the applied ZigZag tape not only plays a role in triggering transition at the specific location, but has much more effect than that. The numerical results shown in these figures are obtained from *Rfoil* (Van Rooij, 1996), which is based on a viscous-inviscid method for wind turbine airfoil analysis. Figure 4.34 clearly demonstrates that *Rfoil* presents very good capability for predicting  $C_p$  distribution for the clean 2D NACA64-418 airfoil. However, there are notable differences observed both on the suction side and pressure side between the numerical result and experimental measurement for the rough 2D NACA64-418 airfoil in Figure 4.35. The transition locations on the suction and pressure sides in *Rfoil* calculation are specified as the exper-

iment but without any roughness height. The amplification factor  $N = 9$  is used in the transition model  $e^N$  for the *Rfoil* computation due to the very low turbulence level in wind tunnel. As can be seen from the comparison, the measured pressure on the suction side with a ZigZag tape height of  $0.2\text{mm}$  presents considerably less pressure suction compared to *Rfoil* results, particularly in the region  $x/c = 0 \sim 0.8$ . The ZigZag tape on the pressure side shows less influence on the pressure, even if the ZigZag tape height of  $0.32\text{mm}$  is larger than the one used on the suction side. To quantitatively evaluate the extra contamination caused by the ZigZag tape object, the experimental result produces 5.7% lower  $c_l$  and 10% higher  $c_d$  compared to numerical result without any roughness height. These extra “negative” effects indicate that the ZigZag tape, as an intrusive device to trigger the transition, significantly affects and disturbs the local flow over the airfoil and further the aerodynamic loads due to its explicit existence. The consequence of attaching ZigZag tape with same height on the rotating blade tip  $r/R = 0.92$  could be more severe than the difference in  $C_p$  on the suction side shown in Figure 4.35, because the ratio of ZigZag tape height to local chord length ( $h/c$ ) in the rotating blade case is larger than the 2D airfoil case. The effect of ZigZag tape is a probable explanation for the aerodynamic loads overprediction by CFD.

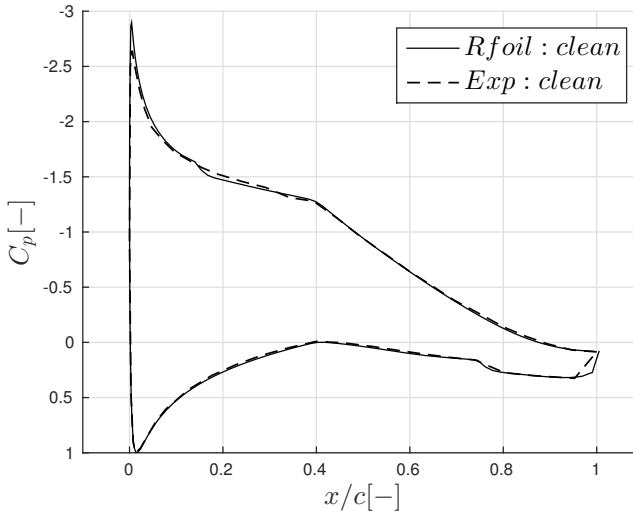


Figure 4.34: The comparison of pressure distribution between *Rfoil* and experiment for the clean NACA64-418 airfoil. The Reynolds number is  $Re = 0.7 \times 10^6$  and the geometric angle of attack is  $\alpha = 8^\circ$ . It demonstrates that *Rfoil* presents good capability for predicting  $C_p$  distribution.

The ZigZag tape effects discussed above are not taken into account by any CFD simulations for the MEXICO rotor. The observation shown can explain why almost all CFD results in the rotating MEXICO experiment consistently overestimate the normal force near the blade tip, even when the rotor is operating at the design tip speed ratio. From the  $c_l$  and  $c_d$  curves shown in Figure 4.31, one can observed that the lift and drag forces are most influenced by the existence of ZigZag tape at conditions when the angle of at-

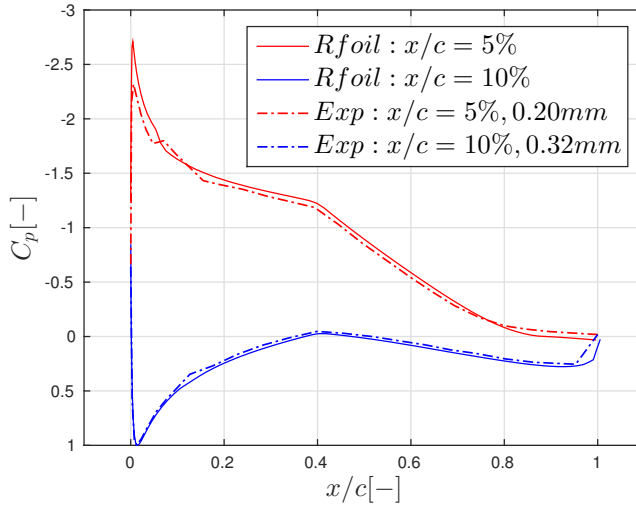


Figure 4.35: The comparison of pressure distribution between *Rfoil* and experiment for the rough NACA64-418 airfoil tripped by ZigZag tape. The Reynolds number is  $Re = 0.7 \times 10^6$  and the geometric angle of attack is  $\alpha = 8^\circ$ . The configurations of ZigZag tapes are: at suction side  $x/c = 5\%$  with ZigZag tape height of  $0.2mm$  and at pressure side  $x/c = 10\%$  with ZigZag tape height of  $0.32mm$ .

tack  $\alpha$  ranges from  $4^\circ$  to  $11^\circ$ . When  $\lambda = 6.7$ , the effective angle of attack estimated at  $r/R = 0.82$  and  $0.92$  on the rotating blade are just in this region ( $7.3^\circ \sim 8.4^\circ$  estimated by BEM code), and consequently the ZigZag tape on the rotating blade most likely shows similar or even stronger effects on the aerodynamic loads as the non-rotating experiment.

According to the above analysis, it can be concluded that the existence of ZigZag tape has a significant impact on the sectional loads and decambers the airfoil. Therefore, it is recommended to exclude these effects from measured results. For that reason, in the new MEXICO experiment carried out in July 2014, the aerodynamic loads were measured with clean blade configuration. Only the outboard part ( $r/R > 0.7$ ) of the blade (NACA profile) is clean, the rest part of the blade is still tripped. Without a tripped boundary layer, transitional flow from laminar to turbulent has to be considered in CFD simulation, which will be discussed in Chapter 5.

#### 4.3.3. FLOW AT HIGH ANGLES OF ATTACK

In Section 4.3.1, the calculated chordwise pressure on three airfoils from CFD simulation at low angles of attack ( $0^\circ, 5^\circ, 8^\circ$ ) are compared with experimental data. When the geometric angle of attack increases further, the flow becomes highly separated and even stalled. It is well known that a RANS approach may fail in dealing with such flows. Therefore, in this section, DDES is used to predict highly separated flow at high angles of attack. Meanwhile, the comparison between DDES and RANS results will indicate whether DDES can provide a better prediction for such specific 3D blade case.

Second order total variation diminishing (TVD) scheme based on central differenc-

ing with Sweby limiter is chosen for the convective term discretization and second order central scheme for the diffusion term. The Spalart-Allmaras delayed detached-eddy simulation (DDES) model is used. The implicit top-hat filter is applied to the spatial and temporal field. The mesh of DDES simulation is the same as the computational mesh of RANS. The time step is  $\Delta t U / c_{0.35R} = 0.018$  and the total simulation is run for  $tU / c_{0.35R} = 300$  convective time units.

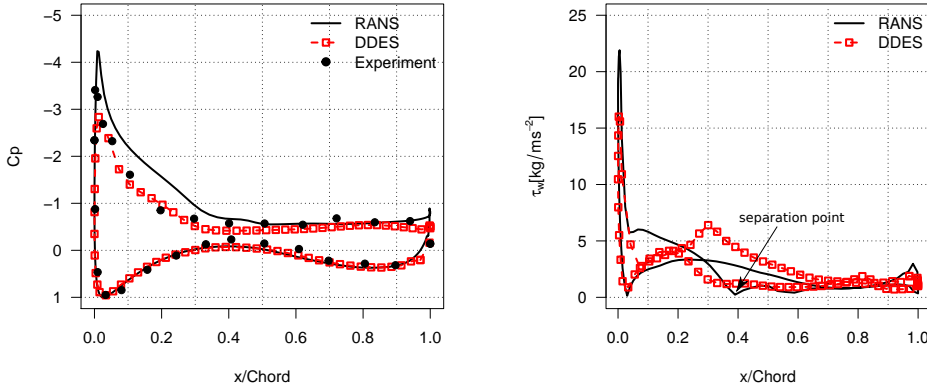


Figure 4.36: The distribution of chordwise pressure and wall shear stress  $\tau_w$  at high geometric angle of attack,  $\alpha = 19^\circ$ . DU airfoil at 35% $R$  section.

The numerical pressure prediction of both DDES and RANS as well as the wall shear stress  $\tau_w$  over DU section at 35% $R$  are plotted in Figure 4.36, and compared to experimental results. The local geometric angle of attack is  $19^\circ$  at this condition. It can be seen that DDES and RANS give the same results on the pressure side, and both methods have good agreement with the measurements. However, massively separated flow occurs at the suction side, which challenges the simulation to predict the flow accurately. The separation point is predicted at around  $x/c \approx 0.4$  by RANS, which means a delayed flow separation compared to the experiment. Consequently, the pressure is underpredicted on the suction side and hence the loads are overpredicted. The cause is well known: turbulence models based on Boussinesq eddy viscosity assumption in RANS assume the flow is isotropic, which is not true in large eddies dominated flow. In contrast, the anisotropic large eddies can be resolved by LES, and isotropic small eddies in the thin boundary layer can be modeled by RANS. Therefore, DDES results show very good agreement with the experimental data, as seen in Figure 4.36.

### 3D VORTICAL STRUCTURE VISUALIZATION

The 3D vortical structure visualization of RANS and DDES calculations is shown in Figure 4.37. The instantaneous vortical structure shown here for DDES is the result of computational time  $T = 0.3s$ . The geometrical angle of attack is  $\alpha = 19^\circ$  at 35% $R$ . As seen from the figures, the flow is massively separated and highly three-dimensional over the



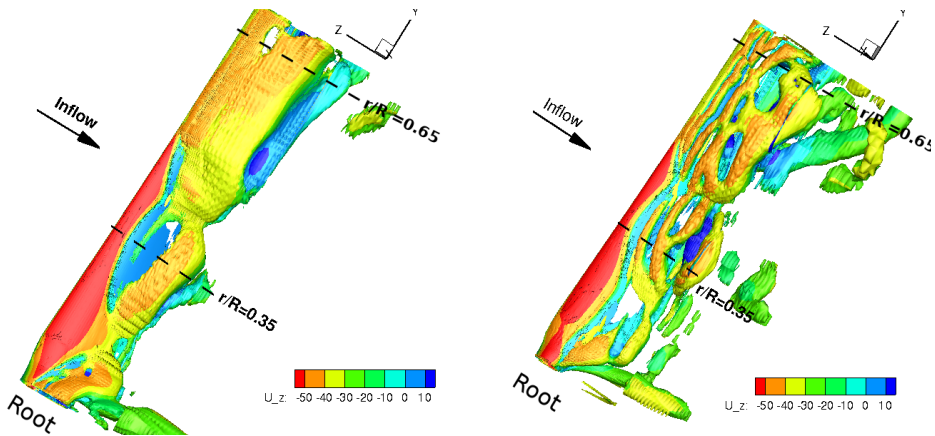


Figure 4.37: Blade 1 configuration: 3D visualization of vortical structure by RANS and DDES calculations, iso-surface  $Q = 3 \times 10^4$ , colored by the velocity. Geometric angle of attack  $\alpha = 19^\circ$  at  $r/R = 0.35$ .

entire blade. Towards to the tip, leading edge separation occurs because of blade twist distribution, which results in an even higher geometrical angle of attack. Compared to RANS, DDES has a much higher turbulent vortical structure resolution. The shed vortices and stall cells can be clearly seen at the outboard part of the blade  $r/R > 35\%$ , which can not be resolved by time-averaged RANS computation.

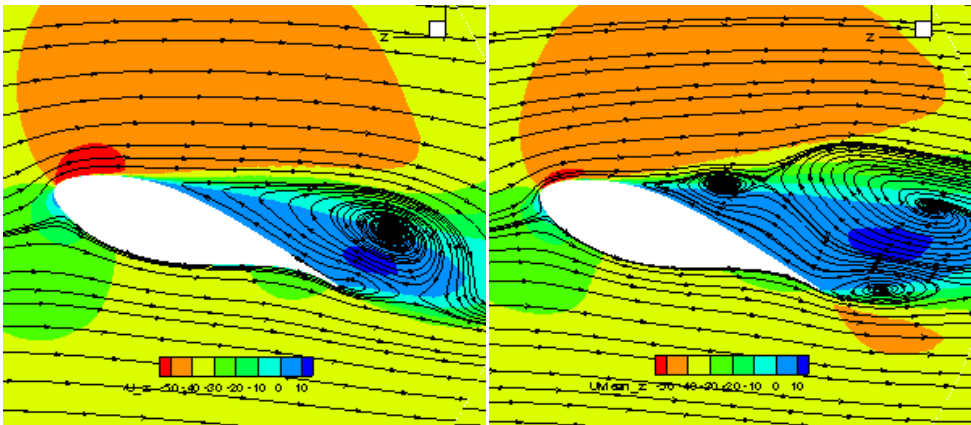


Figure 4.38: Blade 1 configuration: Surface streamtraces pattern of the averaged streamwise flow field over DU91-W2-250 airfoil at  $35\%R$  for RANS and DDES simulations. These streamlines overlap with streamwise velocity field contour, the inflow direction is negative  $Z$ .

Figure 4.38 plots the surface streamtraces of the averaged streamwise flow field at  $r/R = 35\%$  for RANS and DDES, respectively. A large recirculation region rotating in a clockwise direction is formed on the suction side and a small vortex appears at the trailing edge. Apart from that, DDES captures a second clockwise rotating vortex shedding after the first large vortex. At the leading edge, the flow from RANS results shows more

acceleration than DDES. As a consequence, more suction is expected at the area, which is consistent in the  $C_p$  comparison in Figure 4.36. A further downstream turbulent wake with more expansion behind the stalled airfoil is predicted by DDES.

## 4.4. CONCLUSIONS

This chapter presents the experimental and numerical investigations on the non-rotating MEXICO wind turbine blades. The quasi-2D aerodynamic characteristics of the non-rotating MEXICO blades are measured in the LTT experiments, and the CFD simulations are carried out in order to provide more information of 3D flow feature around the blades. Eventually, more insight into the MEXICO blades is given.

For the attached flow condition, the pressure distributions from the CFD calculations at three different sections compare fairly well with the experimental measurements. Excellent match is observed at 92% spanwise section with the NACA 64-418 airfoil. For the DU and the RISØ-A1-21 airfoil sections, located at 35% and 60% span respectively, a reasonably good agreement is found. Considerable differences are found on the suction side at the locations between  $x/c = 0.15$  and  $x/c = 0.34$  on the RISØ airfoil section. Besides that, at  $\alpha_{0.35} = 8^\circ$ , the current computation does not capture the flow separation at the trailing edge for the section  $r/R = 0.35$ .

Experimental oil flow visualization has been compared with CFD limiting streamlines to investigate the flow topology for the blade 3. Overall speaking, the separation line is well predicted by CFD and hence it indicates that the drag force along the blade is calculated reasonably well in the condition  $\alpha_{0.82} = 8^\circ$ .

The lift force distribution along the span is investigated for blade 1 and blade 2. Based on the results, it can be concluded that the intermediate region connecting the RISØ-A1-21 airfoil and the DU91-W2-250 airfoil does not have a smooth enough lift distribution, which leads to a sudden lift drop and significant trailing vorticity at  $r/R = 0.55$  in both cases  $\alpha_{0.35} = 5^\circ$  and  $\alpha_{0.35} = 8^\circ$ . This phenomenon confirms observations from earlier new MEXICO rotor wake analysis.

Large-scale vortical structures are observed over the suction side near the mid-span  $r/R = 0.55$  in the numerical flow field. In addition, a pair of counter-rotating vortices are found in the plane behind blade 1 near the location  $r/R = 0.55$ . Compared 2D experimental data with 3D CFD results, the upwash and downwash effects induced by these vortices at  $r/R = 0.55$  significantly change the 2D aerodynamic characteristics of the RISØ-A1-21 airfoil family. Consequently 3D effects play an important role in the numerical modeling for calculating the aerodynamic loads for the MEXICO rotor.

ZigZag has a notable impact on the measured sectional aerodynamic characteristics of the MEXICO blade. For the DU91-W2-250 airfoil section at  $r/R = 0.35$ , lift reduction is found consistently in the whole range of AoAs, and the influence becomes smaller for separated flow at high angle of attack. For the NACA 64-418 airfoil at  $r/R = 0.92$  section, the influence of ZigZag tape is smaller and ZigZag tape only causes a significant lift reduction at specific flow regimes:  $\alpha = 4^\circ \sim 11^\circ$ . ZigZag tape alters the boundary layer displacement thickness and further the airfoil camber, resulting fully turbulent CFD results to significantly over predict the sectional normal force. Closer agreement in sectional normal force is obtained between CFD result and clean blade measurement. This study can partially explain the reason why all CFD simulations consistently over predict the

normal force on the rotating MEXICO blade tip at the design condition in the MexNext blind comparisons. It is recommended to eliminate the ZigZag effects from measured data in the new MEXICO campaign and laminar-turbulent transition modeling should be included in the CFD simulation.

For the highly separated flow condition, it is found that DDES computation predicts  $C_p$  distribution at 35% $R$  section for non-rotating MEXICO blade much better than RANS. More vortical structures are captured by DDES in separated flow region and a further downstream turbulent wake with more expansion behind the stalled airfoil is observed in DDES computation. By acquiring good prediction on the 3D static MEXICO blade, the superiority of DDES approach should be used for rotating wind turbine rotor simulation at high wind speeds.

# 5

## NUMERICAL INVESTIGATION OF 3D ROTATING MEXICO ROTOR

*Start by doing what's necessary;  
then do what's possible;  
and suddenly you are doing the impossible.*

Francis of Assisi

*This chapter reassesses the numerical simulations of the MEXICO wind turbine rotor by using validated OpenFOAM code, focusing on the turbulent flow over rotating blades. First of all, validation cases are performed on this rotor under three different tip speed ratios,  $\lambda = 4.17, 6.67$  and  $10.0$ . Aerodynamic loads on the twisted blades from CFD simulations are compared against results from both measurements, as well as from a blade element momentum (BEM) method. Apart from the loads comparison, the velocity field surrounding the blades and in the near wake are validated with particle image velocimetry (PIV) data. Especially, 3D effects and rotational augmentation are investigated in depth on the rotating blade, by comparing the difference with the non-rotating blades and 2D airfoil aerodynamics. Second, in order to test the hypothesis that the ZigZag tape plays an important role in affecting the tip loads, the transitional simulation is performed and transitional effects are evaluated in the current chapter. In the previous chapter, conclusions are drawn that transition modeling is necessary to predict the free transition case in order to reduce the deviation between CFD and experiment. This laminar-turbulent transitional effects on aerodynamic loads will be investigated and quantified. The last part of work in this chapter will focus on a challenging simulation case, being the wind turbine rotor operating at  $\lambda = 4.17$ . Highly separated flow exists over the blades in this case, and the performance of DDES approach will be evaluated for this specific 3D case.*

---

Parts of this chapter have been submitted to Journal of Wind Engineering & Industrial Aerodynamics based on the paper "MEXICO rotor aerodynamic loads prediction: ZigZag effects and laminar-turbulent transition modeling in CFD"

## 5.1. INTRODUCTION

In this chapter, 3D CFD simulations of the rotating MEXICO rotor are carried out at three measured tip speed ratios  $\lambda = 4.17$ ,  $\lambda = 6.67$  and  $\lambda = 10.0$ . These cases are selected representing separated flow conditions, design conditions, and turbulent wake state. The numerical predictions obtained from OpenFOAM are compared with experimental results. In addition, an engineering model based on BEM theory is applied to determine the aerodynamic loads. Transitional effects and the performance of DDES approach will be discussed in detail for the specified cases. The questions to be answered in this chapter are

- How does OpenFOAM perform for 3D rotating wind turbine simulations compared to experimental measurements as well as BEM?
- What are the aerodynamic loads in rotating conditions and the flow field compared to a non-rotating blade situation and how do sectional data compare to 2D airfoil data?
- By incorporating the laminar-turbulent transition modeling discussed in Chapter 3, will the numerical prediction have better agreement with the experimental measurement?
- For the separated flow simulation case when the wind turbine is operating at  $\lambda = 4.17$ , how does the DDES approach perform for the loads prediction?

This chapter is organized as follows: Section 5.2 briefly describes the experimental database used to validate the numerical simulation. The methodology of rotating blade modeling in OpenFOAM and the numerical set-up for the simulations are introduced in Section 5.3. The comparison of aerodynamic loads and velocity field between CFD and experimental data, the investigation of rotational and transitional effects are analyzed and presented in Section 5.4. Finally, conclusions are drawn in Section 5.5.

## 5.2. WIND TUNNEL MEASUREMENT DATABASE

### 5.2.1. ROTATING MEASUREMENTS OF THE MEXICO ROTOR AT DNW

The database used for validating the numerical results is obtained from the MEXICO experiments, which were carried out in the German Dutch Wind Tunnel (DNW) for the 1<sup>st</sup> campaign in 2006 and for the 2<sup>nd</sup> campaign in 2014. Figure 5.1 shows the test MEXICO model in DNW wind tunnel which has a test section of  $9.5 \times 9.5 m^2$  and Figure 5.2 depicts a smoke visualization of tip vortices in the second phase of measurement. As seen in the figures, a three-bladed wind turbine with a diameter of  $4.5 m$  was tested at different wind speeds and rotational speeds, for both axial flow and yawed flow conditions. The twisted and tapered blades are designed with three different airfoil families: DU91-W2-250 from 20% to 45.6% span, RISØ A1-21 from 54.4% to 65.6% span and NACA64-418 from 74.4% span to the tip. In between the airfoil families a transition airfoil is present. Details are found in Chapter 4. Table 5.1 summarizes the MEXICO rotor geometry parameters and part of test conditions in the experiment.



Figure 5.1: The MEXICO experiment in DNW wind tunnel (Snel et al., 2007). Three bladed wind turbine with 4.5m diameter rotor.



Figure 5.2: Smoke visualization of tip vortices generated from the blade tip in the second phase of MEXICO experiment (Boorsma and Schepers, 2014)

Table 5.1: Rotor geometry and part of test conditions

Number of blades	$Z[-]$	3
Rotor diameter	$D[m]$	4.5
Tip pitch angle	$\theta[^\circ]$	-2.3
Yaw angle	$\Psi[^\circ]$	0
Rotational speed	$n[\text{rpm}]$	424.5
Wind speed	$U_\infty[m/s]$	10, 15, 24
DU91-W2-250	$r/R[-]$	$20\% < r/R < 45.6\%$
RISØ A1-21	$r/R[-]$	$54.4\% < r/R < 65.6\%$
NACA64-418	$r/R[-]$	$74.4\% < r/R < 100\%$

### 5.2.2. NON-ROTATING MEASUREMENT OF THE MEXICO BLADES AT TUDELFT

Before the 2<sup>nd</sup> campaign of experiments, a non-rotating experiment was conducted in the Low Speed Low Turbulence wind tunnel of TUDelft in November 2013. This wind tunnel is a closed wind tunnel which has exchangeable, octagonal test sections of 1.80m wide, 1.25m high and 2.60m long, see Chapter 4. The maximum velocity of the wind tunnel is 120m/s with a free-stream turbulent intensity around 0.10%. The pressure distribution at two radial sections 35%*R* and 92%*R* were measured at different incoming velocities and a range of angles of attack by using instrumented Kulite pressure transducers. The incoming velocities have been chosen in the non-rotating experiment to ensure that the chord-based Reynolds number  $Re_c$  is virtually the same as in the rotating MEXICO experiment. Due to the test section height limitations, the blade was mounted vertically with the tip protruding outside the test section. A zigzag is placed at the location of 10% chord along the blade, both on the pressure side and the suction side, to trigger fully turbulent flow.

### 5.2.3. 2D STATIC AIRFOIL WIND TUNNEL MEASUREMENT

2D airfoil aerodynamic characteristics from wind tunnel tests are also available for the three airfoil profiles applied in the MEXICO blade. Therefore, the measured lift  $C_L$ , drag  $C_D$  and pressure distribution  $C_p$  in the current experiment can be utilized to quantify the 3D and rotational effects.

## 5.3. ROTATION MODELING IN OPENFOAM

Apart from the available experimental data mentioned above, three-dimensional steady-state CFD simulations are carried out in order to validate the CFD code and provide more insight into the wind turbine aerodynamics. This section describes the rotating flow modeling approach, mesh generation, CFD solver and numerical schemes used in the simulation.

### EQUATION OF FLUID MOTION

Based on Newton's second law, the integral form of the mass and momentum conservation equations of fluid motion in the inertial reference frame is:

$$\frac{\partial}{\partial t} \int_V \rho dv + \int_V \nabla \cdot \rho \mathbf{u}_I dv = 0 \quad (5.1)$$

$$\frac{\partial}{\partial t} \int_V \rho \mathbf{u}_I dv + \int_S \mathbf{n} \cdot (\rho \mathbf{u}_I \mathbf{u}_I) ds = - \int_V \nabla p dv + \int_V \nabla \cdot (\mu_{eff} \nabla \mathbf{u}_I) dv \quad (5.2)$$

where  $V$  is the control volume,  $S$  is the surface of the volume,  $\mathbf{n}$  is the normal vector of surface  $ds$ ,  $\mathbf{u}_I$  is the velocity vector in the inertial reference frame,  $\rho$  and  $p$  are the fluid density and the static pressure, respectively.  $\mu_{eff}$  is effective dynamic viscosity of the fluid, which is modeled by different turbulence models.

Transforming the velocity vector from inertial reference frame to rotating reference frame, yields

$$\mathbf{u}_R = \mathbf{u}_I - \boldsymbol{\omega} \times \mathbf{r}, \quad (5.3)$$

here  $\mathbf{u}_R$  is the velocity vector in the rotating reference frame,  $\boldsymbol{\omega}$  is the angular velocity vector and  $\mathbf{r}$  is the position vector from the origin of the rotating frame.

Therefore, the conservation equations Eq.5.1 and 5.2 can be derived in the rotating reference frame with absolute velocity.

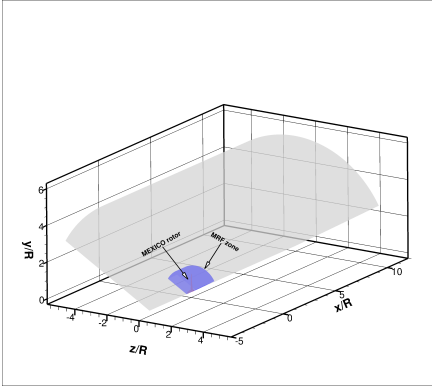
$$\frac{\partial}{\partial t} \int_V \rho dv + \int_V \nabla \cdot \rho \mathbf{u}_I dv = 0 \quad (5.4)$$

$$\frac{\partial}{\partial t} \int_V \rho \mathbf{u}_I dv + \int_S \mathbf{n} \cdot (\rho \mathbf{u}_R \mathbf{u}_I) ds + \underbrace{\int_V \rho (\boldsymbol{\omega} \times \mathbf{u}_I) dv}_{\text{Coriolis force}} = - \int_V \nabla p dv + \int_V \nabla \cdot (\mu_{eff} \nabla \mathbf{u}_I) dv \quad (5.5)$$

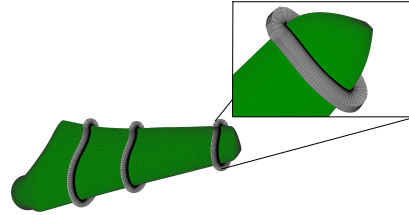
By using the multiple reference frame (MRF) approach, both the flow in a rotational zone and stationary zone are solved based on Eq.5.4 and 5.5. Then the relative face flux convection term  $(\rho \mathbf{u}_R \mathbf{u}_I)_S$  is calculated at the interface between the rotating part and the stationary part.

## MESH GENERATION

5



(a) CFD computational domain. The purple smaller domain represents the MRF zone, where body force will be added.



(b) Fully structured surface mesh on the MEXICO blade and overview of boundary layer mesh used to solve the viscous boundary layer flow.

Figure 5.3: The overview of CFD computational domain and the generated mesh

The layout of the computational domain is shown schematically in Figure 5.3a. The entire far field is modeled as a cylinder with a height  $12D$  and a radius  $3D$ , where  $D$  is the diameter of the turbine rotor. Considering a fully developed turbulent inflow, the domain before the rotor is extended to four times the diameter. A length of  $8D$  is used in the streamwise direction to simulate the turbulent wake generated by the rotor. A smaller cylinder with the height  $1/2D$  and the radius  $3/4D$ , which contains the blades and the hub, is modeled as the rotating zone.



A high-quality multi-block O-type structured grid is generated near the blade by using the hyperbolic method. A fixed growth rate of 1.1 is used for extruding the viscous boundary layer grid, see Figure 5.3b. Besides, the far field grid is generated by using an unstructured tetrahedral grid. By systematically refining the first cell height normal to the blade surface, the number of nodes in the direction of chordwise and far-field mesh resolution, a grid refinement study is performed by using three different grid levels. Eventually, the first cell wall normal distance is about  $4 \times 10^{-6}$  m, which enables to resolve the turbulent boundary layer flow with normalized wall distance  $y^+ < 1$ . There are 225 nodes along the span and 160 nodes along the chordwise direction. The total number of computational cells is  $3.16 \times 10^6$ .

#### CFD SOLVER AND NUMERICAL SCHEMES

The CFD solver used is OpenFOAM (Open Field Operation and Manipulation), an open source CFD code developed with finite volume method. All the flow quantities are stored in the center of the discretized control volume using a collocated methodology. The (Rhie and Chow, 1983) method is used to remove oscillations in the solutions when applying the collocated grid. The steady state incompressible Reynolds-Averaged Navier-Stokes (RANS) equations are decoupled and solved with the SIMPLE (Semi-Implicit Method for Pressure-Linked Equations) algorithm of (Patankar and Spalding, 1972). Menter's two equations eddy viscosity turbulence model  $k - \omega$  SST is applied as the closure relations for solving the N-S equations. A second-order accurate linear-upwind scheme is used to discretize the convection term for the velocity and a total variation diminishing (TVD) scheme based on central differencing with a limiter is chosen for the turbulence convective terms  $k$  and  $\omega$ . Diffusion terms are discretized with a second order centered scheme. The boundary condition at the inlet is the Dirichlet boundary condition for the inflow velocity and turbulent inflow variables, and the von Neumann boundary condition for the pressure. The von Neumann boundary condition is enforced at the outlet for all variables, except for the pressure which uses the Dirichlet condition. In order to reduce the computational cost, Euler slip wall conditions are used at the hub surfaces without considering the viscous effect, while no-slip wall boundary conditions are applied at the surfaces of blades. The arbitrary mesh interface (AMI) technology (Farrell and Maddison, 2011) is imposed at the interfaces connecting the MRF rotating zone and stationary zone. A zero gradient is used for the far-field boundary of the computational domain. In particular, periodic conditions are enforced at the  $120^\circ$  cyclic boundaries to be able to use the simplified domain.

## 5.4. RESULTS AND DISCUSSION

### 5.4.1. AERODYNAMIC LOADS COMPARISON BETWEEN EXPERIMENT AND BEM RESULTS

Figure 5.4 compares the normal and tangential forces calculated by CFD and BEM with experimental measurements at different tip speed ratios. For the low wind speed condition with  $\lambda = 10.0$ , numerical results from both codes present correct trend and are aligned with the measurements. CFD shows a much better agreement with the experiments than BEM, especially near the tip region  $r/R = 0.82$  and  $0.92$ , and also in the root

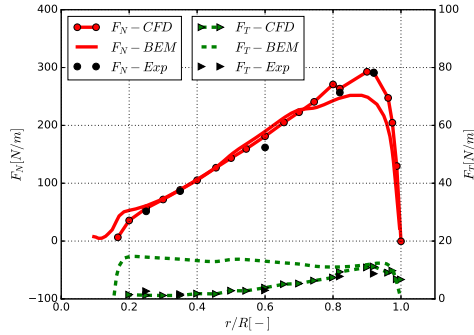
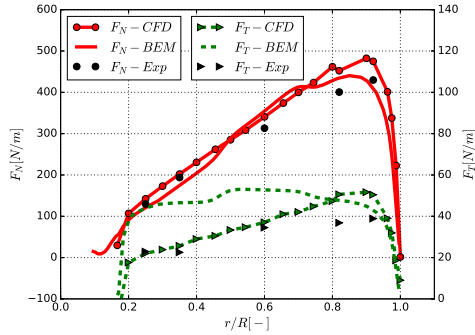
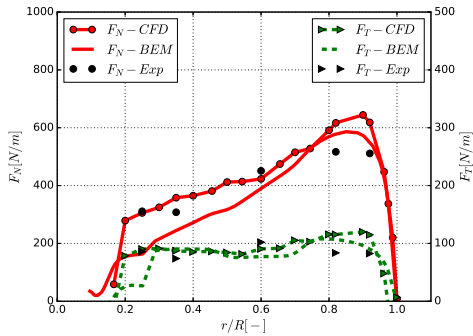
(a)  $\lambda = 10.0$ (b)  $\lambda = 6.67$ (c)  $\lambda = 4.17$ 

Figure 5.4: Comparison of aerodynamic normal force  $F_N$  and tangential force  $F_T$  between numerical results from CFD, BEM and experimental measurement at different wind speeds  $U_\infty = 10\text{ m/s}$ ,  $15\text{ m/s}$  and  $24\text{ m/s}$ , corresponding tip speed ratios  $\lambda = 10.0$ ,  $6.67$  and  $4.17$ .

region. Significant overprediction of tangential force is observed for the BEM code results, and the results from CFD have a good agreement with the experimental data. At  $r/R = 0.60$  the experiment shows a lower normal force than both numerical results. This might indicate an anomaly at the blade surface or a measurement error.

For the design tip speed ratio  $\lambda = 6.67$ , CFD consistently overpredicts the normal force along the blade, whereas BEM underpredicts the normal force in the root region ( $r/R = 0.25 \sim 0.35$ ) and overpredicts the force between  $r/R = 0.60$  and  $r/R = 0.82$ . Near the tip, closer agreement with the experimental results is obtained with BEM code. Similar observation of overprediction by CFD computations can also be found in other work (Bechmann et al., 2011) (Scheepers et al., 2012). Again, overprediction in tangential force is observed at the inboard part of the blade for BEM code.

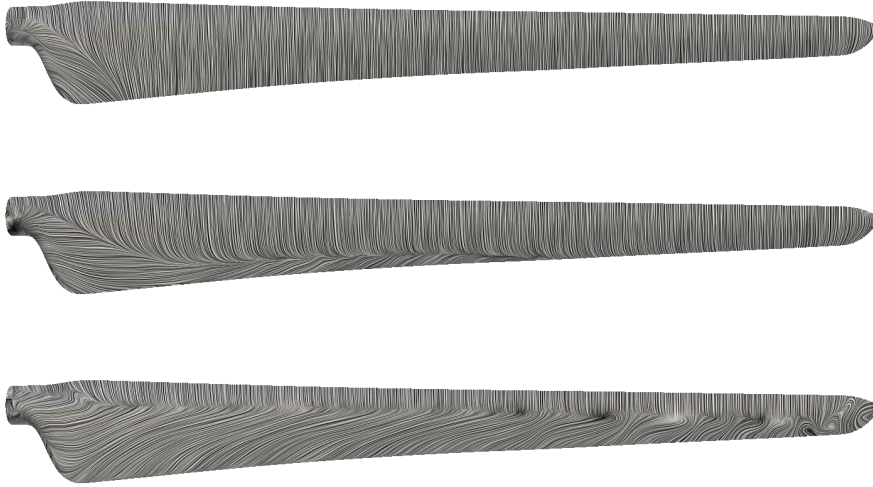
As the wind speed increases to  $24\text{ m/s}$ , the tip speed ratio becomes  $\lambda = 4.17$ . The flow over the entire blade becomes highly separated and unsteady. The loads comparison shows that the results from both models give only fairly good predictions. Tangential force along the blade is obviously overestimated by both codes. In addition, BEM overpredicts the blade tip normal force but significantly underpredicts the root normal force. On the other hand, CFD significantly overpredicts the normal force at the outboard part of the blade but shows a fair agreement with experiments at the inboard part of the blade. A possible explanation can be given in the following way: for a RANS approach with an eddy viscosity turbulence model, it is well known that it poorly resolves the highly unsteady flow. As a consequence, in the CFD simulation flow separation is delayed due to overestimating the eddy viscosity and thus a higher normal force is predicted. This can be clearly seen at the outboard part of the blade  $r/R = 0.82$  and  $r/R = 0.92$ . The detailed flow features on the blade suction surface are visualized in Figure 5.5 by means of limiting streamlines. Partially stalled and unsteady flow mainly occurs at the outboard part of the blade near  $r/R > 0.82$ , RANS approach is challenging for predicting this kind of flow accurately. Same observations can be found for NREL rotor CFD simulations in the work of (Duque et al., 2003).

#### 5.4.2. VELOCITY FIELD COMPARISON WITH PIV

In the MEXICO experiment, not only the aerodynamic loads on the rotor have been measured, but also the velocity field in the near wake has been obtained by means of a PIV technique. The velocity measurements in axial traverses are performed by using phase-locked PIV in the horizontal plane at the 9 o'clock position where the azimuth angle of blade 1 is  $0^\circ$ , see Figure 5.6. Thus, the near wake velocity deficit can be studied numerically and experimentally, by comparing the results.

Figure 5.7 shows the comparisons of numerical and experimental results for the axial velocity along the axial traverse at two positions: the mid-span position at  $r = 1.3769\text{ m}$  ( $r/R = 0.61$ ) and the outboard position at  $r = 1.8479\text{ m}$  ( $r/R = 0.82$ ). As expected, the wind speed decreases along the downstream direction due to transferring kinetic energy from the flow to the turbine rotor. At  $r/R = 0.61$ , the measured velocity shows strong oscillations near the rotor plane at the wind speeds  $15\text{ m/s}$  and  $24\text{ m/s}$ , which can be contributed to either the strong trailing vortex shedding at the mid-span  $x/R = 0.55$  (see Section 4.3.1) or laser reflection in the experiment.

When the measured position moves towards the outboard position near the tip  $r/R =$



5

Figure 5.5: Limiting streamline visualization on the suction side of the MEXICO blades with  $\lambda = 10.0, 6.67$  and  $4.17$ , which corresponds to incoming wind speed  $U_\infty = 10\text{ m/s}, 15\text{ m/s}$  and  $24\text{ m/s}$ , respectively.

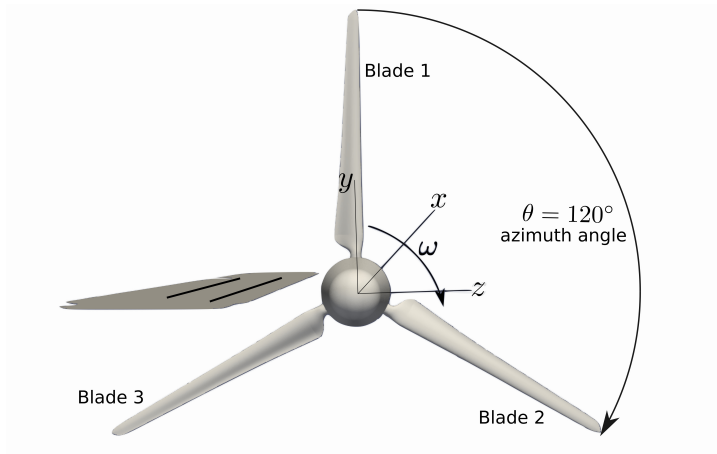


Figure 5.6: Schematic of the measured locations by PIV in the horizontal plane at 9 o'clock, azimuth angle  $\theta = 270^\circ$ . The azimuth angle is  $0^\circ$  when the blade 1 is vertically oriented upwards. The axial velocity traverse is measured at two radial locations  $r/R = 0.61$  and  $r/R = 0.82$ . The radius of this rotor is  $2.25\text{ m}$ .

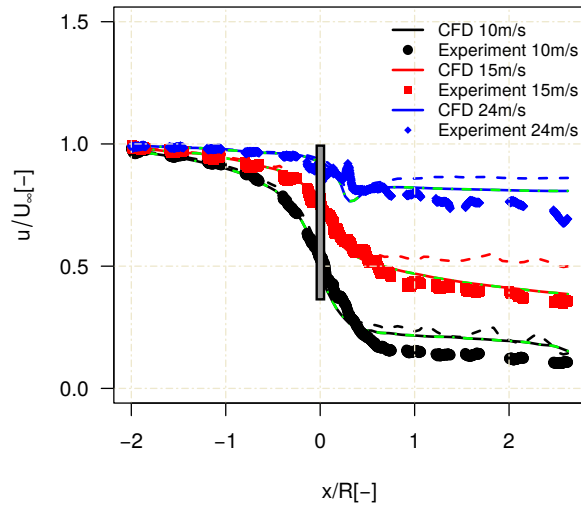
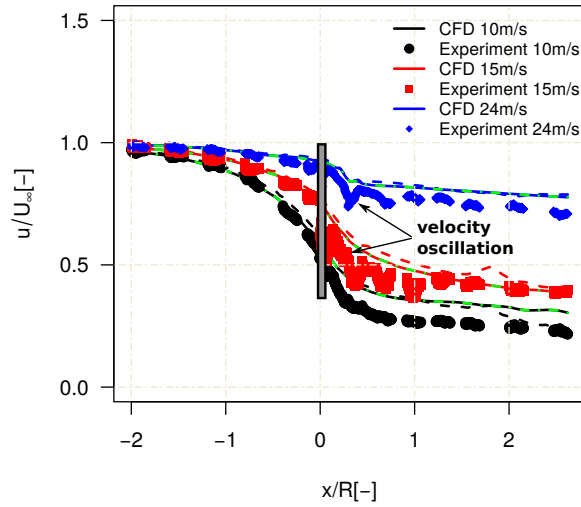


Figure 5.7: Axial velocity component  $u$  along the axial traverse at the mid-span ( $r/R = 0.61$ ) and the outboard positions ( $r/R = 0.82$ ). The grey box at  $x/R = 0$  indicates the location of rotor plane, dashed line represents the numerical results with coarse near wake mesh, the dot dash line represents the results with medium near wake mesh, and solid line represents the numerical results with finest near wake mesh.

0.82, the experimental axial velocity oscillation seems to disappear. At  $U_\infty = 24\text{ m/s}$ , the axial velocity first decreases when the flow passes through the rotor plane, and then increases again because of tip vortex effects. At the wind speed  $U_\infty = 15\text{ m/s}$ , which is the design condition with  $\lambda = 6.67$ , a good agreement is observed between the measurement and the numerical results with a refined wake mesh for both positions. A grid independent solution is achieved for each case through mesh refinement, and the finest mesh significantly increases the solution accuracy. It seems that the condition with  $U_\infty = 15\text{ m/s}$  is more sensitive with the mesh resolution compared to other cases.

At off-design conditions, slightly higher axial velocities are predicted by CFD simulations. The deviation for heavily loaded wind turbine case with tip speed ratio  $\lambda = 10.0$  is much larger than with  $\lambda = 4.16$ . The reason can be found in the fact as the axial induction velocities are high for the case  $\lambda = 10.0$  when a turbulent wake state exists behind the rotor, resulting in unsteady, recirculating wake flow. This condition requires more advanced DES/LES simulation to resolve the small-scale turbulence to better match the experiment.

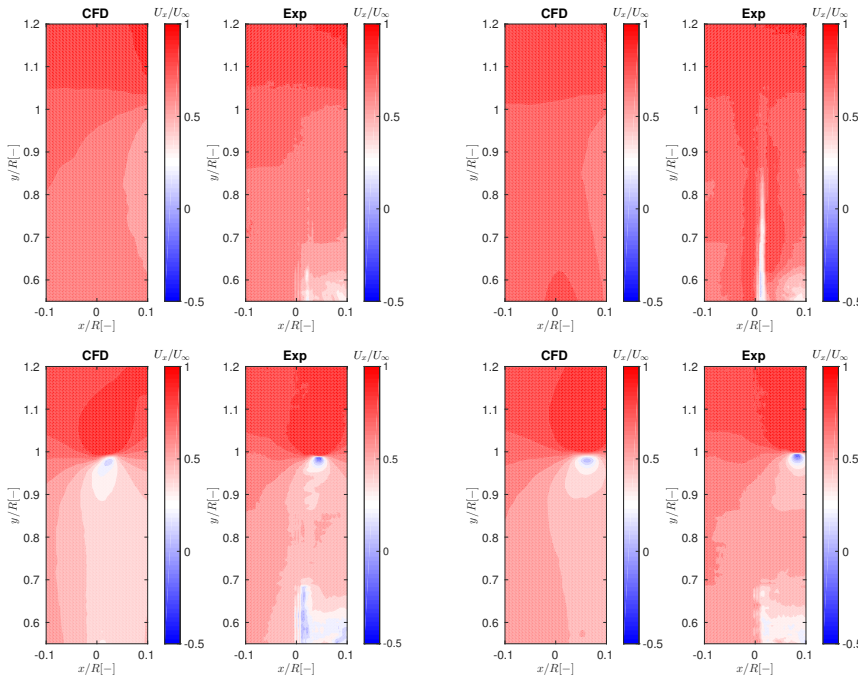


Figure 5.8: Comparison of axial velocity field surrounding the blade between CFD and phase locked PIV measurement at various azimuth angles  $\theta = 240^\circ, 260^\circ, 280^\circ, 300^\circ$  of blade 3 for the optimal tip speed ratio  $\lambda = 6.67$ . The velocity contours are normalized with free-stream velocity  $U_\infty$ .

The comparisons of axial velocity before and after blade passage for the numerical results and experimental PIV results are performed for axial flow condition at the optimal tip speed ratio  $\lambda = 6.67$ . There are provided in Figure 5.8. Before blade passage ( $240^\circ$  and  $260^\circ$ ), the axial velocity with downstream position, which is expected since the ro-

tor extracts energy from the flow. Similar velocity contour plots are obtained for both CFD and experiment. However, the mid-span region shows some discrepancies in the axial velocity distribution. Lower axial velocity can be observed in the experimental results, and this phenomenon becomes more prominent when the blade has just passed the measured plane for an azimuth angle  $\theta = 280^\circ$ . CFD results do not show this behavior and provide a smooth velocity distribution. (Micallef et al., 2013) also found these differences in his numerical investigation when using 3D unsteady potential flow panel code when comparing with the experiments. The reason is contributed to laser sheet reflection on the blade in the experiment (Schepers et al., 2012). The released tip vortex can be clearly seen just after blade passage. As can also be observed, CFD underestimates the tip vortex strength compared to the experiment. It should be noted that both from CFD and experiment, the tip vortex has an inboard motion before expanding to the radial location ( $y/R > 1.0$ ). The mechanism of tip vortex inboard motion is explained through the role of conservative radial force by (van Kuik et al., 2014). CFD successfully captures the expected inboard motion in this simulation. Meanwhile, the convection velocity of tip vortex traveling to the downstream seems to be underpredicted compared to the measured tip vortex positions.

5

#### 5.4.3. CROSSSECTIONAL ROTATIONAL EFFECTS

##### DETERMINATION OF ANGLE OF ATTACK ON ROTATING BLADE

The precise effective angle of attack (AoA) is challenging to acquire on a rotating blade, not only for wind tunnel measurement but also for numerical methods. (Guntur and Sørensen, 2014) evaluated several methods of determining the effective angle of attack on wind turbine blades. In this work, four techniques used for estimating AoA, including experimental methods (inverse BEM method when blade forces are predetermined or comparing pressure side  $C_p$  distribution), theoretical methods (BEM based method) as well as computational methods (extracting velocity from 3D CFD simulation), are compared quantitatively. It was concluded that all methods have a good agreement for the low angles of attack estimation. However, the inverse BEM method consistently estimates a lower AoA in the separated region, at the inboard and outboard sections. Two CFD methods, both averaging annular velocity at a given radial position and obtaining local velocity as a function of the azimuth, show good agreement through the whole range of AoAs.

Table 5.2: Incoming wind speeds and corresponding tip speed ratios of the computations

$U_\infty$ [m/s]	7.5	<b>10</b>	12	<b>15</b>	20	22	<b>24</b>
$\lambda$ [-]	13.3	<b>10</b>	8.3	<b>6.67</b>	5.0	4.5	<b>4.17</b>

In this study, the method proposed by (Hansen et al., 1997) is used to estimate the effective AoA. The idea of Hansen's method is to extract the velocity field from 3D CFD simulation and average the axial velocity in the annular plane at a given radial position. Thus the axial induction factor  $a$  at radial position  $r$  can be obtained. Then the effective angle of attack  $\alpha$  can be calculated as:

$$\alpha = \phi - \theta \quad (5.6)$$

$$\phi = \tan^{-1} \frac{(1-a)U_\infty}{(1+a')\Omega r} \quad (5.7)$$

where  $U_\infty$  is the free-stream velocity,  $\phi$  is the angle between the relative velocity and the rotor plane.  $\theta$  is the angle between the chord and the rotor plane. The tangential induction factor is neglected here  $a' = 0$ .

Several calculations are performed with different incoming velocities in order to obtain the sectional aerodynamic characteristics of rotating blades under a range of angles of attack. The velocity ranges from  $7.5 \text{ m/s}$  to  $24 \text{ m/s}$ . The rotational speed of the turbine is fixed at  $424.5 \text{ rpm}$ . Table 5.2 lists the computational cases with the incoming velocities and corresponding tip speed ratios (TSR). The bold font in Table 5.2 indicates configurations have been measured in the rotating MEXICO experiment.

#### $C_L - \alpha$ CURVE

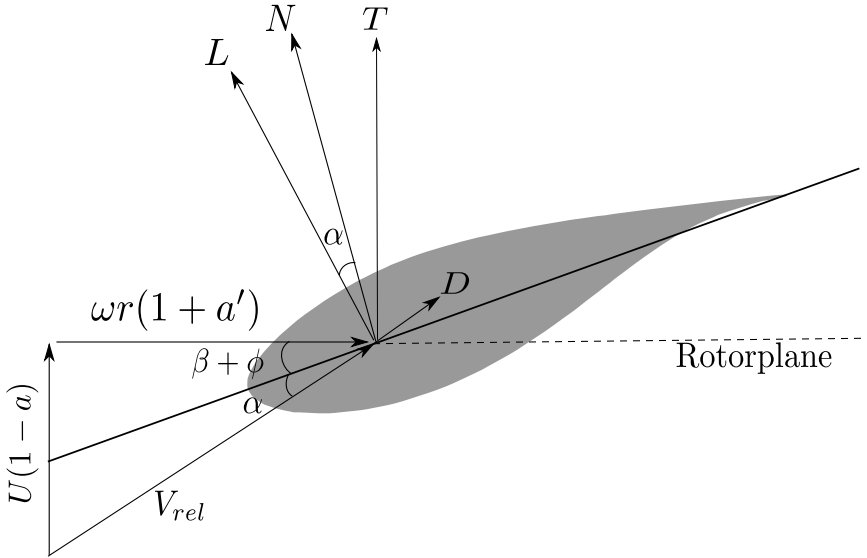


Figure 5.9: Local forces on a blade section and inflow angle  $\alpha$ , twist angle  $\beta$ , pitch angle  $\phi$

Figure 5.9 presents the definition of local forces and velocities on a blade section. The normal force  $N$  is perpendicular to the local chord line (the line through the leading edge and trailing edge). The local angle of attack  $\alpha$  are the angle between the relative velocity  $V_{rel}$  and the local chord line.  $a$  and  $a'$  are the axial and tangential induction factors, respectively.

First of all, the normal force coefficient  $C_N$  and tangential force coefficient  $C_T$  are obtained by integrating the surface pressure on both suction and pressure sides of sectional airfoil without considering the viscous force. Then the lift  $C_L$  and drag  $C_D$  forces



can be derived from the effective angle of attack as:

$$C_L = C_N \cos(\alpha) + C_T \sin(\alpha) \quad (5.8)$$

$$C_D = C_N \sin(\alpha) - C_T \cos(\alpha) \quad (5.9)$$

Figure 5.10 shows the comparison of sectional airfoil aerodynamic characteristics obtained from CFD results of the 3D rotating blade, experimental results of the 3D rotor, experimental results of the 3D static blade and experimental results of a 2D airfoil. There are aerodynamic characteristics on the  $0.35R$ , the  $0.60R$  and the  $0.92R$  blade sections from the non-rotating experiment. As can be seen in the root region ( $r/R = 0.25$  and  $r/R = 0.35$ ), all cases show almost identical results in the linear regime, indicating the flow over these airfoil sections is two dimensional. The result of the 3D static blade in Figure 5.10 (b) presents the same lift slope as the 2D airfoil experimental data, despite the slight difference in  $Re$  number for the two cases. When the effective angle of attack is larger than  $9^\circ$ , significant differences are observed among these cases. Both the results of the 3D CFD and the experiment on the rotating blade show much larger  $C_L$  compared to 2D airfoil data as well as 3D static blade measurement. This phenomenon is known as rotational augmentation or stall delay due to rotational effects. The mechanism of rotational augmentation can be explained as follows: due to blade rotation, the centrifugal force acting on the fluid in the boundary layer pushes the air from the root to the tip, resulting in a radial flow. The Coriolis force determined by the rotation and the radial velocity field (see Eq. 5.5) provides a chordwise direction pressure gradient on the airfoil from leading edge to trailing edge, which thins the boundary layer thickness and delays the flow separation. Meanwhile, the pressure on the upper side has more suction, resulting in lift enhancement. More detailed study of these rotational effects will be discussed afterward. CFD simulation successfully captures this trend of lift enhancement quite well at  $r/R = 0.25$ . The lift coefficient is enhanced up to 1.9 at  $\alpha \approx 26^\circ$ . In terms of the comparison at  $r/R = 0.35$ , CFD overpredicts the measured  $C_L$  at the wind speed  $\alpha = 22^\circ$ . It can also be clearly seen from 2D, and 3D rotating comparison that rotational effect plays a less important role in lift enhancement compared to the section  $r/R = 0.25$  but is still significant. Note that 3D static blade experimental data shows lower sectional  $C_L$  than true 2D measurements at large angles of attack, which seems to indicate that only rotational effects are responsible for lift enhancement in 3D rotating blade case, while 3D local blade geometry has no contribution in lift increase.

Near the blade tip region  $r/R = 0.82$  and  $r/R = 0.92$ , 3D rotating blade experiment shows consistently lower  $C_L$  than 2D case, which is as expected because of the tip vortex effects. The more  $C_L$  reduction can be observed for the same wind speed when moving outwards, where a stronger tip vortex effect exists. Current RANS simulations overpredict  $C_L$  for these two sections at high wind speed. The probable reason, as discussed in the previous chapter, is that RANS simulation does not take the relatively thick ZigZag into account. For the 3D static blade situation, there is also a tip vortex leaving the blade. Interestingly, 3D rotating blade experiment and 3D static blade present almost identical  $C_L$  in the linear region for  $r/R = 0.92$ , although  $C_L$  is influenced by tip vortex releasing from different status of blades, which might indicate that the tip vortex effect on  $C_L$  reduction is similar at low wind speed, no matter the blade is stationary or rotating. However, experimental data of 3D rotating blade shows more  $C_L$  reduction compared to

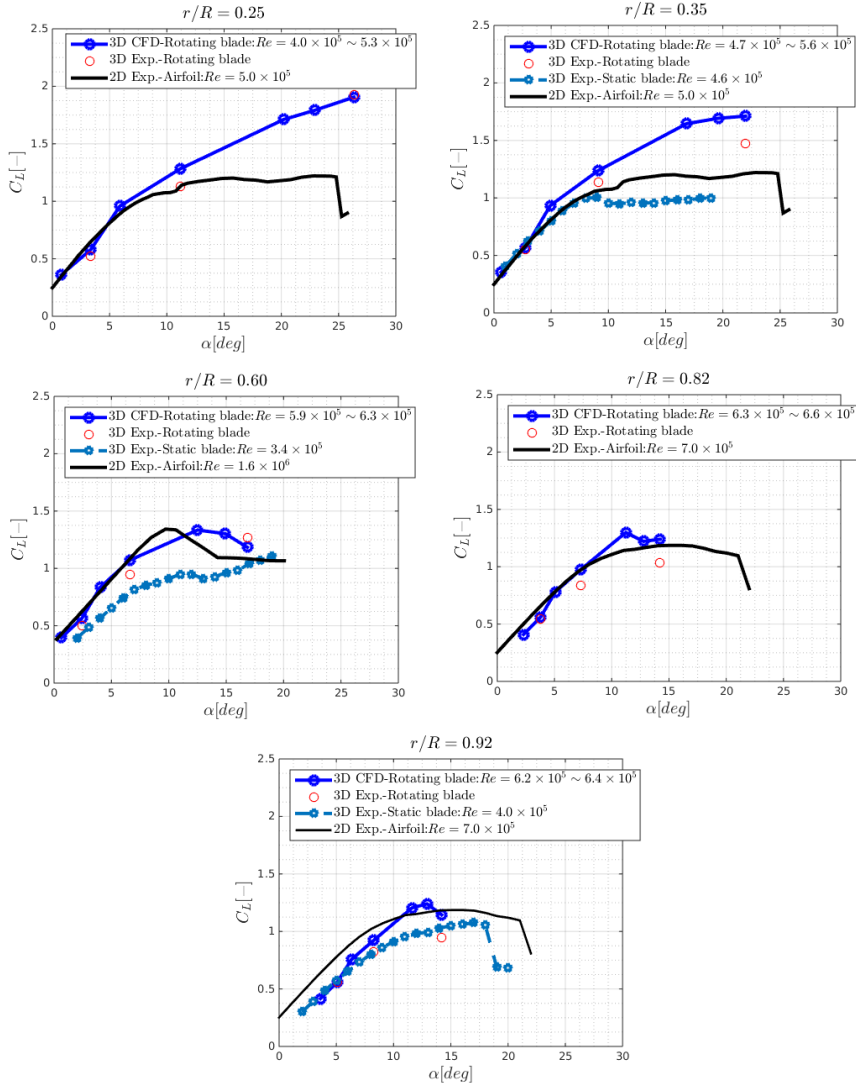


Figure 5.10: The comparisons of sectional lift polar  $C_L - \alpha$  between experimental measurements of 3D rotating blade, non-rotating blade, 2D airfoil and CFD numerical prediction of 3D rotating blade. The sections are located at 0.25R, 0.35R, 0.60R, 0.82R and 0.92R radial positions.

the 3D static blade at the higher angle of attack, which means at high wind speed the tip vortex releasing from rotating blade has a stronger effect on  $C_L$  than the stationary blade.

#### $C_D - \alpha$ CURVE

The comparisons of pressure drag for the 3D rotating blade, 3D static blade, and 2D airfoil are plotted in Figure 5.11. At  $r/R = 0.25$ , 3D rotating blade experiment shows lower  $C_D$  than 2D airfoil case. 3D CFD simulation overestimates the 3D experimental drag force except for the highest angle of attack  $\alpha \approx 26^\circ$ . 3D CFD shows almost the same  $C_D$  as 2D airfoil case in the linear region but underestimates the drag at the maximum angle of attack. At  $r/R = 0.35$ , 3D CFD shows good agreement with experimental measurements with only slightly higher  $C_D$  at  $\alpha \approx 22^\circ$ . Additionally, the pressure drag on the 3D rotating blade is almost the same as 2D airfoil wind tunnel measurement at this section. However, the 3D static blade consistently shows a larger  $C_D$  compared to other cases.

At  $r/R = 0.60$ , there are apparent differences in  $C_D$  between 2D airfoil wind tunnel measurements and 3D rotating and static blade cases, even at a low angle of attack ( $\alpha < 10^\circ$ ). An interpretation can be that  $Re$  number has a large impact on  $C_D$  for this airfoil profile. For 3D case, the  $Re$  number is only around  $5.0 \times 10^5$ , however 2D case the  $Re$  number 2 times is larger. Unfortunately, only 2D wind tunnel measurements with  $Re = 1.6 \times 10^6$  are available to compare. With similar  $Re$  numbers,  $C_D$  at  $0.60R$  on 3D rotating blade show more or less the same results as 3D static blade before  $\alpha < 10^\circ$ . 3D CFD simulation predicts the drag force quite well compared with rotating experimental data.

Near the tip region  $r/R = 0.82$  and  $r/R = 0.92$ , CFD simulation shows a good agreement with measured  $C_D$  on rotating blade. Only at the highest angle of attack, slightly lower  $C_D$  is predicted by CFD. As expected, 3D cases present consistent higher  $C_D$  compared to the 2D case due to tip vortex effect. Moreover, similar behavior is observed as in  $C_L$  at  $r/R = 0.92$  section, that  $C_D$  on the 3D rotation blade is the same as the one on the 3D static blade. A bit lower  $C_D$  is obtained on rotating blade than the drag force on the stationary blade.

#### PRESSURE DISTRIBUTION AT THE INBOARD PART OF THE BLADE

Figure 5.12 and 5.13 shows the sectional pressure distribution comparison between 3D CFD simulation, experimental results on rotating blade and 2D airfoil data at the inboard part of the blade, at  $r/R = 0.25$  and  $0.35$  respectively. Overall speaking, CFD simulation predicts the pressure distribution quite well compared against 3D experiment measurements, except for the location  $r/R = 0.25$  with  $\lambda = 6.67$ , where a good agreement is found between 3D CFD and 2D experiment. For this condition, many pressure sensors are not reliable and do not show realistic pressure value, which has already been pointed out in the final project report (Schepers et al., 2012) and in comparison with other CFD results (Bechmann et al., 2011). The obvious difference between 3D CFD and 2D airfoil can be observed near the trailing edge on the suction side. The 2D  $C_p$  distribution reveals that the flow separates after  $x/c = 0.65$  with constant pressure. However, the  $C_p$  curve of CFD simulation indicates that the flow is still attached over the whole suction surface, which may be contributed to rotational augmentation resulting in favorable pressure gradient. Thus, the flow can overcome the adverse pressure gradient and stay attached. When the  $\lambda$  is 4.17, the effective angle is around  $26^\circ$  at  $r/R = 0.25$ .

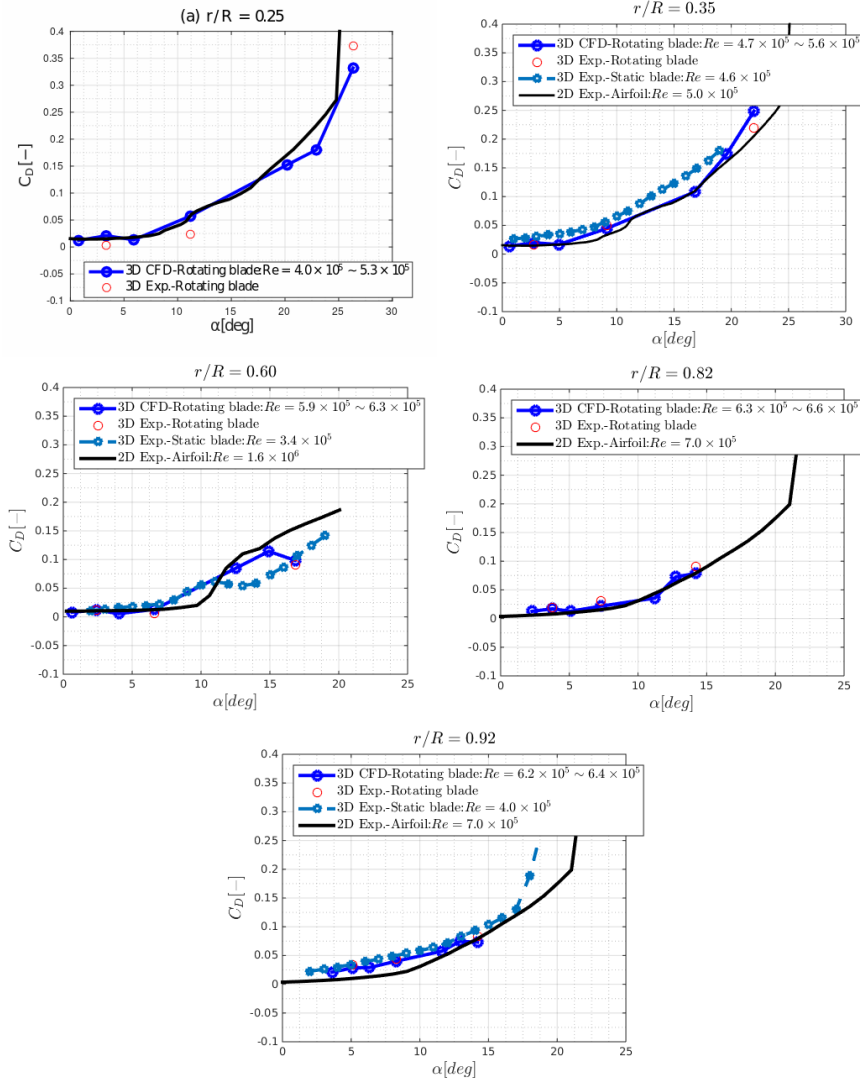


Figure 5.11: The comparisons of sectional lift polar  $C_D - \alpha$  between experimental measurements of 3D rotating blade, non-rotating blade, 2D airfoil and CFD numerical prediction of 3D rotating blade. The sections are located at 0.25R, 0.35R, 0.60R, 0.82R and 0.92R radial positions.

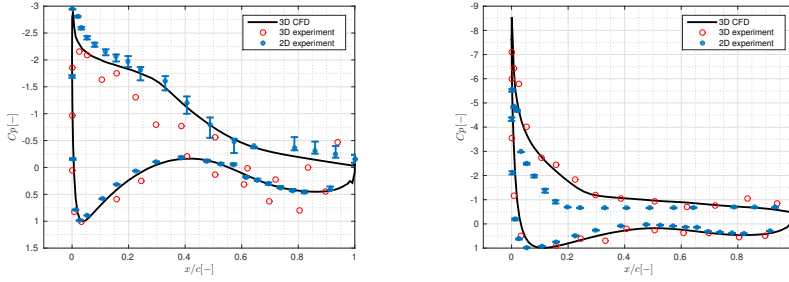


Figure 5.12: Comparison of pressure coefficient  $C_p$  distribution between 3D CFD simulation, experiment on the rotating blade and static 2D airfoil wind tunnel measurement at  $r/R = 0.25$  section with  $\lambda = 6.67$  and  $4.17$ . Estimated local angle of attack  $\alpha \approx 11^\circ$  (left) and  $\alpha \approx 26^\circ$  (right). The 2D airfoil data with upper/lower bar represents the measured results with  $\pm 1^\circ$   $\alpha$  difference.

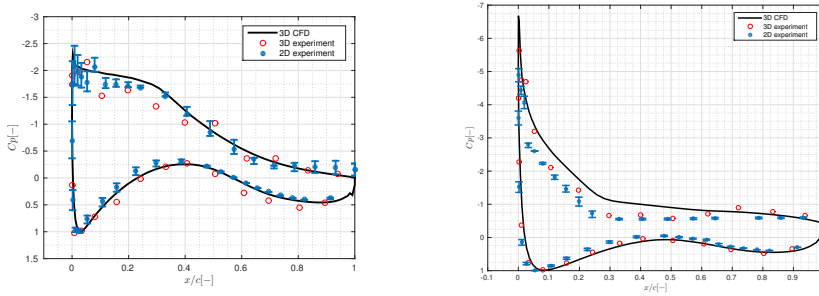


Figure 5.13: Comparison of pressure coefficient  $C_p$  between 3D CFD, experiment on the rotating blade and static 2D airfoil wind tunnel measurement at  $r/R = 0.35$  with  $\lambda = 6.67$  and  $4.17$ . Estimated local angle of attack  $\alpha \approx 9^\circ$  (left) and  $\alpha \approx 22^\circ$  (right). The 2D airfoil data with upper/lower bar represents the measured results with  $\pm 1^\circ$   $\alpha$  difference.

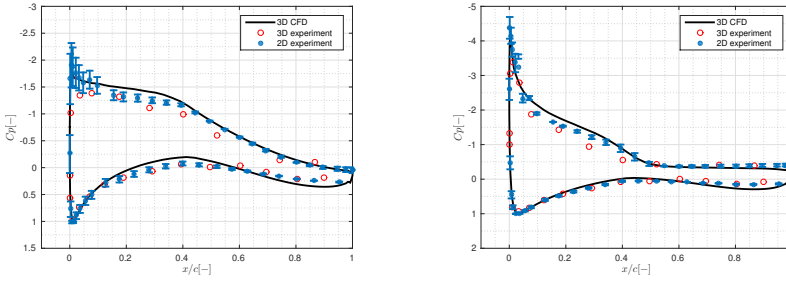


Figure 5.14: Comparison of pressure coefficient  $C_p$  between 3D CFD simulation, experiment on the rotating blade and static 2D airfoil wind tunnel measurement at  $r/R = 0.82$  with  $\lambda = 6.67$  and  $4.17$ . Estimated local angle of attack  $\alpha \approx 7^\circ$  (left) and  $\alpha \approx 14^\circ$  (right). The 2D airfoil data with upper/lower bar represents the measured results with  $\pm 1^\circ$   $\alpha$  difference.

CFD predicts a perfect  $C_p$  distribution as can be observed when compared with the 3D experiment. Moreover, 3D rotating results present significantly more negative pressure than 2D static airfoil on the suction side, while slightly higher positive pressure on the pressure side. This difference is to a large extent explained by the rotational effects of the blade. At this effective angle of attack, the 2D airfoil is in the deep stall since the flow becomes fully separated near  $x/c = 0.30$ .

At  $r/R = 0.35$  with  $\lambda = 6.67$ , the comparison between 3D CFD and 3D experiment shows a fair agreement. A better agreement can be found on the pressure side, while larger deviation appears on the suction side. Similar behavior is observed as  $r/R = 0.25$  at this specific tip speed ratio, that on the suction side ( $x/c = 0.1 \sim 0.4$ ) 3D experimental pressure presents unexpected higher value than 3D CFD result and 2D experimental data. To be noted is that near the trailing edge on the suction side, 2D static airfoil pressure has a lower value than the 3D rotating case. At  $\lambda = 4.17$ , the effective angle of attack at  $r/R = 0.35$  section is estimated as  $22^\circ$ . Apparently, 3D CFD under predicts the pressure on the most part of the suction side. As expected at  $r/R = 0.35$ , rotational effects play a less important role in pressure decrease on the suction surface. Therefore, almost identical pressure distribution can be seen between 3D rotating experiment and 2D static airfoil data. Only a slightly larger suction peak is seen near the leading edge.

#### PRESSURE DISTRIBUTION AT THE OUTBOARD PART OF THE BLADE

As the spanwise location moves outward, where  $r/R = 0.82$  and  $0.92$ , three-dimensional flow on the blade driven by tip vortex effect becomes significant. For  $\lambda = 6.67$ , the main impact of tip vortex on  $C_p$  curve is less suction pressure on rotating blade suction side compared to 2D static airfoil suction side. Especially 2D data shows a higher suction peak at the leading edge, while no big difference exists on the pressure side. It can also be clearly seen from the suction side pressure difference between 2D and 3D experimental data at  $r/R = 0.92$ , that the tip vortex effect becomes larger and stronger compared to  $r/R = 0.82$  as expected. Furthermore, it seems that 3D CFD simulation does not capture the rotating flow near the blade tip as accurate as the measured data since a better agreement between 3D CFD simulation and 2D static airfoil can be found in both plots.

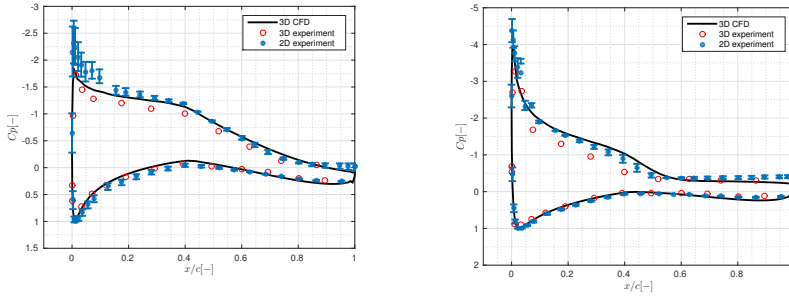


Figure 5.15: Comparison of pressure coefficient  $C_p$  between 3D CFD simulation, experiment on the rotating blade and static 2D airfoil wind tunnel measurement at  $r/R = 0.92$  with  $\lambda = 6.67$  and  $4.17$ . Estimated local angle of attack  $\alpha \approx 8^\circ$  (left) and b)  $\alpha \approx 14^\circ$  (right). The 2D airfoil data with upper/lower bar represents the measured results with  $\pm 1^\circ$   $\alpha$  difference.

## 5

Consequently, the aerodynamic loads of  $C_L$  and  $F_N$  on the blade tip are overpredicted by CFD, also can be seen in Figures 5.10 and 5.4. Only near the very leading edge 3D CFD simulation presents "correct" rotation modeling, where has less pressure suction compared to the 2D static airfoil.

When the tip speed ratio is  $4.17$  (with wind speed  $24\text{ m/s}$ ), a similar behavior is observed. However, the position influenced most by the tip vortex on the suction side is shifted a bit further away from the leading edge, meaning the largest difference between 3D rotating experiment and 2D static airfoil are observed at  $x/c \approx 0.1 \sim 0.4$ . Whereas with  $\lambda = 6.67$ , the difference ranges from  $x/c = 0.1$  to  $x/c = 0.4$ .

### 5.4.4. RADIAL FLOW AND CORIOLIS FORCE

Radial (spanwise) flow in the boundary layer has been known to play a significant role in stall delay. Radial flow alters the stalling characteristics of an airfoil section (Himmelskamp, 1945) (Harris, 1966). The spanwise "pumping" effects due to centrifugal force field push the air flow from the root to the tip. Figure 5.16a shows the radial flow field normalized by the freestream velocity at  $r/R = 0.25$  section. Strong radial flow is seen at the suction side near the trailing edge separation area, whereas no strong radial flow is observed at the pressure side. Figure 5.16b and 5.16c present the distribution of Coriolis force components in  $x$  and  $y$  directions, respectively. The Coriolis force in  $x$ -direction provides a positive force acting on the flow from the leading edge to the trailing edge, which can counter act the adverse pressure gradient and delay flow separation.

As the radial position moves towards larger locations  $r/R = 0.35$ , the effect of the Coriolis force on the airfoil properties decreases. On the suction side of this airfoil section, a smaller area of radial flow exists compared to  $r/R = 0.25$  section, as can be seen in Figure 5.16a. Also, a much weaker radial flow velocity appears than at the  $r/R = 0.25$  section.

#### THE PRESSURE GRADIENT FIELD

Not only Coriolis force has a large effect on stall delay, (Dwyer and Aiccroscopy, 1971), (Lindenbarg, 2004) and (Herráez et al., 2016) point out that the radial pressure gradient

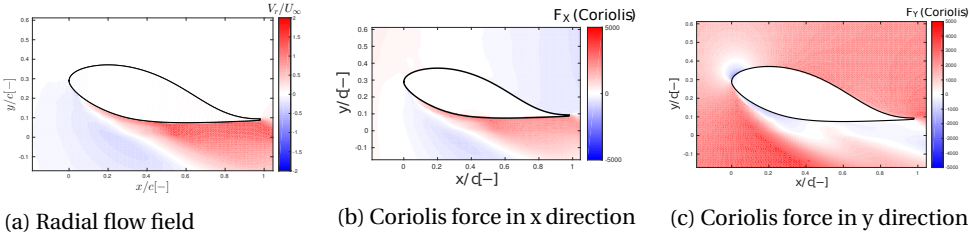


Figure 5.16: Normalized radial flow field distribution at  $r/R = 0.25$  section and corresponding Coriolis force components in x and y directions,  $\lambda = 4.17$ .

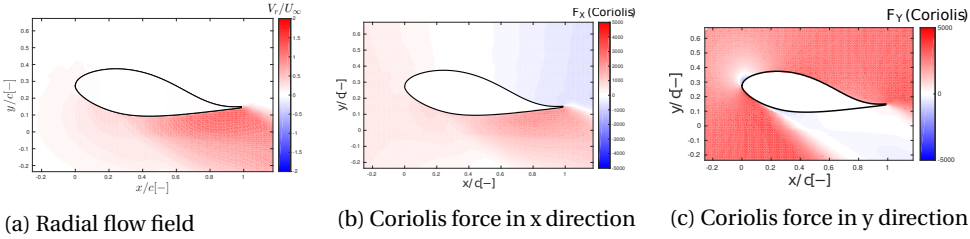


Figure 5.17: Normalized radial flow field distribution at  $r/R = 0.35$  section and corresponding Coriolis force components in x and y directions,  $\lambda = 4.17$ .

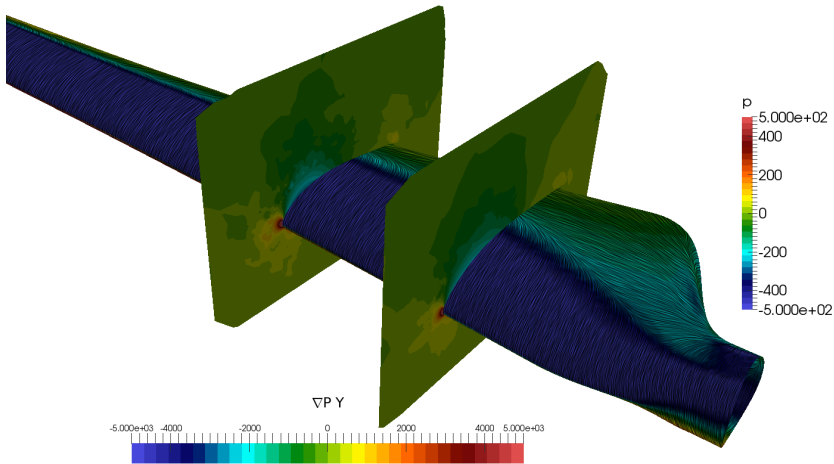
also has a significant influence on the stall delay. The contribution of the radial pressure gradient to the radial flow can be observed from the governing equations in azimuthal and radial directions, see Equations 5.10 and 5.11.

$$\frac{\partial C_p}{r \partial \theta} = \frac{4\sqrt{2}}{r(1 + (\frac{R}{\lambda r})^2)} \quad (5.10)$$

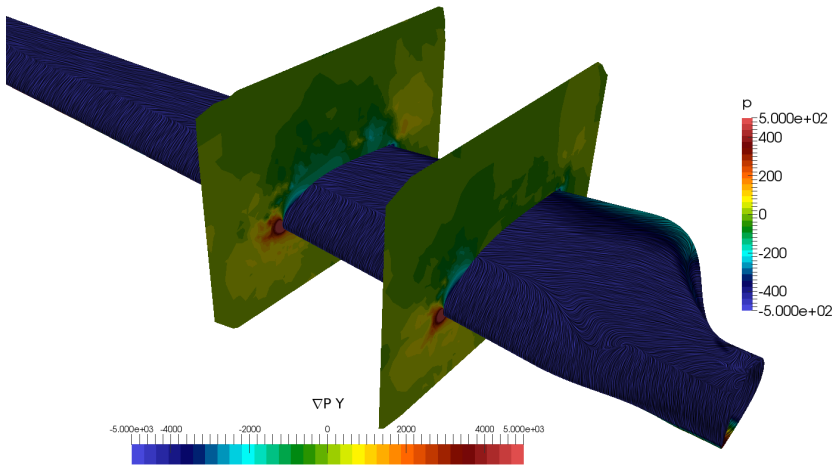
$$\frac{v_r \partial v_r}{\partial r} = r\Omega^2 - \frac{\partial p}{\rho \partial r} \quad (5.11)$$

Figure 5.18 presents the radial pressure gradient distribution at  $0.25R$  and  $0.35R$  sections for two tip speed ratios,  $\lambda = 6.67$  and  $4.17$  respectively. In addition, the oil flow visualization is indicated by wall shear stress with the line integral convolution technique, see (Cabral and Leedom, 1993). From the visualized oil flow, the separation line on the blade suction side can be clearly identified. For the attached flow case with  $\lambda = 6.67$ , the flow with positive radial pressure gradient presents at the leading edge of airfoil sections, whereas most of the flow over airfoil suction surface has negative radial pressure gradient. The negative radial pressure gradient results in positive radial force induced by the pressure derivation acting on the flow. It seems that only the streamwise attached flow near the blade surface undergoes negative radial pressure gradient, as indicating by the oil flow visualization. However, near the trailing edge the attached flow changes orientation from streamwise flow to radial flow, and no apparent negative radial pressure gradient is observed.





(a)  $\lambda = 6.6$ ,  $U_\infty = 15 \text{ m/s}$



(b)  $\lambda = 4.17$ ,  $U_\infty = 24 \text{ m/s}$

Figure 5.18: Radial pressure gradient field distribution at  $r/R = 0.25$  and  $r/R = 0.35$ . Oil flow visualization on the blade surface is also indicated by the wall shear stress with the line integral convolution technique (Cabral and Leedom, 1993)

Similarly, at  $\lambda = 4.7$ , much stronger positive radial pressure gradient exists near the leading edge of airfoil sections at higher wind speed. In the attached flow region, a larger negative radial pressure gradient is found near the blade surface than with  $\lambda = 6.67$ . This indicates that the force due to pressure, driving flow in the turbulent boundary layer radially to the tip at low tip speed ratio is much larger than  $\lambda = 6.67$ . Interestingly to note there are distinct differences in the separated flow region. No apparent radial pressure gradient driving force is observed in the fully separated flow at  $r/R = 0.25$  section. However, at  $r/R = 0.35$  section, the separated flow with a certain degree of the negative radial pressure gradient is present.

#### VORTICITY TRANSPORT

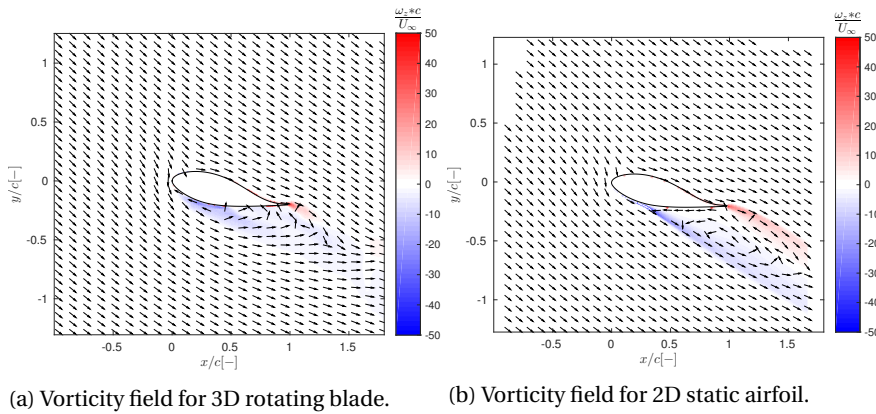


Figure 5.19: Vorticity field comparison between 25%R sectional airfoil of 3D rotating blade and 2D static airfoil at same  $\alpha$  and Reynolds number,  $\lambda = 4.17$ ,  $\alpha = 26^\circ$  and  $Re = 5.0 \times 10^5$ .

Following a similar approach to (Lee and Wu, 2013) in their experimental study of stall delay on vorticity transport on rotating blade, the difference of flow behavior between the 3D rotating blade and 2D airfoil is compared in Figure 5.19. The vorticity field is overlapped with velocity vectors. The relative velocity in the rotating reference frame is used for the 3D rotating case. Distinct differences between the two cases can be observed: First, the recirculation bubble near the trailing edge of the 3D rotating blade is smaller than 2D static airfoil, which indicates that the shed vortex is stabilized and separation bubble is limited due to rotational effects. More importantly, it seems that there is a small leading edge vortex appearing between  $x/c = 0 \sim 0.30$  on the rotating blade suction side. Second, both positive and negative vorticity seems to be transported less far than for the 2D airfoil. After  $1.5c$  downstream location, the vorticity is more or less absent. However, for 2D airfoil case, it can still clearly see the vorticity, extending to the downstream location more than  $1.5c$ . The possible causes of this vorticity transport phenomenon could be contributed to either rotational effects or slightly different mesh resolution for the two cases.

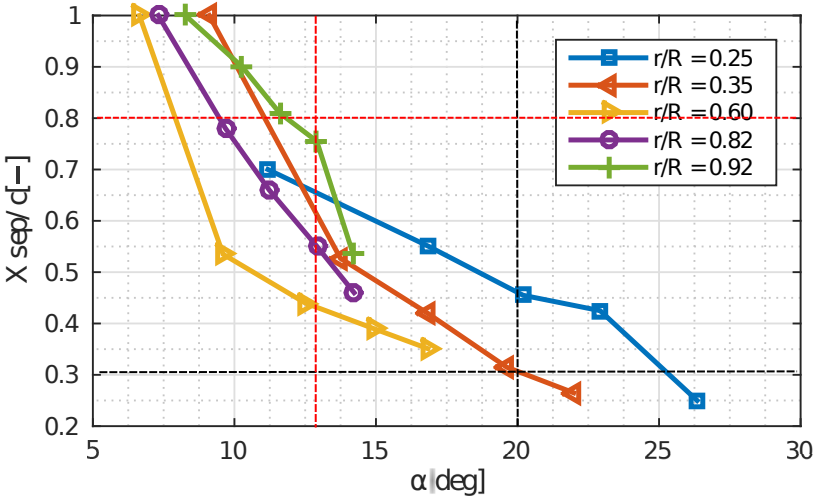


Figure 5.20: The positions of separation point on the suction side of rotating blade at different radial locations.

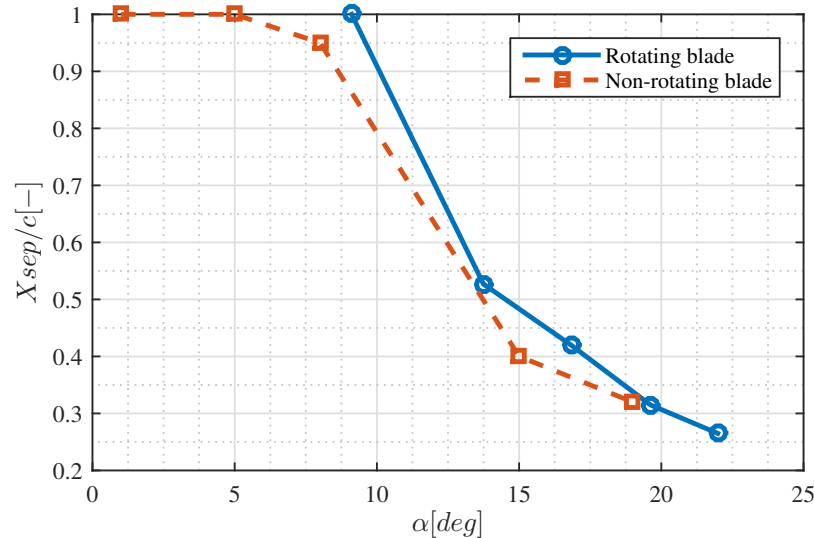


Figure 5.21: Comparison of separation point positions at 35% $R$  radial location on the suction side between rotating and non-rotating blades.

## LOCATION OF SEPARATION POINT

To investigate the rotational effects on flow separation, (Sicot et al., 2008) proposed a method to determine the separation point on the rotating blade by the measured chord-wise pressure gradient in the separated area in his experiment. In CFD simulations, more detailed flow features are acquired such that the separation point can be determined by the local skin friction:

$$Cf_x = \mu \frac{\partial u_x}{\partial y} / \frac{1}{2} \rho (U_\infty^2 + (\omega r)^2) = 0 \quad (5.12)$$

$$Cf_z = \mu \frac{\partial u_z}{\partial y} / \frac{1}{2} \rho (U_\infty^2 + (\omega r)^2) = 0 \quad (5.13)$$

Figure 5.20 compares the positions of separation point versus angles of attack at five radial locations on the rotating blade. For the DU airfoil at 25%R and 35%R sections, the comparisons indicate that separation is delayed due to rotational effects when the section is closer to the inboard part of the blade. The other observation is that when the sectional angle of attack becomes larger, the rotational effects play a more important role in delaying separation, resulting in an increased difference between separation lines for 25%R and 35%R. For the NACA airfoil at 82%R and 92%R, the positions of separation point are postponed again, but now on the sections which are closer to the outboard part of the blade. Meanwhile, when  $\alpha > 13^\circ$ , the postponed separation effect becomes smaller. The different observations of separation point positions can be explained by different flow features. For the root region, the rotational effects play an important and dominant role. However, for the tip region, the rotational effects play no role, but here the three-dimensional effects induced by tip vortex contribute the observed behavior.

Figure 5.21 further illustrates the comparison of separation point between rotating blade and non-rotating blade by using 35%R section data. Slight separation delay is observed on the rotating blade. At the same angle of attack, the positions of separation point seem to occur near the trailing edge due to blade rotation.

## 5.4.5. TRANSITIONAL EFFECTS

In Section 5.4.1, the aerodynamic loads comparisons between numerical predictions (CFD and BEM) and experimental measurements showed that CFD only has fair agreement at  $\lambda = 6.67$ , especially at very tip locations  $r/R = 0.82$  and  $0.92$ . The possible reason analyzed in Section 4.3.2 is due to the presence of a relative thick ZigZag tape at the tip in the measurement, while the CFD calculations do not take this effects into account. Therefore, it is suggested in Chapter 4 that transitional flow simulation is more appropriate and necessary to compare with experimental measurement. In this section, first, the transitional effects on the aerodynamic loads are discussed at  $\lambda = 6.67$ . The numerical predictions considering transitional flow is compared with the new MEXICO experiment which eventually acquires the aerodynamic loads on the blade with a clean configuration. Finally, the transitional lines are identified on the blade surface, and the tip speed ratio effects on the transition onset are shown.

Figures 5.22 and 5.23 compare the sectional normal and tangential force distribution between *corrected*  $kk\Omega$  and fully turbulent  $k-\omega$  SST of CFD calculations. It is shown that both  $F_N$  and  $F_T$  with considering boundary layer transition are higher than

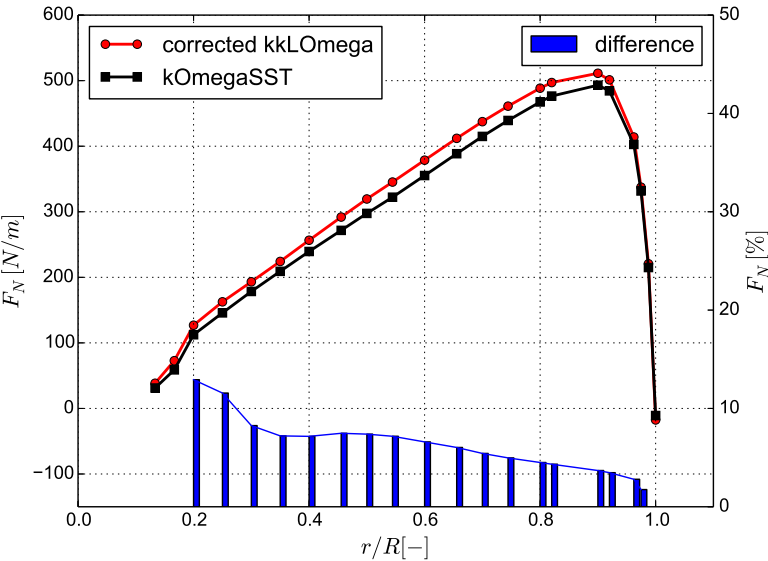


Figure 5.22: Transitional effects on normal force along the blade at optimal tip speed ratio  $\lambda = 6.67$ . The blue bar indicates the relative difference between two predictions.

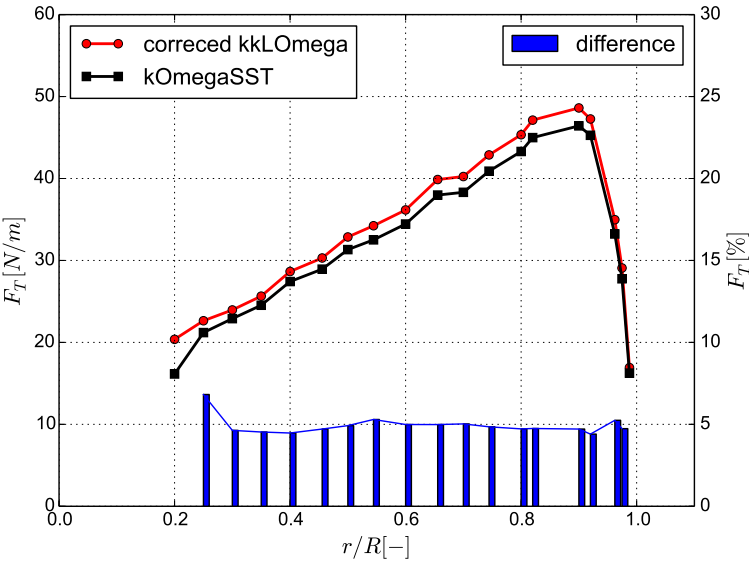


Figure 5.23: Transitional effects on tangential force along the blade at optimal tip speed ratio  $\lambda = 6.67$ . The blue bar indicates the relative difference between two predictions.

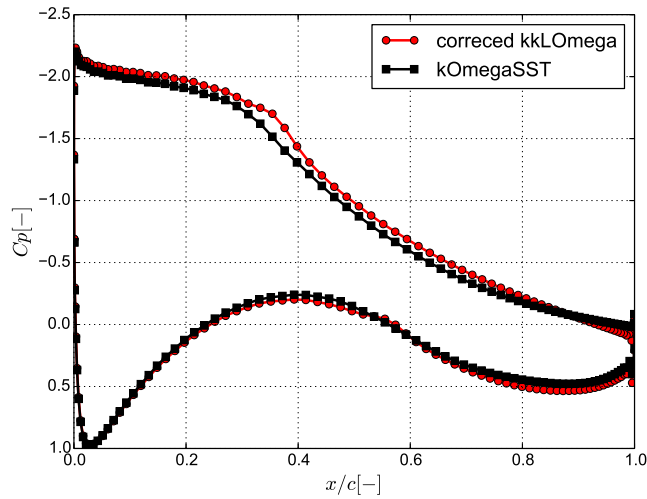


Figure 5.24:  $C_p$  comparison between fully turbulent and transitional flow at  $r/R = 0.35$  radial section

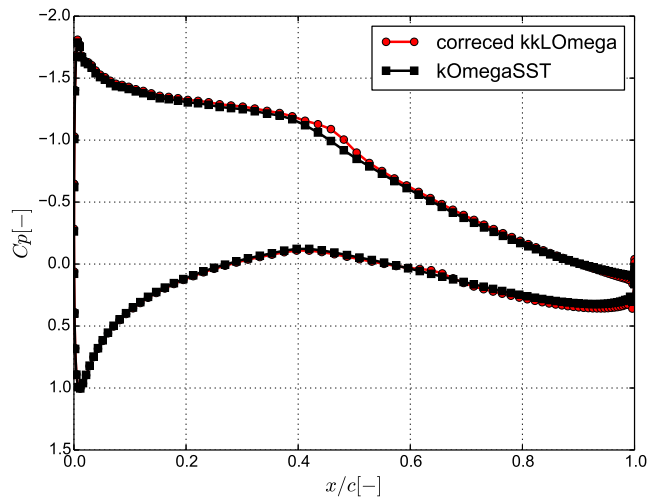


Figure 5.25:  $C_p$  comparison between fully turbulent and transitional flow at  $r/R = 0.92$  radial section

for the fully turbulent results. To quantify the difference in the forces, the relative difference is defined as  $\frac{F_{transition} - F_{turbulent}}{F_{turbulent}}$ . The relative difference in normal force is decreasing towards the tip, which also indicates that transition has more influence at the inboard part of the blade. Approximate 5% tangential force difference is observed for all the sections on the blade. These observations are expected since in general more suction can be obtained on the upper surface when part of flow over airfoil is laminar. Figures 5.24 and 5.25 show more detailed information of sectional pressure distribution at  $r/R = 0.35$  and  $r/R = 0.92$  radial positions. Indeed, the main difference can be seen on the suction side.

#### CFD COMPARISON WITH NEW MEXICO EXPERIMENT

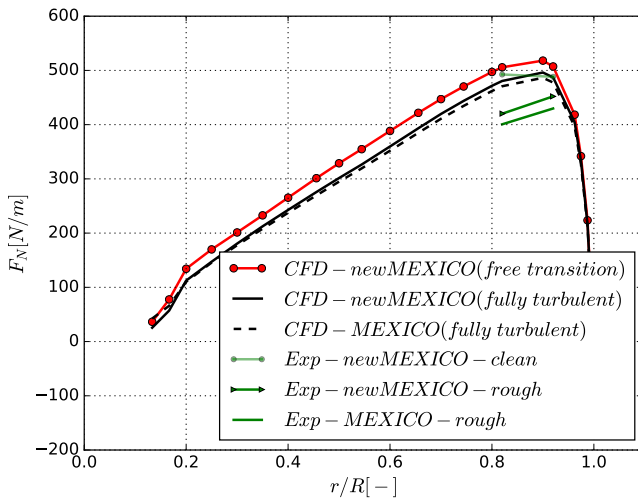


Figure 5.26: Comparison of normal force distribution along the blade between numerical predictions and experimental measurements. Three different experimental conditions are MEXICO rough ( $U_\infty = 14.93 \text{ m/s}$ ,  $n = 424.5 \text{ rpm}$ ,  $\rho = 1.246 \text{ kg/m}^3$ ), new MEXICO clean ( $U_\infty = 15.03 \text{ m/s}$ ,  $n = 425.1 \text{ rpm}$ ,  $\rho = 1.191 \text{ kg/m}^3$ ) and new MEXICO rough ( $U_\infty = 14.86 \text{ m/s}$ ,  $n = 425.1 \text{ rpm}$ ,  $\rho = 1.20 \text{ kg/m}^3$ ).

Figure 5.26 compares the aerodynamic loads between the CFD transitional case, fully turbulent case, MEXICO experiment and new MEXICO experiment. In the new MEXICO experiment, both configurations with and without ZigZag tape are measured, while in the MEXICO experiment only rough blade is measured. It can be clearly seen there are some differences in the normal force  $F_N$  between the first phase MEXICO experiment and the second phase new MEXICO experiment. Consistently higher normal force  $F_N$  is observed at  $r/R = 0.82$  and  $0.92$ . These differences mostly could be attributed to the improved calibration in the new MEXICO experiment. A significant normal force increase is observed at sections of the clean tip compared to the rough tip, which further demonstrates that the ZigZag tape plays a significant role in affecting the tip loads.

Regarding the CFD results, the transitional and fully turbulent simulations are performed with the same conditions as in the experiments. Due to slightly different operat-

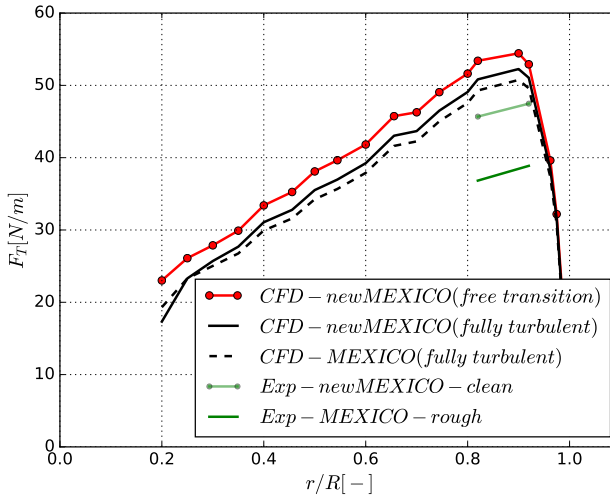


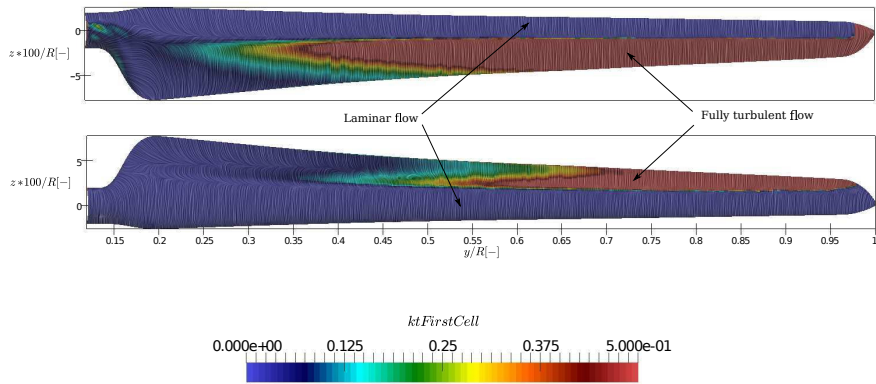
Figure 5.27: Comparison of tangential force distribution along the blade between numerical predictions and experimental measurements. Three different experimental conditions are MEXICO rough ( $U_\infty = 14.93 \text{ m/s}$ ,  $n = 424.5 \text{ rpm}$ ,  $\rho = 1.246 \text{ kg/m}^3$ ), new MEXICO clean ( $U_\infty = 15.03 \text{ m/s}$ ,  $n = 425.1 \text{ rpm}$ ,  $\rho = 1.191 \text{ kg/m}^3$ ) and new MEXICO rough ( $U_\infty = 14.86 \text{ m/s}$ ,  $n = 425.1 \text{ rpm}$ ,  $\rho = 1.20 \text{ kg/m}^3$ ).

ing conditions between the MEXICO and new MEXICO experiments for the rough configurations, small differences in the normal forces are observed from the corresponding fully turbulent simulation results. To be noted is that although the calibration and loads measurements in the new MEXICO experiment are considered to have much higher quality compared to the MEXICO experiment, the results of fully turbulent simulations still significantly overpredict the aerodynamic loads on the rough blade at the tip. Again, this is attributed to the ZigZag tape which decreases the normal force further by performing more than just tripping the boundary layer. By eliminating the ZigZag tape effects, the results of free transitional simulation considering laminar-turbulent boundary layer transition agree very well with the experimental results. Figure 5.27 shows the comparison of tangential force along the blade between CFD and experiment. Only pressure contribution is considered here and the viscous contribution is excluded in the tangential force, both for CFD and experiment. A higher tangential force is predicted at the tip by CFD compared to experimental data, no matter for clean and rough conditions.

#### TRANSITION ONSET

Figure 5.28 shows the contour of turbulent kinetic energy  $k_t$  distribution in the first cells adjacent to the blade surface, which is used to identify the transition onset. The figure clearly shows that a large portion of the flow is still laminar, both on the suction side and the pressure side. The transition line indicated by means of  $k_t$  distribution along the blade is similar to the streaking patterns of the vector field wall shear stress by using line integral convolution (LIC) technique in ParaView. More specifically, Figure 5.29 quantifies the exact transition onset location  $\frac{x_{tran}}{c}$  along the blade at  $\lambda = 6.67$  and  $\lambda = 10.0$ .





5

Figure 5.28: Transition onset on the suction side (upper figure) and pressure side (lower figure) of the blade, overlap with LIC texture for wall shear stress in ParaView.

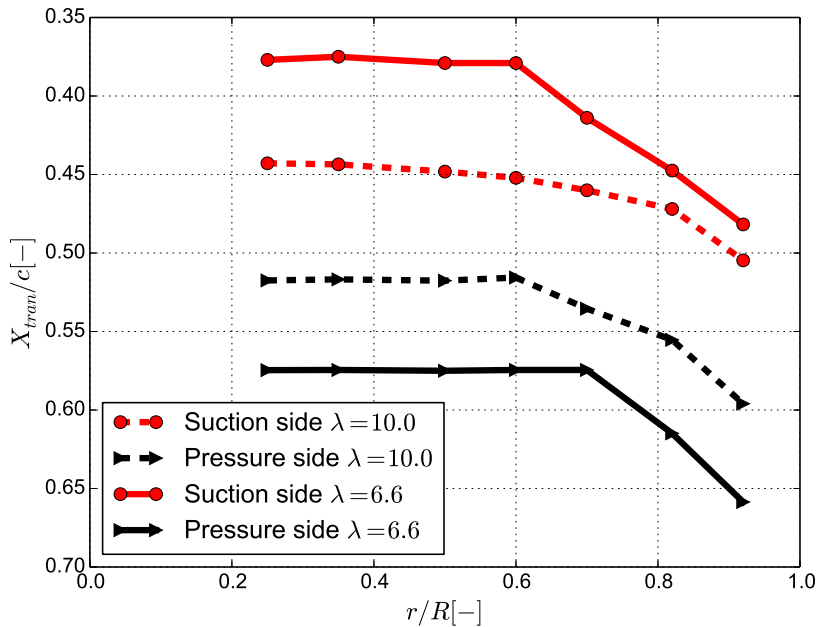


Figure 5.29: Transition onset locations along the blade span at suction and pressure sides with two different tip speed ratios:  $\lambda = 10.0$  and  $6.67$ .

Under these two conditions, the transition from laminar to turbulent on the suction side occurs earlier than the pressure side. As the tip speed ratio increases from optimal value  $\lambda = 6.67$  to off-design condition  $\lambda = 10.0$ , the transition onset along the blade consistently moves backward on the suction side and forward on the pressure side. For a specific tip speed ratio  $\lambda$ , at the inboard part of the blade ( $r/R < 0.60$ ), the location of transition onset along the blade span only slightly changes, while at the outboard part of the blade ( $r/R > 0.60$ ), the transition location shows dramatic variations. The transition location moves closer to the trailing edge as the radius becomes larger.

#### 5.4.6. STALL CONDITION AT $\lambda = 4.17$

As the wind speed increases to  $U_\infty = 24 \text{ m/s}$ , the MEXICO rotor is operating at stalled condition with a tip speed ratio  $\lambda = 4.17$ . This simulated case is very challenging for RANS models, as can be seen in Figure 5.4, where it is shown that the normal and tangential forces are poorly predicted by RANS calculation. Therefore, in this section, the DDES approach which presents quite promising results at deeply stalled airfoil flow in Section 3.2.2 will be evaluated for 3D rotating wind turbine rotor for better prediction.

The numerical setup for DDES calculations are as follows: a second-order backward scheme is used to discretize the terms in time, and a second-order linearUpwind scheme is applied for the convective terms. The PIMPLE algorithm which combines SIMPLE (Patankar and Spalding, 1972) and PISO (Issa et al., 1986) is used to decouple the pressure-velocity for the Navier-Stokes equations. The rotation modeling method is different with steady-state RANS simulation, which uses a multiple reference frame (MRF) approach as shown in Section 5.3. Instead, a sliding mesh technology is chosen to model the rotor motion. The time step for every iteration is  $7.8528e^{-4} \text{ s}$  which corresponds to 180 steps per revolution. There are 10 inner corrections in every outer loop. The total computational time is 12 revolutions which ensure the flow becomes statistically steady.

Figure 5.30 shows the time history of the total thrust on the rotor and the corresponding power spectral density. Chaotic and disordered thrust oscillation is observed during the whole simulation. The transient start-up effect can be seen from the start of thrust force variation where RANS result is used as the initial field. In order to eliminate this influence, the numerical data in last 10 revolutions are applied for the following frequency analysis. A Fast Fourier Transform (FFT) algorithm in Matlab is used to acquire the signal of the frequency domain from time varying thrust force. As can be seen from the spectrum, the main spectral features of significant magnitude can be found in the range  $0 \text{ Hz} \leq f \leq 100 \text{ Hz}$ . The highest sharp peak appears at the principal frequency (1P rotor frequency)  $8.35 \text{ Hz}$  with a magnitude of  $8.38 \text{ N}^2/\text{Hz}$ . A lower magnitude of  $6.45 \text{ N}^2/\text{Hz}$  is found at lower frequency  $2.78 \text{ Hz}$ .

Figure 5.31 compares the numerical predictions of normal force from conventional RANS and DDES calculations with measured data. It can be clearly seen that DDES performs much better than RANS for this case. The numerical results by DDES capture the measured normal force very well. The relative error of prediction is reduced from  $\sim 20\%$  to  $\sim 5\%$  at the tip ( $r/R = 0.82$  and  $0.92$ ), see Figure 5.32. Some differences can be observed in the measured results of normal force in the two different experiments, and DDES simulation presents much better agreement with new MEXICO experimental result, which is believed to have more accuracy due to better instrument calibration. The

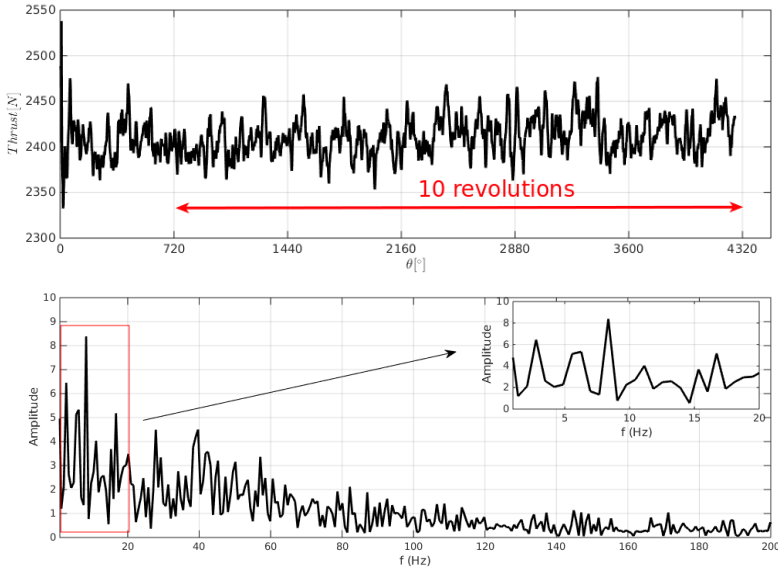


Figure 5.30: Unsteady thrust force on the rotor and power density spectrum of thrust force.

other observation from the standard deviation of DDES results indicates that at this high wind speed, the variation of normal force at the inboard part of the blade is larger compared to the outboard part. The possible reason is that the root region has more highly unsteady flow which contributes higher normal force variation.

#### VORTEX SHEDDING ON THE ROTATING BLADE

Figure 5.33 shows the unsteadiness of flow field from DDES computation by visualization of flow field over the inboard blade section ( $r/R = 0.25$ ) for different azimuth angles ( $\theta = 0^\circ, 40^\circ, 80^\circ, 120^\circ$ ). The instantaneous pressure field at every azimuth angle is also overlapped with streamline. Clearly, distinct flow patterns can be observed over the suction side for different blade position, which demonstrate a process of vortex shedding is present. At  $\theta = 0^\circ$ , a counter-clockwise vortex starts to shed from airfoil surface. As the blade locates at  $\theta = 40^\circ$ , this vortex travels much further downstream, and a larger recirculation zone is formed. Slightly lower pressure is found at the leading edge of airfoil suction side at  $\theta = 80^\circ$  compared to previous azimuth angles, and similar vortex shedding process can be seen from  $\theta = 80^\circ$  to  $\theta = 120^\circ$ .

To further describe the oscillating flow at different blade sections, the dimensionless Strouhal number  $St$  is calculated. The number is defined as

$$St = \frac{f * h}{U_{eff}} = \frac{f * c * \sin(\alpha)}{U_{eff}}, \quad (5.14)$$

where  $f$  is the frequency of vortex shedding,  $h$  is the characteristics length,  $c$  is the local chord length,  $\alpha$  is the local inflow angle,  $U_{eff}$  is the effective flow velocity.

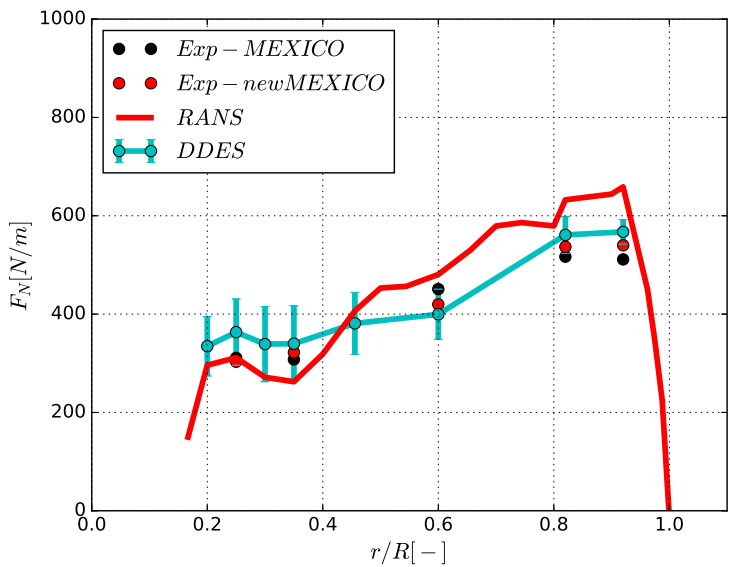


Figure 5.31: Normal force prediction along the blade with tip speed ratio  $\lambda = 4.17$ . The numerical results are obtained from RANS and DDES computations, comparing against with MEXICO experiment and new MEXICO experiment.

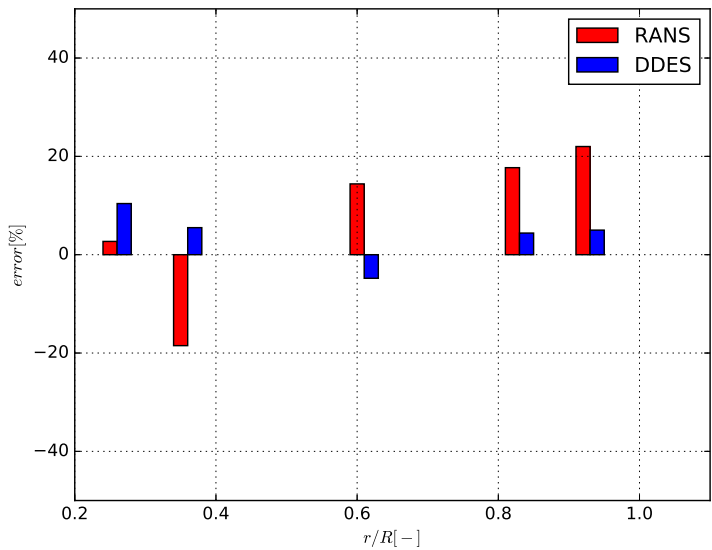


Figure 5.32: Relative error along the blade with tip speed ratio  $\lambda = 4.17$  for RANS and DDES.

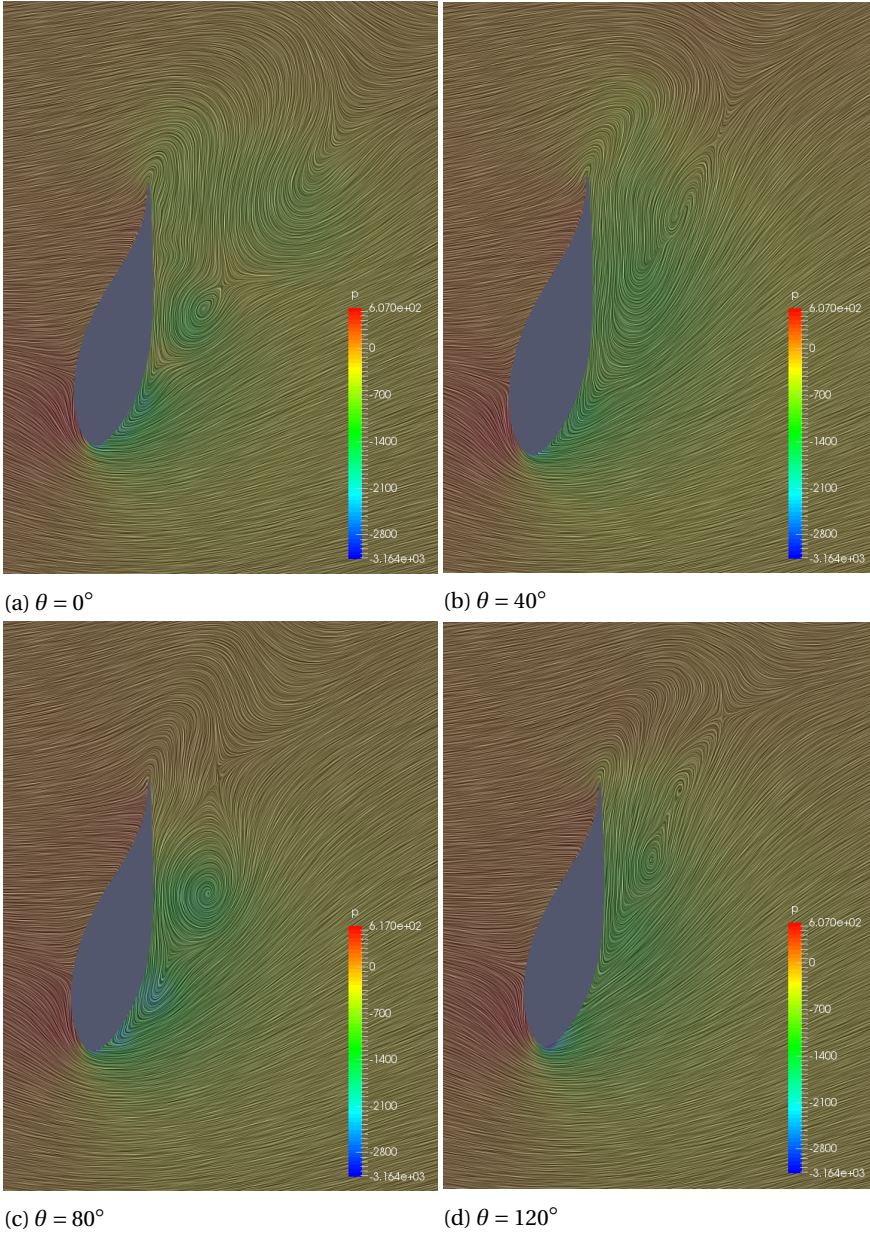


Figure 5.33: Instantaneous flow field at azimuth angles  $\theta = 0^\circ, 40^\circ, 80^\circ, 120^\circ$  over the blade section  $r/R = 0.25$ ,  $\lambda = 4.17$ .

Table 5.3: Shedding frequencies and Strouhal numbers for  $\lambda = 4.17$  case.

$r/R[-]$	$U_{eff}[m/s]$	$\alpha[^\circ]$	$c[m]$	$St[-]$	$f[Hz]$
0.25	34.58	26.3	0.2235	0.165	57.98
0.60	64.50	16.7	0.1420	0.200	323.6
0.82	85.32	14.24	0.1127	0.168	516.7
0.92	94.97	14.13	0.0987	0.018	72.5

The results of Strouhal numbers and shedding frequencies at different blade sections are listed in Table 5.3. For  $r/R = 0.25$ ,  $0.60$  and  $0.82$ , the Strouhal numbers are in the range  $0.16 \leq St \leq 0.20$ . These values correspond to the flow regime commonly associated with two-dimensional bluff body vortex shedding that occurs in stall or deep stall conditions (Schreck, 2010). The Strouhal frequency at  $r/R = 0.82$  is almost 8 times higher than the one at  $r/R = 0.25$ , which indicates that the vortex sheds much faster at  $r/R = 0.82$  than  $r/R = 0.25$ . A very low Strouhal number  $St$  is observed at  $r/R = 0.92$  with a value of  $0.018$ . Similar low values are also found in the experimentally study of NREL wind turbine blade at high wind speed (Schreck, 2010). The low value of  $St$  corresponds the flow at  $r/R = 0.92$  section is in the near post-stall regime, with three-dimensional surface flow typologies, with periodic switching between stalled and unstalled conditions (Schreck, 2007) (Bragg et al., 1996).

## 5.5. CONCLUSIONS

In this chapter, the numerical investigation of the 3D MEXICO wind turbine rotor in axial conditions is carried out at three different tip speed ratios. The numerical results of RANS and BEM code are compared with experimental measurements. The rotational effects are specifically studied by comparing the aerodynamic loads and flow features on rotating and non-rotating blades. In addition, transitional flow over MEXICO rotor is simulated, and the deviations shown in the literature between RANS and experimental measurements are explained. Eventually, for the challenging condition with the tip speed ratio  $\lambda = 4.17$ , detached eddy simulation has been performed to better resolve the highly separated flow over the rotor. The main conclusions in this chapter can be summarized:

- For the aerodynamic loads comparisons, both RANS and BEM present good results at higher tip speed ratio  $\lambda = 10.0$ , but RANS performs better for the prediction of normal force at the very tip. In particular, RANS also shows much closer agreement with measurements than BEM.
- At the optimal tip speed ratio  $\lambda = 6.67$ , the overprediction of the normal force at the tip, found in all literature, is also observed in our study. The reason for these deviations is explained by the existence of relatively thick ZigZag tape at the tip, which is not modeled in CFD computations. This conclusion is also proved by the following transitional flow study, that the predicted aerodynamic loads considering laminar-turbulence boundary layer transition shows improved comparisons with the new MEXICO measurements with clean blade configuration.



- The study of rotational effects clearly shows lift enhancement at the inboard part of the 3D rotating blade compared to the 2D airfoil and the 3D static blade and therefore delay the stall. Radial flow in the boundary layer and separated flow areas are observed, and the Coriolis forces generated by the radial flow in these regions are quantified. The Coriolis force provides a positive force acting on the flow from the leading edge to the trailing edge of the sectional airfoil, which counteracts the adverse pressure gradient and delays flow separation. The effects of Coriolis forces observed in this study are consistent with the literature. The rotational effects delay the flow separation at 25%R and 35%R sections and postpone the separation location compared to the static blade, and the rotational effects stabilize the shed vortex on the suction side compared to the 2D case.
- The DDES simulation is preferred to be used for the challenging case  $\lambda = 4.17$  with a highly separated flow. The numerical results of DDES simulation clearly show significant improvements of aerodynamic loads prediction compared to RANS results, especially at the tip  $r/R = 0.82$  and  $0.92$ . Large force variation due to flow unsteadiness is found at the inboard part of the blade. The Strouhal number quantifying this unsteady vortex shedding varies from  $0.16 \sim 0.2$ .

# 6

## AERODYNAMICS STUDY OF THE TUDelft BLADE 2 ROTOR

*A theory can be proved by experiment;  
but no path leads from experiment to the birth of a theory.*

Manfred Eigen

*It doesn't matter how beautiful your theory is,  
it doesn't matter how smart you are.  
If it doesn't agree with experiment, it's wrong.*

Richard P. Feynman

*This chapter presents another test case of aerodynamic study of the TUDelft Blade 2 rotor which eventually excludes the possible uncertainties caused by blade design and ZigZag tripping device in the experiment. To further test the hypothesis and evaluate the performance of OpenFOAM code, the computed aerodynamic forces from CFD results are compared with BEM and panel results. Apart from that, in the previous chapter, the comparison between CFD prediction and experimental measurement has been performed on the MEXICO rotor in terms of integrated sectional aerodynamic loads, chordwise pressure distribution and near wake velocity deficit. Unfortunately, the pressure and velocity fields surrounding blade sections were not measured and therefore unavailable from the experiment. This chapter also presents a more detailed and quantitative study of the blade flow around TUDelft Blade 2 rotor, a two bladed smaller rotor, which blade flow is extensively measured by Stereoscopic Particle Image Velocimetry (SPIV) technique in the Open Jet Facility (OJF) of TUDelft. Spanwise velocity field near the blade and sectional aerodynamic loads are derived from SPIV measurements and will be compared with CFD results. Aerodynamic forces acting on the blade sections are decomposed and discussed in detail.*



## 6.1. INTRODUCTION

In this chapter, a detailed flow field near the blade itself will be investigated by using CFD method (RANS) and by experimental data of the TUDelft Blade 2 rotor. This two-bladed rotor has been measured under design condition with  $\lambda = 7.0$  in the Open Jet Facility (OJF) of TUDelft. The distinct differences between the TUDelft Blade 2 rotor and the MEXICO rotor which has been discussed in the previous two chapters are:

- There is no boundary layer tripping on the TUDelft rotor blade in the experiment. The tripping device (ZigZag strip) introduced big uncertainty in the comparison of the CFD and the MEXICO experiment, as shown in Chapter 5.
- The design of the rotor blade. Only one type of airfoil is used on the blade, which is different with MEXICO rotor blade designed with three different airfoils with transitional airfoils in between. Due to different stall characteristics and different zero angle of attack of each airfoil, strong vortex shedding may occur at mid-span location, which causes another aspect of uncertainty in aerodynamic loads prediction.

Through this study, the following questions are addressed:

- How well does the predicted velocity field near the blade matches the SPIV measurements at the different blade radial locations?
- By eliminating the possible uncertainties which have been found in MEXICO experiments, how does CFD perform in aerodynamic loads prediction for the TUDelft Blade 2 rotor?
- By decomposing and analyzing the aerodynamic forces, what is the contribution of the force terms to the sectional normal and tangential forces for different radial locations?

## 6.2. EXPERIMENTAL AND NUMERICAL DESCRIPTION OF TUDelft BLADE 2 ROTOR

The work in this chapter is inline with other approaches based on the same experiment. The experimental data of the TUDelft Blade 2 rotor used in the study through this chapter have been acquired by (Akay, 2016) in her Ph.D research, and the postprocessing work such as loads determination has been done following the procedure as proposed by Vanessa del Campo and Daniele Ragni. More detailed measured results can be found in other work (Akay, 2016).

The Open Jet Facility of TUDelft is a closed circuit wind tunnel with an octagonal test section of 2.85m. The maximum velocity in the test section can achieve 35m/s. The schematic of Open Jet Facility is shown in Figure 6.1.

The measured rotor has two tapered blades with a radius  $R = 1m$  (from hub center to blade tip), see Figure 6.2. The airfoil used for this blade is DU-96-W180 with 18% thickness. The chord and twist distribution along the blade is shown in Figure 6.3. The pitch angle at the tip of this blade is fixed at  $0^\circ$  in the experiment. During the experiment, the rotor is operated at the rotational speed of 400rpm, combined with inflow velocity

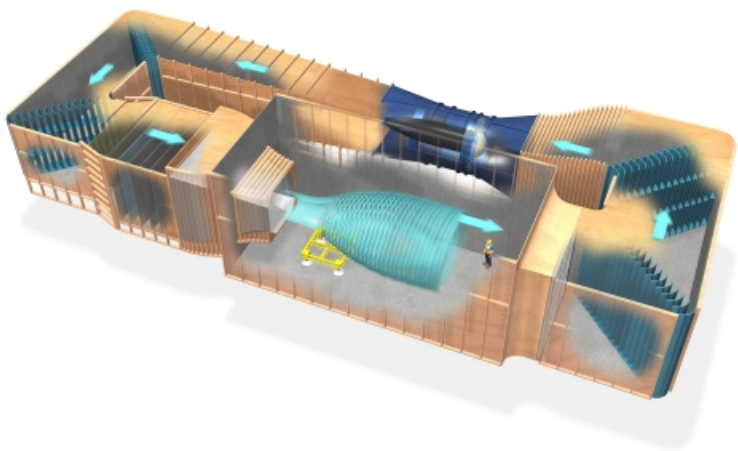


Figure 6.1: Schematic of Open Jet Facility.

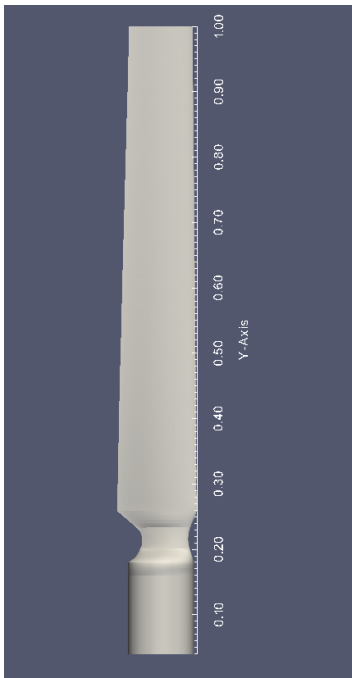


Figure 6.2: Geometry of the Blade 2 TUDELFT rotor.

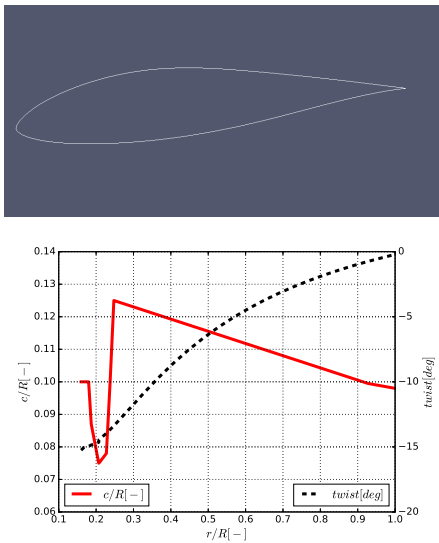


Figure 6.3: DU-96-W180 airfoil, chord and twist distribution along the blade.

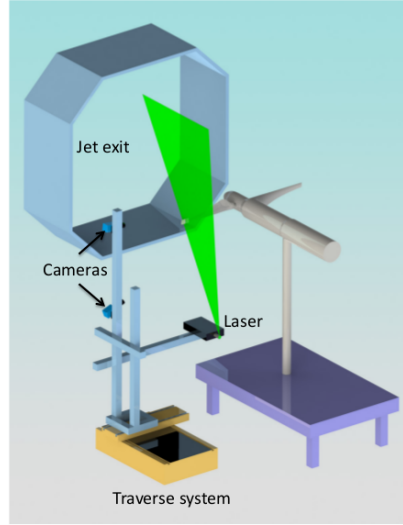


Figure 6.4: Experimental setup of the TUDelft Blade 2 rotor at Open Jet Facility.

## 6

$6\text{ m/s}$ , resulting the rotor has an optimal tip speed ratio  $\lambda = 7.0$ . The Reynolds number at the tip is  $Re = 2.75 \times 10^5$  and the free-stream turbulent intensity is about 0.3%. A detailed description of the rotor blade geometry and operating conditions can be seen in Table 6.1.

Table 6.1: Blade geometry and operating conditions of TUDelft Blade 2 rotor

Number of blades $B[-]$	2	Rotational speed $n[rpm]$	400
Rotor radius $R[m]$	1	Free-stream velocity $U_\infty[m/s]$	6
Hub radius $r_{hub}[m]$	0.147	Tip speed ratio $\lambda[-]$	7.0
Blade max chord $c[m]$	0.123	Tip Reynolds number $Re_{tip}[-]$	$2.75 \times 10^5$
		Pitch angle $[\circ]$	0

Figure 6.4 shows the experimental setup of TUDelft rotor and the setup of the SPIV system. In this setup, the measured plane is in the chordwise direction, perpendicular to the blade axis. 25 planes have been acquired in the spanwise direction using this setup, which covers the entire blade length. Several images are needed to be taken on both pressure and suction side. Due to the shadowing effect, the pressure side and suction side of each blade section have to be measured separately. Then the two groups of acquired images are combined during the image processing in order to obtain a complete view of the flow around the blade sections.

The numerical setup is similar to the RANS simulation of MEXICO rotor. The computational domain is shown in Figure 6.6. The rotational zone indicated by the gray half cylinder is the region where Coriolis and centrifugal forces are added to the CFD solver. The mesh refinement study shows that the final design of the cylinder mesh surrounding the blade is  $261 \times 106 \times 100$  points in spanwise, chordwise and normal to the blade

surface directions, respectively. The first cell height is below  $5 \times 10^{-5} \text{m}$  to achieve dimensionless wall distance  $y^+ \approx 1$ . The total number of mesh cells is  $3.4 \times 10^6$ . The boundary condition and numerical schemes used in this study are the same as for the settings of MEXICO rotor, which are described in Section 5.3.

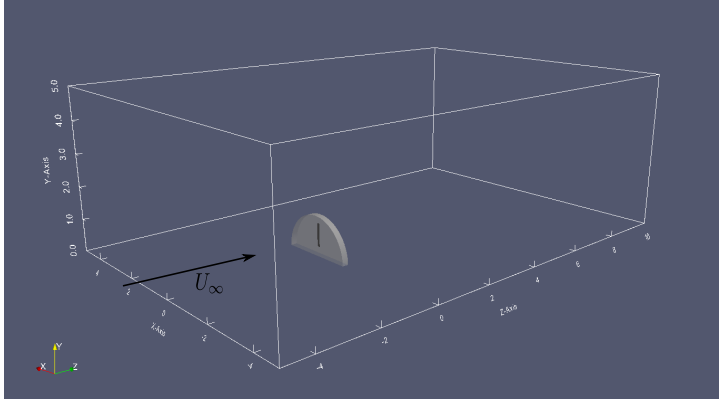


Figure 6.5: The computational domain of the TUDelft Blade 2 rotor in the simulation.

## 6.3. RESULTS AND ANALYSIS

In this section, the velocity field surrounding the blade itself obtained from CFD simulation is compared with experimental results. A detailed comparison of velocity components provides more insight into flow properties near the blade. The integrated forces will be compared with the estimated loads derived from SPIV velocity field by means of momentum balance. Eventually, the force decomposition will give the contribution of every force term to the sectional normal and tangential force at different blade sections.

### 6.3.1. VELOCITY DECOMPOSITION

In order to know more about the flow characteristics near the blade, the detailed velocity field surrounding the blade itself from PIV and CFD computation at three radial locations ( $r/R = 0.40, 0.61, 0.91$ ) will be discussed. The velocity is decomposed into axial, tangential and radial velocity components. Due to laser reflections from the blade surface, the PIV data in the regions around the airfoil leading and trailing edge are not taken into account.

#### AXIAL VELOCITY

Figure 6.7 presents the distribution of the axial velocity normalized by the free-stream velocity  $\frac{u}{U_\infty}$  around blade airfoil sections. In general, a good agreement can be observed for all radial locations between experimental and numerical results. At each location, the axial velocity on the suction side is decreasing towards to the trailing edge. The maximal axial velocity is about two times the free-stream velocity, appearing near the leading edge region over the first half of the suction side ( $x/R = 0 \sim 0.03$ ). Towards to the trailing edge, the axial velocity changes from positive to negative on the suction side. As the radial

6

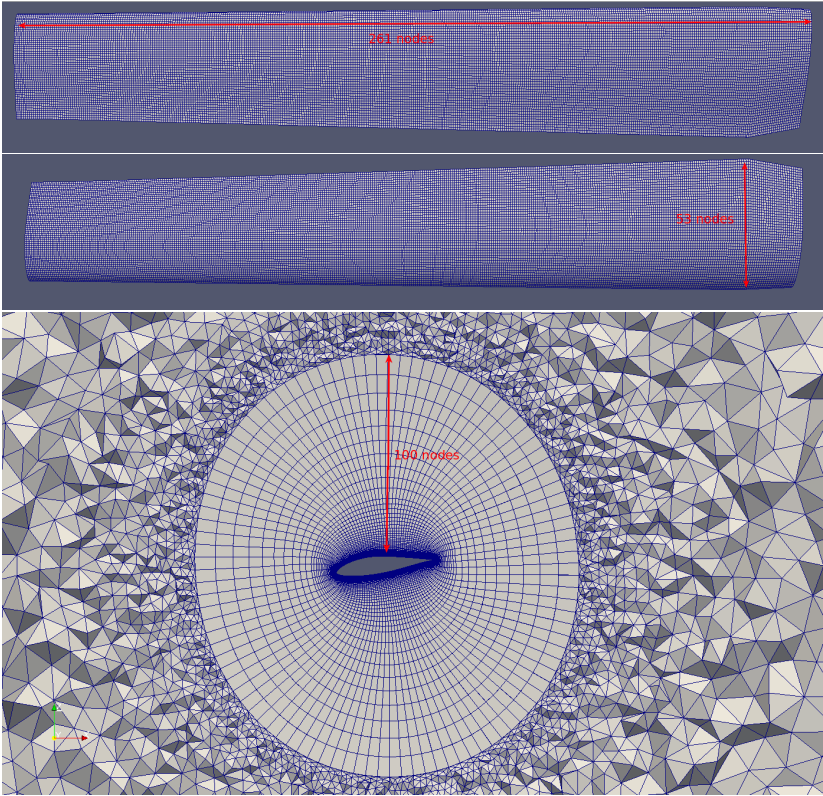


Figure 6.6: Surface mesh on the pressure and suction sides of blade, and hybrid mesh near blade section  $r/R = 0.50$ .

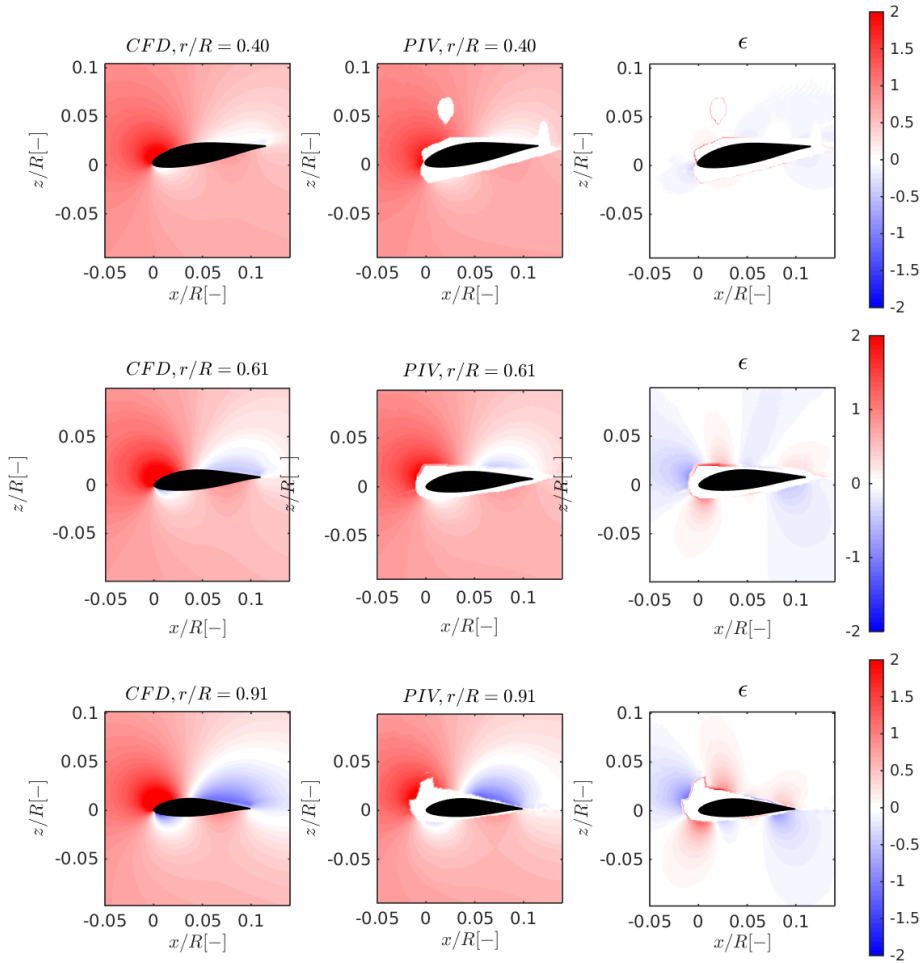


Figure 6.7: Axial velocity distribution at three different radial locations from  $r/R = 0.40$  to  $r/R = 0.91$ , normalized with the free-stream wind speed  $U_\infty$ . Inflow direction is  $+z/R$ . The PIV data at  $x/R = 0.025$  and  $z/R = 0.05$  of section  $r/R = 0.40$  is marked due to laser reflection.

location increases, the negative axial velocity over second half airfoil ( $x/R = 0.05 \sim 0.10$ ) becomes larger.

#### TANGENTIAL VELOCITY

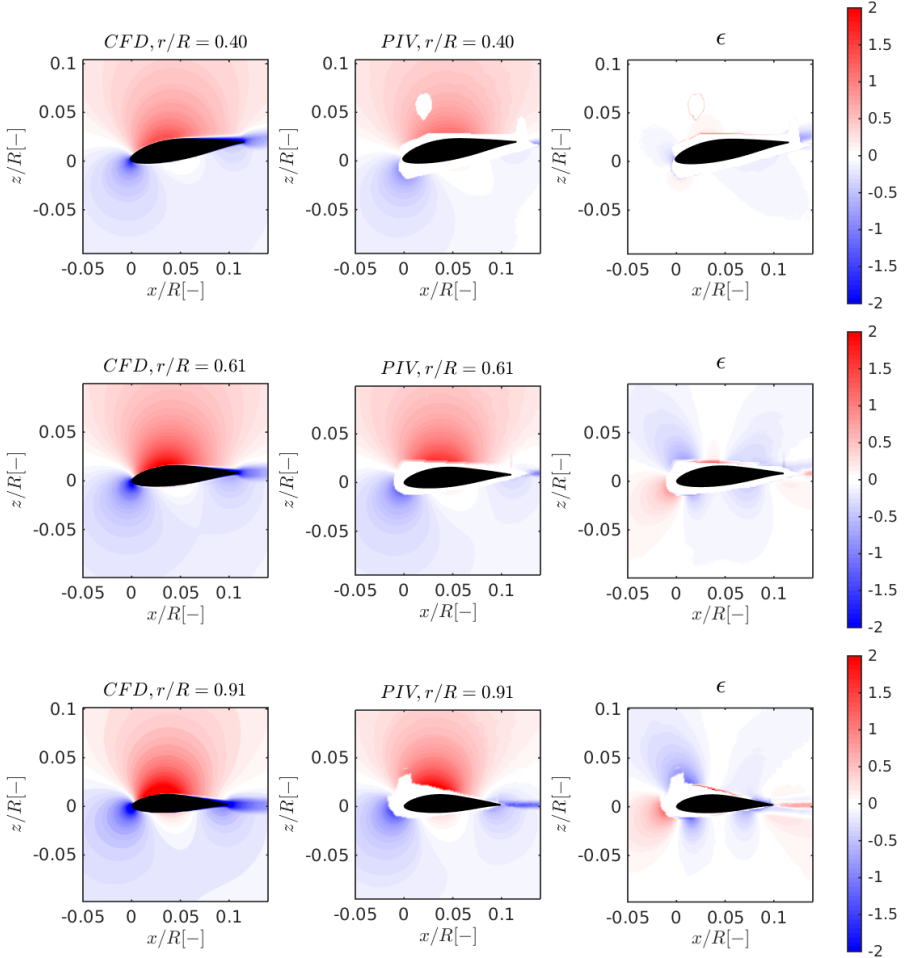


Figure 6.8: Tangential velocity distribution at three different radial locations from  $r/R = 0.40$  to  $r/R = 0.91$ , normalized with the free-stream wind speed  $U_\infty$ . Inflow direction is  $+z/R$ . The PIV data at  $x/R = 0.025$  and  $z/R = 0.05$  of section  $r/R = 0.40$  is marked due to laser reflection.

The experimental and numerical results of tangential velocity field around blade sections is shown in Figure 6.8. A very good agreement can be seen between PIV data and CFD simulation for most regions near airfoil, except for the trailing edge region. The negative tangential velocity in the wake indicates the shed vorticity sheet after the trailing edge. With increasing the radial location from  $r/R = 0.40$  to  $r/R = 0.91$ , the tangential velocity on the suction side increases due to increase local circumferential velocity.

Meanwhile, the vorticity sheet becomes significant outboard, which can be clearly seen both in PIV data and CFD simulation. CFD predicts a larger wake region behind the airfoil. At  $r/R = 0.91$ , CFD slightly overpredicts the tangential velocity over the suction side and at the same time underpredicts the tangential velocity at the pressure side.

#### RADIAL VELOCITY

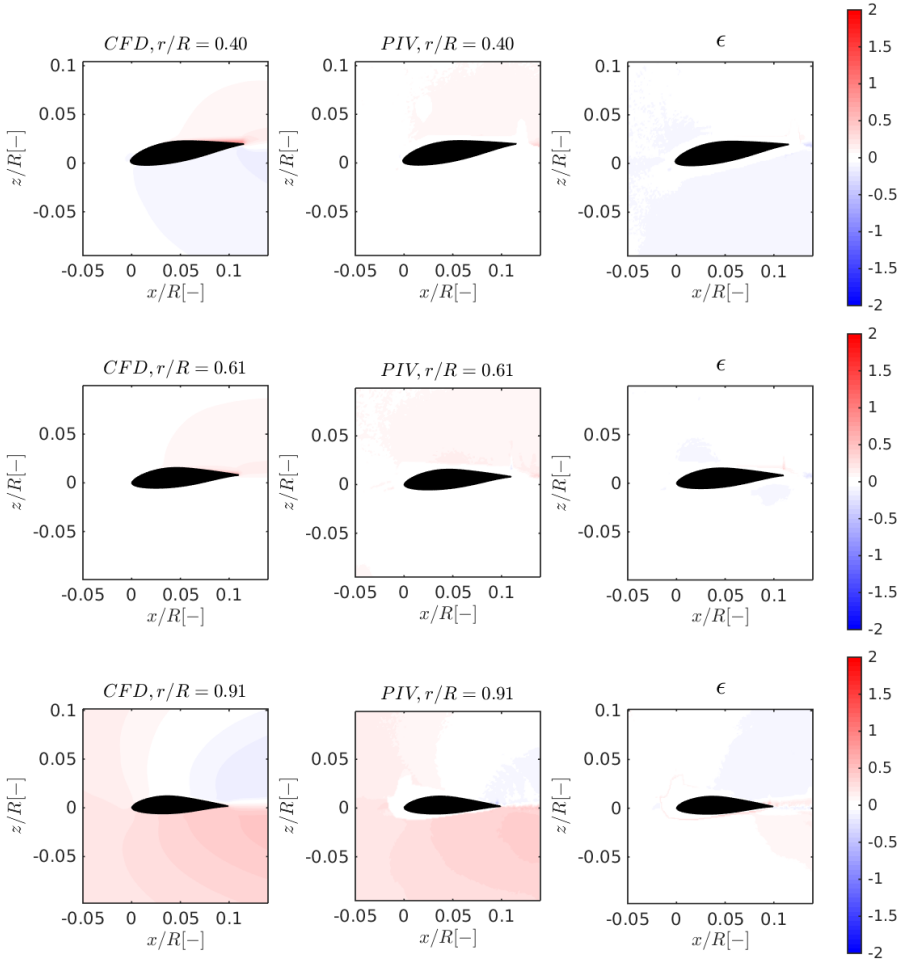


Figure 6.9: Radial velocity distribution at three different radial locations from  $r/R = 0.40$  to  $r/R = 0.91$ , normalized with the free-stream wind speed  $U_\infty$ . Inflow direction is  $+z/R$ . The PIV data at  $x/R = 0.025$  and  $z/R = 0.05$  of section  $r/R = 0.40$  is marked due to laser reflection.

Figure 6.9 shows the radial velocity field from PIV and CFD for three radial locations. No obvious radial flow is observed at  $r/R = 0.40$  and  $r/R = 0.61$  on the pressure side from PIV data, however low radial flow ( $< 0.25U_\infty$ ) is predicted by CFD at  $r/R = 0.40$ . Only rather low radial velocity at the trailing edge on the suction side at  $r/R = 0.40$  section is



observed, with a magnitude of  $0.5 \times U_\infty$ . This radial flow is directed outboard. As the radial location increases, the outboard radial velocity on the suction side decreases and eventually becomes negative at  $r/R = 0.91$ . The latter can be explained by the presence of the tip vortex, which contributes to the high outboard radial velocity on the pressure side at these radial stations.

### 6.3.2. FORCE ESTIMATION AND DECOMPOSITION

#### FORCE ESTIMATION FROM SPIV VELOCITY FIELD

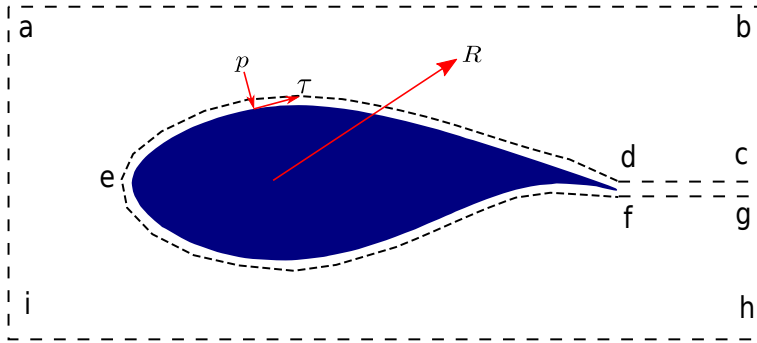


Figure 6.10: Contour approach to calculate aerodynamic forces on 2D airfoil. Figure is adapted from (Anderson Jr, 2010).

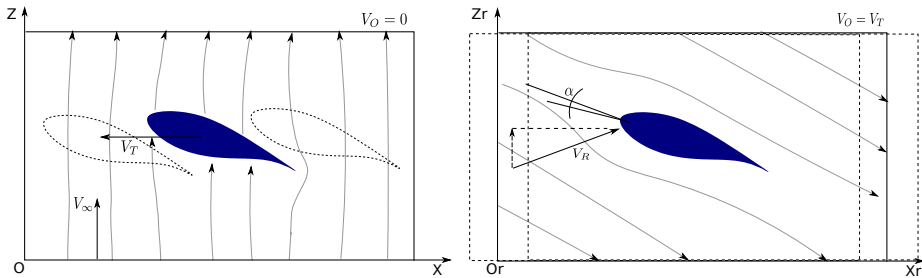


Figure 6.11: Airfoil flow representation in the absolute (left) and relative (right) reference frame. Figure is adapted from (Ragni, 2012).

To determine the aerodynamic loads on a wind turbine blade sections from mea-

sured SPIV velocity field, the contour approach (Anderson Jr, 2010) based on the application of the integral form of the momentum equation is used. Figure 6.10 presents the basic idea of this method for determining the forces acting on a 2D static airfoil. There are two contribution terms to the resultant aerodynamic force  $R$  on the airfoil. The first one is the pressure force on the airfoil surface, and the second is the viscous shear stress. Thus when considering the control volume (rectangular contour)  $abhi$  in Figure 6.10, based on Newton's third law, the force at the airfoil gives the fluid the force calculated from the contour. Hence, writing the integral form of the momentum equation for this contour, one gets:

$$\frac{\partial}{\partial t} \iiint_V \rho \vec{V} dv + \oint_S (\rho \vec{V} \cdot \vec{n} dS) = - \iint_{abhi} p \vec{n} dS + \iint_{abhi} \bar{\tau} \vec{n} dS - R, \quad (6.1)$$

where  $\vec{V}$  is the velocity vector,  $\bar{\tau}$  is the Reynolds stress and viscous contribution,  $\vec{n}$  is the unit vector normal to the surface  $S$ ,  $V$  is the control volume and  $\rho$  is the density.

When applying this method to calculate the sectional loads on a rotating wind turbine blade, a moving contour placed on the blade itself which represents a relative reference frame is preferred such that the flow can be seen as quasi-steady over the airfoil. The difference of flow over airfoil between absolute and relative frames is illustrated in Figure 6.11. Therefore, the time derivative term in Equation 6.1 can be neglected and the differential equation can be simplified. However, the centrifugal and Coriolis force due to blade rotation should be added in the relative reference frame. Thus, the final equation becomes

$$\begin{aligned} R = & - \oint_S (\rho \vec{V} \cdot \vec{n} dS) - \iint_{abhi} p \vec{n} dS + \iint_{abhi} \bar{\tau} \vec{n} dS \\ & - \iiint_V 2\rho(\vec{\Omega} \times \vec{V}_r) dV - \iiint_V \rho(\vec{\Omega} \times (\vec{\Omega} \times \vec{r})) dV. \end{aligned} \quad (6.2)$$

where  $\vec{V}_r$  is the relative velocity vector, which can be calculated by  $\vec{V}_r = \vec{V} - \vec{\omega} \times \vec{r}$ .

To calculate the force on the airfoil using Equation 6.2, the pressure field is needed in the second term of right hand side. (Unal et al., 1997) solve the momentum equations to explicitly determine the pressure term in order to predict the force acting on a circular cylinder by using measured velocity field data. In the rotating reference frame, (Ragni, 2012) successfully uses this approach to determine the aerodynamic loads on aircraft propellers. More recently, (Campo et al., 2014) apply this method to calculate the forces on wind turbine blades. The relation between pressure gradient and velocity field in a rotating reference frame is

$$\nabla p = - \frac{d}{dt} (\rho \vec{V}_r) - \rho \vec{V}_r \cdot \nabla \vec{V}_r + 2\rho(\vec{\Omega} \times \vec{V}_r) + \rho(\vec{\Omega} \times (\vec{\Omega} \times \vec{r})) + \mu \Delta \vec{V}_r \quad (6.3)$$

Once the pressure gradients are obtained, the pressure field can be evaluated from the spatial integration for the entire domain inside the contour. In the present study, the pressure is solved by using the Poisson pressure equation, see (Ragni, 2012). This approach has been demonstrated to have a very small error accumulation. In this method,

a forcing function  $g$  according to Equation 6.4 is derived from the momentum equation (see Equations 6.5 and 6.6).

$$\nabla^2 p \approx \mathbf{D}p = g(u, v) \Rightarrow p = \mathbf{D}^{-1}g(u, v) \quad (6.4)$$

$$\mathbf{D}p = \left[ \frac{p_{i+1,j} - 2p_{i,j} + p_{i-1,j}}{\Delta x^2} + \frac{p_{i,j+1} - 2p_{i,j} + p_{i,j-1}}{\Delta y^2} \right]_{i=1..n, j=1..m} \quad (6.5)$$

$$g(u, v)_{i,j} = \frac{[\frac{\partial p}{\partial x}]_{i+1,j} - [\frac{\partial p}{\partial x}]_{i-1,j}}{2\Delta x} + \frac{[\frac{\partial p}{\partial y}]_{i,j+1} - [\frac{\partial p}{\partial y}]_{i,j-1}}{2\Delta y} \quad (6.6)$$

For the boundary conditions on the outer contour, the flow can be considered irrotational, and Dirichlet condition is used. The pressure on the boundary is calculated with Bernouli's theorem. For other boundaries, including the inner contour and the marked airfoil region, the von Neumann condition is applied. With the approach mentioned above, the aerodynamic loads along the span, which are derived from SPIV velocity fields, on TUDelft rotor blade can be calculated and compared with numerical results.

To compare the CFD results with forces derived from measured velocity field, two other aerodynamic models BEM and 3D free wake panel codes are used to calculate the aerodynamic loads as well. The descriptions of BEM and 3D panel codes are briefly introduced here.

The BEM code used in the loads calculation utilizes the momentum theory of the axial actuator disk for an idealized wind turbine, assuming that each annular ring on the disk is independent of the other annular rings. In other words, there is no interaction between the fluids of neighboring annular rings. However, near the tip region, this assumption is not valid due to the existence of tip vortices, which play a major role in the induced velocity distribution at the rotor (Moriarty and Hansen, 2005). Therefore, the Prandtl tip-loss correction (Glauert, 1935) is used to correct BEM theory. The correction factor is

$$F = \frac{2}{\pi} \cos^{-1} e^{-\frac{B}{2} \frac{R-r}{r \sin \varphi}}, \quad (6.7)$$

where  $B$  is the blade number,  $\varphi$  is the inflow angle and  $r$  is the radial location. This factor  $F$  is used in the momentum equations of BEM theory to get more accurate aerodynamic loads prediction near the tip (Shen et al., 2005).

The 3D unsteady numerical panel code is developed by (Dixon, 2008) in his work of vertical axis wind turbine aerodynamics study, and follows the formulations presented by (Katz and Plotkin, 1991). This code is further validated both for vertical and horizontal wind turbine applications (Dixon et al., 2008) (Ferreira, 2010) (Campo et al., 2014) (Miccallef et al., 2016). The model discretizes the blades into 3D surface panels of sources and doublets, and solves the Laplace equation for the inviscid and incompressible flow. A Dirichlet boundary condition is imposed on the blade surface and the Kutta condition is enforced at the trailing edge. As the blades rotate, doublet panels are shed from the trailing edge and constitute the wake, and the strength of wake doublets are determined by the vorticity strength released by the blade. The numerical setup and verification of model parameters can be found in (Miccallef, 2012).

## SPANWISE AERODYNAMIC FORCES COMPARISONS

The aerodynamic loads calculation along the blade by using different numerical methods, including CFD, BEM and panel codes, are shown in Figure 6.12. All the numerical results are compared against the forces derived from PIV velocity measurements. It can be seen that all numerical codes show the correct trend of normal force distribution, both CFD and panel code give almost the same radial location for the maximal normal force. However, BEM method predicts the largest normal force much closer to the tip, which indicates that the tip correction method used for BEM code need to be further improved. Due to the inviscid solver used in panel code, approximately 10% higher normal force is obtained (Campo et al., 2014). CFD results show very good agreement with estimated loads derived from measured velocity field by PIV.

Regarding the tangential force along the blade, distinct differences can be observed between the estimated tangential force and numerical results of CFD and BEM. Much smaller tangential force  $F_T$  is predicted by CFD and BEM codes, but these two codes present very close predictions. Surprisingly, panel code without considering viscous effects presents better agreement with estimated tangential force, even if the normal force is overpredicted.

## FORCE DECOMPOSITIONS

Figure 6.13 shows the contribution of different force terms on the right-hand side of Equation 6.2 to the normal and tangential forces at four radial locations. The results are obtained by calculating each force term in Equation 6.2 for the integrated contour. The different integration paths have been chosen and examined such that the final path produces a converged solution in both normal and tangential forces. Regarding the normal force, the pressure force and convective force terms are main contributors. As the location moves to the inboard part of the blade, the convective force becomes more important. At  $r/R = 0.40$ , the convective force has almost the same contribution to the normal force as the pressure force. The convective force provides less contribution, and the pressure force dominates the normal force when the radial location is closer to the tip. The viscous, Reynolds stress and Coriolis force terms are very small at those locations. Similarly, the pressure and convective terms mainly contribute to the tangential force, and the Coriolis force needs to be considered, especially close to the inboard blade where the radial flow is significant.

## 6.4. CONCLUSIONS

In this chapter, the flow over the TUDelft rotor has been simulated by means of a CFD RANS approach. The predicted aerodynamic loads and flow field surrounding the blade itself are compared quantitatively with available PIV experimental data. To answer the questions proposed in Section 6.1, the chapter can be concluded as follows:

There is good agreement between experiment and CFD predictions in near blade velocity field, in terms of axial, tangential and radial velocity components. CFD presents very good predictions in the inviscid flow region and can provide more flow characteristics of the boundary layer on the rotating blade where PIV is extremely difficult to apply.

By eliminating the possible uncertainties in the MEXICO comparison, CFD provides very good aerodynamic loads prediction for the TUDelft Blade 2 rotor. The contour ap-

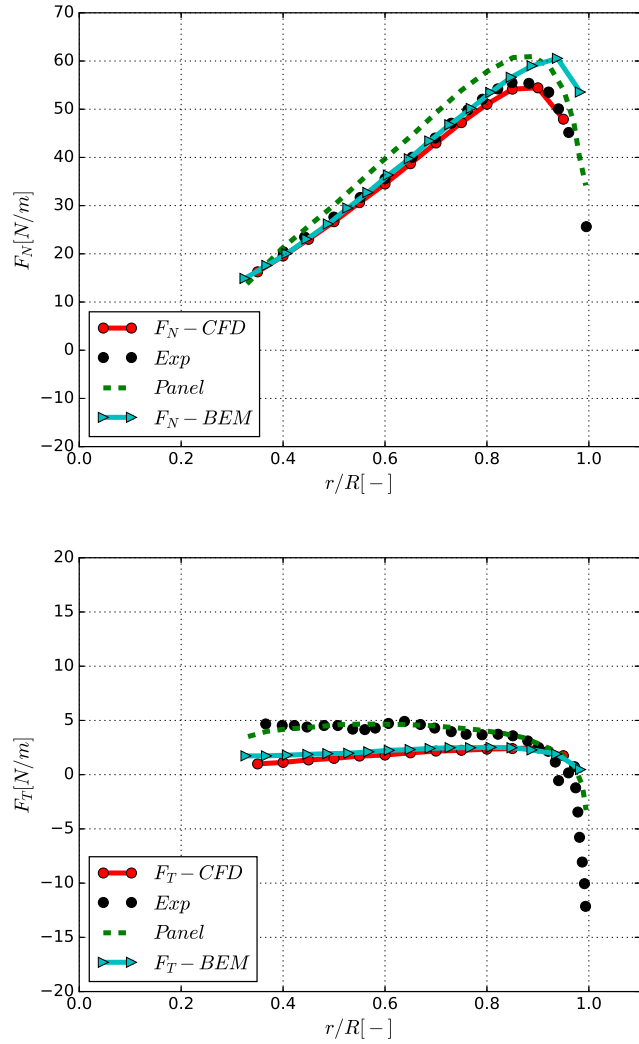


Figure 6.12: Aerodynamic loads comparisons along the blade between PIV results and numerical methods, including CFD, BEM, panel codes.(left: normal force and right: tangential force).

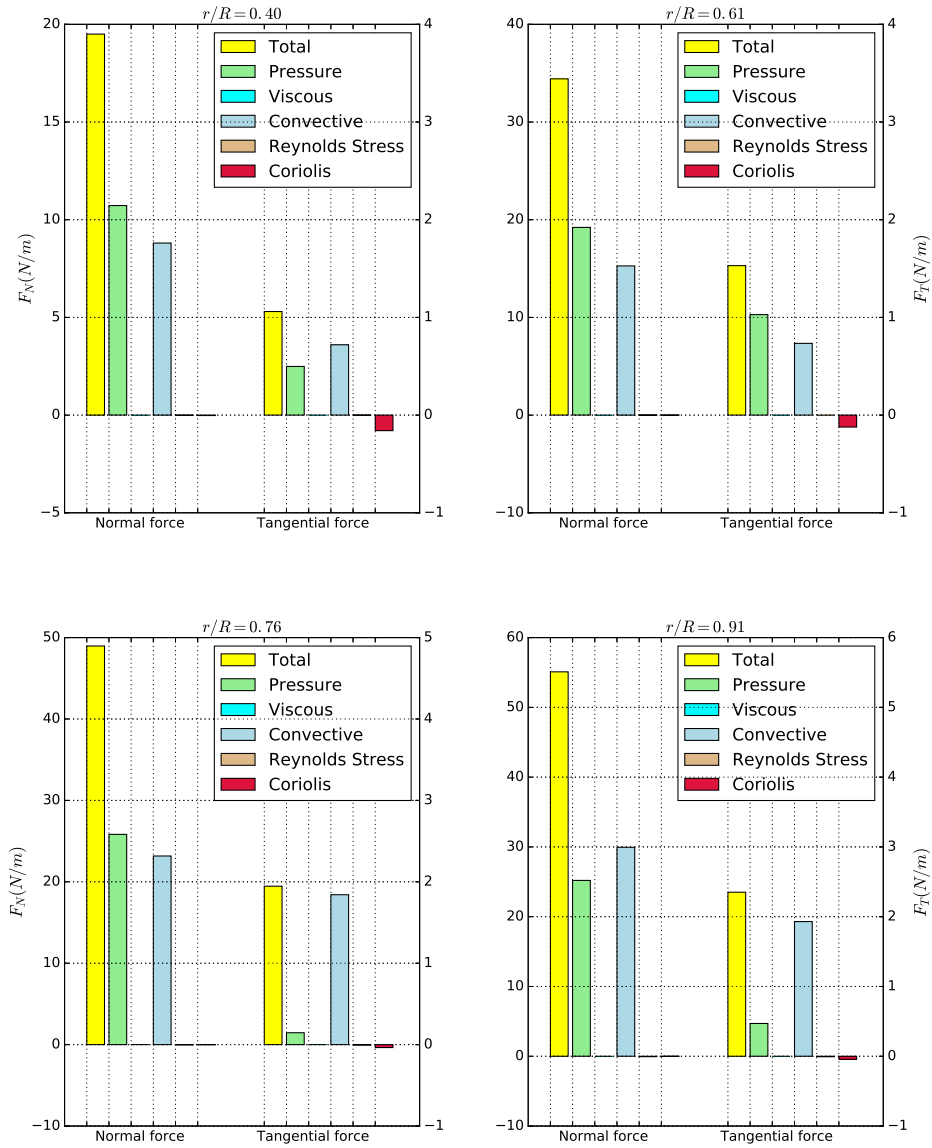


Figure 6.13: The contribution of different force terms to the normal and tangential forces at different radial locations ( $r/R = 0.40, 0.61, 0.76, 0.91$ ).

proach based on momentum balance is used to derive aerodynamic loads on the blades with the measured velocity field, and the comparison between derived normal force and CFD prediction is excellent. CFD shows much better agreement with experimental data than BEM and panel codes, which fail to predict the normal force near the tip due to imperfect tip correction model and inviscid limitation, respectively.

By decomposing the integrated aerodynamic forces into different terms, the contribution of different force terms to the normal and tangential forces at different radial locations are determined. This analysis indicates that the pressure and convective force terms give the main contributions to the normal force, and Coriolis force plays a considerable role in tangential force determination at the location where radial flow is significant.

# 7

## CONCLUSIONS AND RECOMMENDATIONS

*Don't cry because it's over, smile because it happened.*

Dr. Seuss

*In this thesis, the detailed wind turbine aerodynamics under controlled conditions have been studied experimentally and numerically. In order to investigate the probable causes of large discrepancies between numerical predictions and measurement in MEXICO experiment, measurements of non-rotating MEXICO blade have been carried out at low speed low turbulence wind tunnel of Delft University of Technology. Meanwhile, numerical modeling of wind turbine rotor aerodynamics based on CFD (RANS/DDES) method has been investigated and improved, especially for modeling transitional flow and turbulent flow. The models ( $k-\omega$  SST,  $k-k_L-\omega$  and DDES-SA) in the open source code (OpenFOAM-2.1.1) has been validated for wind turbine simulation at different tip speed ratios in axial flow conditions, aiming to better predict aerodynamic loads for wind turbine rotor operating under different conditions. Based on the presented work, some conclusions and recommendations are given below.*



## 7.1. CONCLUSIONS

The main contribution of this thesis is that the MEXICO rotor has been comprehensively investigated numerically and experimentally, in order to identify the possible causes of large discrepancies between numerical results and experimental measurement. Apart from the calibration error in the MEXICO experiment, one reason could be attributed to complex blade design resulting in 3D flow dominated rotor aerodynamics. The other reason is that the ZigZag tape used to trip the boundary layer flow on the blade plays an important role in affecting the aerodynamic tip loads. Furthermore, the key conclusions presented in this thesis are summarized in terms of OpenFOAM performance, causes of deviation found in the blind comparison between numerical predictions and experimental measurements, and advanced numerical modeling.

### 7.1.1. OPENFOAM PERFORMANCE

An open source CFD code (OpenFOAM-2.1.1) based on finite volume method has been validated and further improved in this study, particularly for wind turbine aerodynamics.

A series of computations from simple 2D flat plate to complicated 3D rotating wind turbine rotor has been performed in order to evaluate the code implementation and model performances in OpenFOAM. The results in Chapter 3 show that the popular linear eddy viscosity models (Spalart-Allmaras and  $k-\omega$  SST) perform well for 2D flat plate and NACA0012 benchmark test cases, by comparing the computational results with the theoretical solution or numerical results from a well-validated code.

The code implementation error of transition model  $k-k_L-\omega$  in OpenFOAM-2.1.1 has been corrected and the modified case has been used to simulate boundary layer transitional flow of DU91-W2-250 wind turbine airfoil at  $Re = 1.0 \times 10^6$ . In the linear regime, much closer agreement with experimental data has been observed when taking laminar to turbulent transition modeling into account than the fully turbulent simulation with  $k-\omega$  SST. At the flow regime after stall ( $\alpha = 60^\circ$ ), hybrid LES/RANS approach predicts the aerodynamic characteristics  $C_L$  and  $C_D$  of NACA0021 airfoil with promising accuracy of about 10% difference, showing significant improvement than steady RANS ( $\sim 25\%$ ) and unsteady RANS ( $\sim 55\%$ ) predictions.

Regarding CFD predictions of aerodynamic loads on wind turbine blades, two different rotors have been simulated at several tip speed ratios, the results of which can be found in Chapters 5 and 6.

### MEXICO ROTOR

The comparison of aerodynamic loads for the MEXICO rotor indicates that for the highly loaded rotor ( $\lambda = 10.0$ ), CFD simulations with  $k-\omega$  SST turbulence model present better normal and tangential forces prediction along the blade than conventional engineering BEM model, especially at the near tip region. The flow field and tip vortex motion in the near wake have been compared between CFD results and PIV measurement. Overall speaking, good agreements are obtained: CFD slightly overpredicts the axial velocity behind the rotor which is operating at the off-design condition, but a good prediction is seen at the design condition  $\lambda = 6.67$ .

The inboard motion of the tip vortex after releasing has been successfully captured by CFD simulation and agrees with PIV measurement. A stall delay phenomenon as-

sociated with strong radial flow in the inboard part of rotating blade enhances the lift, compared to 2D airfoil aerodynamic characteristics. This rotational effect results in the delay of flow separation to some extent and the stabilization of vortex shedding compared to the non-rotating blade.

#### TUDELFT BLADE 2 ROTOR

The second CFD analysis of using TUDelft Blade 2 rotor geometry indicates at the design condition  $\lambda = 7.0$ , CFD presents superior performance in the loads calculation, better than advanced panel model and engineering BEM model, which both fail to predict the normal force at the tip. Very detailed 3D flow fields in terms of axial, tangential and radial velocity components are compared quantitatively between numerical results from CFD and stereoscopic PIV measurements, indicating that the numerical results in the inviscid flow regions are compared reasonably well with the SPIV measurement. More flow characteristics in the boundary layer could be numerically investigated from CFD results, which can not obtain from SPIV measurements. The numerical studies of two different wind turbine rotors reveal that the tip loss corrections in BEM model can be still potentially improved in the future.

#### 7.1.2. CAUSES OF DEVIATION

The main motivation of this thesis came from large differences in aerodynamic loads on wind turbine blade between numerical prediction and experimental results in MEXICO experiment, especially at the tip region ( $r/R = 0.82, 0.92$ ), which has been observed in the publications of many researchers. In order to figure out the causes of these deviations, detailed measurements under controlled conditions have been carried out on the non-rotating wind turbine blade. The quasi-2D aerodynamic characteristics of three blade sections have been measured and compared with numerical simulation performed afterward. Apart from fairly good comparisons of chordwise pressure distribution between CFD and experiment, more insight into three-dimensional vortical structures has been revealed near the MEXICO wind turbine blade. Due to the different aerodynamic post-stall characteristics of two different airfoils (RISØ and DU) on the blade, a pair of counter-rotating vortices is generated behind the blade at position  $r/R = 0.55$ , resulting in a significant kink observed in sectional aerodynamic force distribution along the blade. The induced velocity caused by these vortices alters the local inflow at each section, and therefore the upwash/downwash effects change the aerodynamic characteristics of RISØ family. Consequently, 3D effects play an important role in the numerical modeling for calculating the aerodynamic loads for MEXICO rotor. This might be the first reason that low fidelity model (lifting line and BEM) can not accurately model the highly three-dimensional flow in the comparison.

The second reason can be contributed to the ZigZag effect. Since almost all CFD simulations significantly overpredict the normal force at the tip ( $r/R = 0.82, 0.92$ ), a hypothesis has been proposed that the deviation between CFD and experiment is caused by the existence of ZigZag, which (apart from the effect of tripping the BL) has not been modeled in any of CFD simulations because of meshing challenge. The ZigZag effect has been experimentally investigated in Section 4.3.2 for the non-rotating blade, indicating that ZigZag plays an important role in lift reduction at specific flow regimes, for

angles of attack  $\alpha = 4^\circ \sim 11^\circ$ . ZigZag alters the boundary layer displacement thickness and further the effective airfoil camber, resulting in significantly overpredicting the normal force at  $r/R = 0.92$  for fully turbulent CFD simulation without ZigZag stripe. This hypothesis is further numerically and experimentally confirmed in the rotating wind turbine simulation in Chapter 5. The new MEXICO experiment with clean blade configuration shows significant differences with rough blade configuration which has ZigZag at the tip, demonstrating that the ZigZag indeed seriously affects the aerodynamics loads on the tip. The simulation of 3D flow about the rotating wind turbine blade by considering laminar-turbulent boundary layer transition shows improved predictions with new MEXICO measurements with clean blade configuration.

### 7.1.3. ADVANCED NUMERICAL MODELING

In this thesis, more advanced modeling approaches have been considered and applied in Chapter 5, particularly for the 3D wind turbine rotor aerodynamics, which presents the latest state of the art of CFD modeling approach. The transitional flow simulation with  $k-k_L-\omega$  model first gives insight into transition onset on 3D rotating blade surface, and the transitional locations are quantitatively identified along the blade. At the design tip speed ratio  $\lambda = 6.67$  for the MEXICO rotor, the transition from laminar to turbulent on the suction side occurs earlier than the pressure side. As the tip speed ratio increases from optimal value  $\lambda = 6.67$  to off-design condition  $\lambda = 10.0$ , the transition onset along the blade consistently moves backward on the suction side and forward on the pressure side. For specific tip speed ratios, the chordwise location of transition onset has slight changes at the inboard part of the blade ( $r/R < 0.60$ ), while dramatic variations of chordwise transition onset locations are found at the outboard part of the blade ( $r/R > 0.60$ ). The transition location moves closer to the trailing edge as the radius becomes larger.

In the DDES simulation, a hybrid LES/RANS approach which is originally designed to cope with massively separated flow simulation has been investigated and utilized in this thesis particularly for wind turbine aerodynamics (wall-bounded airfoil flow and rotating blade flow) study. Not only very promising results are obtained for 2D airfoil simulation, but DDES simulations are successfully extended to the application of predicting massively separated 3D flow around non-rotating and rotating MEXICO wind turbine blades. Excellent pressure distribution ( $C_p$ ) prediction is obtained by DDES at ( $r/R = 0.35$ ) radial section for the non-rotating blade. Meanwhile more vortical structures are resolved by DDES in the separated flow region. These improvements are also found in wind turbine rotor simulations: at the tip speed ratio ( $\lambda = 4.17$ ), DDES simulation clearly shows significant improvements of aerodynamic loads prediction compared to RANS results, especially at the tip regions ( $r/R = 0.82$  and  $0.92$ ). The conclusion is in contrast with the DDES study of NREL blade by Johansen et al. (2002), who concludes that DDES simulation shows more 3D flow structures compared to conventional two-equations RANS model, but no particular improvements are seen in global blade characteristics. The DDES simulation of MEXICO wind turbine rotor presents large force variation due to flow unsteadiness at the inboard part of the blade, which is known as a typical flow feature for wind turbine aerodynamics. The observed Strouhal number quantifying this unsteady vortex shedding varies from  $0.16 \sim 0.20$ .

## 7.2. RECOMMENDATIONS

Regarding the numerical modeling of wind turbine rotor aerodynamics based on CFD method, the following recommendations are presented.

### 7.2.1. 3D FLUID STRUCTURE INTERACTION

The current research mainly focused on small wind turbine rotor models. Since the commercial wind turbine size, especially offshore, becomes larger and larger, wind turbine blades are more flexible. Therefore, Fluid Structure Interaction (FSI) should be considered for long and flexible 3D blades. High fidelity CFD model should be coupled with a structure model to investigate the structural response caused by the surrounding fluid. Meanwhile, computational cost and accuracy should also be considered in order to effectively and successfully use high fidelity models for 3D complex wind turbine simulation. Currently, such efforts are being made at the Delft University of Technology by implementing efficient numerical algorithms in FSI simulation to achieve these goals. The efficient numerical algorithm is achieved by implementing advanced time integration for partitioned FSI models and mesh deformation, and these simulations are demonstrated with efficiency and accuracy for 2D wind turbine airfoil with trailing edge flaps. The application of efficient FSI simulation in 3D wind turbine case still needs to be further investigated.

### 7.2.2. FLOW CONTROL MODELING ON WIND TURBINE BLADE

As an effective way of aerodynamic loads reduction, flow control techniques becomes more and more popular utilizing on large wind turbines. Numerical modeling of the effects of flow control techniques, including passive flow control devices (e.g., such as vortex generator) and active flow control (e.g. plasma actuators), on wind turbine blade is very interesting and challenging. Similar work has been carried out in terms of modeling the accurate body forces caused by vortex generator or plasma actuators within OpenFOAM at the Delft University of Technology, and the numerical models are validated with experimental results for simple test cases (2D airfoil). The extension of CFD numerical models to 3D models capable of simulating rotor blades including flow control devices is highly recommended.



# BIBLIOGRAPHY

- IH Abbott and AE Von Doenhoff. *Theory of wing sections, including a summary of airfoil data*. Courier Corporation, 1959.
- B Akay. *The root flow of horizontal axis wind turbine blades: Experimental analysis and numerical validation*. PhD thesis, Delft University of Technology, Delft, the Netherlands, 2016.
- B Akay, D Ragni, CJ Simão Ferreira, and GJW Bussel. Experimental investigation of the root flow in a horizontal axis wind turbine. *Wind Energy*, 17(7):1093–1109, 2014.
- JD Anderson Jr. *Fundamentals of aerodynamics*. Tata McGraw-Hill Education, 2010.
- GA Ashford and KG Powell. An unstructured grid generation and adaptive solution technique for high-reynolds-number compressible flows. *Lecture series-van Karemán Institute for fluid dynamics*, 6:J1–J110, 1996.
- A Bechmann, NN Sørensen, and F Zahle. Cfd simulations of the mexico rotor. *Wind Energy*, 14(5):677–689, 2011.
- K Boorsma and JG Schepers. New mexico experiment, preliminary overview with initial validation. Technical report, Energy Research Center of the Netherlands, ECN, 2014.
- BM Bragg, DC Heinrich, FA Balow, and KBMQ Zaman. Flow oscillation over an airfoil near stall. *AIAA journal*, 34(1):199–201, 1996.
- AL Braslow and EC Knox. *Simplified method for determination of critical height of distributed roughness particles for boundary-layer transition at Mach numbers from 0 to 5*. National Advisory Committee for Aeronautics, 1958.
- P Brøndsted and RPL Nijssen. *Advances in wind turbine blade design and materials*. Elsevier, 2013.
- B Cabral and LC Leedom. Imaging vector fields using line integral convolution. In *Proceedings of the 20th annual conference on Computer graphics and interactive techniques*, pages 263–270. ACM, 1993.
- V Campo, D Ragni, D Micallef, B Akay, FJ Diez, and C Simão Ferreira. 3d load estimation on a horizontal axis wind turbine using spiv. *Wind Energy*, 17(11):1645–1657, 2014.
- FN Coton and T Wang. The prediction of horizontal axis wind turbine performance in yawed flow using an unsteady prescribed wake model. *Proceedings of the Institution of Mechanical Engineers, Part A: Journal of Power and Energy*, 213(1):33–43, 1999.

- Global Wind Energy Council. Global wind report 2015 - annual market update. *GWEC, Brussels*, 2015.
- M Dimchev. Experimental and numerical study on wingtip mounted propellers for low aspect ratio uav design. Master of science thesis, Delft University of Technology, Delft, the Netherlands, 2012.
- K Dixon. The near wake structure of a vertical axis wind turbine. Master of science thesis, Delft University of Technology, Delft, the Netherlands, 2008.
- K Dixon, CJ Simao Ferreira, C Hofemann, GJW Van Bussel, and GAM Van Kuik. A 3d unsteady panel method for vertical axis wind turbines. In *The proceedings of the European Wind Energy Conference & Exhibition EWEK Brussels, 1-10*. European Wind Energy Association EWEA, 2008.
- Earl PN Duque, Michael D Burklund, and Wayne Johnson. Navier-stokes and comprehensive analysis performance predictions of the nrel phase vi experiment. *Journal of Solar Energy Engineering*, 125(4):457–467, 2003.
- HA Dwyer and WJ Aiccrokey. Crossflow and unsteady boundary-layer effects on rotating blades. *AIAA Journal*, 9(8):1498–1505, 1971.
- CP VanDam R Cortes EP Duque, W Johnson and K Yee. Numerical predictions of wind turbine power and aerodynamic loads for the nrel phase ii combined experiment rotor. Technical report, DTIC Document, 2000.
- EWEA. *Wind energy-the facts: a guide to the technology, economics and future of wind power*. Routledge, 2012.
- EWEA. *Wind Energy Scenarios for 2030*. Ewea, 2015.
- PE Farrell and JR Maddison. Conservative interpolation between volume meshes by local galerkin projection. *Computer Methods in Applied Mechanics and Engineering*, 200(1): 89–100, 2011.
- CJ Simao Ferreira. *The near wake of the VAWT: 2D and 3D views of the VAWT aerodynamics*. PhD thesis, Delft University of Technology, Delft, the Netherlands, 2010.
- JH Ferziger and M Peric. *Computational methods for fluid dynamics*. Springer Science & Business Media, 2012.
- J Fürst, J Přihoda, and P Straka. Numerical simulation of transitional flows. *Computing*, 95(1):163–182, 2013.
- H Glauert. *The analysis of experimental results in the windmill brake and vortex ring states of an airscrew*. HM Stationery Office, 1926a.
- H Glauert. *A general theory of the autogyro*, volume 1111. HM Stationery Office, 1926b.
- H Glauert. Airplane propellers. In *Aerodynamic theory*, pages 169–360. Springer, 1935.

- S Guntur and N N Sørensen. An evaluation of several methods of determining the local angle of attack on wind turbine blades. In *Journal of Physics: Conference Series*, volume 555, page 012045. IOP Publishing, 2014.
- W Haans. *Wind turbine aerodynamics in yaw: unravelling the measured rotor wake*. PhD thesis, Delft University of Technology, Delft, the Netherlands, 2011.
- W Haans, GAM van Kuik, and GJW van Bussel. Experimentally observed effects of yaw misalignment on the inflow in the rotor plane. In *Journal of Physics: Conference Series*, volume 75, page 012012. IOP Publishing, 2007.
- W Haans, T Sant, G van Kuik, and G van Bussel. Hawt near-wake aerodynamics, part i: axial flow conditions. *Wind Energy*, 11(3):245–264, 2008.
- M Maureen Hand, DA Simms, LJ Fingersh, DW Jager, JR Cotrell, S Schreck, and SM Larwood. *Unsteady aerodynamics experiment phase VI: wind tunnel test configurations and available data campaigns*. National Renewable Energy Laboratory Golden, Colorado, USA, 2001.
- M Hansen. *Aerodynamics of wind turbines*. Earthscan, 2000.
- M Hansen, N N Sørensen, and JA Michelsen. Extraction of lift, drag and angle of attack from computed 3-d viscous flow around a rotating blade. In *1997 European Wind Energy Conference*, 1997.
- F Harris. Preliminary study of radial flow effects on rotor blades. *Journal of the American Helicopter Society*, 11(3):1–21, 1966.
- I Herráez, B Akay, G van Bussel, J Peinke, and B Stoevesandt. Detailed analysis of the blade root flow of a horizontal axis wind turbine. *Wind Energy Science*, 1(2):89–100, 2016.
- H Himmelskamp. *Profile Investigations on a Rotating Airscrew*. PhD thesis, Göttingen, 1945.
- H Horton. *Laminar separation bubbles in two and three dimensional incompressible flow*. PhD thesis, University of London, London, UK, 1968.
- J Hunt, AA Wray, and P Moin. Eddies, streams, and convergence zones in turbulent flows. Technical report, Center for Turbulence Research, 1988.
- RI Issa, AD Gosman, and AP Watkins. The computation of compressible and incompressible recirculating flows by a non-iterative implicit scheme. *Journal of Computational Physics*, 62(1):66–82, 1986.
- J Johansen, NN Sorensen, JA Michelsen, and S Schreck. Detached-eddy simulation of flow around the nrel phase-vi blade. In *ASME 2002 Wind Energy Symposium*, pages 106–114. American Society of Mechanical Engineers, 2002.
- J Katz and A Plotkin. *Low-speed aerodynamics*, volume 13. McGraw-Hill, New York, 1991.



- SL Krist, RT Biedron, and CL Rumsey. Cfl3d user's manual (version 5.0). 1998.
- BE Launder and BI Sharma. Application of the energy-dissipation model of turbulence to the calculation of flow near a spinning disc. *Letters in heat and mass transfer*, 1(2): 131–137, 1974.
- HM Lee and Y Wu. An experimental study of stall delay on the blade of a horizontal-axis wind turbine using tomographic particle image velocimetry. *Journal of Wind Engineering and Industrial Aerodynamics*, 123:56–68, 2013.
- JG Leishman. Challenges in modeling the unsteady aerodynamics of wind turbines. In *ASME 2002 Wind Energy Symposium*, pages 141–167. American Society of Mechanical Engineers, 2002.
- Y Li, KJ Paik, T Xing, and PM Carrica. Dynamic overset cfd simulations of wind turbine aerodynamics. *Renewable Energy*, 37(1):285–298, 2012.
- C Lindenburg. Modelling of rotational augmentation based on engineering considerations and measurements. In *European Wind Energy Conference (EWEC 2004), London, UK, Nov*, pages 22–25, 2004.
- RE Mayle and A Schulz. Heat transfer committee and turbomachinery committee best paper of 1996 award: the path to predicting bypass transition. *Journal of turbomachinery*, 119(3):405–411, 1997.
- F Menter. Two-equation eddy-viscosity turbulence models for engineering applications. *AIAA journal*, 32(8):1598–1605, 1994.
- F Menter and T Esch. Elements of industrial heat transfer predictions. In *16th Brazilian Congress of Mechanical Engineering (COBEM)*, volume 109, 2001.
- D Micallef. *3D flows near a HAWT rotor: A dissection of blade and wake contributions*. PhD thesis, Delft University of Technology, Delft, the Netherlands, 2012.
- D Micallef, G van Bussel, C Simão Ferreira, and T Sant. An investigation of radial velocities for a horizontal axis wind turbine in axial and yawed flows. *Wind Energy*, 16(4): 529–544, 2013.
- D Micallef, Carlos Simão Ferreira, T Sant, and G van Bussel. Experimental and numerical investigation of tip vortex generation and evolution on horizontal axis wind turbines. *Wind Energy*, 19(8):1485–1501, 2016.
- R Mikkelsen. *Actuator disc methods applied to wind turbines*. PhD thesis, Technical University of Denmark, Lyngby, Denmark, 2003.
- PJ Moriarty and AC Hansen. *AeroDyn theory manual*. National Renewable Energy Laboratory Golden, Colorado, USA, 2005.
- RD Moser, J Kim, and NN Mansour. Direct numerical simulation of turbulent channel flow up to  $Re = 590$ . *Phys. Fluids*, 11(4):943–945, 1999.

- I Nezu and A Tominaga. *Sugaring*. Asakura Shoten, 2000.
- SV Patankar and DB Spalding. A calculation procedure for heat, mass and momentum transfer in three-dimensional parabolic flows. *International journal of heat and mass transfer*, 15(10):1787–1806, 1972.
- SD Pesmajoglou and JMR Graham. Prediction of aerodynamic forces on horizontal axis wind turbines in free yaw and turbulence. *Journal of Wind Engineering and Industrial Aerodynamics*, 86(1):1–14, 2000.
- DM Pitt and DA Peters. Theoretical prediction of dynamic-inflow derivatives. *Vertica*, 5(1):21–34, 1981.
- SB Pope. *Turbulent Flows*. Cambridge University Press, 2000.
- D Ragni. *PIV-based load determination in aircraft propellers*. PhD thesis, Delft University of Technology, Delft, the Netherlands, 2012.
- CM Rhie and WL Chow. Numerical study of the turbulent flow past an airfoil with trailing edge separation. *AIAA journal*, 21(11):1525–1532, 1983.
- DJ Robison, FN Coton, RAM Galbraith, and M Vezza. The development of a prescribed wake model for performance prediction in steady yawed flow. Technical report, American Society of Mechanical Engineers, New York, NY (United States), 1995a.
- DJ Robison, FN Coton, RAMcd Galbraith, and M Vezza. Application of a prescribed wake aerodynamic prediction scheme to horizontal axis wind turbines in axial flow. *Wind Engineering*, 19(1):41–51, 1995b.
- W Rodi, G Constantinescu, and T Stoesser. *Large-eddy simulation in hydraulics*. Crc Press, 2013.
- AM Feingold RP Coleman and CW Stempin. Evaluation of the induced-velocity field of an idealized helicopter rotor. Technical report, DTIC Document, 1945.
- C Rumsey. Nasa langley research center turbulence modeling resource, 2014.
- CL Rumsey, DO Allison, RT Biedron, PG Buning, TG Gainer, JH Morrison, SM Rivers, SJ Mysko, and DP Witkowski. Cfd sensitivity analysis of a modern civil transport near buffet-onset conditions. Technical report, NASA, 2001.
- JG Schepers and K Boorsma. *IEA Wind Task 29 MexNext*, 2015. URL <http://www.mexnext.org/>.
- JG Schepers and H Snel. Model experiments in controlled conditions. *ECN Report: ECN-E-07-042*, 2007.
- JG Schepers, K Boorsma, T Cho, S Gomez-Iradi, P Schaffarczyk, A Jeromin, WZ Shen, T Lutz, K Meister, B Stoevesandt, et al. Final report of iea task 29, mexnext (phase 1): Analysis of mexico wind tunnel measurements. Technical report, Energy Research Centre of the Netherlands ECN, 2011.

- JG Schepers, K Boorsma, T Cho, S Gomez-Iradi, P Schaffarczyk, A Jeromin, Wen Zhong Shen, T Lutz, K Meister, B Stoevesandt, et al. Analysis of mexico wind tunnel measurements. Technical report, Energy Research Centre of the Netherlands ECN, 2012.
- S Schreck. Spectral content and spatial scales in unsteady rotationally augmented flow fields. In *Journal of Physics: Conference Series*, volume 75, page 012024. IOP Publishing, 2007.
- S Schreck. Low frequency shedding prompted by three-dimensionality under rotational augmentation. In *48th AIAA Aerospace Sciences Meeting Including the New Horizons Forum and Aerospace Exposition*, page 640, 2010.
- MS Selig. *Summary of low speed airfoil data*, volume 1. SoarTech, 1995.
- WZ Shen, R Mikkelsen, JN Sørensen, and C Bak. Tip loss corrections for wind turbine computations. *Wind Energy*, 8(4):457–475, 2005.
- M Shur, PR Spalart, M Strelets, and A Travin. Detached-eddy simulation of an airfoil at high angle of attack. *Engineering turbulence modelling and experiments*, 4:669–678, 1999.
- C Sicot, P Devinant, S Loyer, and J Hureau. Rotational and turbulence effects on a wind turbine blade. investigation of the stall mechanisms. *Journal of wind engineering and industrial aerodynamics*, 96(8):1320–1331, 2008.
- DA Simms, S Schreck, M Hand, and LJ Fingersh. *NREL unsteady aerodynamics experiment in the NASA-Ames wind tunnel: a comparison of predictions to measurements*. National Renewable Energy Laboratory Golden, CO, USA, 2001.
- H Snel. Review of the present status of rotor aerodynamics. *Wind Energy*, 1(s 1):46–69, 1998.
- H Snel and JG Schepers. *Joint investigation of dynamic inflow effects and implementation of an engineering method*. Netherlands Energy Research Foundation ECN, 1995.
- H Snel, JG Schepers, and B Montgomerie. The mexico project (model experiments in controlled conditions): The database and first results of data processing and interpretation. In *Journal of Physics: Conference Series*, volume 75, page 012014. IOP Publishing, 2007.
- H Snel, JG Schepers, A v Garrel, and S Barth. The mexico project: Analysis of yaw measurements and comparison with existing models. *Proceedings of European Wind Energy Conference*, 2008.
- N Sorensen and M Hansen. Rotor performance predictions using a navier-stokes method. In *Proceedings 1998 ASME Wind Energy Symposium, 36th AIAA Aerospace Sciences Meeting and Exhibit, AIAA-98-0025, Reno, NV*, 1998.
- NN Sørensen. Cfd modelling of laminar-turbulent transition for airfoils and rotors using the  $\gamma$ - model. *Wind Energy*, 12(8):715–733, 2009.

- PR Spalart, WH Jou, M Strelets, and SR Allmaras. Comments on the feasibility of les for wings, and on a hybrid rans/les approach. *Advances in DNS/LES*, 1:4–8, 1997.
- PR Spalart, S Deck, ML Shur, KD Squires, M Kh Strelets, and A Travin. A new version of detached-eddy simulation, resistant to ambiguous grid densities. *Theoretical and computational fluid dynamics*, 20(3):181–195, 2006.
- KE Swalwell, J Sheridan, and WH Melbourne. Frequency analysis of surface pressures on an airfoil after stall. *AIAA Paper*, 3416:2003, 2003.
- NN Sørensen, J. A. Michelsen, and S. Schreck. Navier–Stokes predictions of the NREL phase VI rotor in the NASA ames 80 ft x 120 ft wind tunnel. *Wind Energy*, 5(2-3): 151–169, 2002.
- NS Tachos, AE Filios, DP Margaritis, and JK Kaldellis. A computational aerodynamics simulation of the nrel phase ii rotor. *Open Mechanical Engineering Journal*, 3:9–16, 2009.
- JL Tangler. The nebulous art of using wind-tunnel airfoil data for predicting rotor performance. In *ASME 2002 Wind Energy Symposium*, pages 190–196. American Society of Mechanical Engineers, 2002.
- JL Tangler. Insight into wind turbine stall and post-stall aerodynamics. *Wind Energy*, 7(3):247–260, 2004.
- LAM Tossas and S Leonardi. Wind turbine modeling for computational fluid dynamics: December 2010-december 2012. Technical report, National Renewable Energy Laboratory (NREL), Golden, CO., 2013.
- N Troldborg. *Actuator line modeling of wind turbine wakes*. PhD thesis, Technical University of Denmark, Lyngby, Denmark, 2009.
- MF Unal, J-C Lin, and D Rockwell. Force prediction by piv imaging: a momentum-based approach. *Journal of Fluids and Structures*, 11(8):965–971, 1997.
- A van Garrel. *Development of a Wind Turbine Aerodynamics Simulation Module*. ECN.: C-serie. Energy research Centre of the Netherlands ECN, 2003.
- GAM van Kuik, D Micallef, I Herraiez, AH van Zuijlen, and D Ragni. The role of conservative forces in rotor aerodynamics. *Journal of Fluid Mechanics*, 750:284–315, 2014.
- RPJOM Van Rooij. Modification of the boundary layer calculation in rfoil for improved airfoil stall prediction. *Report IW-96087R TU-Delft, the Netherlands*, 1996.
- RPJOM Van Rooij and WA Timmer. Roughness sensitivity considerations for thick rotor blade airfoils. *Journal of Solar Energy Engineering*, 125(4):468–478, 2003.
- LJ Vermeer, JN Sørensen, and A Crespo. Wind turbine wake aerodynamics. *Progress in aerospace sciences*, 39(6):467–510, 2003.
- T von Kármán. Mechanische Ähnlichkeit und turbulenz, nachr. ges. wiss gottingen, math. phys. klasse; 1930, 5. *English translation, NACA TM*, 611:58–76, 1931.

- D Keith Walters and Davor Cokljat. A three-equation eddy-viscosity model for reynolds-averaged navier–stokes simulations of transitional flow. *Journal of fluids engineering*, 130(12):121401, 2008.
- DK Walters and JH Leylek. A new model for boundary-layer transition using a single-point rans approach. In *ASME 2002 International Mechanical Engineering Congress and Exposition*, pages 67–79. American Society of Mechanical Engineers, 2002.
- DK Walters and JH Leylek. Computational fluid dynamics study of wake-induced transition on a compressor-like flat plate. *Journal of Turbomachinery*, 127(1):52–63, 2005.
- H Weller. Controlling the computational modes of the arbitrarily structured c grid. *Monthly Weather Review*, 140(10):3220–3234, 2012.
- J Whale, CG Anderson, R Bareiss, and S Wagner. An experimental and numerical study of the vortex structure in the wake of a wind turbine. *Journal of Wind Engineering and Industrial Aerodynamics*, 84(1):1–21, 2000.
- Y Zhang, A Van Zuijlen, and G Van Bussel. Comparison of cfd simulations to non-rotating mexico blades experiment in the ltt wind tunnel of tudelft. In *Journal of Physics: Conference Series*, volume 524, pages 012013–012024. IOP Publishing, 2014.
- Y Zhang, A Van Zuijlen, and G van Bussel. Massively separated turbulent flow simulation around non-rotating mexico blade by means of rans and ddes approaches in openfoam. In *33rd AIAA Applied Aerodynamics Conference*, pages 2716–2726, 2015.
- Y Zhang, T Gillebaart, A van Zuijlen, G van Bussel, and H Bijl. Experimental and numerical investigations of aerodynamic loads and 3d flow over non-rotating mexico blades. *Wind Energy*, 20(4):585–600, 2017.

# ACKNOWLEDGEMENTS

This thesis is the outcome of my research during the past four years in Wind Energy (WE) Group at Delft University of Technology. My research is also funded by the continuous financial support from Chinese Scholarship Council (grant no. 201206060043). At this moment, I would like to thank all their support during my doctoral study.

First of all, most thanks go to my daily supervisor Dr. Alexander van Zuijlen for his supervision during past years. You always have incredible patience and unique vision when we encounter any problems. Your professional knowledge and strong motivation guide me smoothly to finish my Ph.D study. I also would like to give my sincere gratitude to my promoter, Prof. Gerard van Bussel for his endless love and trust. To him, I am still a baby in the world of wind energy. Gerard, thank you for bringing me up in this wonderful research field. Special thanks will be given to Prof. Hester Bijl for her help and fruitful discussion.

Particular thanks are given to my fellow Thijs Gillebaart for his OpenFOAM related help. It was really excellent experience working with you, and I enjoyed it a lot. Meanwhile, my project partners Koen Boorsma and Gerard Schepers from ECN are gratefully acknowledged for the collaboration.

I want to thank our secretary Sylvia for her efficiency and patience. Besides, I would like to express my appreciation to all my colleagues: Gijs, Carlos, Nando, Lars, Ricardo, Etana, Maarten, Cyril, Daniele, Bursa, Daniel, Lorenzo, Gael, Rene, Carlos Baptista, Sebastian, Wouter. Thank you all for interesting conversation and all kinds of help. I also want to thank my friends Sun Zhengzhong, Deng Shuanghou, Xu Xiaojun, Li Qingxi, Yang Yannian, Guo Yuanhao, Ye Qingqing, Wang Zi, Yu Wei, Tang Juan, Zhao Xiaojia, Cheng Lei for our happy time.

I also would like to thank all my brothers and sisters at Delft Fellowship, from whom I have learned not only a lot of biblical knowledge but also faith, hope, love, and humility.

Many thanks go to my parents for their endless support, encouragement, and love.

Last but not least, I would like give my great thanks to my wife Shiyao, for her understanding, encouragement and unconditional love.

Ye Zhang  
Delft, September 2016



# LIST OF PUBLICATIONS

**Zhang, Y**, van Zuijlen, A, van Bussel, G, & Bijl, H(2017), *Experimental and numerical investigations of aerodynamic loads and 3D flow over non-rotating MEXICO blades*. Wind Energy. 20(4):585-600.

**Zhang, Y**, van Zuijlen, A, & van Bussel, G (2014), *Comparison of CFD simulations to non-rotating MEXICO blades experiment in the LTT wind tunnel of TUDelft*. Journal of Physics: Conference Series. 524:012013-012024.

**Zhang, Y**, van Zuijlen, A, & van Bussel, G (2017), *The MEXICO rotor aerodynamic loads prediction: ZigZag effects and laminar-turbulent transition modeling in CFD*. Journal of Wind Engineering & Industrial Aerodynamics. submitted.

Mehta, D, **Zhang, Y**, van Zuijlen, A, & Bijl, H (2017), *LES for industrial wind farm aerodynamics: a note on special discretisation*. Journal of Wind Engineering and Industrial Aerodynamics. submitted.

**Zhang, Y**, Sun, Z, van Zuijlen, A, & van Bussel, G (2017), *Numerical simulation of transitional flow on a wind turbine airfoil with RANS-based transition model* Journal of Turbulence. accepted

**Zhang, Y**, Van Zuijlen, A. H, & van Bussel, G (2015), *Comparison of different rotating modelling techniques for 3D wind turbine rotor simulation*. 11th PhD seminar on Wind Energy in Europe (pp.1-4). Stuttgart, Germany.

**Zhang, Y**, Van Zuijlen, A. H, & van Bussel, G (2015), *Massively separated turbulent flow simulation around non-rotating MEXICO blade by means of RANS and DDES approaches in OpenFOAM*. 33rd AIAA Applied Aerodynamics Conference 2015 (pp.1-10). Dallas, USA.

**Zhang, Y**, Gillebaart, T, van Bussel, G, & Bijl, H.(2013), *Validation of a transition model for the DU91-W2-250 airfoil*. 9th PhD seminar on Wind Energy in Europe (pp.1-5). Visby, Sweden.

**Zhang, Y**, Van Zuijlen, A. H, & van Bussel, G (2016), *The influence of ZigZag strip on wind turbine aerodynamic loads in wind tunnel measurement and CFD predictions*. 2016 Applied Aerodynamics Conference. Bristol, UK.

**Zhang, Y**, Van Zuijlen, A. H, & van Bussel, G (2016), *Boundary layer transition prediction for wind energy application using OpenFOAM*. The Fourth Symposium on OpenFOAM in Wind Energy. Delft, the Netherlands.





# CURRICULUM VITÆ

Ye Zhang was born on July 10<sup>th</sup> 1986, in KeShan, China.

He obtained his bachelor degree in 2009 with honour at Dalian University of Technology. Three years later, he finished his study in Turbomachinery and Fluid Dynamics Engineering in the same university and obtained his MSc degree with honour. After that, Ye came to Delft with Chinese Government Scholarship program to continue study in the Faculty of Aerospace Engineering at Delft University of Technology.

Besides his study, he loves cooking, traveling and experiencing different culture across the world. He is always amazed by the incredible beauty of the nature.

He is married to Shiyao. She was his classmate at Dalian University of Technology and had been being happy time together for 7 years. Currently, they are planning to receive wonderful gifts from God: two happy children.